VALIDATION OF THE BACKGROUND MODEL FOR THE MAJORANA DEMONSTRATOR

Jacqueline MacMullin

A dissertation submitted to the faculty of the University of North Carolina at Chapel Hill in partial fulfillment of the requirements for the degree of Doctor of Philosophy in the Department of Physics and Astronomy.

Chapel Hill
2015

Approved by:

John Wilkerson

Reyco Henning

David Radford

Jonathan Engel

Christian Iliadis

ABSTRACT

Jacqueline MacMullin: Validation of the Background Model for the MAJORANA DEMONSTRATOR.
(Under the direction of John Wilkerson.)

The observation of neutrinoless double-beta decay would confirm the Majorana nature of the neutrino and would allow one to potentially determine the mass of neutrinos. The goal of the MAJORANA collaboration is to develop a tonne-scale Ge-76-based neutrinoless double-beta decay experiment. Currently, efforts are underway to construct the MAJORANA DEMONSTRATOR, a 44.8-kg array of germanium crystals, located at the 4850′ level of the Sanford Underground Research Facility (SURF) in Lead, SD. The goal of the DEMONSTRATOR is to demonstrate the ability to construct a detector composed of an array of germanium crystals while maintaining an unprecedented low background that is essential for the observation of neutrinoless double-beta decay.

Before the assembly and operation of the DEMONSTRATOR, a single test cryostat was built. This cryostat, referred to as the Prototype Cryostat, was built to test the clean assembly procedures that are to be used for the DEMONSTRATOR. Understanding the backgrounds of the MAJORANA DEMONSTRATOR is of the upmost importance and for this reason, much effort has been put into creating an accurate background model. While achieving the lowest possible background is the goal of the DEMONSTRATOR, this is not necessarily true of the Prototype Cryostat, whose main purpose is to improve on cryostat assembly procedures, analysis routines and the like. Nevertheless, understanding the backgrounds of the Prototype Cryostat can help to verify the background model of the DEMONSTRATOR. Thus a background model of the Prototype Cryostat has been developed using the same techniques that are being used to develop the background

model of the DEMONSTRATOR. This dissertation discusses the development of the Prototype Cryostat background model, its successes and failures, and the implications for the DEMONSTRATOR.

To Mom and Dad. Thank you for your endless love and support.

TABLE OF CONTENTS

LIST OF FIGURES

LIST OF TABLES

LIST OF ABBREVIATIONS

$0\nu\beta\beta$	neutrinoless double-beta decay
$2\nu\beta\beta$	two-neutrino double-beta decay
BEGe	Broad Energy Germanium
CDF	Cumulative Distribution Function
CP	charge-parity
DAQ	data acquistion
DQ	data quality
GAT	Germanium Analysis Toolkit
GDMS	Glow Discharge Mass Spectroscopy
HPGe	High-Purity Germanium
ICPMS	Inductively-Coupled Plasma Mass Spectrometry
JSON	JavaScript Object Notation
KS test	Kolmogorov-Smirnov test
KURF	Kimballton Underground Research Facility
LMFE	Low Mass Front End
LNGS	Laboratori Nazionali del Gran Sasso
MALBEK	MAJORANA Low-background BEGe at KURF
MC	Monte Carlo
NAA	Neutron Activation Analysis
NERSC	National Energy Research Scientific Computing Center
NLL	Negative Log-Likelihood
NME	Nuclear Matrix Elements
OFHC	Oxygen-Free High thermal Conductivity
ORCA	Object-oriented Real-time Control and Acquisition
PC	Prototype Cryostat
PDF	Probability Distribution Function

PDSF	Parallel Distributed Systems Facility
PEEK	Polyether Ether Ketone
PMNS	Pontecorvo-Maki-Nakagawa-Sakata
P-PC	p-type point contact
PSA	pulse-shape analysis
PTDB	Parts Tracking Database
PTFE	Polytetrafluoroethylene
QRPA	Quasiparticle Random Phase Approximation
ROI	region of interest
SBC	Single Board Computer
SS	Stainless Steel
STC	String Test Cryostat
SURF	Sanford Underground Research Facility
UGEFCu	Underground Electroformed Copper
WIMPs	Weakly-Interacting Massive Particles

CHAPTER 1: INTRODUCTION

1.1 Neutrino Oscillation and Mass

In 1930 Pauli first proposed the existence of the neutrino to explain the continuous - rather than delta - energy distribution of the beta decay spectrum. Pauli proposed that the neutrino is a neutral particle that only interacts weakly. In 1956 the neutrino was first detected by Cowan and Reines [CC56]. In the following 60 years much progress has been made in understanding the properties of the neutrino. It is now known that there are three flavors of neutrinos – electron, muon and tau – with each flavor constituting a unique eigenstate. Furthermore there are three mass eigenstates and they can be written as a superposition of the flavor eigenstates and vice versa. The mixing of the flavor and mass eigenstates is described by Eq. 1.1, where the mixing matrix (with elements U_{fi}) is the Pontecorvo-Maki-Nakagawa-Sakata (PMNS) matrix in Eq. 1.2 [Aal04, Ell02, LC08].

$$\begin{bmatrix} \nu_e \\ \nu_\mu \\ \nu_\tau \end{bmatrix} = \begin{bmatrix} U_{e\,1} & U_{e\,2} & U_{e\,3} \\ U_{\mu\,1} & U_{\mu\,2} & U_{\mu\,3} \\ U_{\tau\,1} & U_{\tau\,2} & U_{\tau\,3} \end{bmatrix} \begin{bmatrix} \nu_1 \\ \nu_2 \\ \nu_3 \end{bmatrix} \tag{1.1}$$

$$U = \begin{bmatrix} c_{12}c_{13} & s_{12}c_{13} & s_{13}e^{-i\delta} \\ -s_{12}c_{23} - c_{12}s_{23}s_{13}e^{i\delta} & c_{12}c_{23} - s_{12}s_{23}s_{13}e^{i\delta} & s_{23}c_{13} \\ s_{12}s_{23} - c_{12}c_{23}s_{13}e^{i\delta} & -c_{12}s_{23} - s_{12}c_{23}s_{13}e^{i\delta} & c_{23}c_{13} \end{bmatrix} \begin{bmatrix} e^{i\alpha_1/2} & 0 & 0 \\ 0 & e^{i\alpha_2/2} & 0 \\ 0 & 0 & 1 \end{bmatrix} \tag{1.2}$$

In Eq. 1.2, $c_{ij} = cos\theta_{ij}$ and $s_{ij} = sin\theta_{ij}$, where θ_{ij} are referred to as the mixing

angles. Because the flavor and mass eigenstates are not the same, neutrinos oscillate between the three flavors as they propagate through space; hence the term "mixing". The probability that a f-flavored neutrino will oscillate to a f'-flavored neutrino is given by Eq. 1.3 [Aal04].

$$P\left(\nu_f \to \nu_{f' \neq f}\right) = \left| \sum_i U_{fi}\, e^{-i\frac{m_i^2 L}{2E}}\, U_{f'i}^* \right|^2$$
$$P\left(\nu_f \to \nu_{f' \neq f}\right) = \sin^2 2\theta \sin^2 \left[1.27 \left|\Delta m_{ji}^2\right| \left(\mathrm{eV}^2\right) \frac{L(\mathrm{km})}{E_\nu(\mathrm{GeV})} \right] \tag{1.3}$$

It can be seen from Eq. 1.3 that neutrino oscillation requires that neutrinos have a non-zero mass. Furthermore neutrino oscillation experiments are limited in that they can only determine the differences in the squares of the neutrino masses (i.e. Δm_{ji}^2; Eq. 1.4).

$$\Delta m_{ji}^2 = m_j^2 - m_i^2 \tag{1.4}$$

To measure the absolute differences in neutrino masses (Δm_{ji}^2) and the mixing angles (θ_{ij}), neutrino oscillation experiments must optimize the distance between the detector and the source of neutrinos (i.e. L of Eq. 1.3) relative to the energy of the neutrinos from the source (i.e. E_ν of Eq. 1.3). Based on observations of solar neutrino oscillations, it is known that $\Delta m_{21}^2 > 0$, however it is unknown if Δm_{32}^2 is positive or negative. The unknown sign of Δm_{32}^2 presents two possible neutrino hierarchies: a normal mass hierarchy if Δm_{32}^2 is positive and an inverted mass hierarchy if Δm_{32}^2 is negative. The current values of Δm_{32}^2 and Δm_{21}^2 are in Eq. 1.5. Equation 1.6 gives the current values of the neutrino mixing angles [Oli14].

Based on observations of solar neutrino oscillations, it is known that $\Delta m_{21}^2 > 0$,

however it is unknown if Δm^2_{32} is positive or negative. The unknown sign of Δm^2_{32} presents two possible neutrino hierarchies: a normal mass hierarchy if Δm^2_{32} is positive and an inverted mass hierarchy if Δm^2_{32} is negative. The current values of Δm^2_{32} and Δm^2_{21} are in Eq. 1.5 [Oli14]. Equation 1.6 gives the current values of the neutrino mixing angles.

$$\begin{aligned} \Delta m^2_{21} &= (7.53 \pm 0.18) \cdot 10^{-5} \text{eV}^2 \\ \Delta m^2_{32} &= \begin{cases} (2.44 \pm 0.06) \cdot 10^{-3} \text{eV}^2 & \text{Normal Hierarchy} \\ (2.52 \pm 0.07) \cdot 10^{-3} \text{eV}^2 & \text{Inverted Hierarchy} \end{cases} \end{aligned} \tag{1.5}$$

$$\begin{aligned} sin^2\left(\theta_{12}\right) &= 0.846 \pm 0.021 \\ sin^2\left(\theta_{13}\right) &= (9.3 \pm 0.8) \cdot 10^{-2} \\ sin^2\left(\theta_{23}\right) &= \begin{cases} 0.999^{+0.001}_{-0.018} & \text{Normal Hierarchy} \\ 1.000^{+0.000}_{-0.017} & \text{Inverted Hierarchy} \end{cases} \end{aligned} \tag{1.6}$$

The remaining three variables in the PMNS matrix (Eq. 1.2) are the phase factors: α_1, α_2 and δ. If neutrino oscillation violates charge-parity (CP) symmetry the phase factor δ is non-zero. Given that the neutrino is a neutrally-charged particle, it is possible that the neutrino and anti-neutrino are the same particle that simply have a different chirality. If the neutrino is a Majorana particle (i.e. it is the same as its anti-particle), the phase factors α_1 and α_2 are required to fully describe the system.

1.1.1 Neutrinoless Double-Beta Decay

For some even-even nuclei, beta decay is energetically forbidden or strongly suppressed. It has been observed that these nuclei undergo two-neutrino double-beta

decay ($2\nu\beta\beta$) (Eq. 1.7).

$$(A, Z) \rightarrow (A, Z + 2) + 2e^- + 2\bar{\nu_e} \tag{1.7}$$

If the neutrino is a Majorana particle, it is possible for such nuclei to decay via neutrinoless double-beta decay ($0\nu\beta\beta$) (Eq. 1.8).

$$(A, Z) \rightarrow (A, Z + 2) + 2e^- \tag{1.8}$$

While $2\nu\beta\beta$ has been observed, $0\nu\beta\beta$ has not yet been observed. The observation of this decay mode would confirm the Majorana nature of the neutrino [Sch82]. Furthermore, the observation of $0\nu\beta\beta$ would allow one to determine the mass of neutrinos. Assuming light neutrino exchange moderates the neutrinoless double-beta decay process, the half-life is

$$\left[T_{1/2}^{0\nu\beta\beta}\right]^{-1} = G_{0\nu} \left|M_{0\nu}\right|^2 m_{\beta\beta}^2 \tag{1.9}$$

where $G_{0\nu}$ is the phase-space factor and $M_{0\nu}$ is the Nuclear Matrix Elements (NME). The effective Majorana mass, $m_{\beta\beta}$, is expressed in Eq. 1.10 where m_i are the mass eigenstates and U_{ei} are the elements of the PMNS matrix (Eq. 1.2) that describe how the electron flavor mixes with the neutrino masses.

$$m_{\beta\beta} = \left| \sum_i U_{ei}^2 \, m_i \right| \tag{1.10}$$

The phase factor is calculable however the NME is more complex and must be approximated with a model. Several models exist including the Shell Model and the Quasiparticle Random Phase Approximation (QRPA), however many of the models

Table 1.1: The half-life of $2\nu\beta\beta$ and $0\nu\beta\beta$ in ^{76}Ge, ^{136}Xe and ^{130}Te.

Nuclide	$T^{2\nu}_{1/2}$ [10^{21} yr]	$T^{0\nu}_{1/2}$ [10^{25} yr]
^{76}Ge	$1.84^{+0.14}_{-0.10}$ [Col13]	> 3.0 (90% C.L.) [Mac14]
		> 1.9 (90% C.L.) [KK01]
^{136}Xe	$2.165 \pm 0.016_{\text{stat}} \pm 0.059_{\text{sys}}$ [Alb14]	> 1.9 (90% C.L.) [Gan13]
		> 1.6 (90% C.L.) [Aug12]
^{130}Te	$0.7 \pm 0.09_{\text{stat}} \pm 0.11_{\text{sys}}$ [Arn11]	≥ 0.3 (90% C.L.) [Arn08]

disagree with one another up to a factor of two or three [Ber12]. Therefore it is important that if $0\nu\beta\beta$ is discovered it should be verified with another nuclide. This is true not only because of the uncertainty of the NME but also because of the rare nature of $0\nu\beta\beta$. Even the most stringent upper limits on the half-life of $0\nu\beta\beta$ are no less than 10^{25} years, as seen in Table 1.1. There are about a dozen even-even nuclides that are candidates for $0\nu\beta\beta$; the three nuclides listed in Table 1.1 were chosen because, to date, they place the best upper limit on the half-life of $0\nu\beta\beta$. The best limit for ^{130}Te has been placed by the CUORICINO experiment [Arn08]. The best limit for ^{136}Xe has been placed by both the EXO-200 and KamLAND-Zen experiments [Aug12, Gan13]. And currently the best limit for ^{76}Ge has been placed by the Heidelberg-Moscow and GERDA experiments [KK01, Mac14].

The nuclide ^{76}Ge is particularly interesting since, being a semiconductor, germanium has the advantage that it can serve as both the detector and source of $0\nu\beta\beta$. The signature of $0\nu\beta\beta$ in ^{76}Ge is a mono-energetic peak at 2039 keV; the endpoint of the $2\nu\beta\beta$ continuous beta spectrum. Several experiments, past and present, are searching for $0\nu\beta\beta$ in ^{76}Ge. While Table 1.1 states an upper limit on the half-life of $0\nu\beta\beta$ in ^{76}Ge, there has been a controversial claim of discovery. This claim was made by a subset of the Heidelberg-Moscow collaboration. Located at the Laboratori Nazionali

del Gran Sasso (LNGS) in Italy, the collaboration operated 11 kg of detectors enriched in ^{76}Ge and collected 71.7 kg-years of data. The collaboration did not claim discovery and put an upper limit on the half-life, as seen in Table 1.1. Later, a subset of the collaboration made a claim of discovery of $0\nu\beta\beta$ of ^{76}Ge with a half-life of $1.19^{+2.99}_{-0.50} \cdot 10^{25}$ yrs [KK06, KK04]. As seen in Table 1.1, recent $0\nu\beta\beta$ experiments disagree with this claimed observation. This is particularly true of the GERDA experiment, which recently placed an upper limit (with the same nuclide, ^{76}Ge) at $3.0 \cdot 10^{25}$ years.

1.2 The Majorana Demonstrator

Presently the Majorana collaboration is preparing to search for $0\nu\beta\beta$ in ^{76}Ge. In order to fully probe the inverted hierarchy, a tonne-scale ^{76}Ge $0\nu\beta\beta$ experiment is needed. The ultimate goal of the Majorana collaboration is to create a tonne-scale ^{76}Ge $0\nu\beta\beta$ experiment that can probe the inverted hierarchy mass region with background rates not exceeding 1 cnts/ROI/ton/yr. (Where the region of interest (ROI) is 2037-2041 keV.)

Figure 1.1 shows a tonne-scale Ge experiment's sensitivity to $0\nu\beta\beta$ as a function of exposure and the background rate. From Fig. 1.1 it can be seen that with a background rate less than 3 cnts/ROI/ton/yr the Klapdor-Kleingrothaus claim can be fully tested after 0.03 tonne-years of exposure. Furthermore, with a background rate less than 1 cnts/ROI/ton/yr it would take roughly 10 tonne-years of exposure to fully probe the inverted hierarchy assuming the most optimistic NME.

This is an unprecedented low background for such an experiment and therefore great care is being taken to ensure such a background goal can be obtained. To achieve such a low background one must design an experiment that not only focuses on background reduction but background rejection. Backgrounds can generally be classified into two types: depth-dependent and depth-independent backgrounds.

Depth-independent backgrounds typically include natural radioactivity intrinsic to

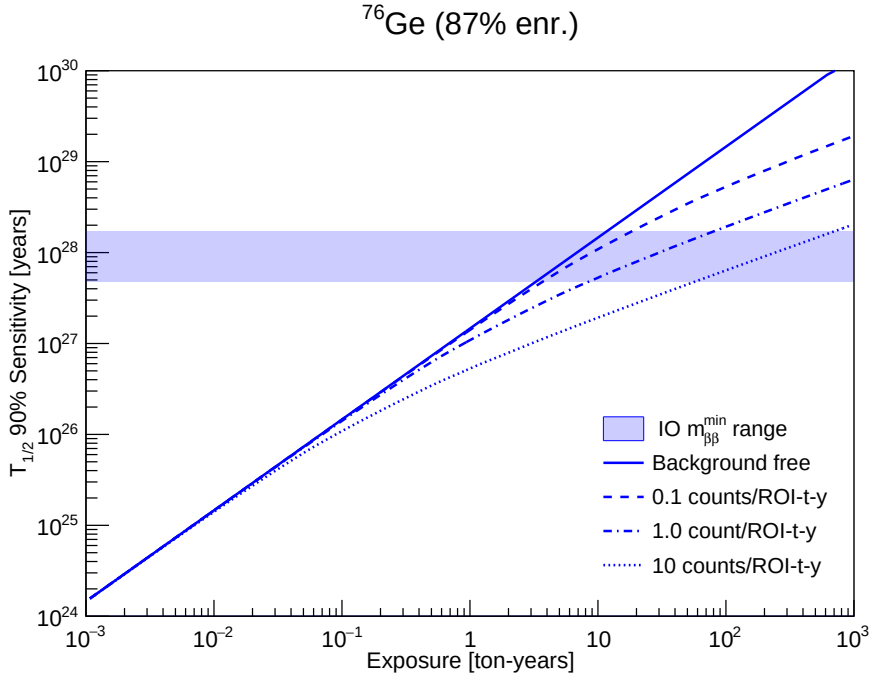

Figure 1.1: A tonne-scale ^{76}Ge $0\nu\beta\beta$ experiment's sensitivity as a function of exposure and the background rate. With a background rate less than 3 cnts/ROI/ton/yr the Klapdor-Kleingrothaus claim can be fully tested after 0.03 tonne-years of exposure. With a background rate less than 1 cnts/ROI/ton/yr it would take roughly 10 tonne-years of exposure to fully probe the inverted hierarchy [Det15].

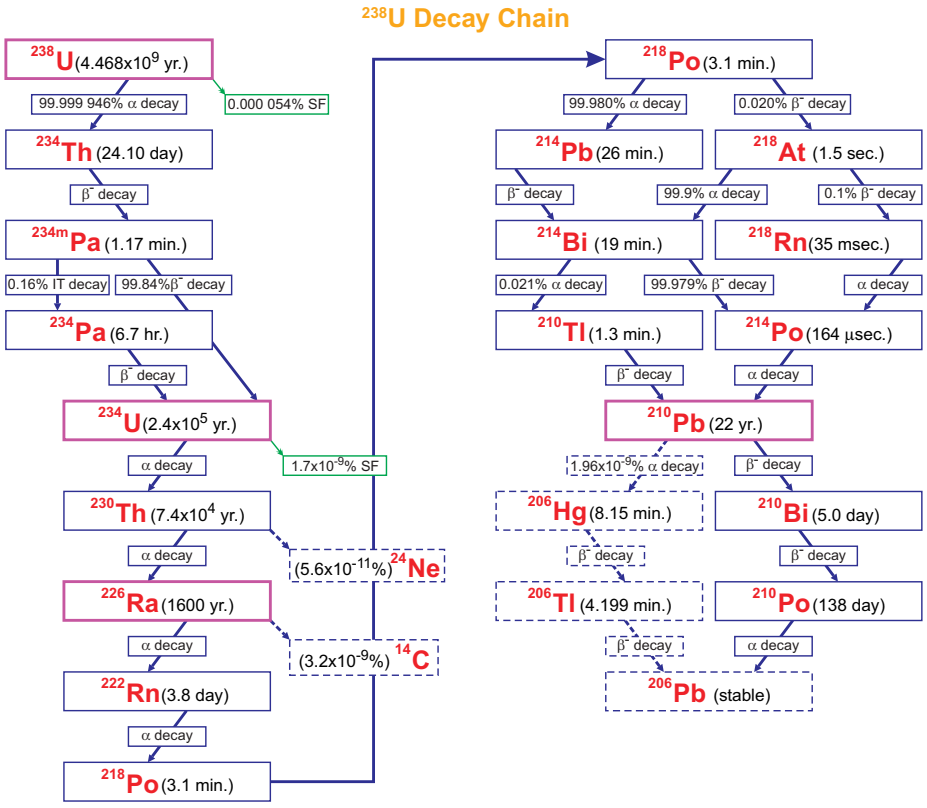

Figure 1.2: The ^{238}U decay chain. Figure taken from [INL].

the detector or from surrounding materials; namely backgrounds from the decay of ^{238}U, ^{232}Th and ^{40}K. The radioactive nuclide ^{40}K predominantly (89%) beta-decays to the stable nuclide ^{40}Ca with the emission of a 1.3-MeV gamma. About 10% of the time it electron-captures to ^{40}Ar with the emission of a 1.46-MeV gamma. The radioactive nuclides ^{238}U and ^{232}Th prove particularly troublesome since their daughter nuclides are not stable and therefore each nuclide has an associated decay chain, as pictured in Figs. 1.2 and 1.3. Considering the expected endpoint energy of the $0\nu\beta\beta$, the main concern from the ^{232}Th decay chain is the beta-decay of ^{208}Tl with the emission of a 2.64-MeV gamma, and the main concern from the ^{238}U decay chain is the beta-decay of ^{214}Bi with the emission of a 2.1-MeV gamma.

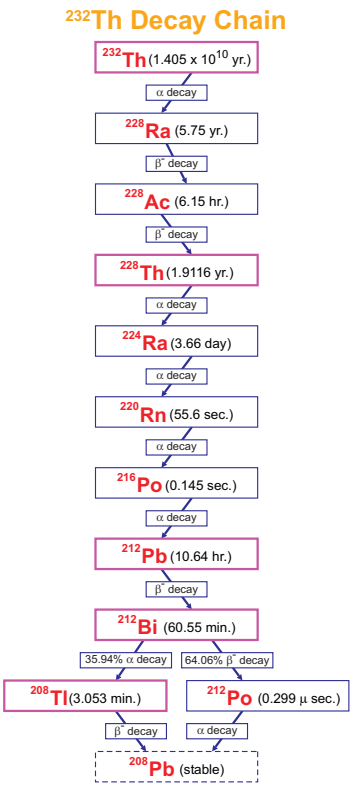

Figure 1.3: The ^{232}Th decay chain. Figure taken from [INL].

Another concern is ^{222}Rn which is part of the ^{238}U decay chain. This nuclide is also present in the air. If present, ^{222}Rn (or its daughter nuclides) can plate-out on exposed surfaces and then alpha decay. If any parts that have a direct line-of-sight to the detectors – or if the detectors themselves – are exposed to ^{222}Rn, any emitted high-energy alphas could pose a threat to the ROI.

Depth-dependent backgrounds, as the name implies, reduces as the depth of the experiment's location increases. This includes through-going and stopping muons and muon-induced fast neutrons [Mei06]. Also of concern are cosmogenically-induced backgrounds, such as the production of ^{60}Co in copper and ^{68}Ge in the germanium crystals. Regardless of the depth, additional shielding is needed to reduce the backgrounds from natural radioactivity in the surrounding environment. In designing a tonne-scale experiment, one of the biggest questions is whether to use an active liquid shield or whether to use a passive compact shield. To help answer this question the MAJORANA and GERDA collaborations are working together to design a tonne-scale experiment while also operating differing – and yet complementary – experiments. The MAJORANA collaboration is employing a compact shield design, while the GERDA collaboration is operating detectors inside of a liquid argon shield [Mac14]. By designing and operating complementary experiments, the MAJORANA and GERDA collaborators are are able to combine their experiences to optimally design a tonne-scale experiment.

The MAJORANA collaboration is building the MAJORANA DEMONSTRATOR: an array of High-Purity Germanium (HPGe) detectors inside of a compact shield located at the 4850′ level at Sanford Underground Research Facility (SURF). The DEMONSTRATOR consists of 44.8 kg of p-type point contact (P-PC) detectors with 29.7 kg enriched to 87% ^{76}Ge and the remaining detectors fabricated from natural germanium (7.8% ^{76}Ge). The DEMONSTRATOR will demonstrate that the technology and the low backgrounds needed to build a tonne-scale experiment are feasible. The MAJORANA DEMONSTRATOR is

also able to test the Klapdor-Kleingrothaus claim and search for physics beyond the Standard Model (e.g. light Weakly-Interacting Massive Particles (WIMPs) and axions) [Fin13]. The DEMONSTRATOR will also play an important role in verifying simulations of expected depth-dependent backgrounds. Previous studies have shown disagreement between muon-induced neutron production rates between different Monte Carlo (MC) codes. These neutrons do not pose a threat to the backgrounds of the DEMONSTRATOR but could pose a threat to a tonne-scale experiment. Therefore it is crucial that the DEMONSTRATOR help verify the muon-induced production rate by comparing simulations to data. Additionally, these simulations will help to verify the experiment's overburden and rock composition that will be crucial to the success of a tonne-scale experiment if it is to be placed at the SURF facilities.

1.2.1 Low-Mass Design and Shielding

To reduce backgrounds the detectors of the DEMONSTRATOR are housed in low-mass assembly strings. Figures 1.4 and 1.6 are renderings of the low-mass detector unit and string respectively; Figs. 1.5 and 1.7 are photographs of a detector unit and string respectively. Nearly all the components of the detector and string parts are made from electroformed copper (shown in Figures 1.4 and 1.6 as the reddish-brown parts). This electroformed copper is grown at SURF, at the same depth as the location of the DEMONSTRATOR and is referred to as Underground Electroformed Copper (UGEFCu). Any parts in the detector and string designs that are not made from UGEFCu are made from NXT-85. The Polytetrafluoroethylene (PTFE) NXT-85 is a Teflon® manufactured by DuPont and specially made in a clean-room environment.

The strings are arranged in arrays and positioned so to provide as much self-shielding as possible, while also giving shielding preference to the enriched detectors. The string arrays are attached to a coldplate and housed in vacuum-sealed cryostats. The

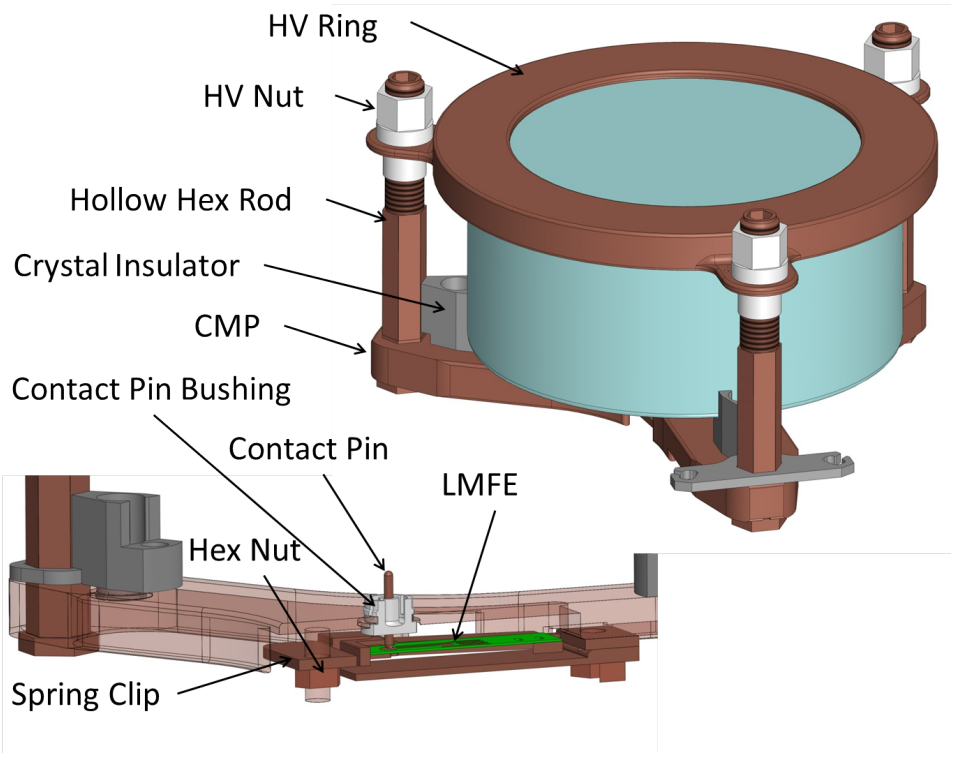

Figure 1.4: A rendering of the detector unit in the MAJORANA DEMONSTRATOR. The upper-right image is a top view of the detector unit; the detector is partially blocking the Crystal Mounting Plate (CMP). Therefore the bottom-left image is a side-view of the CMP and its attached components. The CMP is made slightly transparent so that the Low Mass Front End (LMFE) board can be seen. Also included is the naming convention used for each part in the detector unit.

Figure 1.5: A photograph of a detector unit in the MAJORANA DEMONSTRATOR. Note, the detector unit is upside-down relative to Fig. 1.4.

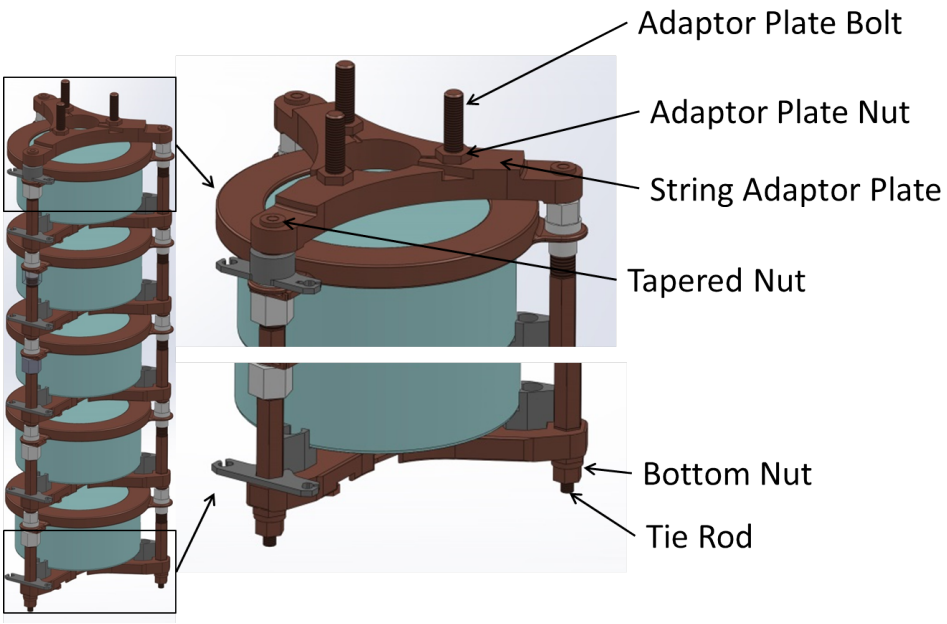

Figure 1.6: The string design for the MAJORANA DEMONSTRATOR. Also included is the naming convention used for each part in the string.

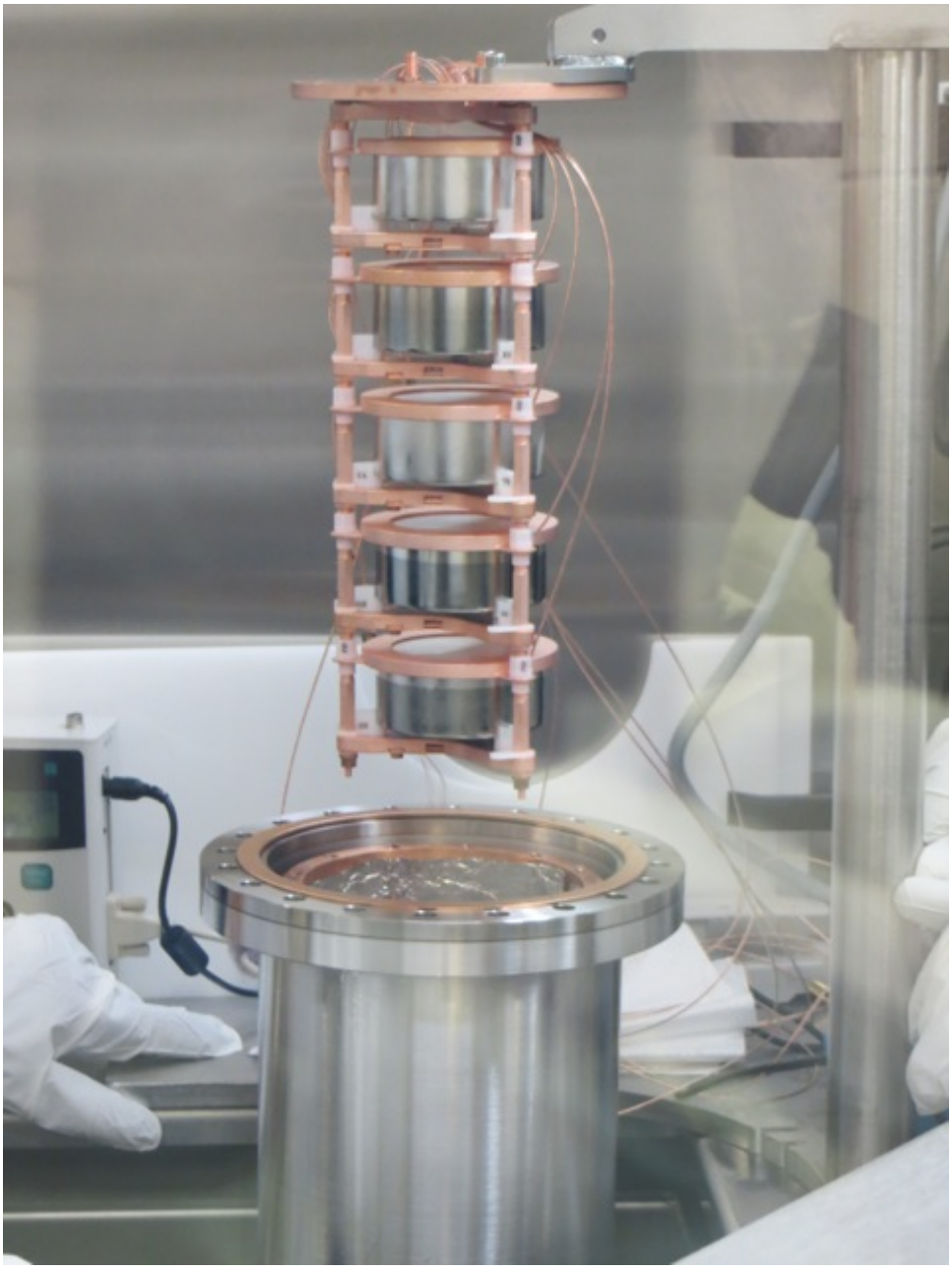

Figure 1.7: A photograph of a string in the MAJORANA DEMONSTRATOR.

DEMONSTRATOR will contain a total of two vacuum-sealed cryostats, with each cryostat mounted to its own vacuum system. Each cryostat also has its own thermosyphon and liquid nitrogen dewar. The dewars and vacuum systems for the cryostats sit outside of the compact shield. Even at a depth of 4850′, cosmogenic activity can be a concern and therefore additional shielding and vetoing capabilities are needed. The compact shield also provides the detectors protection from natural radioactivity in the surrounding environment (e.g. rock walls, concrete floor and lab furniture). Starting from the innermost cavity, the shielding consists of an inner layer of UGEFCu, an outer layer of Oxygen-Free High thermal Conductivity (OFHC) Cu, lead, an active muon veto, polyethylene and borated polyethylene. The cryostats, copper shields and lead shield are all enclosed in an air-tight Stainless Steel (SS) box that is purged with N_2 gas that has been scrubbed free of ^{222}Rn. The thermospyhon and all other copper components that sit inside the inner Cu shield are made from UGEFCu. Figure 1.8 is a cross-sectional rendering of the two cryostats of the DEMONSTRATOR situated inside the shielding. Each cryostat has its own thermosyphon, dewar and vacuum system but only one (of the two) is shown in the cross-sectional view. Further details on the vacuum, cryogenics and ^{222}Rn-purge systems can be found in Ref. [Abg14].

1.2.2 Assay and Material Preparation

Nearly all the components inside the cryostats, the cryostats themselves and the innermost layer of the shielding are made form UGEFCu. That the experiment is built almost entirely from UGEFCu is a trait unique to the MAJORANA DEMONSTRATOR and should significantly contribute to the success of the DEMONSTRATOR achieving an ultra-low background. By electroforming its copper at the 4850′ level of SURF, the MAJORANA collaboration has been able to grow copper with low natural radioactivity and low cosmogenically-induced radioactivity. Furthermore the collaboration has been able to tightly control the machining process and surface exposure of the copper. After

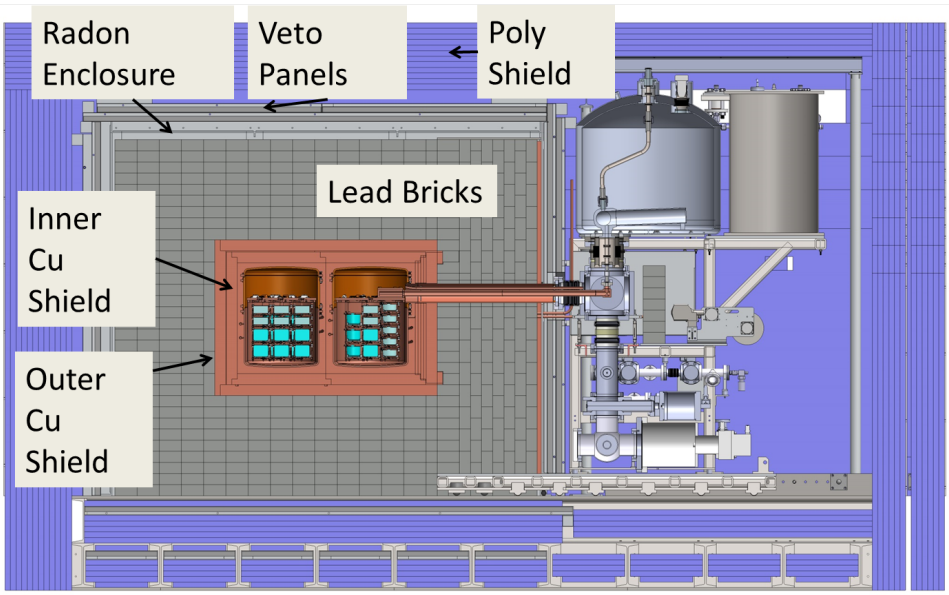

Figure 1.8: A cross-sectional view of the compact shield design for the MAJORANA DEMONSTRATOR. The polyethylene and muon veto panels are colored purple for visualization purposes. Each cryostat has its own vacuum system, thermosyphon and dewar but only one (of the two) is shown in the cross-sectional view.

the UGEFCu is grown it is transferred to the MAJORANA underground machine shop, which is also located at the 4850′ level of SURF and is a class 2,000 clean room. All that separates the MAJORANA underground machine shop from the detector hall – where the DEMONSTRATOR is located – is a door and a pressure gradient. The MAJORANA detector hall is designed as a class 2,000 cleanroom but typically shows particle counts at the class 100-200 level. Inside the detector hall there is another soft-walled class 10 cleanroom that contains a fume hood and is where all the parts are cleaned with ultra-pure chemicals [Hop08, NO13, Str12]. After undergoing a thorough cleaning, parts that are inside the cryostat are moved into a nitrogen-purged glovebox that sits in the detector hall. All detector work is performed in the glovebox to ensure the detectors are never exposed to air; this work includes assembling the detector units and strings, attaching the strings to the coldplate and sealing the cryostat. By eliminating the detectors' exposure to air the detectors are not only protected from particulate in the

air but also from possible ^{222}Rn plate-out.

While most of the DEMONSTRATOR support structures and cryostats are made from UGEFCu there are other materials as well. All materials in the cryostat components and shielding have been carefully selected and then prepared for an ultra-clean environment. The MAJORANA collaboration has conducted an extensive assay program to ensure all the materials used for the DEMONSTRATOR are of sufficient purity. Every material used in the DEMONSTRATOR has been assayed by at least one of the following methods: gamma-ray spectroscopy, Neutron Activation Analysis (NAA) or mass spectroscopy (in particular, Glow Discharge Mass Spectroscopy (GDMS) and Inductively-Coupled Plasma Mass Spectrometry (ICPMS)). Furthermore, just as the UGEFCu is handled in a cleanroom environment and cleaned with ultra-pure chemicals, so are all the materials in the DEMONSTRATOR. Reference [Abgon] details each material that has been assayed by the MAJORANA collaboration, the method used, and the material's radiopurity. Table 1.2 is a selected list of some of the materials, namely those that are present in the DEMONSTRATOR and the Prototype Cryostat (PC) (section 1.3) and frequently referenced throughout this thesis.

1.2.3 Detector Technology

To summarize thus far, the MAJORANA DEMONSTRATOR has been designed to reduce backgrounds by as much as possible using the following techniques.

- The DEMONSTRATOR is located deep underground to limit cosmogenic backgrounds.
- A majority of the DEMONSTRATOR parts are made from UGEFCu; the copper is grown underground to limit cosmogenically-induced backgrounds.
- The cryostats are surrounded by several layers of passive and active shielding to remove cosmogenic backgrounds and to reduce backgrounds from natural activity

Table 1.2: A selected list of materials used in the DEMONSTRATOR and PC and their assay values. For a complete list and further details see Ref [Abgon].

Material	Method of Assay	Radioactive Nuclide	Activity [μBq/kg]
UGEFCu	ICPMS	^{238}U	0.17 ± 0.03
		^{232}Th	0.06 ± 0.02
OFHC Cu	ICPMS	^{238}U	1.25 ± 0.24
		^{232}Th	1.10 ± 0.21
NXT-85	NAA	^{238}U	<5
		^{232}Th	0.10 ± 0.01
LMFEs	ICPMS and γ-counting	^{238}U	10570 ± 370
		^{232}Th	6530 ± 120
Lead (Shield)	ICPMS, GDMS and γ-counting	^{238}U	<36
		^{232}Th	<5
SS	γ-counting	^{238}U	<5000
		^{232}Th	13000 ± 4000
PEEK	NAA	^{238}U	<63000
		^{232}Th	<16000

in the surrounding environment.

- Through an extensive assay campaign it has been confirmed that the bulk of the materials (used in the DEMONSTRATOR) are low in natural radioactivity. Furthermore every part is subjected to a through cleaning with ultra-pure chemicals to ensure little-to-no surface contamination.

- Following their manufacture, the detectors are never exposed to air and great efforts are made to ensure the string parts have limited air exposure; doing so limits the possibility of ^{222}Rn plate-out on surfaces.

- A low-mass string design is used to hold the detectors.

The MAJORANA collaboration is using techniques not only in background reduction but also background rejection to achieve the lowest possible backgrounds. Two analysis

cuts are being implemented on the detectors of the DEMONSTRATOR: a pulse-shape analysis (PSA) cut and a granularity cut. The MAJORANA collaboration utilizes P-PC HPGe detectors. In a traditional coaxial detector the electrode is a well that extends from the bottom face of the cylindrical crystal, along the z-axis. On the other hand a P-PC detector has a point-like, shallow contact giving an extended range of drift times – the time it takes an electron-hole to drift to the point-contact. This allows one to better distinguish single-site events from multi-site events through PSA. A $0\nu\beta\beta$ event would be a single-site event whereas many backgrounds (such as a gamma-ray interactions) are multi-site events. Thus the backgrounds of the DEMONSTRATOR can be further reduced by implementing a PSA cut. An additional benefit of using P-PC HPGe detectors is that they have a low intrinsic capacity, giving them great energy resolution.

The detectors of the DEMONSTRATOR are contained in strings and in turn, the strings are mounted to a coldplate in arrays. While the string-array configuration provides additional shielding to the inner-most detectors it also allows for an additional analysis cut: a granularity cut. Given that a $0\nu\beta\beta$ is an internal event in a detector, a granularity cut can be made to veto events that scatter in multiple detectors within a pre-determined time window. The granularity cut will reduce backgrounds from external gammas as well as cosmogenic backgrounds.

1.3 Prototype Cryostat

Before the assembly and operation of the DEMONSTRATOR, a single test cryostat was built. This cryostat, referred to as the PC, was built to test the clean assembly procedures and data acquistion (DAQ) that are to be used for the DEMONSTRATOR. The PC contained three strings with a total of ten natural germanium detectors. Of the ten detectors, eight were modified-Broad Energy Germanium (BEGe) detectors from CANBERRA; these are the same type of natural detectors used in the DEMONSTRATOR.

The other two detectors were larger-mass ORTEC® detectors. ORTEC® has fabricated the enriched detectors for the DEMONSTRATOR and initially fabricated two detectors similar in size to the enriched detectors but made from natural germanium; these were the two ORTEC® detectors in the PC.

The work in this thesis focuses primarily on the PC and therefore a naming convention is used to discuss the individual detectors and strings. The strings are referred to as Strings 1, 2 and 3. String 1 (S1) holds four detectors: two BEGes and the two ORTEC® detectors. In Fig. 1.9 it is the string pictured in the background to the left. String 2 (S2) holds one BEGe detector and is in the background to the right in Fig. 1.9. String 3 (S3) holds five BEGe detectors and is in the foreground in Fig. 1.9. The detectors in the strings are numbered in increasing value as one moves away from the coldplate, with SxD1 being the detector closest to the coldplate. As an example, in Fig. 1.9, S3 is in the foreground and its top detector is S3D1 while its bottom detector is S3D5. Seven of the ten detectors are used in the analysis presented here. The status and mass of each detector of the PC can be found in Table 1.3.

Table 1.3: The masses of the PC detectors.

Detector	Mass [g]	Status
S1D1	631	NOT included; unstable gain
S1D2	633	Included in analysis
S1D3	904	Included in analysis
S1D4	1013.5	Included in analysis
S2D1	644	NOT included; unstable gain
S3D1	622	Included in analysis
S3D2	646	Included in analysis
S3D3	630	NOT included; no HV connection
S3D4	631	Included in analysis
S3D5	627	Included in analysis

In order to best test the construction and assembly procedures for the DEMONSTRATOR

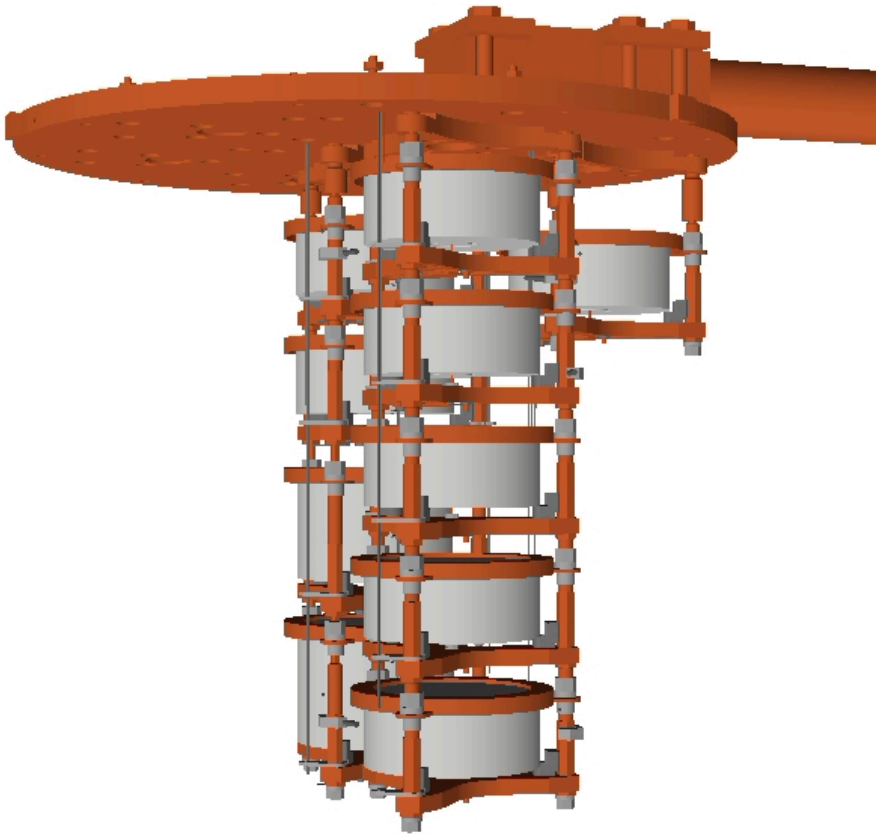

Figure 1.9: The three strings of the PC. In the foreground is String 3 which holds five detectors. In the background to the left is String 1 which holds four detectors. In the background to the right is String 2 which holds one detector. The detectors in the strings are numbered in increasing value as one moves away from the coldplate, with SxD1 being the detector closest to the coldplate.

the PC is designed to mimic the DEMONSTRATOR as much as reasonably possible. However there are several differences between the PC and the DEMONSTRATOR. While achieving the lowest possible background is the goal of the DEMONSTRATOR this was not necessarily true of the PC. Therefore some modifications were made that sacrificed the ultra-low background for cost and scheduling purposes. For example, while the PC uses the same low-mass detector and string designs as the DEMONSTRATOR, many of the copper parts are made from OFHC Cu rather than the cleaner UGEFCu that are being used in the DEMONSTRATOR. As another example, the PC is located in the compact shield at the 4850′ level at SURF that is to be used for the DEMONSTRATOR, however the shielding was not entirely complete during the time that the PC was being operated. The following is a complete list of the important differences between the PC and the DEMONSTRATOR.

1. **Temperature Sensor Assemblies** For testing purposes, five temperature sensors were installed in the PC (and are not installed in the DEMONSTRATOR). The temperature sensors were soldered to their cabling. A clamp made of Polyether Ether Ketone (PEEK) and a stainless steel screw were used to clamp the sensor to the string to monitor temperature stability and cooling. The temperature sensors, solder, cabling and SS screws were not assayed. The material PEEK – which is what the clamps were made of – has been assayed and is known to have a relatively high amount of natural radioactivity compared to the preferred polymer, NXT-85, that is being used in the DEMONSTRATOR.

2. **OFHC Cu** Several parts in the PC were made of OFHC Cu, while their DEMONSTRATOR counterparts are made of UGEFCu. Also, the time that the OFHC Cu parts spent above ground was not tightly controlled and therefore the cosmogenically-induced radioactivity (e.g. ^{60}Co) in the OFHC Cu is expected to be higher.

3. **SS** Several parts in the PC were made of SS, while their DEMONSTRATOR counterparts are made of UGEFCu. These SS parts include some of the cryostat clamping hardware and some of the outer copper shield fasteners.

4. **Silicon Bronze** Some parts of the PC cryostat clamping hardware were made of silicon bronze, while their DEMONSTRATOR counterparts are made of UGEFCu.

5. **Metal Spinning** The top and bottom cryostat lids of the PC were fabricated via metal spinning. The top and bottom cryostat lids of the DEMONSTRATOR were not fabricated this way as there is no known assay on the procedure.

6. **Radon Purge** The radon purge system was not in its final state and therefore higher levels of ^{222}Rn were expected in the inner cavity volume during the operation of the PC (than for the DEMONSTRATOR).

7. **Active and Passive Shielding** The inner copper shield was not installed in the PC. The poly shield and muon veto were only partially installed. Additional shielding is required where the cross arm tube penetrates the passive shielding and was not installed in the PC. Additionally there was SS hardware in the outer copper shield of the PC.

8. **Gasket** The PC cryostat was vacuum-sealed with a Viton gasket rather than with a cleaner parylene film that is being used in the DEMONSTRATOR.

9. **Cables** The signal cables in the PC were known to be higher in radioactivity than the cables in the DEMONSTRATOR.

10. **Thermosyphon Supports** The thermosyphon supports were made of PEEK, while their DEMONSTRATOR counterparts are made of a cleaner polymer.

11. **Detector Cosmogenics** Unlike the detectors of the DEMONSTRATOR, the time that the detectors of the PC spent above ground was not tightly controlled.

Therefore the cosmogenically-induced radioactivity in the detectors was expected to be higher than for the detectors of the DEMONSTRATOR.

Much of the work presented in this thesis attempts to understand the prototype module backgrounds and exactly how the differences between the PC and DEMONSTRATOR modules contribute to the backgrounds of the PC. As previously mentioned, all of the materials used in the DEMONSTRATOR are assayed and extensive MC simulations have been performed to predict the backgrounds that the materials are expected to contribute to the energy spectrum of each detector. A background model for the PC was created using the same tools used to create the DEMONSTRATOR background model. By creating a background model of the PC and comparing it to data, the background model of the DEMONSTRATOR can be verified and possible future issues can be identified. Creating an accurate background model also requires understanding the energy resolution of each detector. Chapters 3 and 4 look at thoroughly characterizing the energy response function for each detector of the PC. Chapter 5 describes the PC background model created for this work. Chapter 6 compares the PC background model to data. This chapter also discusses the implications for the background model for the DEMONSTRATOR and ongoing and future work. The conclusions of this work and the current status of the PC and DEMONSTRATOR are discussed in Chapter 7.

CHAPTER 2: DATA ACQUISITION, PROCESSING AND SELECTION

2.1 Overview

2.1.1 Detector Readout and Data Acquisition

The Prototype Cryostat contains ten detectors organized into three string arrays. Each detector is housed in its detector unit, with each detector unit containing a Low Mass Front End (LMFE) for detector readout. The LMFE is connected to the preamplifier through long signal cables that thread down the cross arm tube. (The cross arm tube can be seen in Fig. 1.8 where it is the outer-most copper tube that penetrates the lead shielding.) The detector preamplifiers sit on a motherboard outside of the cryostat and shielding. The preamplifiers provide both a low-gain and a high-gain signal for each detector in the cryostat. A controller card communicates between the motherboard and the GRETINA digitizer boards [Zim12] and is capable of sending a square-wave pulse to each detector in the cryostat. The GRETINA boards are housed in VME crates, with each crate containing a Single Board Computer (SBC). The SBC reads out the VME module and communicates with the DAQ computer. The DAQ (e.g. HV, run control, etc.) is managed via Object-oriented Real-time Control and Acquisition (ORCA) which, among other things, allows the user to control the high voltage applied to the detectors[How04]. The DAQ accumulates data into a file until a user-set length of time is reached, at which point the file is closed (i.e. the run ends) and a new file is opened (i.e. a new run is started). A copy of this file is transferred to the National Energy Research Scientific Computing Center (NERSC) project file system, where further data processing is done via NERSC's Parallel Distributed Systems Facility (PDSF) Linux cluster [NER]. Figure 2.1 shows an overview of the DAQ system for the PC. As seen in

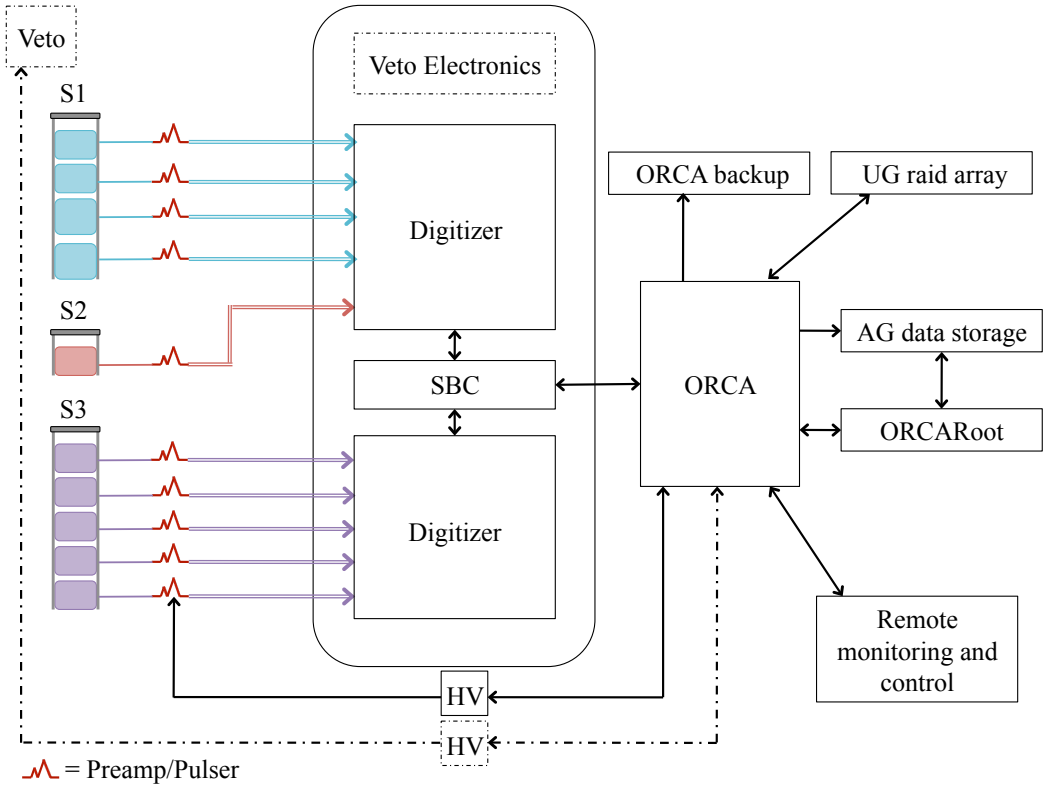

Figure 2.1: An overview of the PC DAQ system. The data collected from the veto system are not used in the work presented here. This figure is a modification of the figure in reference [Abg14] of the MAJORANA DEMONSTRATOR DAQ. See text for more details.

Fig. 2.1 each file is saved in two separate locations; at SURF and on PDSF. In Fig. 2.1 the SURF location is referred to as the underground (UG) raid array, and the PDSF location is referred to as the above ground (AG) data storage.

There are notable differences between the PC DAQ in Fig. 2.1 and the DAQ system that is being used for the MAJORANA DEMONSTRATOR [Abg14]. During the operation of the PC, work was still being done to install the veto panels and the trigger clock hardware that is used to synchronize data from the veto electronics and the digitizers. Thus, although the muon veto was collecting data during times when the discussed data was accumulated, the veto data are not included in any analysis presented here.

For this reason, the borders of the veto components are dashed – rather than solid – in Fig. 2.1, and the clock synchronization is omitted. Also, in Fig. 2.1 it is clearly shown which detectors of the PC share a digitizer, as this information will be referred to later. Two GRETINA boards are used for the PC: one card reads out the five detectors from String 3, and the other card reads out the four detectors from String 1 and the one detector from String 2.

2.1.2 Data Processing

The raw ORCA files contain run-level information (e.g. the start and stop time of the run) and the digitized waveform data. Once the raw ORCA files are transferred to PDSF they undergo a first round of processing with OrcaROOT where they are converted to built ROOT files. (OrcaROOT is a C++ toolkit designed by the MAJORANA collaboration and is shown in Fig. 2.1.) In the built files the data are stored in a ROOT `TTree`, where each recorded event is an entry in the tree. Each entry in the built files contains run-level information, the event's waveform and certain information regarding the event (e.g. the ID of the detector in which the event occured). The built files then undergo one to two rounds of processing with the Germanium Analysis Toolkit (GAT), a software package developed by MAJORANA. Like the built files, in the GATified files the data are stored in a ROOT `TTree`, where each event is an entry in the tree. GAT contains a number of C++ classes that are able to extract needed information from the waveform of an event and further interpret register settings of the GRETINA boards. As an example, one class of GAT is designed to calibrate the energy spectrum of each detector, and then add a branch to the `TTree` with each event's calibrated energy.

2.1.3 The GRETINA Digitizer Cards

The GRETINA cards digitize at a frequency of 100 MHz. Each card has a 14 bit ADC precision and ten input channels. The uncalibrated energy of an event can be obtained from two different sources. The first of these is obtained from the GRETINA

board itself; this is referred to as the onboard energy. The GRETINA boards have a built-in trapezoidal energy filter with a user-set integration time and gap time. Here, gap time refers to the width of the flat top of the trapezoid and the integration time refers to the time in which the leg of the trapezoid is increasing from the base of the trapezoid to the flat top. (Or similarly – since the trapezoid is symmetric – the integration time is the time in which the leg of the trapezoid is decreasing from the flat top to the base of the trapezoid.) For the data presented here, the internal GRETINA board filter is set to have a gap time between 1.5μs and 2.0μs and an integration time of 4μs. Secondly, the energy can be calculated offline from the digitized signal using a trapezoidal filter; this is referred to as the offline energy. The offline energy has been calculated for several different integration times: 500 ns, 1 μs, 2 μs, 4 μs and 8 μs. At the time that this analysis was being performed, the calculation of the offline energies was still under development. Therefore, for this work, the onboard energy (of each detector's high-gain channel) is chosen. Analyses of the DEMONSTRATOR data are expected to use the calculated offline energies, as there are known issues with the onboard energy. These issues, among others, and the resulting data selection cuts are discussed later in this chapter. Some issues may be specific to the onboard energy, such as the issue discussed in Section 2.2.7. Others may point to issues with the DAQ system in general. One must remember that part of the purpose of the PC is to test things such as the DAQ system, and therefore part of the purpose of this work is to check the operation of the DAQ system and point out problems for the MAJORANA collaboration to address before $0\nu\beta\beta$ data are acquired with the DEMONSTRATOR.

2.2 Data Selection

The analysis in this work uses background data taken with the PC from July 2014 to December 2014, with an effective runtime (before any data quality cuts are made) of roughly 75 days. The times when background data were taken can be seen in

Fig. 2.2, where the periods of data taking are represented in gray. Five times during this time period, data were acquired with a ^{228}Th line source. The ^{228}Th data are used to calibrate the spectra and for several other analyses that are discussed below. The times when calibration data were taken can be seen in Fig. 2.2, where the periods of data are represented in red. In this analysis, the first data are from the ^{228}Th line source taken on July 22nd 2014; this is considered "Day 0" in Fig. 2.2.

The data cleaning tools that are being used for the MAJORANA DEMONSTRATOR are still under development. Some rudimentary cuts are used for looking at the data from the PC. All calibration and background data used in this work first undergo the data selection cuts presented in this chapter. All data quality (DQ) cuts presented here are done using the GATified files, which will not necessarily be true of the data cleaning tools developed for the MAJORANA DEMONSTRATOR. The primary goal of the PC data cleaning tools is to remove any data that might affect the gamma-peak shape in the energy spectra. During the time period when the background and calibration data were acquired the DAQ system was still being commissioned, and therefore some of the DQ cuts are designed to remove temporary bugs that should not be present with the MAJORANA DEMONSTRATOR DAQ.

The DQ cuts made on the PC data are as follows, and are performed in the order in which they are listed. Each DQ cut is discussed in detail in its associated section.

1. Omit runs with a corrupted raw data file. (Section 2.2.1)

2. Omit events with a bad timestamp and omit pulser events. (Section 2.2.2)

3. Find high-rate data by looking for runs with a run time that is too short. Omit any high-rate runs (for all detectors). (Section 2.2.3)

4. Look for channel and/or digitizer card outage. (i.e. Ensure that all the detectors and digitizers are operational for a given run.) Omit runs for affected detectors

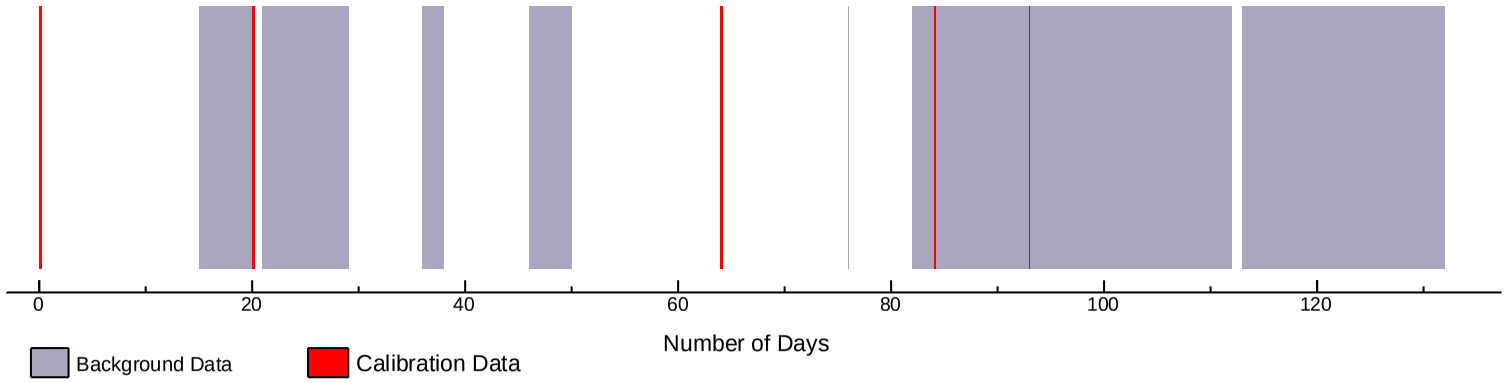

Figure 2.2: An overview of the background data (blue) and calibration data (red) taken with the PC. In this analysis, the first data is ^{228}Th-calibration data taken on July 22nd 2014; this is considered "Day 0" in the figure. An absence of color indicates that either the PC was not running or that the data taken during the time are unusable due to commissioning tasks.

accordingly. (Section 2.2.4)

5. Look for a shift in a detector's gain. Omit runs for affected detectors accordingly. (Section 2.2.5)

6. Look for problems with the onboard energy determination. Omit runs for affected detectors accordingly. (Section 2.2.6)

7. Find high-rate data by monitoring the integrated count rate of each detector's energy spectrum on a run-by-run case. Omit runs for affected detectors accordingly. (Section 2.2.3)

8. Omit events that have an incorrect onboard energy assignment. (Section 2.2.7)

The number of calibration (background) runs before and after the DQ cuts are performed on each detector can be found in Table 2.1 (2.3). Further details on exactly how many calibration (background) runs are excluded from each individual DQ cut can be found in Table 2.2 (2.4). Table 2.1 (2.3) also contains the total runtime of each detector's calibration (background) data set after all DQ cuts are made. The effect that each DQ cut has on a detector's total runtime is explored in the following sections of this chapter.

2.2.1 Corrupted Raw Data File

The first DQ cut performed removes runs with a corrupted raw file. One unresolved problem is that occasionally the header data read out of the GRETINA board is corrupted. One way to pick these files out from a data set is by looking at the run's start and stop times. In the corrupted headers, the start and stop times are incorrectly logged and after going through processing will both be interpreted as being equal to zero. Thus the first cut to the GATified data is to omit a run if either its start time or stop time is zero. This DQ cut is labeled as "Cut #1" in Tables 2.2 and 2.4, and only

Table 2.1: Number of calibration runs before and after DQ cuts. See Table 2.2 for a breakdown on the percentage of runs that are omitted after each cut.

Detector	Number of Runs		Overall Percentage	Runtime
	Before Cuts	After Cuts	of Runs Cut	After Cuts (hrs)
S1D2	125	116	7%	17.92
S1D3	125	115	8%	17.76
S1D4	125	117	6%	18.07
S3D1	125	117	6%	18.07
S3D2	125	118	6%	18.24
S3D4	125	117	6%	18.09
S3D5	125	88	30%	13.46

Table 2.2: Percentage of calibration runs cut from each detector after an individual DQ cut is performed. Each cut's identifying number corresponds to the enumerated cuts described in Section 2.2. Cuts #2 and #8 remove individual events rather than an entire run and are therefore not considered in this table.

Detector	Percentage of Runs Cut From Individual Cut							
	#1	#2	#3	#4	#5	#6	#7	#8
S1D2	1%	-	5%	1%	1%	0%	0%	-
S1D3	1%	-	5%	1%	2%	0%	0%	-
S1D4	1%	-	5%	1%	0%	0%	0%	-
S3D1	1%	-	5%	0%	1%	0%	0%	-
S3D2	1%	-	5%	0%	0%	0%	0%	-
S3D4	1%	-	5%	0%	1%	0%	0%	-
S3D5	1%	-	5%	24%	2%	0%	0%	-
Average	**1%**	**-**	**5%**	**4%**	**1%**	**0%**	**0%**	**-**

Table 2.3: Number of background runs before and after DQ cuts. See Table 2.4 for a breakdown on the percentage of runs that are omitted after each cut.

Detector	Number of Runs		Overall Percentage	Runtime
	Before Cuts	After Cuts	of Runs Cut	After Cuts (hrs)
S1D2	1804	1585	12%	1448.5
S1D3	1804	1570	13%	1434.8
S1D4	1804	843	53%	770.41
S3D1	1804	904	50%	826.16
S3D2	1804	907	50%	828.90
S3D4	1804	864	52%	789.60
S3D5	1804	851	53%	777.72

Table 2.4: Percentage of background runs cut from each detector after an individual DQ cut is performed. Each cut's identifying number corresponds to the enumerated cuts described in Section 2.2. Cuts #2 and #8 remove individual events rather than an entire run and are therefore not considered in this table.

Detector	Percentage of Runs Cut From Individual Cut							
	#1	#2	#3	#4	#5	#6	#7	#8
S1D2	1%	-	5%	1%	5%	0%	1%	-
S1D3	1%	-	5%	1%	4%	0%	3%	-
S1D4	1%	-	5%	1%	47%	0%	5%	-
S3D1	1%	-	5%	15%	-	34%	5%	-
S3D2	1%	-	5%	15%	1%	34%	2%	-
S3D4	1%	-	5%	15%	0%	34%	9%	-
S3D5	1%	-	5%	15%	0%	37%	6%	-
Average	**1%**	**-**	**5%**	**9%**	**9%**	**19%**	**4%**	**-**

affects ∼1% of data. Since this DQ cut removes entire runs, the runtime is adjusted after the cut is made.

2.2.2 Bad Timestamp

For every event a timestamp is recorded. The GRETINA boards digitize at a frequency of 100 MHz, so an event with a timestamp of t, is an event that is recorded $t \cdot 10^{-8}$ seconds after the start of the run. The second DQ cut removes events with a bad timestamp. These events typically have a timestamp that is many orders of magnitude larger than expected. Therefore, since each background run is set to last for one hour, the first event cut is to require that all events have a timestamp corresponding to 3600 seconds or less.

Unlike the first DQ cut described in Section 2.2.1, this second cut removes individual events rather than an entire run. The effect that this cut has on livetime (if any) has not been explored, and thus the livetime is not adjusted after this cut. For this reason, this cut is not considered in Tables 2.2 and 2.4 (columns labeled "Cut #2").

For this cut, the pulser events are removed from the energy spectra as well. A detector's pulser is only enabled during background runs, so this portion of the cut is only performed on background data. The pulser is set to run for the first five minutes of a background run, while some pulser events have been seen to linger a few seconds past the five minute cut-off. Therefore to remove all pulser events, an event is required to have a timestamp corresponding to 310 seconds or greater. The livetime is adjusted accordingly after this portion of the cut is performed.

In summary, the second DQ cut is to require that events in the calibration data have a timestamp t such that $t \leq 3600 \cdot 10^8$, and that events in the background data have a timestamp t such that $310 \cdot 10^8 \leq t \leq 3600 \cdot 10^8$. As a result of this DQ cut, each calibration run contributes 3600 s to the livetime and each background run contributes 3290 s to the livetime.

2.2.3 High Rate

A drastic increase in the event rate has the potential to cause pile-up, which could cause a change in a detector's gamma-peak shape. The two DQ cuts described in this section are designed to remove data with abnormally high rates from the background and calibration data sets.

During data taking, an upper limit is placed on the size of the raw data file. If the upper limit is reached, the run is ended and a new run is started. At times during background runs, an individual run is less than the pre-set run time (one hour), indicating the upper limit of the file size has been reached. This is a strong indication that there is a dramatic increase in noise in the run. For this reason, any background run with a run time of less than one hour is excluded. For the high-rate calibration data, a less stringent lower limit cut of 400 seconds is placed on the run's runtime. This is the third DQ cut performed on the background and calibration data, as seen in Section 2.2.1. Since this cut removes entire runs, the runtime of the data set is adjusted after the cut. This cut is found to remove $\sim$5% of both calibration and background data, as seen in Tables 2.2 and 2.4 (columns labeled "Cut #3").

A second, more subjective, cut is done to exclude runs with a high rate. This DQ cut is performed later during the data selection routine; as described in Section 2.2.1, it is typically the seventh DQ cut applied to a data set. To look for high rates, this cut integrates a detector's energy spectrum above 20 keV for each individual run. For each detector, an acceptable rate is decided and any run with an event rate above that limit is excluded. Note that this DQ cut works on a detector-by-detector case, unlike the first high-rate cut (Cut #3) which omits an entire run for *all* detectors. However this cut still removes entire runs, and therefore the runtime of the data set is adjusted after the cut is performed. This DQ cut is labeled as "Cut #7" in Tables 2.2 and 2.4. No calibration data is excluded from this cut, and on average only 4% of background

data is excluded from this cut.

2.2.4 Digitizer Board and/or Channel Outage

The fourth DQ cut is designed to look for runs where a channel (or channels) on the GRETINA board stopped recording data. During high-rate calibration runs it is clear if a channel or a digitizer board stops recording data for a longer period of time. Because of the low background rates, channel outage is not so clear during background runs. For this reason, there are some differences in how this DQ cut is implemented on the calibration data versus the background data.

To search for channel outage in the calibration data, a $\pm$3.5-keV region at the 583-keV peak is integrated for each detector and for each individual run. If a detector's integrated count during a run is equal to zero, the run is omitted for that detector (and that detector only).

For the background data, one would ideally like to search for channel outage by examining each detector's pulser rate for each individual run. This would work for most detectors of the PC, however some detectors do not have their pulser enabled. Furthermore, it has been observed that at times the pulser is (unexpectedly) absent for a detector during a run, but the digitizer still records events from that detector during the same run. Therefore, pulser outage alone does not imply channel outage. In the calibration data, channel outage is seen as one of two cases; either a single channel is out for several sequential runs, or all channels on a single GRETINA board are out for a run. (See Fig. 2.1 for a reminder on which detectors share a GRETINA board.) Keeping this in mind, two tests are done to the background data: one searches specifically for digitizer board outage, the other for channel outage.

First, for every individual run, each detector's total rate is calculated (including pulser events). If the total rate for all detectors on a single GRETINA board is equal to zero, that run is rejected for all the detectors that are read out by that particular

board. As an example, Fig. 2.3 shows one of the digitizer's hourly event rate for a subset of the background data. The background runs with a total digitizer count rate of zero are omitted for all detectors read out by this particular digitizer; these runs are shown in red. In Fig. 2.3 there is a clear population of event rates around 10^4 counts per hour, and then there are several runs which deviate from this population and have an event rate around 10 counts per hour. The background runs with an event rate of 10^4 counts per hour are expected. There are four detectors with an enabled pulser on the pictured digitizer board, and the event rate for each detector's pulser is roughly 3.8 Hz. This gives a total event rate of roughly $5.5 \cdot 10^4$ counts per hour. Given that the event rate for the background runs should be dominated by the pulser events, an event rate on the order of 10^4 counts per hour is expected for Fig. 2.3. For the background runs with an event rate around 10 counts per hour; during these runs the pulser is unexpectedly absent for all the detectors and the only events seen are from the detectors themselves. There is no indication that these events are not real physical events, and therefore these background runs are not omitted from the detectors' final background data set.

After searching for digitizer board outage (and omitting the relevant runs for certain detectors), single-channel outage is searched for. If a single detector has a zero rate for several sequential runs in the background data, those runs are rejected for that particular detector. Almost all of the data removed as a result of this DQ cut has been from digitizer outage rather than channel outage. On average, this DQ cut as a whole removes 4% of the calibration data, as seen in the "Cut #4" column in Table 2.2, and 9% of the background data, as seen in Table 2.4. This DQ cut removes entire runs and therefore each detector's runtime is adjusted after this DQ cut is performed.

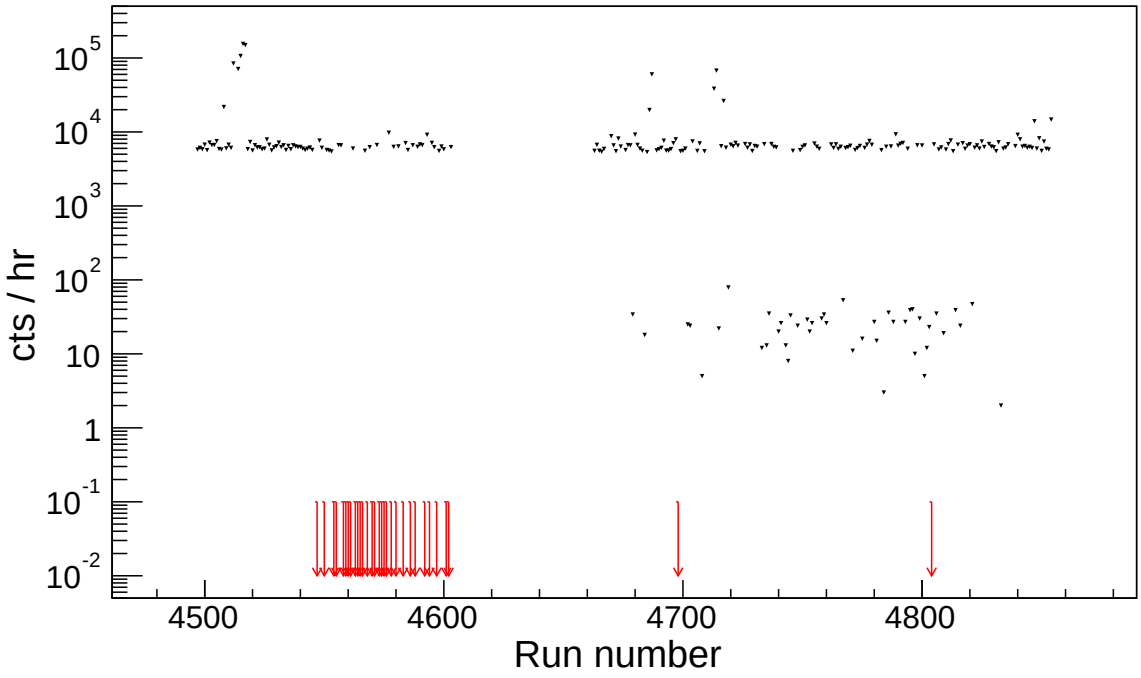

Figure 2.3: A digitizer's total event rate for individual runs during a subset of the background data. The rates shown are for the digitizer which reads out detectors S3D1, S3D2, S3D4 and S3D5. Due to the logarithmic y-axis, a run with a zero count rate cannot be precisely placed. Instead it is shown as an upper limit of 0.1 counts per hour. Any background run with a total digitizer count rate of zero is omitted on the presumption that the digitizer stopped recording data, and is therefore also shown in red. See text for more details.

2.2.5 Change in Detector Gain

The fifth DQ cut is designed to look for times when a detector has a change in gain, and omit those runs from the detector's data set. This cut uses the pulser to look for a change in a detector's gain during background runs. The pulser is not enabled while taking calibration data, and therefore for calibration runs Cut #5 uses the ^{208}Tl's 583-keV peak to look for a change in a detector's gain. The pulser for detector S3D1 is disabled and therefore this cut can only be performed on S3D1's calibration data set, and not on its background data set. Cut #5 is done with each detector's binned, uncalibrated, energy spectrum and is as follows:

1. For each run, the average centroid of each detector's peak is calculated. In other words, for each detector, μ_i is calculated for the i^{th} run, such that

$$\mu_i = \frac{\sum\limits_n y_n x_n}{\sum\limits_n y_n}, \tag{2.1}$$

   where y_n is the number of entries in the n^{th} bin, and x_n is the location of the center of the n^{th} bin. The range of the n bins corresponds to roughly ±3-keV around the peak of interest. For the calibration data, the peak of interest is ^{208}Tl's 583-keV peak; for the background data, the peak of interest is the pulser.

2. For each run, the standard deviation of each detector's peak is calculated. In other words, for each detector, σ_i is calculated for the i^{th} run, such that

$$\sigma_i = \sqrt{\frac{\sum\limits_n y_n \left(x_n - \mu_i\right)^2}{\left(\sum\limits_n y_n\right) - 1}}, \tag{2.2}$$

   where μ_i, y_n, x_n and the range of n are defined in Eq. 2.1.

3. For each detector, the average of its peak's centroid over the span of the entire

data set is calculated. That is, for each detector, μ is calculated such that

$$\mu = \frac{\sum_i \mu_i}{\sum_i 1}, \tag{2.3}$$

where μ_i is the peak centroid for run i, as defined in Eq. 2.1, and i spans over all the runs of the data set.

4. For each detector, the standard deviation from the average of the centroids is calculated. That is, for each detector, σ is calculated such that

$$\sigma = \sqrt{\frac{\sum_i (\mu_i - \mu)^2}{\left(\sum_i 1\right) - 1}}, \tag{2.4}$$

where μ_i is the peak centroid for run i, as defined in Eq. 2.1, and μ is the average of the centroids, as defined in Eq. 2.3.

5. If several (five or more) consecutive runs have a peak centroid (μ_i) that deviates from the average (μ) by $\pm 1.5\sigma$ or more, those runs are omitted from the detector's data set.

As an example, Fig. 2.4 shows the gain-shift cuts made to a subset of the background data for each of the six detectors with an enabled pulser. The detectors are, from top to bottom, left to right: S3D5, S3D4, S3D2, S1D4, S1D3, S1D2. In order to better compare the pulser's centroid from run to run, each run's pulser centroid (μ_i; Eq. 2.1) is shown as the number of standard deviations (σ; Eq. 2.4) away from the centroids' average (μ; Eq. 2.3). In the example shown in Fig. 2.4, a few cases can be seen where for several consecutive runs the pulser's centroid significantly deviates from the average. These runs, whose data points are shown in red, are omitted. S1D2 appears to have a change in gain during two, independent sets of runs. It is interesting to note that in

both of these sets of runs, another detector also shows a change in gain; when S3D2 shows a change in its gain, S1D2 also shows a change in its gain, and when S1D3 later shows a change in its gain, S1D2 also shows a change in its gain. S1D2 and S1D3 share a digitizer however S1D2 and S3D2 do not share a digitizer.

A check was performed to look for possible correlations between the event rate and changes in a detector's gain. Figure 2.5 shows the hourly rate for each run displayed in Fig. 2.4. As with Fig. 2.4, the detectors are, from top to bottom, left to right: S3D5, S3D4, S3D2, S1D4, S1D3, S1D2. Each detector's hourly rate is determined from integrating its energy spectrum above 20 keV. As seen from Figs. 2.5 and 2.4, there is no clear correlation between a detector's event rate and its peak's centroid location.

This DQ cut typically removes 0% – 2% of each detector's calibration data, as seen in column "Cut #5" of Table 2.2. With the exception of S1D4, this DQ cut typically removes 0% – 5% of each detector's background data, as seen in Table 2.4. (Note, this cut is not performed on the background data set for S3D1 since the detector's pulser is not enabled. Therefore, it is not featured in this table.) Since this DQ cut is performed on a detector-by-detector case and omits entire runs, each detector's runtime is individually adjusted after this cut is applied.

The results from this DQ cut on S1D4's background data are quite different from the rest, in that it omits 47% from the detector's background data set. For roughly 35 days, this centroid of the detector's pulser is unstable (Fig. 2.6), and therefore the background runs taken during this time period are omitted. Since the detector's pulser is unstable for such a significant amount of time, it is not used when calculating the centroid average and standard deviation (Eqs. 2.3 and 2.4).

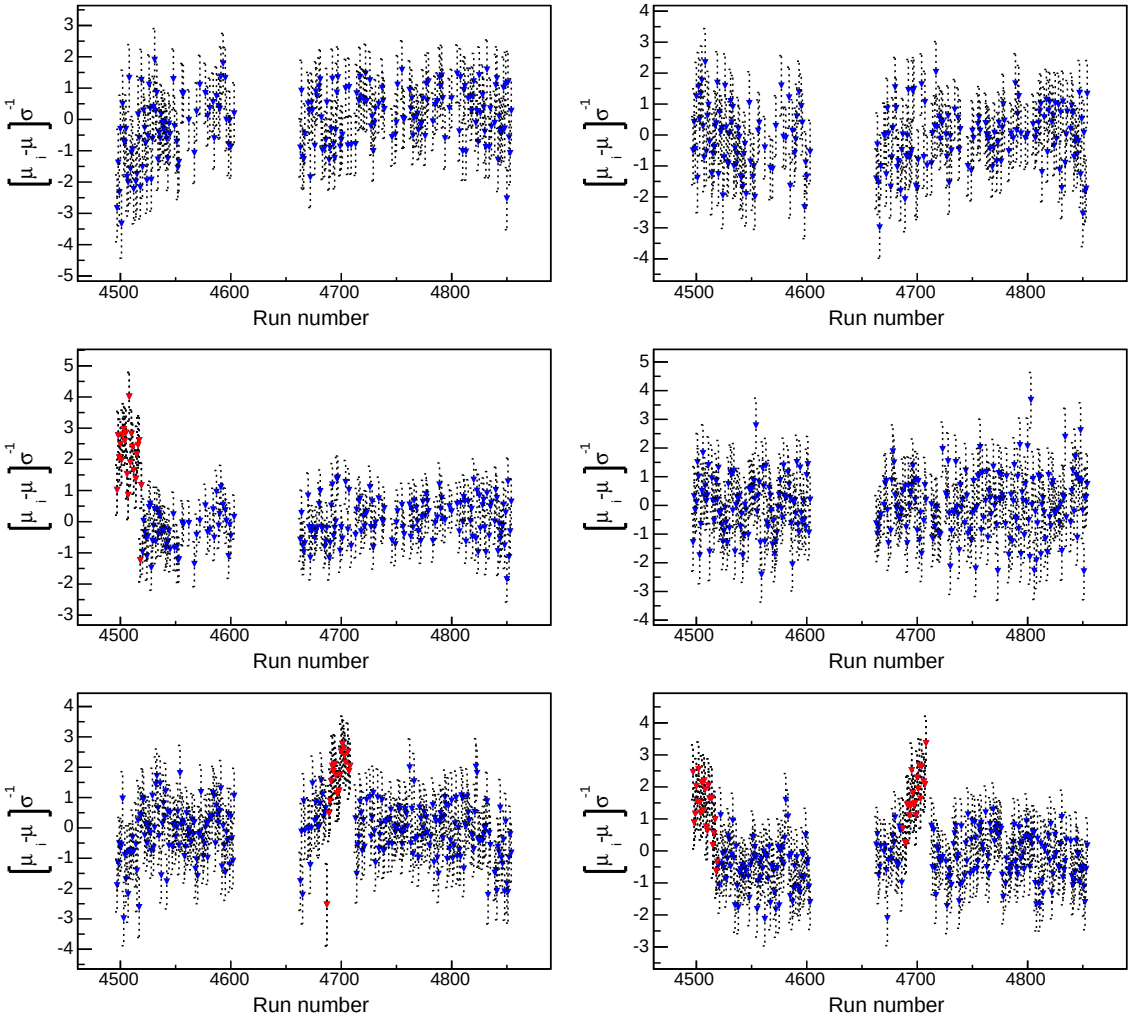

Figure 2.4: The centroid of each detector's pulser, for each individual run during a subset of the background data. Each graph corresponds to a different detector. The detectors are, from top to bottom, left to right: S3D5, S3D4, S3D2, S1D4, S1D3, S1D2. The red data points are runs that are omitted based on the premise that the detector showed a significant change in gain for the several consecutive runs. The y-axis is in units of $[\mu - \mu_i]\,\sigma^{-1}$, where μ, μ_i and σ are defined in Eqs. 2.3, 2.1 and 2.4 respectively. The y-error bars of each point are in units of $\sigma_i\,\sigma^{-1}$ where σ_i and σ are defined in Eqs. 2.2 and 2.4 respectively.

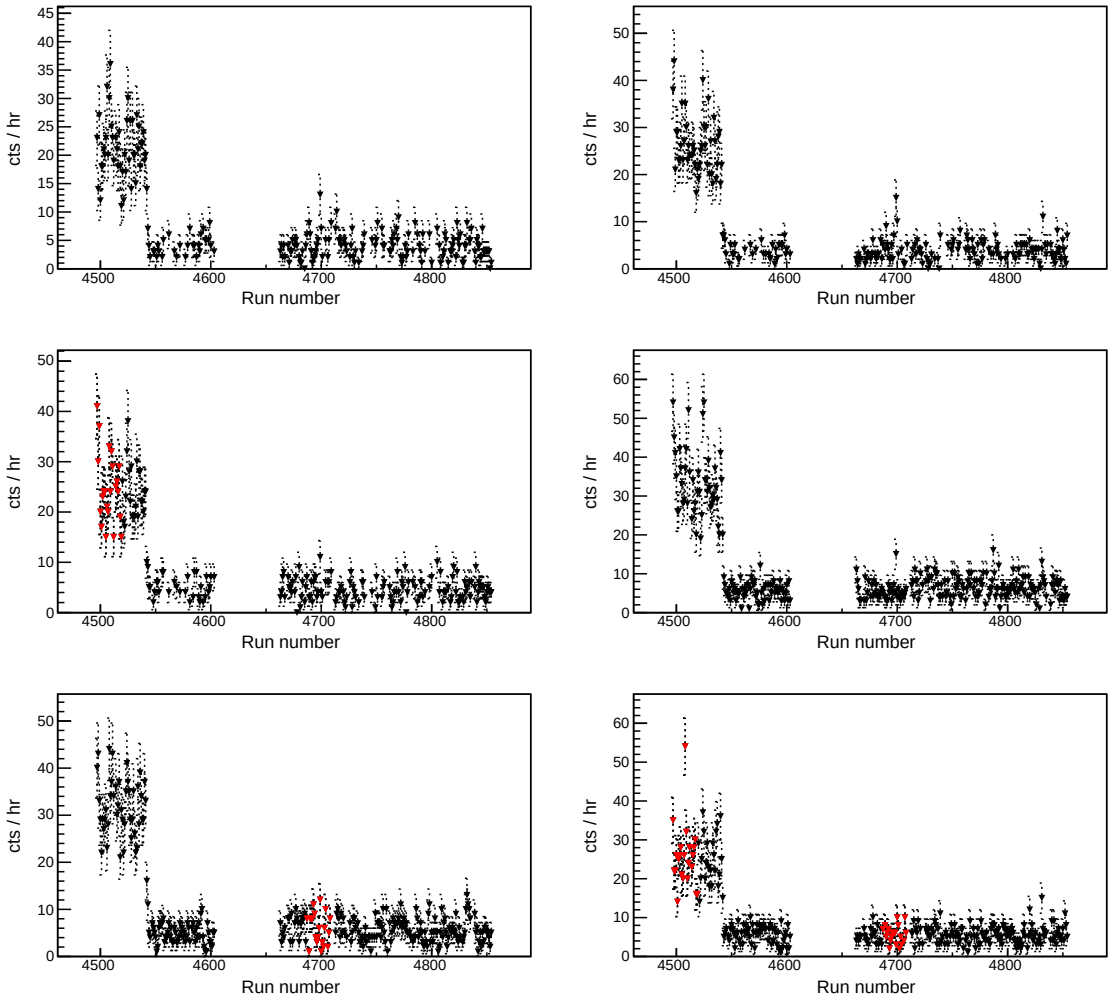

Figure 2.5: The hourly event rate of each detector during a subset of the background data. The subset of background data in this figure is the same as that seen in Fig. 2.4. Each graph corresponds to a different detector. The detectors are, from top to bottom, left to right: S3D5, S3D4, S3D2, S1D4, S1D3, S1D2. The red data points are runs that are omitted based on the premise that the detector showed a significant change in gain during the run (Fig. 2.4).

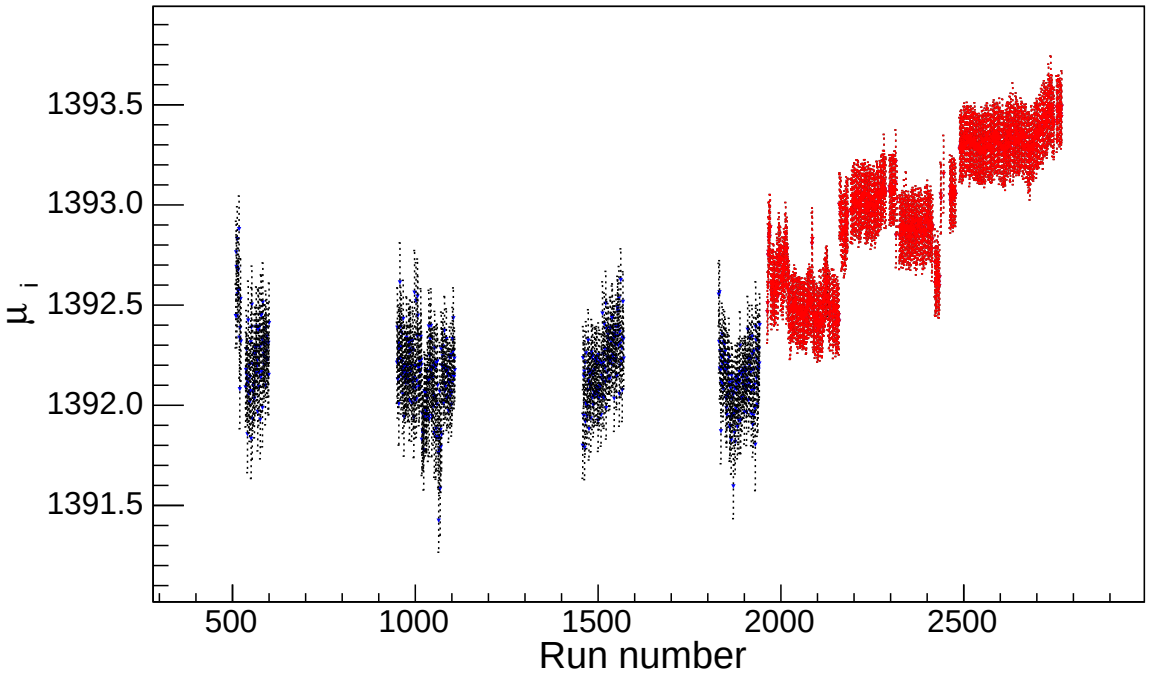

Figure 2.6: The centroid of the pulser (μ_i) for S1D4 for a subset of background data. For roughly 35 days, this detector's pulser is unstable and therefore these runs are omitted from the detector's data set; the omitted runs are shown in red.

2.2.6 Shift in Onboard Energy Determination

The sixth DQ cut has only found problematic runs in the background data and has yet to discover any problems in the calibration data. The DQ cut #6 looks at a two-dimensional histogram of the uncalibrated, onboard energy versus the uncalibrated, offline, 4-μs-trapezoidal energy. Both are expected to behave linearly with respect to energy, and therefore should also behave linearly with respect to each other. Figure 2.7 shows this linear trend for a subset of the background data for S3D5. (There is some unexpected scatter from the linear trend and this issue is discussed later in Section 2.2.7.) The subset of the background data shown in Fig. 2.7 is all the background data taken before November 7th 2014. Figure 2.8 shows this same two-dimensional histogram but now for all of the background data for S3D5. The data are divided into two groups: the gray data are the events from background data taken before November 7th (i.e. the

data pictured in Fig. 2.7); the blue data are the events from background data taken after November 7th. The events from the background data taken after November 7th populate a new line that deviates from the main line (main because the majority of the events populate this line). In fact, all the detectors that share the same digitizer board as S3D5 show this exact same behavior for background data taken before versus after November 7th. As a reminder, the operational detectors which share a common digitizer board with S3D5 are S3D1, S3D2 and S3D4, as seen in Fig. 2.1. Because this odd behavior cannot be explained, and the inclusion of background data taken after November 7th affects the event cut described in Section 2.2.7, the data is excluded from the final background data set. The omitted data accounts for 34% of the detectors' background data, as seen in column "Cut #6" of Table 2.4. Note, that in Table 2.4, S3D1, S3D2 and S3D4 are shown to have 34% of their background data omitted from cut #6, while S3D5 is shown to have 37% of its background data omitted. In fact, this same issue is seen a second time in S3D5, for roughly two consecutive days. Unlike the other instance, the issue is not seen in any other detectors. Nevertheless, it is problematic and omitted, thus accounting for the additional 3% in Table 2.4.

2.2.7 Incorrect Onboard Energy Assignment

The eighth, and final, DQ cut's purpose is to omit events where the onboard energy is incorrectly assigned. This issue can most clearly be seen in Fig. 2.9; a two-dimensional histogram of the uncalibrated, onboard energy versus the uncalibrated, offline, 4-μs-integration-time trapezoidal energy. The data in Fig. 2.9 is for a single detector, S3D5, and is from a ^{228}Th calibration run. (The issue can also seen in Fig. 2.8, though not as prominently due to lower statistics.) While there is some scattered deviation from the expected linear trend, the most troublesome features are the horizontal and vertical lines. The waveforms of the events in the vertical and horizontal lines have been investigated and, if it is assumed that the digitized waveforms are correct, then the

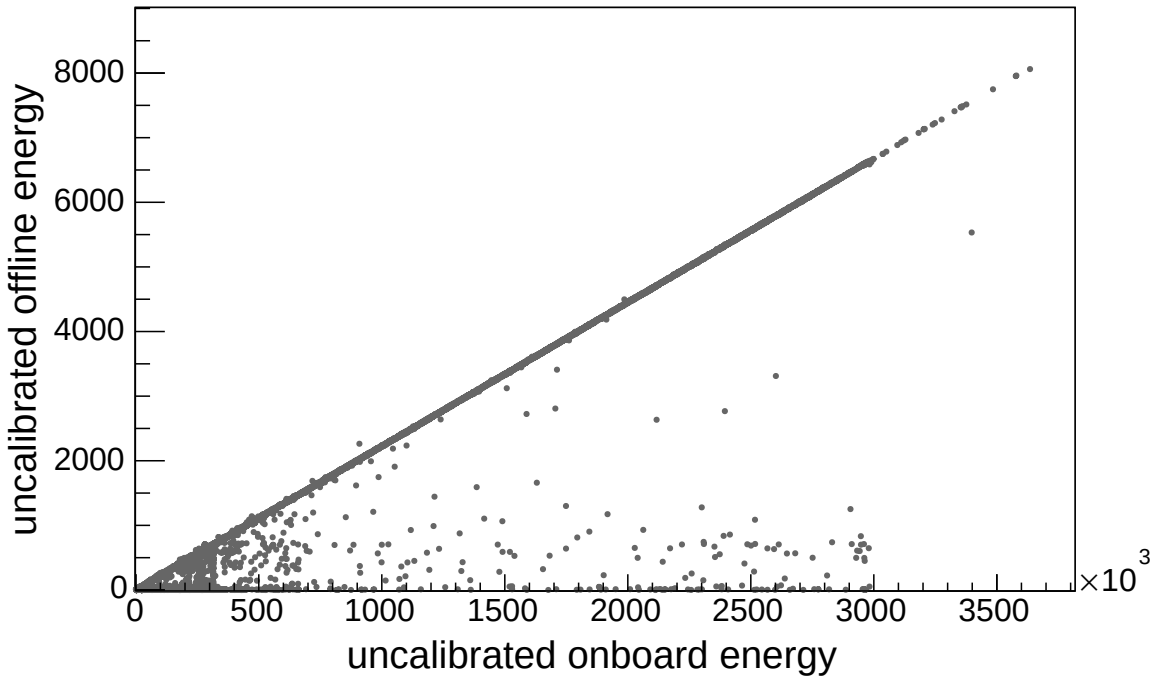

Figure 2.7: A two-dimensional histogram of uncalibrated, onboard energy versus uncalibrated, offline, 4-μs-trapezoidal energy. The data is for a single detector, S3D5, and is from a subset of the background data. The data is expected to follow a linear trend.

events in the lines have an incorrectly assigned onboard energy [Mas15]. However first it must be verified that the waveforms themselves are correct. This work is currently ongoing within the MAJORANA collaboration. Regardless of whether the issue is an incorrect waveform or an incorrect assignment of onboard energy, the exact cause of either of these is unknown and is also being explored. In the meantime, this issue creates false gamma peaks in the energy spectrum and gives incorrect amplitudes to existing gamma peaks. For this reason, a cut is performed on the data to omit all events that do not follow the expected linear trend. The cut parameters are extracted from the ^{228}Th-line-source data and are obtained as follows.

1. With the ^{228}Th data, a two-dimensional histogram of uncalibrated, onboard energy versus uncalibrated, offline, 4-μs-trapezoidal energy is fit with a first-order polynomial. The fit range roughly corresponds to 650-3000 keV (Fig. 2.10).

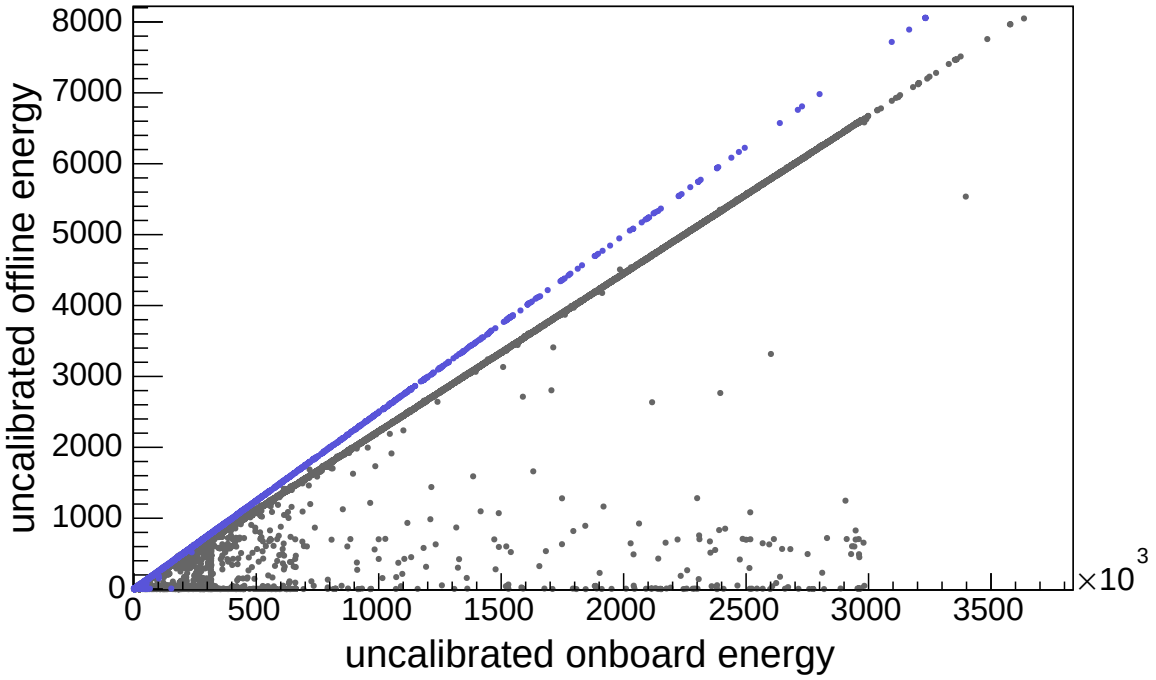

Figure 2.8: A two-dimensional histogram of uncalibrated, onboard energy versus uncalibrated, offline, 4-μs-trapezoidal energy. The data is for a single detector, S3D5, and is from all of the background data. The data is expected to follow a single linear trend. The gray data are the events from background data taken before November 7th 2014 (i.e. the data pictured in Fig. 2.7). The blue data are the events from background data taken after November 7th. These events deviate from the main line and therefore background runs taken after November 7th are excluded for S3D5.

2. A ±5-sigma band is found for the entire data range (Fig. 2.11). (i.e. The 5-sigma upper (lower) limit is: $y = (b \pm 5 \cdot \Delta b) + (m \pm 5 \cdot \Delta m) \cdot x$. Here, m and b are the slope and y-intercept from the best linear fit to the data; Δm and Δb are their uncertainties; x is the uncalibrated, onboard energy; y is the uncalibrated, offline energy.

3. Any event outside the ±5-sigma band is omitted from the final spectrum (Fig. 2.12).

Each detector's slope and y-intercept values found from the best fit are listed in Table 2.5. The values in Table 2.5 are found from fitting the five ^{228}Th data sets pictured in Fig. 2.2. While the slope and y-intercept parameters are obtained from the ^{228}Th data only, this particular cut is performed on the ^{228}Th and background data.

Tables 2.6 and 2.7 and Figs. 2.13 and 2.14 show the event cut's effect on the energy spectrum and on the event rate. Table 2.6 (2.7) is each detector's total rate after the cut, and the rate of cut events for the calibration (background) data. Tables 2.6 and 2.7 also show the runtime for each detector, which is not adjusted after applying this event cut. Figure 2.13 (2.14) is the energy spectra of the *cut* events for all detectors for the calibration (background) data. The dominant feature of Figs. 2.13 and 2.14 is an unphysical peak at a location corresponding to roughly 115 keV.

The purpose of this cut was to identify the origin of the unphysical 115-keV "peak" in the energy spectra and remove it – and it did. However, it should be noted that since the origin of these problematic events is unknown, the efficiency of this cut could depend on energy which could cause problems during the analysis of the final energy spectra. However, as seen in Tables 2.6 and 2.7 this cut excludes no more than 3% of the events for a single detector. Given the small rate – even if this cut did have an energy dependence – it is highly unlikely that the cut would effect the final energy spectra enough to affect future analysis.

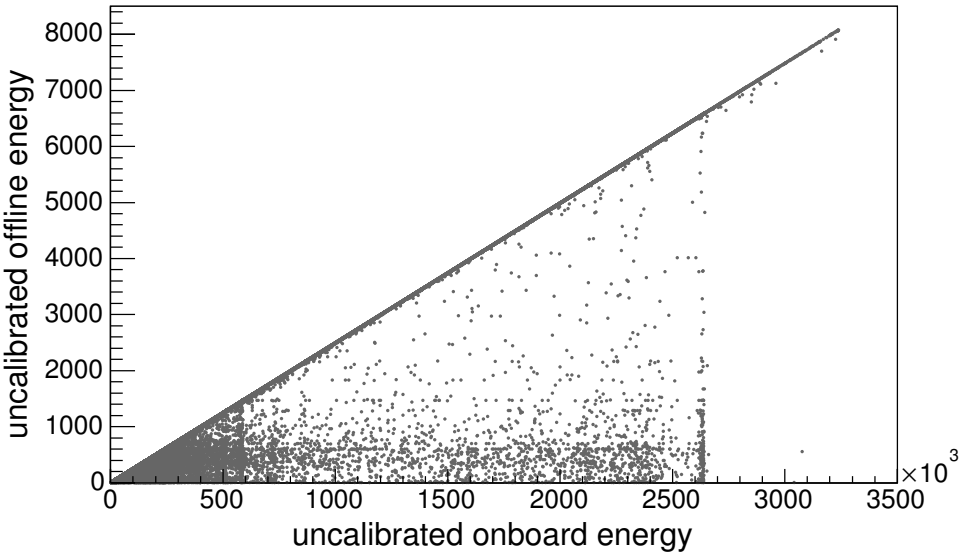

Figure 2.9: A two-dimensional histogram of uncalibrated onboard energy versus uncalibrated offline 4-μs-trapezoidal energy. The data is for a single detector, S3D5, and is from a ^{228}Th calibration run. The data is expected to follow a linear trend.

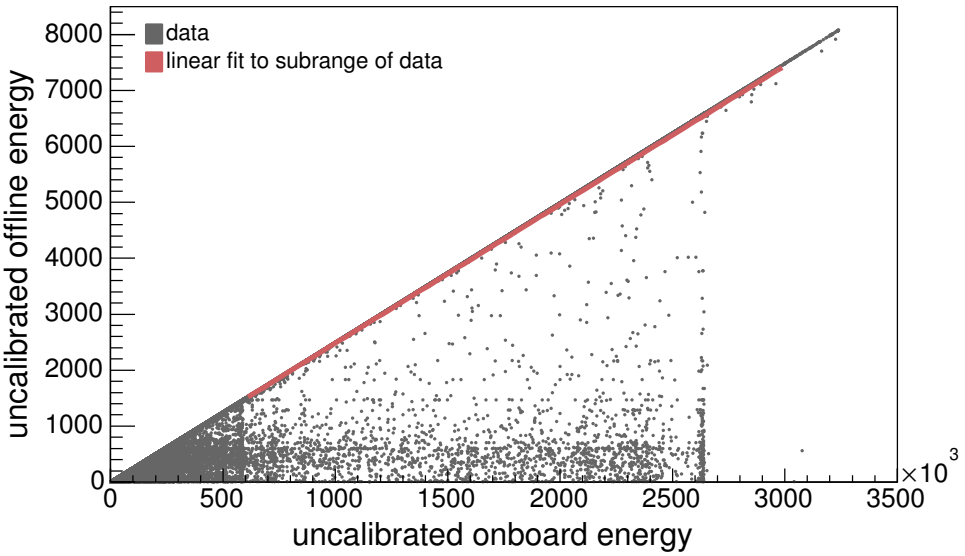

Figure 2.10: The same data seen in Fig. 2.9, with its first-order polynomial fit. The fit was done on a limited range, corresponding to roughly 650-3000 keV.

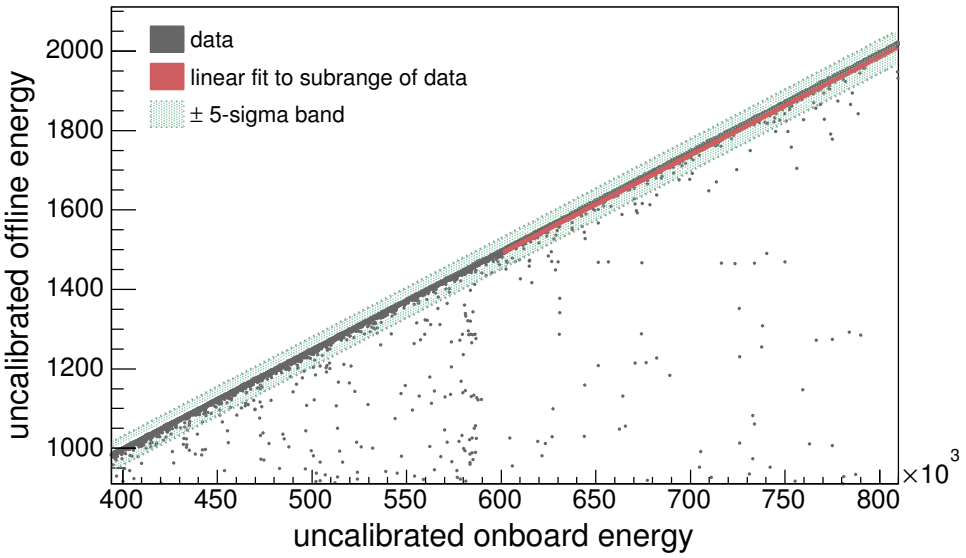

Figure 2.11: The same data and fit seen in Fig. 2.10 with the ±5-sigma band resulting from the best fit. All events within the ±5-sigma band are kept for the final spectrum; all events outside the ±5-sigma band are omitted from the final spectrum. A limited x- and y-range are shown (as compared with Figs. 2.9 and 2.10) so that the upper and lower limits can be better visualized. Note that, although the linear fit to the data is performed on a limited range, the omission of events outside of the ±5-sigma band is done for the entire range of the data.

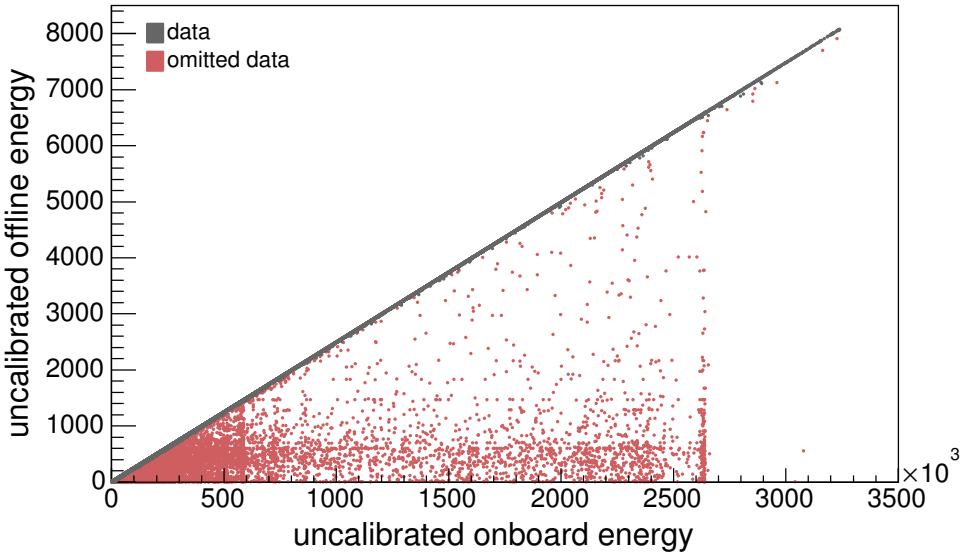

Figure 2.12: The same data seen in Fig. 2.9, now divided into two cases. The gray data are the events that lie within the ±5-sigma band seen in Fig 2.11 and are kept for the final spectrum. The red data are the events that lie outside the ±5-sigma band and are rejected.

Table 2.5: Results from Linear Fit to Onboard versus Offline Energy.

Detector	m (Δm)	b (Δb)
S1D2	2.476 (4) $\cdot 10^{-3}$	5 (6)
S1D3	2.48 (1) $\cdot 10^{-3}$	-10 (30)
S1D4	2.473 (4) $\cdot 10^{-3}$	4 (6)
S3D1	2.484 (3) $\cdot 10^{-3}$	0 (5)
S3D2	2.482 (3) $\cdot 10^{-3}$	2 (5)
S3D4	2.475 (4) $\cdot 10^{-3}$	2 (6)
S3D5	2.479 (3) $\cdot 10^{-3}$	3 (6)

Table 2.6: Performance of Event Cut in Section 2.2.7 on Calibration Data.

Detector	Runtime (hrs)	Event Rate (cts/s)	
		Cut Events	After Cut
S1D2	17.92	0.536 (3)	47.01 (3)
S1D3	17.76	0.591 (3)	61.94 (3)
S1D4	18.07	0.340 (2)	58.58 (3)
S3D1	18.07	0.093 (1)	36.76 (2)
S3D2	18.24	0.338 (2)	54.55 (3)
S3D4	18.09	0.891 (4)	61.05 (3)
S3D5	13.46	0.941 (4)	46.18 (3)

Table 2.7: Performance of Event Cut in Section 2.2.7 on Background Data.

Detector	Runtime (hrs)	Event Rate (cts/s)	
		Cut Events	After Cut
S1D2	1448.5	$0.76\ (4) \cdot 10^{-4}$	$31.7\ (2) \cdot 10^{-4}$
S1D3	1434.8	$0.22\ (2) \cdot 10^{-4}$	$8849\ (4) \cdot 10^{-4}$
S1D4	770.41	$0.20\ (3) \cdot 10^{-4}$	$701\ (2) \cdot 10^{-4}$
S3D1	826.16	$0.024\ (9) \cdot 10^{-4}$	$11992\ (6) \cdot 10^{-4}$
S3D2	828.90	$0.47\ (4) \cdot 10^{-4}$	$13.8\ (2) \cdot 10^{-4}$
S3D4	789.60	$0.29\ (3) \cdot 10^{-4}$	$10144\ (6) \cdot 10^{-4}$
S3D5	777.72	$0.16\ (2) \cdot 10^{-4}$	$4813\ (4) \cdot 10^{-4}$

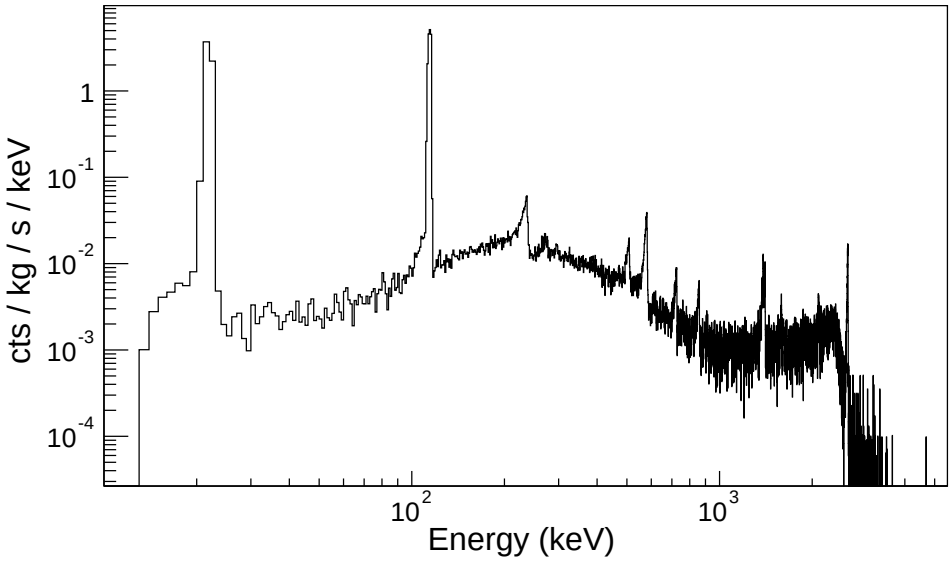

Figure 2.13: The data selection described in Section 2.2.7 omits detectors' individual events (as supposed to an entire run). This is the energy spectrum of the cut events for all detectors for the ^{228}Th calibration data.

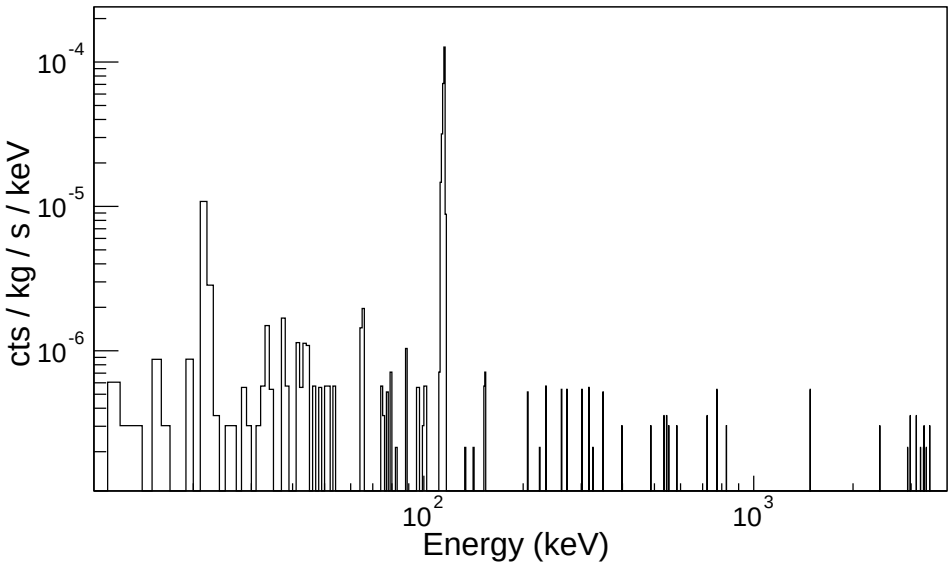

Figure 2.14: The data selection described in Section 2.2.7 omits detectors' individual events (as supposed to an entire run). This is the energy spectrum of the cut events for all detectors for the background data.

CHAPTER 3: GAMMA-PEAK CHARACTERIZATION

3.1 An Introduction to the Peak-Fitting Function

In gamma-ray spectrometry, to characterize the shape of a peak from a detected source of mono-energetic gammas, the observed peak is often fit with a Gaussian (Eq. 3.1).

$$\text{Gaussian} \propto \exp\left[-\left(\frac{x-\mu}{\sigma\sqrt{2}}\right)^2\right] \tag{3.1}$$

The Gaussian depends on two parameters: the first, μ, is the centroid of the Gaussian and is the energy of the mono-energetic gammas; the second, σ, is related to the width of the Gaussian peak (i.e. the resolution). The parameter σ depends on energy such that:

$$\sigma = \sqrt{\sigma_0^2 + \sigma_1^2\, E + \sigma_2^2\, E^2}. \tag{3.2}$$

The first term, σ_0^2, characterizes the electronic noise. The second term, $\sigma_1^2\, E$, reflects the uncertainty in the number of electron-hole pairs created, and can be equivalently written as

$$\sigma_1^2\, E = \left(0.128^2\,\text{keV}\right) F\, E, \tag{3.3}$$

where F is the Fano factor. For germanium detectors, typical values of the Fano factor have been measured from 0.057 to 0.12 [Gil07]. The third term, $\sigma_2^2\, E^2$, is linear in energy and is typically associated with charge trapping or other effects resulting in incomplete charge collection.

In some applications a Gaussian is sufficient to describe a gamma peak. However, a Gaussian does not fully characterize the creation and collection of charge from a gamma interacting in a HPGe detector. And so, in cases where the accuracy of a peak's centroid

and resolution are of upmost importance, an additional low-energy tail component is needed. This low-energy tail can be a direct result of incomplete charge collection within the detector, whether it be from charge trapping, from crystal imperfections and impurities, or by any other means. A low-energy tail can typically be observed best in larger sized detectors, whose pulses have longer rise-times and could press the limitations of the amplifier's shaping time. The low-energy tail is best described by an exponential times a complimentary error function as in Eq. 3.4 [Rad00, Rad13, Lon90].

$$\text{Low-Energy Tail} \propto \exp\left(\frac{x-\mu}{\tau}+\frac{\sigma^2}{2\tau^2}\right)\operatorname{erfc}\left(\frac{x-\mu}{\sigma\sqrt{2}}+\frac{\sigma}{\tau\sqrt{2}}\right) \tag{3.4}$$

The low-energy tail is dependent on three parameters, two of which are the same parameters as in the Gaussian: μ and σ. It also introduces a new parameter, τ, which is related to the low-energy tail's width. An additional high-energy tail may be present in a gamma peak's shape. This high-energy tail is typically an indication that the pole zero cancelation has been over-compensated [Par91]. Given that the high-energy tail is indicative of a problem which can be fixed, it is not further discussed and the low-energy tail is simply referred to as the "Tail".

While the Gaussian and the Tail describe the actual signal observed from a mono-energetic source of gammas, the signal's peak typically sits on top of a background, which consists of two components. The first, a polynomial (often of second- or first-order), mainly results from the Compton scattering of higher-energy gammas. For this work, a second-order polynomial is used and is thus referred to as the "Quadratic".

The second, referred to as the "Step", is properly named as it describes the observation that the background on the low-energy side of a gamma-peak is greater than on the high-energy side. The Step is thought to mainly arise from the charge cloud overlapping with the lithium transition layer, thus causing part of the signal to be collected at a later time. Another contribution to the Step is thought to be from the Compton

scattering of photons into the detector. The Step takes on the form of a complimentary error function (Eq. 3.5).

$$\text{Step} \propto \text{erfc}\left(\frac{x-\mu}{\sigma\sqrt{2}}\right) \tag{3.5}$$

The area of the Step can not be well quantified and does not contribute to the peak's energy resolution; hence, it is classified as part of the background rather than the signal. However, the Step is dependent on the same μ and σ as in the Gaussian and Tail, since the shape of the Step is dependent upon the detector's energy resolution. In the limit where a peak has no Tail and its energy resolution tends to zero, the Gaussian becomes a delta function, and the Step becomes a true step function (Eq. 3.7) [Hel80].

$$\lim_{\sigma\to 0}\text{Gaussian} = \begin{cases} \infty & x = \mu \\ 0 & x \neq \mu \end{cases} \tag{3.6}$$

$$\lim_{\sigma\to 0}\text{Step} = \begin{cases} 1 & x < \mu \\ 0 & x > \mu \end{cases} \tag{3.7}$$

When fitting a single peak, the peak is simultaneously fit with functions describing both the background and the signal. As discussed above, the signal is comprised of the Gaussian and the Tail, and the background is comprised of the Step and the Quadratic. In the peak-fitting function, the Gaussian and Tail are normalized so that

$$\int_{-\infty}^{+\infty}(\text{signal})\ dx = \int_{-\infty}^{+\infty}(\text{Gaussian} + \text{Tail})\ dx = A\,, \tag{3.8}$$

where the parameter A is the area of the signal. This results in the peak-fitting function:

$$\text{Fit Function} = \text{Gaussian} + \text{Tail} + \text{Step} + \text{Quadratic} \tag{3.9}$$

where the Gaussian, Tail, Step and Quadratic are given by Eqs. 3.10 – 3.13.

$$\text{Gaussian} = \frac{A\ (1 - H_{\text{tail}})}{\sigma\sqrt{2\pi}}\ \exp\left[-\left(\frac{x-\mu}{\sigma\sqrt{2}}\right)^2\right] \tag{3.10}$$

$$\text{Tail} = \frac{A\,H_{\text{tail}}}{2\tau}\ \exp\left(\frac{x-\mu}{\tau} + \frac{\sigma^2}{2\tau^2}\right)\ \text{erfc}\left(\frac{x-\mu}{\sigma\sqrt{2}} + \frac{\sigma}{\tau\sqrt{2}}\right) \tag{3.11}$$

$$\text{Step} = A\,H_{\text{step}}\ \text{erfc}\left(\frac{x-\mu}{\sigma\sqrt{2}}\right) \tag{3.12}$$

$$\text{Quadratic} = \alpha + \beta x + \gamma x^2 \tag{3.13}$$

The fit function has a total of 9 free parameters: A is the area of the peak's signal, H_{tail} is the fraction of the area of the peak's signal that is from the Tail, μ is the centroid of the Gaussian, σ is the width of the Gaussian, τ is related to the width of the Tail, H_{step} is proportional to the height of the Step, and α, β and γ are the constant, linear, and quadratic terms of the Quadratic respectively.

The centroid of the peak, M, and the variance of the peak, Σ^2, are defined in Eq. 3.14 and 3.15 respectively. Appendix A contains the calculations for determining the peak's centroid and peak's variance, as well as their uncertainties, which are found using the standard technique of propagation of uncertainties.

$$M = \mu - \tau H_{\text{tail}} \tag{3.14}$$

$$\begin{aligned}\Sigma^2 &= \sigma^2 - \tau^2 H_{\text{tail}}^2 + 2\tau^2 H_{\text{tail}} \\ &= \sigma^2 + \tau^2 H_{\text{tail}}\,(2 - H_{\text{tail}})\end{aligned} \tag{3.15}$$

Table 3.1: The parameters resulting in the best fit to the peak in Fig. 3.1.

Parameter	Value
μ	583.12 (2) keV
A	2490 (20)
H_{tail}	0.12 (8)
σ	0.563 (7) keV
τ	0.5 (1) keV
H_{step}	1.4 (10)$\cdot 10^{-3}$
α	5 (3)$\cdot 10^{2}$
β	-0.9 (6) keV^{-1}
γ	4 (5)$\cdot 10^{-4}$ keV^{-2}

All fitting is performed over a $M \pm 10\Sigma$ fit region. Figure 3.1 shows an example of a fit to a gamma peak of the HPGe detector designated S3D2 installed in the MAJORANA PC. The binned data shown are from a calibration run taken with a ^{228}Th line source. For this particular peak, the best fit results from the free parameters having the values listed in Table 3.1. From the fit parameters, the centroid, M, and the variance, Σ^2 can be calculated. The centroid is found to be at 583.051 (8) keV. It is interesting to note that this is a slightly lower value than the centroid of the Gaussian (μ) because of the presence of the Tail, as seen in Eq. 3.14. The square-root of the variance, Σ, is 0.616 (10) keV. As seen in Eq. 3.15, it is a weighted sum of the width of the Gaussian and the width of the Tail.

3.2 Minimization Techniques and Parameter Errors

A peak's best fit is the fit function with the set of parameters which result in the smallest log-likelihood value. The method of least squares is not used, as it is known to be biased such that it tends to underestimate the area of the signal [Poo01, Bev69]. However, for the sake of the robustness of the peak-fitting routine, minimizing the chi-squared is often utilized if there are convergence problems with the log-likelihood

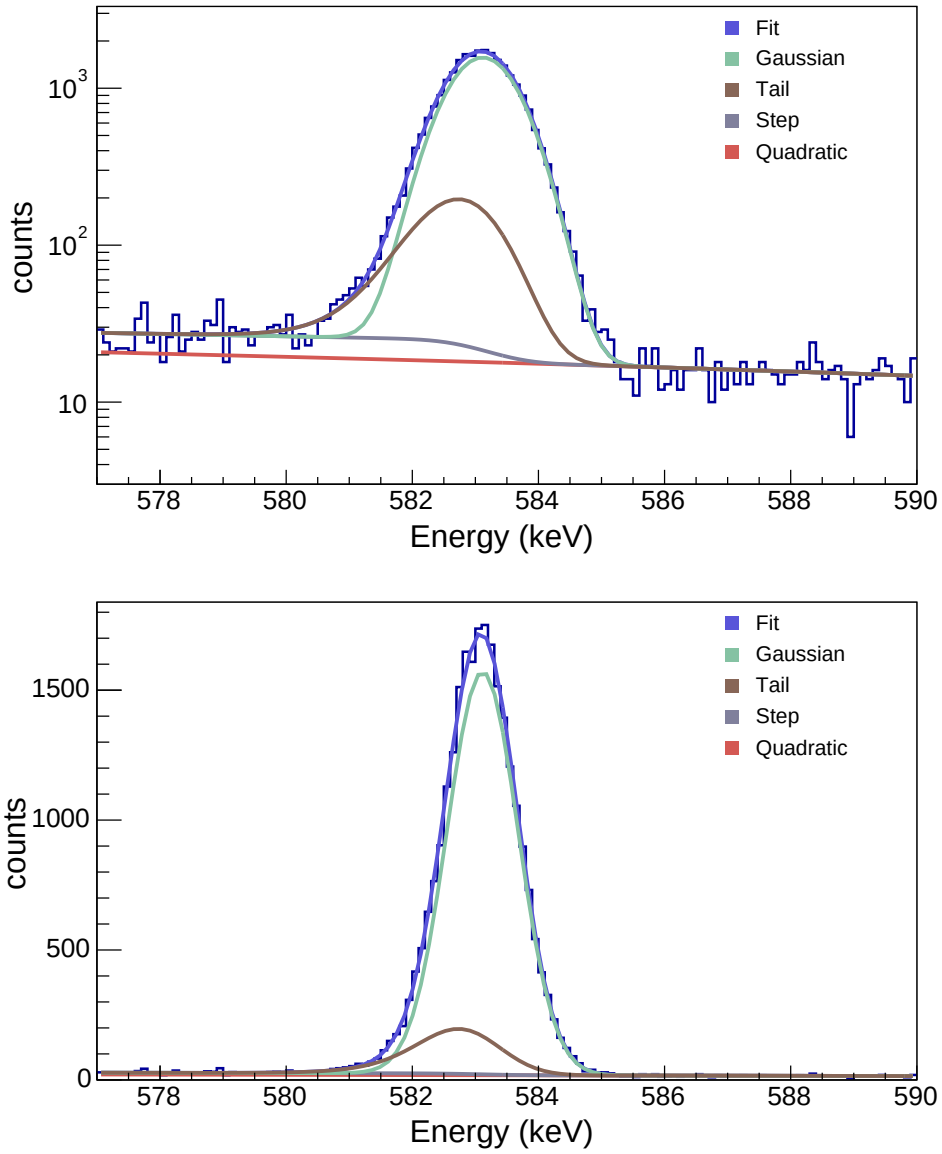

Figure 3.1: The best fit to S3D2's 583-keV-gamma peak with a logarithmic y-axis (top) and linear y-axis (bottom). The binned data shown are from a calibration run taken with a ^{228}Th line source. The parameter values obtained from the best fit can be found in Table 3.1.

function. The peak is initially fit by minimizing the chi-squared function, and then those best-fit parameters are used in a second fit that minimizes the log-likelihood function.

All fitting is done with the ROOT Fitter class [Bru97, Bru96]. ROOT has several different tools built into its framework which can be used to find the minimum value of the minimization function (e.g. log-likelihood, chi-squared). MINUIT is one of these tools and is used for all the work presented here [Jam04b]. MINUIT itself has a few processors from which to choose, most notably the processors MIGRAD and MINOS. The difference between the two is mainly in their parameter error calculations. In some cases MIGRAD's parameter errors are acceptable and the processor is preferred since it is typically more robust during a fitting routine. However, the MIGRAD parameter errors are not reliable if the fit function is not (roughly) linear with respect to its fit parameters or if there are correlations between the parameters themselves [Jam04a]. If either of these cases is true, the MINOS processor is used. For the peak-fitting function described in the previous section (Eqs. 3.10 – 3.12), the MINOS processor is always used when obtaining the best fit. It is often difficult to obtain convergence when fitting with MINOS, and therefore a peak is first fit with MIGRAD, and then those best-fit parameters are used in a second fit that uses the MINOS processor. Coupled with the choice of which minimization function to use, the following sequence of fitting routines is used to find the best fit to a gamma peak.

1. Chi-Squared minimization function; MIGRAD processor
2. Log-Likelihood minimization function; MIGRAD processor
3. Log-Likelihood minimization function; MINOS processor

As discussed, the best-fit parameters are determined from a final fit which minimizes the log-likelihood function using the MINOS processor. During this final fit, no parameters

of the fit function are fixed in value or limited in range.

3.3 Single Peak-Fitting Function Parameter Correlations

Finding a single and unique best fit is difficult if two or more of the fit function's parameters are correlated. For this reason, it is important to understand the parameters' dependence on one another. MINUIT has the capability of producing n-sigma contours for the different combinations of parameters in the fit function. If a 1-sigma contour plot is made for parameters A and B, with parameter A on the x-axis and parameter B on the y-axis, the maximum width of the contour is equal to the uncertainty of parameter A reported by MINUIT, and the maximum height of the contour is equal to the uncertainty of parameter B. Furthermore, the shape of the n-sigma contours gives insight into how the parameters correlate with each other. The n-sigma contours for the peak-fitting function are made from simulations based on typical parameter values. The parameter values are used to create a Probability Distribution Function (PDF) describing the energy response function. Then several random numbers are generated according to the distribution of the PDF until the desired statistics are acquired. The parameters are modeled from values seen by the unshielded PC detectors for the 1461-keV peak from ^{40}K. The parameter H_{tail} can greatly vary from one detector to another, and for that reason, several simulations are done for different values of H_{tail}. The parameter values used for the simulations are found in Table 3.2. For simplicity, the quadratic background is made constant; i.e. $\beta = \gamma = 0$, as seen in Table 3.2.

Any asymmetry in two parameters' n-sigma contours is an indication that there is a correlation between the two parameters. All two-parameter permutations are investigated and the only parameters that show significant correlation are: μ, H_{tail}, σ and τ. Figure 3.2a is an example of typical 1- and 2-sigma contours that are deemed to not show "significant correlation"; this particular figure is for the parameters μ and H_{step}. Figures 3.2c, e and g are the 1- and 2-sigma contours for μ and H_{tail}, σ and

Table 3.2: The parameters used in the single gamma-ray peak simulations.

Parameter	Value
μ	1461 keV
A	$1{\cdot}10^4$
H_{tail}	0.2, 0.4, 0.6 and 0.8
σ	0.8 keV
τ	0.9 keV
H_{step}	$5{\cdot}10^{-3}$
α	6
β	0
γ	0

τ respectively. It can be seen that even though μ is tightly constrained, there is still a dependence on its value and the value of H_{tail}, σ and τ. In fact, it has been seen that those correlations change at different values of H_{tail}, as seen in the figures in the right column of Fig. 3.2 (b, d, f and h). These figures are the n-sigma contours from simulations with the H_{tail} parameter set to 0.8, which differs from the figures in the left column of Fig. 3.2 (a, c, e and g), where H_{tail} is set to 0.2 in the simulations. With the exception of the H_{tail} parameter, all other aspects of the two simulation are identical.

Two additional notes must be made about Fig. 3.2. For one, any discontinuities in a contour is a result of the fact that the best fit is at a very local minimum. This fact is especially true for when $H_{\text{tail}} = 0.8$, and can most clearly be seen in Fig. 3.2f. Secondly, during the fitting routine (and when n-sigma contours are generated), no parameters are fixed or constrained. Some parameters do have limited ranges for which the parameter value makes physical sense, and a final fit is never accepted unless all parameter values lie within their physical range. However, because no parameters are constrained, some n-sigma contours do cross into unphysical regions of parameter values. This is true for the 1- and 2-sigma contours from simulations with the H_{tail} parameter set to 0.8 (i.e.

the right column of Fig. 3.2). It is unphysical to have a H_{tail} value greater than 1.0, because by doing so, the Gaussian amplitude would be negative. And while the best fit gave a physical H_{tail} value of 0.80 (2), the 1- and 2-sigma contours do press into the unphysical region where H_{tail} >1. The black line of Fig. 3.2d is at the value $H_{\text{tail}} = 1$. The points at which the 2-sigma contour crosses the value of $H_{\text{tail}} = 1$ are seen as the red lines. They lie roughly at 1461.18 and 1461.15 keV. The values in the 1- and 2-sigma contours of Fig. 3.2f that lie beyond the red lines represent unphysical values. The same lines are drawn on Figs. 3.2b, f and h. While all these figures have parameter values within physical ranges, it still holds true that a value of μ between 1461.15 and 1461.18 keV and beyond results in a best-fit where *a different* parameter (i.e. H_{tail}) has an unphysical value.

3.4 Multiple Peak-Fitting Function

There are known correlations between the peak's centroid and sigma, tau and H_{tail}; they can be expressed by Eqs. 3.16 – 3.18.

$$\sigma = \sqrt{\sigma_0^2 + \sigma_1^2\, M + \sigma_2^2\, M^2} \tag{3.16}$$

$$\tau = b_\tau + m_\tau\, M \tag{3.17}$$

$$H_{\text{tail}} = b_H + m_H\, M \tag{3.18}$$

When fitting a single peak, often times there are multiple solutions for a peak's best fit. However, if the fit function is restated so that the fit parameters are forced to adhere to these detector-specific global parameterizations, a single, unique best fit can be obtained for a given peak. This is done by simultaneously fitting multiple peaks, with each individual peak's fit function containing a signal and background component

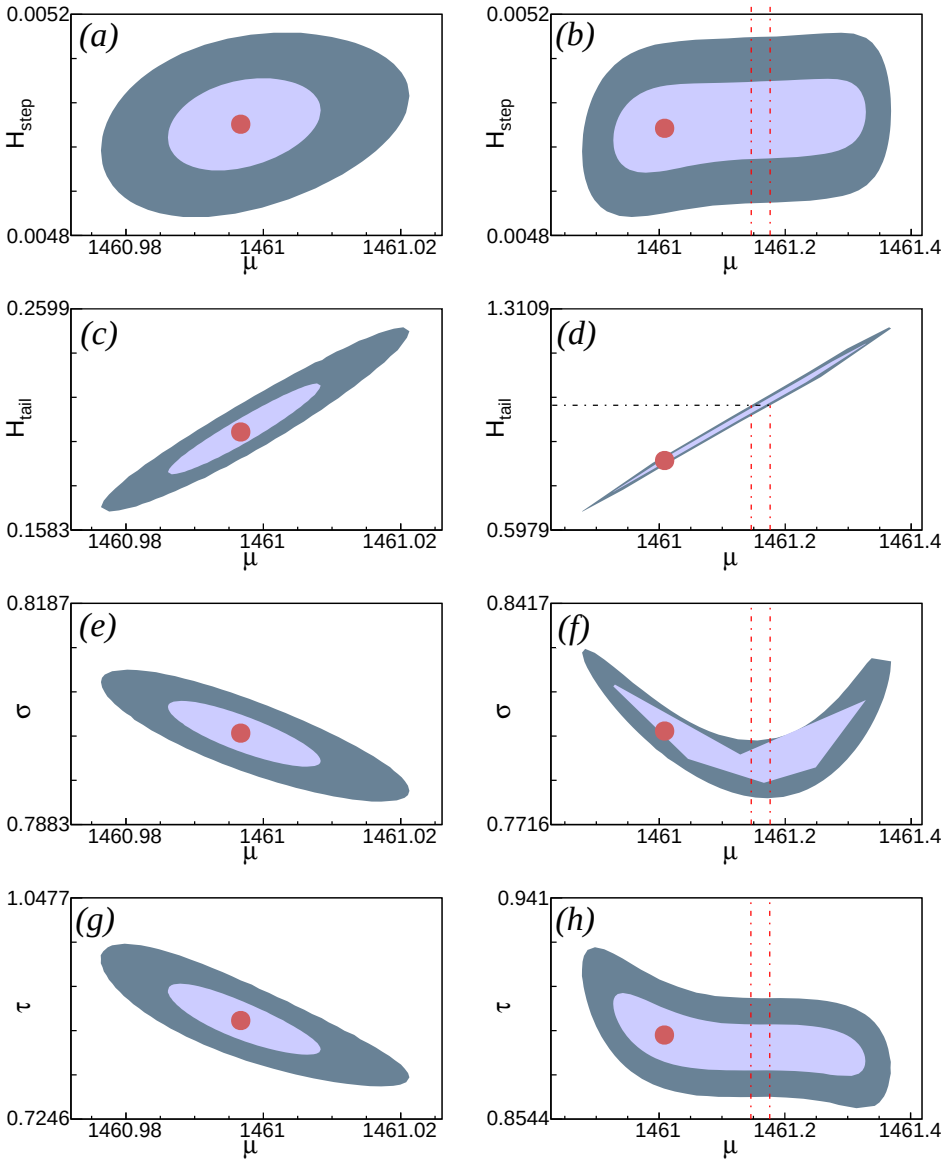

Figure 3.2: The 1-sigma (light blue) and 2-sigma (dark blue) contours for the single-peak-fitting-function parameters μ and: H_{step} (row 1), H_{tail} (row 2), σ (row 3), and τ (row 4). The figures in the left column are the n-sigma contours from simulations with the H_{tail} parameter set to 0.2; the figures in the right column are from simulations with the H_{tail} parameter set to 0.8. The red point in each figure indicates the parameter values that result in the best fit to the simulated peak. See text for more information.

as described in Eqs. 3.10 – 3.12. However, in this multi-peak fitting function, σ, τ and H_{tail} are replaced with Eqs. 3.16, 3.17 and 3.18 respectively. Equations 3.16, 3.17 and 3.18 introduce the new free parameters: σ_0, σ_1, σ_2, b_τ, m_τ, b_H and m_H. These parameter values are common among all the peaks that are being fit, but specific to a single detector. In addition to these common parameters, a peak's fit function also includes free parameters that are unique from the parameters in the other peaks' fit functions: μ, A, H_{step}, α, β and γ. Thus, if fitting n peaks simultaneously, there are $(7 + 6\,n)$ free parameters in the global fit function.

For the case of fitting a single peak, the peak's centroid is a function of μ, τ and H_{tail}. Since τ and H_{tail} are known to be functions of the peak's centroid, a new expression for the peak's centroid must be found for the case of fitting multiple peaks simultaneouly. Substituting Eq. 3.17 and Eq. 3.18 into Eq. 3.14 and solving for M yields

$$M = \frac{-\left(1 + b_\tau\, m_H + m_\tau\, b_H\right) + \sqrt{\left(1 + b_\tau\, m_H + m_\tau\, b_H\right)^2 - 4\, m_\tau\, m_H\, (b_\tau\, b_H - \mu)}}{2\, m_\tau\, m_H}\,. \tag{3.19}$$

Each peak's centroid and variance can be calculated from the best fit of the multi-peak fitting function using Eqs. 3.15 – 3.19. The errors are found using the standard technique of propagation of uncertainties. For reference, the calculations used in finding the errors are in Appendix A.

The energy response function for each detector in the PC is characterized using the multi-peak fitting function on ^{228}Th calibration data. For the results and more discussion on the multi-peak fitting function see Chapter 4.

3.4.1 Parameter Correlations

Similar n-sigma contours are made for the multi-peak fitting function parameters, as are for the single-peak fitting function. The parameters in the multi-peak simulation are modeled from values determined from measurements of S3D2 in the shielded PC with

a ^{228}Th line source. Most of the parameters used for the multi-peak simulations can be found in Table 3.3. Due to the large number of free parameters in the multi-peak fitting function and due to the fact that the minimum is very localized, a more limited set of parameter permutations are considered for the multi-peak fitting function than for the single-peak fitting function; namely the permutations of one peak's Gaussian centroid (μ_i) and all other parameters. Some contours for the single-peak fitting function display some discontinuities due to the fact that the best fit is at a very local minimum. This is even more prevalent in the n-sigma contours for the multi-peak fitting function. For some parameters the minimum is so localized that the contours cannot be generated. Table 3.4 summarizes the parameter permutations that are considered and whether the n-sigma contour plot was able to be generated. Figure 3.3 shows some of the 1- and 2-sigma contours for the multi-peak function. The selected parameters for Fig. 3.3 are μ_i and: σ_0, σ_2, m_τ, b_H, m_H and A_i. The index i in the parameters μ_i and A_i, indicates that they are the μ and A parameters of peak i. For Fig. 3.3, the peak i is the 300-keV peak. The other parameters (σ_0, σ_2, m_τ, b_H and m_H) have no specified index because these are the common parameters among all peaks in the multi-peak fitting function. From Fig. 3.3 one can safely conclude that there is no correlation between μ_i and the other parameters.

3.5 Conclusions and Future Work

The multi-peak fitting function was developed to remove parameter correlations seen with the single-peak fitting function while also improve on the accuracy of the calculated peak centroid and width. As demonstrated in Section 3.4.1, the parameters of the multi-peak fitting function show little to no correlation and as seen in Chapter 4, the multi-peak fitting function was successfully used to characterize the energy response function for each detector of the PC. Considering these successes, the multi-peak fitting function will be used to characterize each detector of the DEMONSTRATOR.

Table 3.3: The parameters used in the multiple gamma-ray peak simulations.

Parameter	Value					
σ_0 [keV]	0.34					
σ_1 [keV$^{1/2}$]	0.017					
σ_2	$2.7{\cdot}10^{-4}$					
b_τ [keV]	0.03					
m_τ	$8.4{\cdot}10^{-4}$					
b_H	0.11587					
m_H [keV^{-1}]	$1.1{\cdot}10^{-5}$					
	Peak 0	Peak 1	Peak 2	Peak 3	Peak 4	Peak 5
μ [keV]	277.381	300.099	583.115	727.321	860.318	2613.54
A	263	385	2492	509	304	1201
H_{step}	$2.4{\cdot}10^{-2}$	$1.1{\cdot}10^{-7}$	$1.4{\cdot}10^{-3}$	$4.4{\cdot}10^{-4}$	$2.3{\cdot}10^{-3}$	$3.2{\cdot}10^{-8}$

Table 3.4: Status of the n-sigma contours for μ_i in the multi-peak fitting function.

Parameter	1-σ	2-σ
σ_0	✓	✓
σ_1	unable to generate	unable to generate
σ_2	✓	✓
b_τ	unable to generate	✓
m_τ	✓	✓
b_H	✓	✓
m_H	✓	✓
A_i	✓	✓
$H_{\text{step},i}$	unable to generate	unable to generate
α_i	unable to generate	unable to generate
β_i	unable to generate	unable to generate
γ_i	unable to generate	unable to generate
μ_k	✓	✓

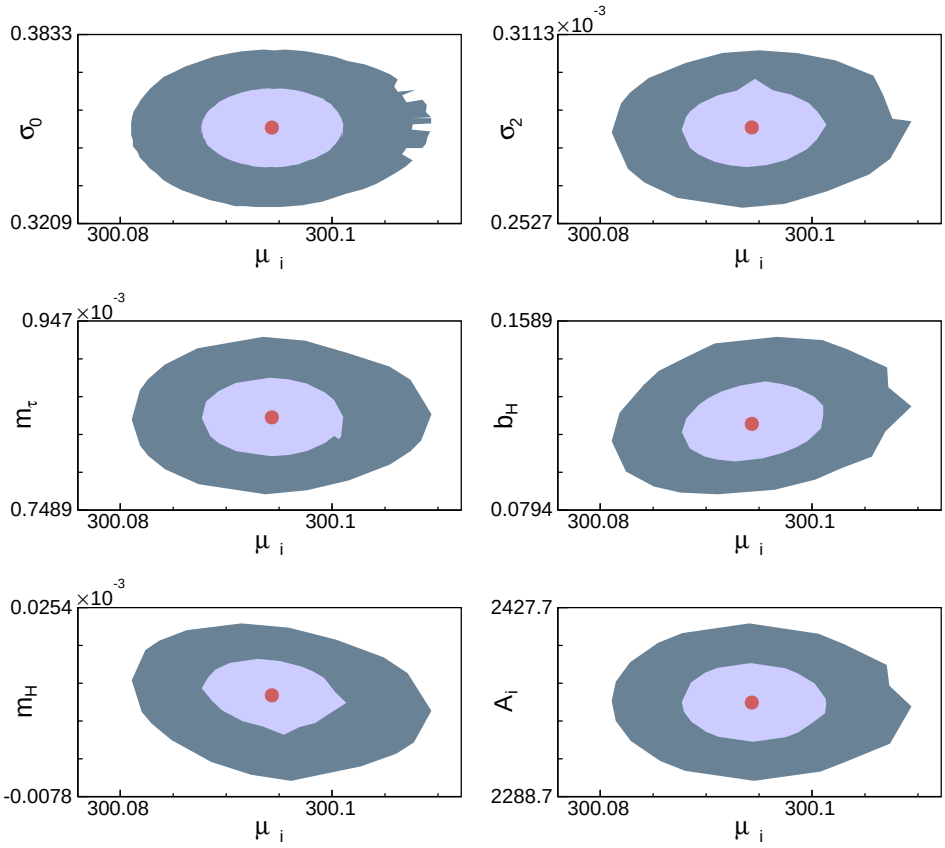

Figure 3.3: The 1-sigma (light blue) and 2-sigma (dark blue) contours for the multi-peak-fitting-function parameters μ_i and (from left to right; top to bottom): σ_0, σ_2, m_τ, b_H, m_H and A_i The red point in each figure indicates the parameter values that result in the best fit to the simulated peak. See text for more information.

One possible enhancement that could be made to the current multi-peak fitting function is as follows. Currently, the multi-peak fitting function can only be used on a calibrated energy spectrum since some parameters depend on energy. Therefore to accurately calibrate an energy spectrum and classify the peak shape the following routine must be followed.

1. Fit several peaks in the uncalibrated spectrum with the single peak-fitting function.

2. For each fit peak, plot the calculated peak centroid as a function of the uncalibrated channel number and fit with a line.

3. Use the parameters from the linear fit to create a calibrated energy spectrum.

4. Fit several peaks in the calibrated energy spectrum with the multi-peak fitting function.

Rather than go through this entire procedure the multi-peak fitting function could be rewritten so that it could be used with an uncalibrated energy spectrum. By doing so the multi-peak fitting function could not only characterize the peak shape as a function of energy, but also create a calibrated energy spectrum – all in one iteration. To do this, every x variable in Eqs. 3.10–3.13 should be replaced with

$$x \rightarrow ax + b \tag{3.20}$$

where a and b are parameters mapping the uncalibrated channels to calibrated energy.

Future work could also be done to better understand any parameter correlations in the multi-peak fitting function. Figure 3.3 only displays the parameter correlations for the 300-keV peak. In future work the n-sigma contours could be made for several other peaks such as the 2614-keV peak. Furthermore, n-sigma contours could be investigated

for parameter values where the detector has a larger value of H_{tail}. The value of H_{tail} has an effect on the n-sigma contours for the single peak-fitting function and therefore may also have an effect on the contours for the multi-peak fitting function.

CHAPTER 4: GAMMA-PEAK CHARACTERIZATION FOR THE DETECTORS OF THE PROTOTYPE CRYOSTAT

4.1 Multi-Peak Fitting Routine

Understanding the energy response function for each detector is crucial to the success of the MAJORANA DEMONSTRATOR. While a detector's energy resolution must be known for $0\nu\beta\beta$ analysis, it is also crucial to understand a detector's resolution as a function of energy in order to appropriately compare MC simulations to data (Chapter 5). A detector's energy resolution can be well quantified if the detector's response function is known, and as discussed in Chapter 3, a detector's response function is best classified by simultaneously fitting several gamma peaks over a broad range of energy.

The multi-peak fitting function is used to classify the response function for each working detector of the PC. The multi-peak fitting routine performs best with higher statistics and therefore is used on binned data taken with a ^{228}Th line source. The routine is used on a total of five calibration sets in order to investigate how the peak fitting parameters change over time. The five calibration sets that are used in this analysis are referred to as calibration data sets: A, B, C, D and E. They are listed in chronological order and their relative timing with respect to one another can be found in Fig. 2.2. For each detector in each calibration data set, the multi-peak fitting routine is used to fit five gamma peaks, which are listed in Table 4.1. These five peaks are chosen because they have high relative intensities and are well separated (by at least 10σ) from other gamma peaks. For each peak, a fit range corresponding to $(M \pm 10\Sigma)$ is used for the multi-peak fitting routine.

Table 4.1: The five gamma peaks fit for each detector in each calibration data set [NND].

Expected Pk Centroid (keV)	Isotope	Relative Intensity
277.371 (5)	^{208}Tl	6.6% (3) †
300.087 (10)	^{212}Pb	3.30% (4)
583.187 (2)	^{208}Tl	85.0% (3) †
860.557 (4)	^{208}Tl	12.5% (10) †
2614.511 (10)	^{208}Tl	99.754% (4) †

† To compare ^{208}Tl intensities to ^{212}Pb intensity, multiply the ^{208}Tl intensities by 0.3594.

To fit multiple peaks over a range of energy, the parameters of the multiple peak-fitting function must be initialized. Because there are numerous parameters and the best fit is often at a very local minimum, it is crucial that the parameters be initialized with accuracy to aid the minimizing processor. Therefore the multi-peak fitting routine begins with two fitting algorithms to find the best values for parameter initialization. Upon successful completion of the first two algorithms, a good estimation for each parameter of the multi-peak fitting function is found and used for parameter initialization in the third – and final – algorithm. The final algorithm ends with a "final fit" where no parameters are fixed and the minimization function and minimizer processor are optimized.

4.1.1 Fitting Algorithm I

The first algorithm finds approximate values for: μ_i, A_i, σ_0, σ_1 and σ_2. The parameters μ_i and A_i are the Gaussian centroid and signal area of the i^{th} peak, respectively. The parameters σ_0, σ_1 and σ_2 are three of the common parameters described in Section 3.4. The algorithm consists of the following.

1. Find y_{max}, the maximum bin content of the i^{th} peak. Use the energy corresponding to the center of the bin as an approximation for μ_i.

2. Calculate the FWHM of each peak. Use the FWHM to find an approximate σ_i and A_i.

   - The variance of the Gaussian of the i^{th} peak, σ_i, is approximated as:

$$\sigma_i = \frac{\text{FWHM}_i}{2.355}, \tag{4.1}$$

     where FWHM_i is the FWHM of the i^{th} peak.

   - The area of the i^{th} peak, A_i, is approximated as:

$$A_i = y_{max}\sqrt{2\pi}\,\sigma_i, \tag{4.2}$$

     where y_{max} is the maximum bin content of the i^{th} peak.

3. Fit σ as a function of μ to find an approximate σ_0, σ_1 and σ_2, where the fit function is:

$$\sigma = \sqrt{\sigma_0^2 + \sigma_1^2\mu + \sigma_2^2\mu^2} \tag{4.3}$$

4.1.2 Fitting Algorithm II

The second algorithm finds the best initialization values for the parameters related to the tail in the multi-peak fitting function: b_τ, m_τ, b_H and m_H. In the second algorithm, the multi-peak fitting function is used (Eqs. 3.9– 3.13, 3.16 – 3.18) but with the parameters b_H and m_H fixed in value. Based on experience, m_H is typically on the order of 10^{-6} and is therefore fixed to be $1. \cdot 10^{-6}$ in the fitting algorithm.

The parameter b_H can vary greatly from detector to detector. The parameter b_H should never be less than zero as that would imply a negative tail component of the signal, and it should never be greater than one as that would imply a negative gaussian component of the signal. Since the realistic range of the parameter is limited, it is possible to explore the entire spectrum of possible b_H values. To do this the parameter

is fixed at five different values: 0.0, 0.2, 0.4, 0.6 and 0.8. A new fit is performed for each different value of b_H, where the parameters b_H and m_H are fixed and all other parameters are allowed to vary. If a reasonable fit is obtained, the parameters resulting in that best fit are used as the initialization values for the parameters in the third and final algorithm.

It should be noted that for some detectors a reasonable fit can be found for more than one fixed b_H value. In these cases the final algorithm is performed multiple times for one detector, and as a result several "final fits" are attempted. However the parameter values that result from each attempted final fit are in agreement with one another and therefore only one unique best fit is found for each detector in a given data set.

4.1.3 Fitting Algorithm III

After the first two algorithms are performed and good parameter initialization values are found, the final algorithm is performed. As discussed in Section 3.2, the final fit minimizes the log-likelihood function using the MINOS processor. It is often difficult to obtain convergence with the log-likelihood function and the MINOS processor, and hence the final algorithm is implemented. The final algorithm, which is further explained in Section 3.2 is:

1. Chi-Squared minimization function; MIGRAD processor
2. Log-Likelihood minimization function; MIGRAD processor
3. Log-Likelihood minimization function; MINOS processor

The last step of the algorithm is the final fit. During this fit, no parameters of the fit function are fixed in value or limited in range. The one exception to this is when a detector's best fit results in the parameter b_H being consistent with zero (i.e. there is no low-energy tail portion of the signal). In this case the final fit is performed with b_τ, m_τ, b_H and m_H fixed to be zero.

4.2 Results

Each detector is fit for each calibration data set. All fitting is performed on binned data with a 0.1-keV bin width. The parameter values resulting in the best fit for each detector during each data set can be found in Appendix B. As an example, the best fit for S3D2 during calibration data set A can be seen in Fig. 4.1. Fig. 4.1 shows the fit for each of the five gamma peaks (left) as well as the residual (right).

To investigate how the common parameters of the multi-peak fitting function might change with time, each detector's common parameters are plotted as a function of the calibration data set. This information can be found in Appendix B. For certain analysis it is desirable to have a single value for each of the parameters in the fit function. This is particularly true of the common parameters in the multi-peak fitting function (i.e. σ_0, σ_1, σ_2, b_τ, m_τ, b_H and m_H). For each common parameter, a single parameter value is obtained by fitting the five parameter values with a constant. The best fit to each detector's common parameters can be found in Table 4.2, as well as in Appendix B. As an example, the fit to S3D2's parameter σ_0 is shown in Fig. 4.2. The values of σ_0 for S3D2 in calibration data sets A, B, C, D and E are shown. The σ_0 parameters are fit with a constant, with the best fit giving a value of σ_0 to be 0.38 ± 0.02 keV. This is the value of σ_0 that is used in analysis for S3D2, such as in Chapter 5.

Note that in Fig. 4.2 the fit to σ_0 only includes calibration data sets A, B, C and D. Calibration data set E is problematic for many of the detectors and is therefore not used when fitting any of the detector's common parameters. In part, this may be due to low statistics; the runtime for data set E is less than a quarter of the other data sets' runtimes. The issues seen with calibration data set E are as follows.

- One of the detectors (S3D1) shows a shift in its gain during calibration data set E.

- One of the detectors (S3D5) has its pulser enabled during calibration data set

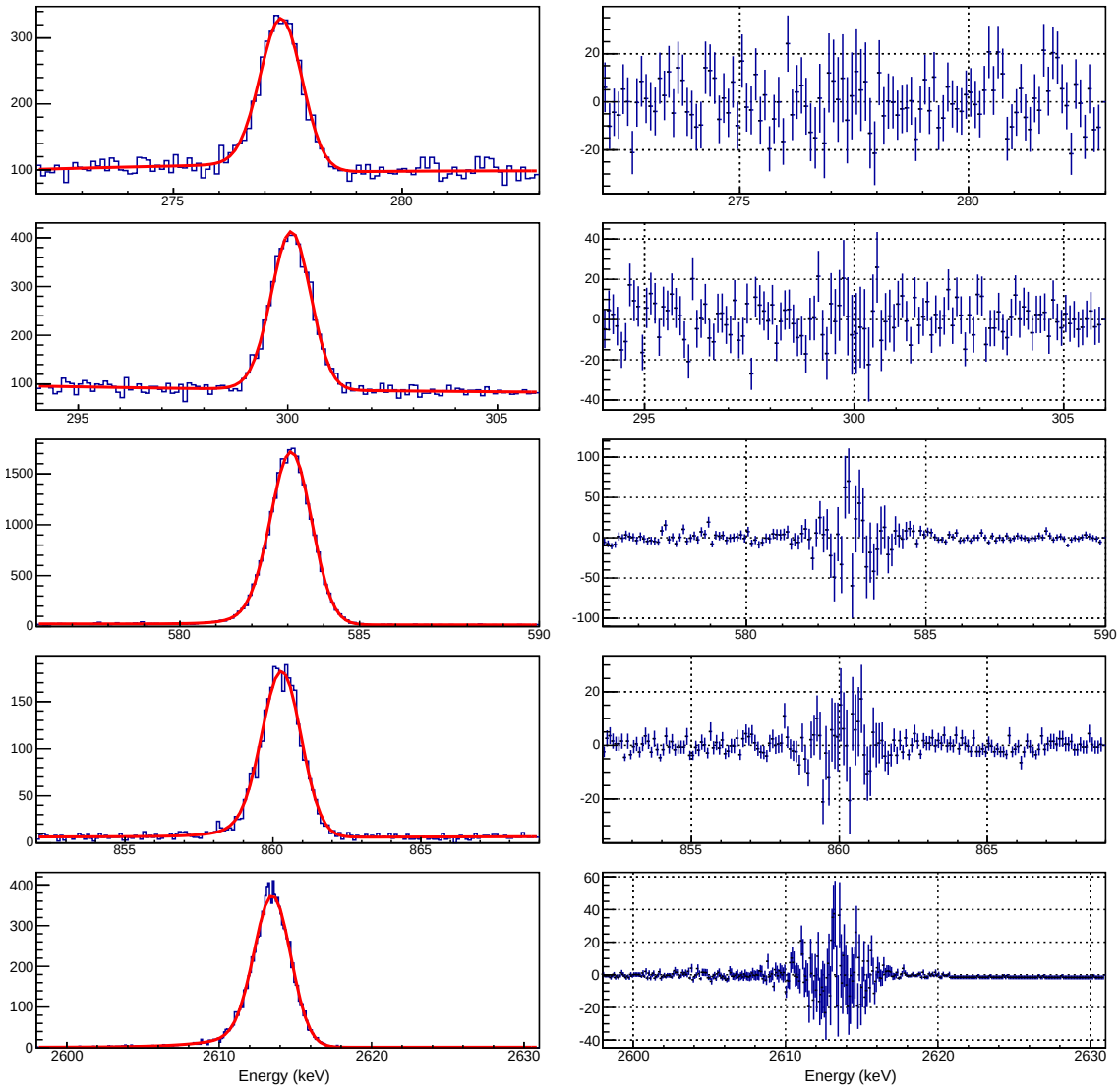

Figure 4.1: The five gamma peaks of S3D2 in calibration data set A that are fit with the multi-peak fitting routine. Shown on the left is each of the five peaks with the best fit of the multi-peak fitting function shown in red. Shown on the right is the residual of the fit for each peak.

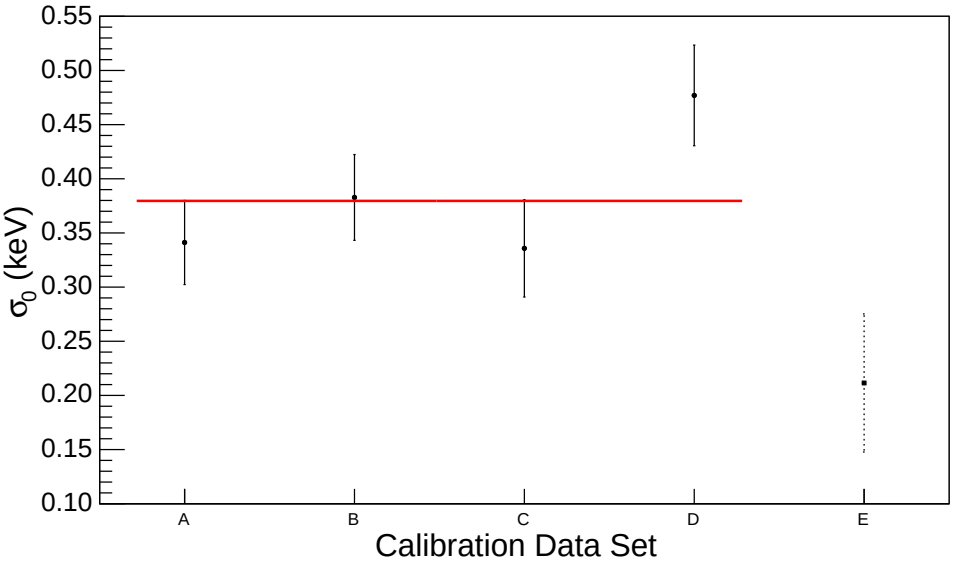

Figure 4.2: The parameter σ_0, for S3D2, for each of the five calibration data sets. Data with solid error bars are fit with a constant to find a single parameter value. Parameter σ_0 from Calibration Data Set E has dashed error bars indicating it is not included in the fit range. The best fit results in a value of $\sigma_0 = 0.38$ (2) keV.

Table 4.2: Each detector of the PC is fit for multiple calibration data sets. From each best fit, seven parameter values are obtained that can be used to characterize the detector's energy response function. While multiple data sets are fit to explore how a detector's response function might change in time, only a single set of parameter values are desired for certain analyses. This single parameter value is obtained by fitting the multiple parameter values with a constant. The values of the constants from the fits are used in future analyses and are listed below. As a reminder, S1D2 and S1D3 are ORTEC detectors and the rest are BEGe detectors.

	σ_0 [keV]	$\sigma_1/10^{-2}$ [keV$^{1/2}$]	$\sigma_2/10^{-4}$	$b_\tau/10^{-2}$ [keV]	$m_\tau/10^{-4}$	b_H	$m_H/10^{-5}$ [keV^{-1}]
S1D2	0.12 (5)	1.91 (2)	2.92 (9)	2 (7)	8.5 (1)	0.487 (9)	4 (3)
S1D3	0.01 (1)	2.12 (6)	4.9 (3)	0 (6)	24.3 (4)	0.71 (3)	3 (2)
S3D1	0.40 (3)	1.9 (1)	3.7 (2)	0†	0†	0†	0†
S3D2	0.38 (2)	1.94 (10)	2.4 (3)	3 (1)·10^1	6.4 (8)	0.12 (3)	3 (2)
S3D4	0.39 (2)	2.01 (8)	3.8 (2)	0†	0†	0†	0†
S3D5	0.43 (4)	2.3 (1)	3.2 (3)	0†	0†	0†	0†

† The best fit results in the parameter b_H being consistent with zero. Therefore the final fit is performed with b_τ, m_τ, b_H and m_H fixed to be zero.

E. The pulser events interfere with one of the five gamma peaks used in the multi-peak fitting routine: the 277-keV peak.

- For S1D3, the best fit yields unphysical parameter values. Therefore the fit is rejected and no best fit is reported.

- For three of the detectors (S1D2, S3D2, S3D4) a best fit can be found, however the parameter values from the fit are puzzling and inconsistent with the parameter values found from the other data sets.

Therefore, while a best fit can be found for three of the detectors, the parameters from the fit to data set E are not used in any further analysis. Hence, while σ_0 is shown for data set E in Fig. 4.2, it is not used in the fit.

It is also interesting to note that S1D4 is operable but not listed in Table 4.2. This detector has an odd peak shape, which becomes especially apparent in high-rate calibration energy spectra. Consequently, a best fit cannot be found and the detector's response function cannot be characterized. (See Section 4.3.1 for more details.) There are some other cases where a detector cannot be fit for a particular calibration data set, or its fit is performed on a limited number of gamma peaks. Table 4.3 shows, for each data set, in which detectors a best fit can be found (indicated by a green checkmark). A red X indicates that a best fit cannot be found and is further discussed in Section 4.3. A yellow checkmark indicates that a best fit can be found, but with only four of the five gamma peaks in Table 4.1. A yellow checkmark is indicated twice; for S3D5, calibration data sets B and E. During both of these calibration runs the pulser for S3D5 is enabled. The pulser events for S3D5 interfere with the 277-keV peak, which is one of the five peaks used in the multi-peak fitting function. Therefore, the 277-keV peak is not used in the analysis for S3D5.

Table 4.3: The status of the multi-peak fitting routine for each detector during each calibration data set. A green checkmark indicates a best fit can be found. A yellow checkmark indicates a best fit can be found, but with only four of the five gamma peaks typically used in the peak-fitting routine. A red X indicates a best fit cannot be found. Calibration data set A, S3D5 is listed as "n/a" because after all data quality cuts, the detector has a zero effective runtime.

	Calibration Data Set				
	A	B	C	D	E
S1D2	✓	✓	✓	✓	✓
S1D3	✓	✓	✓	✓	✗
S1D4	✗	✗	✗	✗	✗
S3D1	✓	✓	✓	✓	✗
S3D2	✓	✓	✓	✓	✓
S3D4	✓	✓	✓	✓	✓
S3D5	n/a	✓	✓	✓	✓

4.3 Peak Shape Issues

To rid each calibration set of problematic data that might affect a detector's peak shape, each calibration set goes through a series of data selection criteria before the multi-peak fitting routine is performed, as discussed in Section 2.2. Despite these selection criteria, some problems still persist. As a result the multi-peak fitting routine cannot be used with some detectors during certain calibration data sets, as seen in Table 4.3. The data sets where a best fit cannot be found are:

- **Calibration Data Set E for S1D3** During data set E, S1D3 has a considerably shorter runtime than its other calibration data sets. Therefore low statistics can most likely explain why a best fit cannot be found.

- **All Calibration Data Sets for S1D4**. Due to double peaking in S1D4, the detector cannot be fit for any calibration run. See Section 4.3.1 for more details.

- **Calibration Data Set E for S3D1** No changes in gain are detected for S3D1 during data set E using the data selection tools described in Section 2.2. However after undergoing all data quality cuts, visual inspection of S3D1's energy spectrum shows a clear change in the detector's gain during calibration set E. Therefore the multi-peak fitting routine cannot be used to fit S3D1 during data set E.

4.3.1 Double Peaking in S1D4 of the PC

One issue is with S1D4 of the PC (i.e. Ponama I) and is seen in all five calibration data sets used in this analysis. For this detector, where one gamma peak is expected in the energy spectrum, two appear. This second peak appears on the higher-energy side of the main gamma peak and is offset from the main peak by roughly one or two sigma. This behavior is referred to as double peaking. As seen in Fig. 4.3, the double peaking becomes more pronounced at higher energies. Each of the peaks are populated uniformly over time, as seen in Fig. 4.4, and therefore no time cut can be used to exclude the double peaking feature. As a result the peak shape cannot be characterized and therefore this detector is not used in the analysis presented here.

4.4 Future Work

For each detector, the multi-peak fitting routine is used on each of the five calibration sets. Therefore five unique values are found for each parameter of the multi-peak fitting function. However it is desirable to have a *single* value for these parameters (rather than five different values) since they are used in further analysis. As discussed in Section 4.2, a single value is obtained by fitting the five parameter values with a constant and using the constant from the best fit in future analysis. Some multi-peak fitting results yield unphysical parameter values, and when this occurs the unphysical parameter values are not used in the constant fit. This can be seen in Fig. 4.5 which shows the b_τ parameter values for S1D3. Only one calibration set yields a physical b_τ parameter: calibration set A. Therefore the b_τ value used in future analysis is that from the fit to calibration

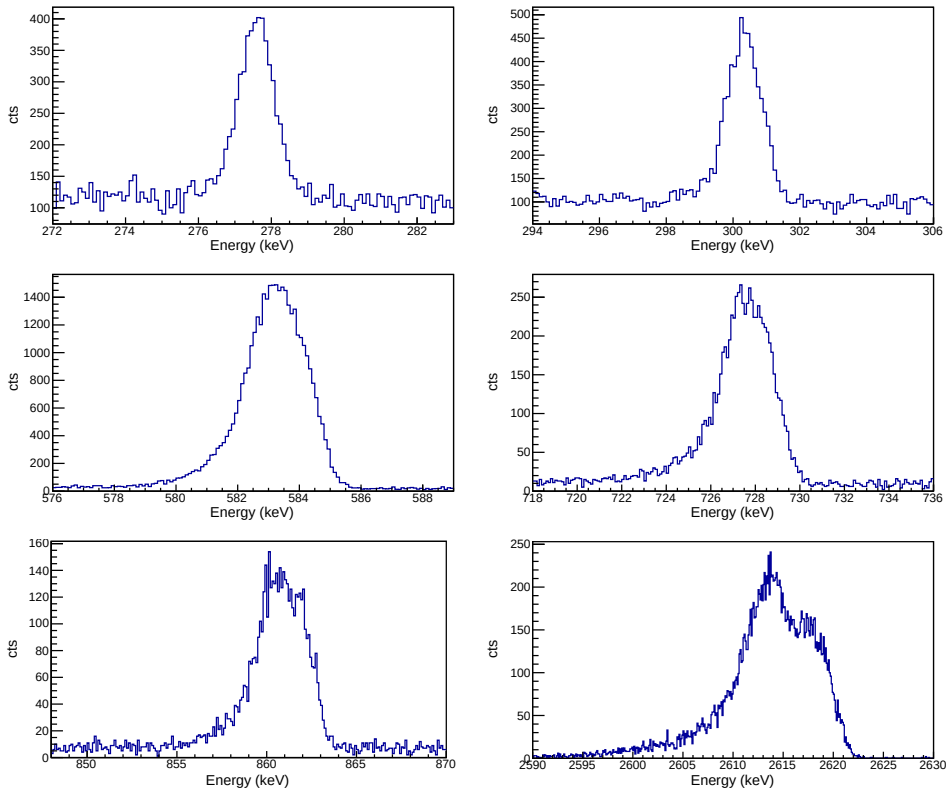

Figure 4.3: Several of S1D4's gamma peaks over a broad range of energy during one calibration data set. As energy increases, another peak appears to emerge on the higher-energy side of the main gamma peak. This behavior is referred to as double peaking.

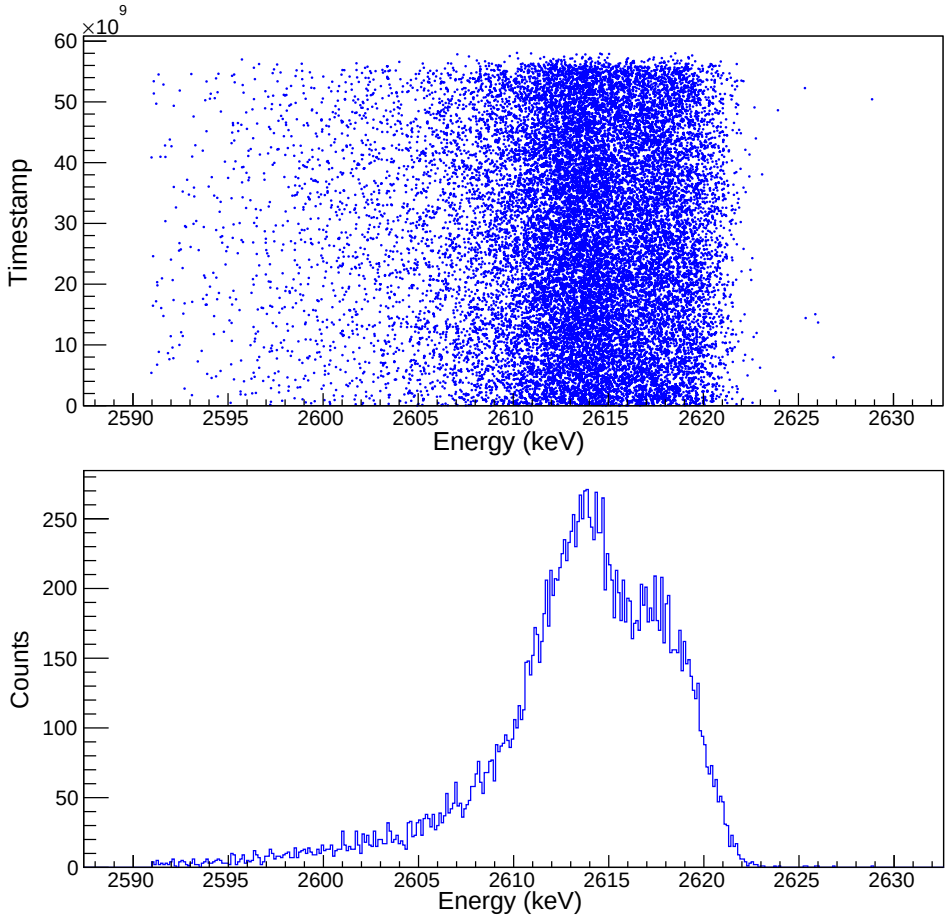

Figure 4.4: The top figure is each event's timestamp in S1D4's 2614-keV double peak. As a reminder, an event recorded t seconds after the start of a run has a timestamp of $t \cdot 10^8$. The bottom figure is a projection of the top figure's events onto its x-axis. There is no clear correlation between the timestamp and the population of any of the two double peaks.

Figure 4.5: Parameter b_τ for S1D3 over time. Data with dashed error bars are unphysical parameter values, and data with solid error bars are fit with a constant over time. Since only one calibration set yields a best fit with a physical b_τ parameter, it is the value used in future analysis: $b_\tau = 0\ (6)\cdot 10^{-2}$ keV.

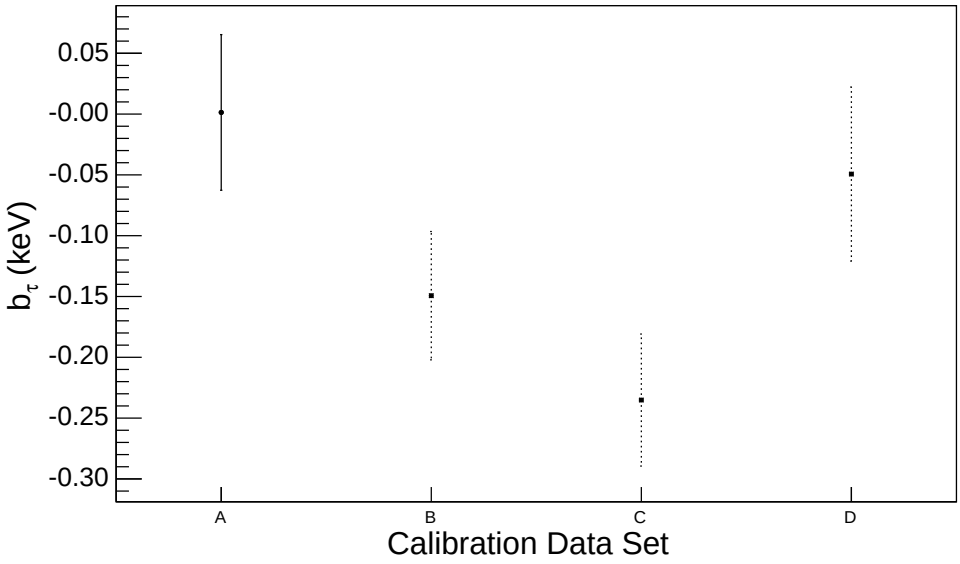

set A: $0\ (6)\cdot 10^{-2}$ keV.

The problem lies with how m_τ was handled. Given that the calibration sets B, C and D yield unphysical b_τ results, those calibration sets should be excluded from the constant fit to m_τ as well. However as seen occasionally throughout Appendix B, and in Fig. 4.6, in this work the fit to m_τ was (incorrectly) considered independently from b_τ and included all four calibration data sets. In future work, only calibration set A should be considered for fitting m_τ. One might even argue that only calibration set A should be considered for all of the parameters. This is something that should be considered in future work.

Figure 4.6: Parameter m_τ for S1D3 over time. Data with solid error bars are fit with a constant over time, resulting in an average value of $m_\tau = 2.43\ (4)\cdot 10^{-3}$. Since the parameter values for b_τ yield unphysical results for calibration sets B, C and D, the m_τ parameters from those calibration sets should have been excluded from the constant fit.

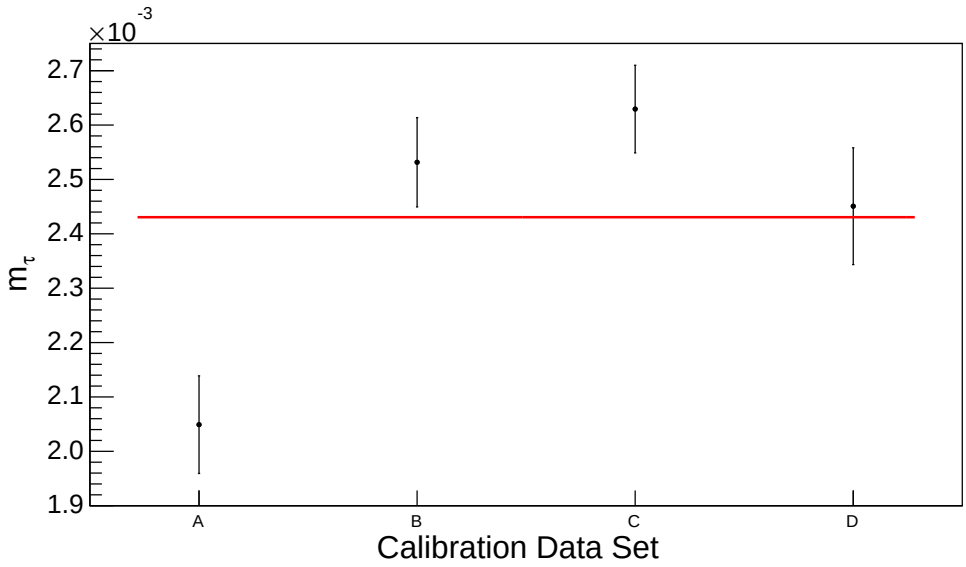

CHAPTER 5: PROTOTYPE CRYOSTAT BACKGROUND MODEL

5.1 Introduction

Understanding the backgrounds of the MAJORANA DEMONSTRATOR is of the upmost importance and for this reason, much effort has been put into creating an accurate background model. All of the materials used in the DEMONSTRATOR are assayed and extensive MC simulations are performed to predict the backgrounds that the materials are expected to contribute to the energy spectrum of each detector.

While achieving the lowest possible background is the goal of the DEMONSTRATOR, this is not necessarily true of the PC, whose main purpose is to improve on cryostat assembly procedures, the DAQ system, analysis routines, and the like. Nevertheless, understanding the backgrounds of the PC can help to verify the background model of the DEMONSTRATOR. Therefore, a background model of the PC is developed using many of the same techniques that are used to develop the background model of the DEMONSTRATOR.

The background model of the PC takes into account the naturally-occurring radioactivity of the materials used for the components inside of the passive shielding. It also takes into account the cosmogenically-activated backgrounds from the OFHC Cu and SS components and backgrounds from ^{222}Rn in the nitrogen-purged volume inside of the shield. From the background model, a MC-generated energy spectrum for each detector of the PC is made and then compared to data. What follows in this chapter are details on how the background model of the PC is generated. A discussion on the comparison between the MC-generated energy spectra and the data can be found in Chapter 6.

5.2 MaGe: The Majorana and Gerda Simulation Toolkit

All simulations are done with MaGe, a Geant4-based package developed and maintained jointly by the Majorana and Gerda collaborations [Bos11, All06, All03]. To understand the dynamics between MaGe and Geant4 consider the following example: suppose a MaGe user wants to model a detector's response to a nearby ^{60}Co source. The user must first add the detector geometry into the MaGe framework; at the bare minimum the detector geometry must include the detector itself and, depending on the goal of the simulation, the user might also want to include certain geometries describing the detector's environment (e.g. the detector's cryostat, the detector's front end electronics, etc.). After the geometry is added to the framework, MaGe is compiled and then run as an executable. During runtime the user tells MaGe several key pieces of information, including but not limited to: what is to be simulated (the radioactive decay of ^{60}Co), where to place the initial ^{60}Co nuclide, and how many decays to simulate. From here Geant4 takes over in implementing the physical processes that take place. A non-exhaustive list of what Geant4 determines is:

- The time at which the nuclide decays, assuming the nuclide is created at $t = 0$.
- The process by which the nuclide decays.
- All particle interactions, the time of the interaction and the exact location of the interaction.

Given the abundance of information from Geant4, MaGe determines which information to store in the user-designated output file. In the current MaGe framework, as soon as a particle interacts with a sensitive volume (i.e. a detector) several pieces of information are stored in the output file, including the:

- Physical process that had created the particle (e.g. radioactive decay, Compton scattering, etc.)

- Type of particle (e.g. gamma, electron, alpha, etc.)
- Energy of the particle
- Amount of energy that the particle deposits in the detector as a result of the interaction that is taking place
- Time of the interaction, assuming the original nuclide (which in this example is ^{60}Co) is created at $t = 0$
- Location of the interaction, including the (x, y, z) coordinates and the MaGe-given name of the sensitive volume

5.3 Modeling the Prototype Cryostat Geometry

To create an accurate background model of the PC, the geometry of the detectors and the surrounding components must be accurately modeled in MaGe. The PC and Demonstrator contain many of the same parts, and therefore the framework of the PC geometry is designed so that it closely resembles the framework of the Demonstrator, and thus both can share common parts and assemblies. The framework of the PC and Demonstrator geometries are organized so that they contain several assemblies and, in turn, these assemblies contain several parts, with each assembly and part being its own C++ class. Organizing the geometry in this fashion facilitates the sharing of parts between the two geometries while also optimizing the placement of repeated parts throughout the geometry (e.g. a screw). The main components of the PC geometry are as follows.

- Surrounding rock cavern in the Majorana experimental hall
- Concrete walls and floor in the Majorana experimental hall
- Veto Panels

- Passive Shielding
- Cryostat and Clamping Hardware
- Thermosyphon
- Thermal Shield
- ColdPlate
- String Arrays
- Detector Mounts
- Temperature Sensor Assemblies
- Germanium Crystals

Appendix C further breaks down each component and lists the material and mass of each part. Table C.1 details the first eight components; namely those that make up the Prototype module's cryostat and surrounding environment. Table C.2 details the components that make up the string arrays of the PC, Table C.3 details the components that make up the detector mounts and Table C.4 details the components that make up the temperature sensor assemblies. There are two important points to note regarding Tables C.1–C.4; for one, the parts that are made of OFHC Cu are entered as UGEFCu in the MaGe geometry. This is because the isotopic composition and density of the two are the same in the MaGe materials database, so for simulation purposes they are essentially the same. Secondly, some string components vary string-to-string and some detector components vary detector-to-detector. For example in Table C.2 the "String Tie Rods" have a different total mass for String 1, 2 and 3. The string tie rods are thin, hexagonal rods that thread through the assembled detector mounts to make a rigid string array. With each string containing a different number of detectors,

and with detectors having different heights, the effective height of each string is very different. It is undesirable to have an excess length of string tie rod, and therefore each string has its own custom-length set of string tie rods. This is reflected in the PC MaGe geometry, and hence the total mass of each string's tie rods are unique.

The string tie rod is just one example of a part that is affected by the different detector sizes and the different string configurations in the PC and Demonstrator. Rather than manually create the geometry for each of the unique detector mounts and string arrays, the detector and string geometries are calculated and created automatically by MaGe during runtime through the use of JavaScript Object Notation (JSON) files. For each experiment (e.g. the PC and Demonstrator) a JSON file is created. The JSON file contains the following pieces of information.

- The number of cryostats in the experiment and their relative positions
- The number of strings in each cryostat and their relative positions
- The number of detectors in each string and their relative positions
- The dimensions and form factor of each detector

During runtime, the information is read by MaGe and the appropriate detectors and strings are created and placed. Table C.5 lists the detector masses as calculated by MaGe, compared with the actual detector masses. The MaGe masses are calculated based on the crystal dimensions input and the density of natural germanium (taken to be 5.551 g/cm^3). Differences between the two masses are most likely due to inaccuracies in the measurements of the crystals' dimensions.

Below are figures of the PC geometry as modeled in MaGe. Figure 5.1 shows the three strings of the PC, the coldplate and a portion of the thermosyphon tube; Fig. 5.2 shows the thermal shield and Fig. 5.3 shows the cryostat lids and clamping hardware.

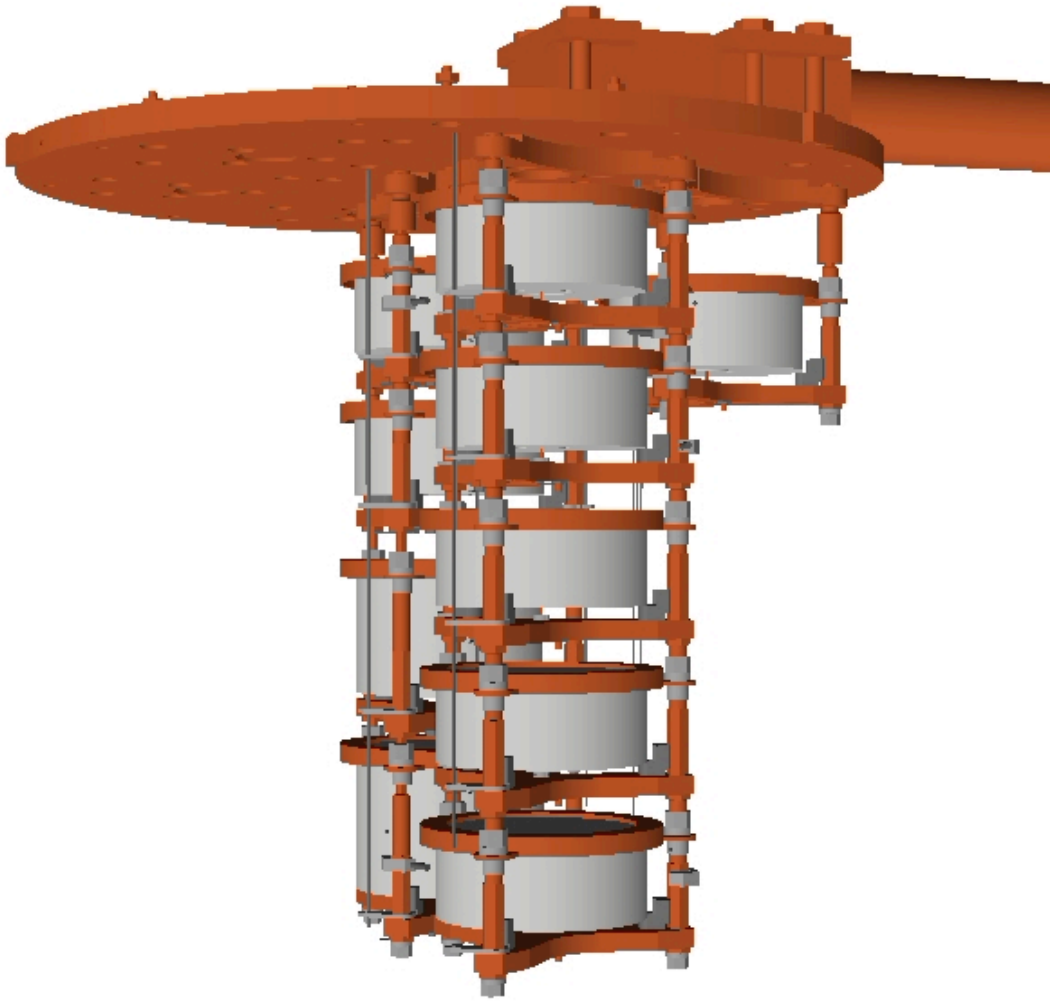

Figure 5.1: The PC string arrays as modeled in MaGe. The coldplate and a portion of the thermosyphon tube are also shown.

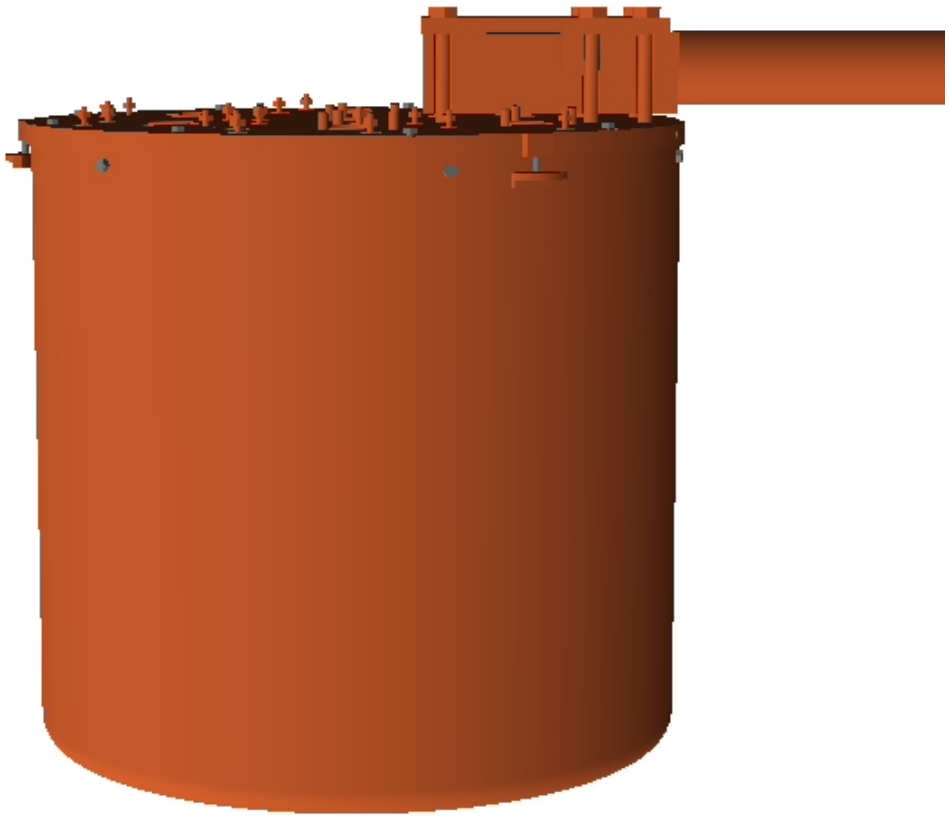

Figure 5.2: The PC thermal shield as modeled in MaGe. The coldplate and a portion of the thermosyphon tube are also shown. The hardware components shown in gray are made out of SS.

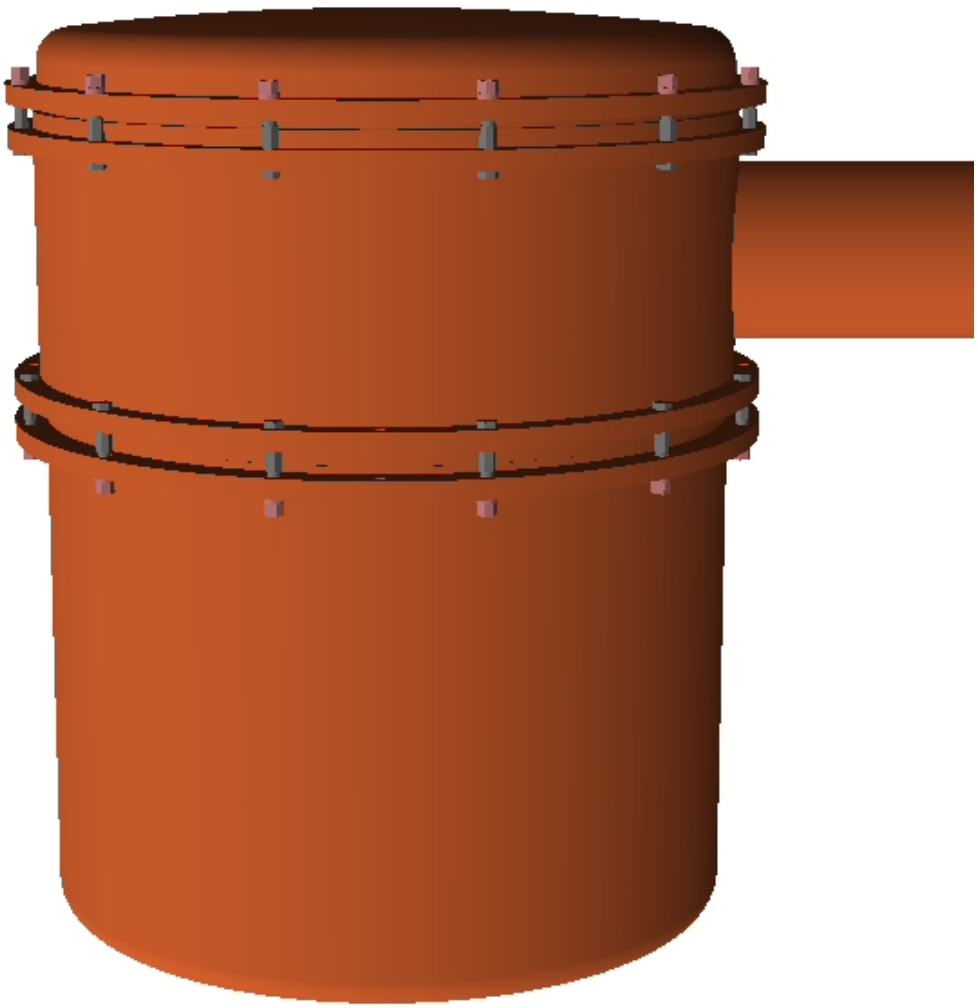

Figure 5.3: The PC cryostat lids and clamping hardware as modeled in MaGe. The cryostat hoop and a portion of the crossarm are also shown. The hardware components shown in gray are made out of SS and the hardware components shown in redish-gray are made out of silicon bronze.

5.3.1 Inaccuracies in the PC Geometry

There are known inaccuracies with the PC geometry in MaGe; they are listed below. Most of the inaccuracies are a result of missing components and in some of these cases the contribution that these missing components are expected to make to the PC background can be estimated from similar components in the PC and Demonstrator background model. The inaccuracies with the PC background model are listed below by order of importance.

1. **Gasket** The Viton gasket is not in the PC geometry and therefore is not included in the PC background model. The PC cryostat is vacuum-sealed with two Viton gaskets rather than with the cleaner parylene film that is being used in the Demonstrator; therefore their contribution to the PC background is higher than what is expected for the Demonstrator.

   The gaskets are expected to contribute 56 cts/ROI/ton/yr (as detailed in Section A.3.1). Of all the inaccuracies listed, the gaskets are expected to contribute the most to the PC backgrounds.

2. **Passive Shielding and Cavern** The passive shielding and cavern are not included in the PC background model; this includes the outer copper shield, lead shield, radon purge box, liquid nitrogen, muon veto panels, concrete walls, floors and cavern. Furthermore there is SS hardware in the outer copper shield that is not included in the PC background model.

   The outer copper shield is expected to contribute 6.88 cts/ROI/ton/yr (as detailed in Section A.3.2).

   The contribution from the lead shielding is assumed to be the same as for the Demonstrator background: 0.627 cts/ROI/ton/yr. This rate is found from the Demonstrator background model, where both the inner and outer Cu shields

are installed. However since the inner Cu shield is not installed in the PC the rate at which the lead shield contributes to the PC background will be slightly higher.

3. **Cables** The signal and HV cables are not included in the PC background model. The PC cable geometry in MaGe is outdated; so much so that certain portions of cable conflict with other components in the PC geometry. Therefore several portions of the cable geometry have been removed from the PC geometry, and no simulations have been done with what is remaining. The signal cables in the PC are known to be higher in radioactivity than the cables in the Demonstrator and therefore their contribution to the PC background is higher than what is expected for the Demonstrator.

   The cables are expected to contribute 1.4 cts/ROI/ton/yr (as detailed in Section A.3.3).

4. **Components On Top of the Coldplate** The signal connectors sitting on top of the coldplate are not included in the PC background model. Additionally, there are two temperature sensor assemblies above the coldplate that are not included in the PC background model.

   The contributions from the connectors are assumed to be the same as for the Demonstrator background: 0.299 cts/ROI/ton/yr. However this count rate is found using outdated connectors; several modifications have been made to the components that sit on top of the coldplate and work is ongoing to include these updates into the Demonstrator background model. One main difference is that the collective mass of the (current) components is higher than that used in the Demonstrator background model. Furthermore, for the PC, two temperature sensors are above the coldplate; the temperature sensors are known to be high

in radioactivity (see Chapter 6) and therefore the expected contribution of 0.299 cts/ROI/ton/yr is most likely an underestimate.

5. **Calibration System** The calibration system is not included in the PC background model. At the time of this work the geometry of the calibration system was still being implemented into the PC and DEMONSTRATOR geometries. Therefore it is not included in the PC geometry, even though it is present in the actual experimental setup. The contribution from the calibration system is assumed to be the same as for the DEMONSTRATOR background: $1.3{\cdot}10^{-3}$ cts/ROI/ton/yr.

6. **Coldplate** During the commissioning of the PC the geometry of the coldplate was changed. This is not reflected in the PC geometry in MAGE. As a result, the shielding of detectors from what sits about the coldplate is different in the MAGE geometry than from the actual module.

7. **Temperature Sensor Assemblies** The geometry and location of the temperature sensor assemblies is approximated based on pictures taken in the lab while the PC was being commissioned. Because the components are small and located very close to the detectors, a small change in the geometry or location could cause a drastic change in how the detectors are shielded from the assembly. Furthermore, the PC background model does not include the temperature sensors themselves nor the masses of Kapton tape that are located at roughly the same position as the sensors. It is assumed that any activity in the sensor itself (and/or the Kapton tape) can be distributed among the other components that clamp the sensor to the string (i.e. the solder, sensor clamp and screw).

8. **Cable Guides** The cable guides are not included in the PC background model. Given that the cable guides are attached to the hollow hex rods it is assumed that any activity in the cable guides can be distributed among the hollow hex

rods and other nearby string parts.

9. **Tie Rod Split Nuts for S1 and S3** The tie rod split nuts for strings 1 and 3 are not included in the PC background model. Their total mass is 13.56 g. It is assumed that any activity in the nuts can be distributed among the tie rods and other nearby string parts.

10. **Thermal Shield Supports and Wedges** The thermal shield support and wedges are not included in the PC background model. Their total mass is roughly 112.5 g. It is assumed that any activity in the supports and wedges can be distributed among the thermal shield.

11. **HV Rings** In the current geometry, there is only one geometry for the HV ring and it is used for all the detector units. This is not accurate; the HV rings for S1D3 and S1D4 are incorrect in the current PC geometry.

12. **Material Composition of Silicon Bronze** The cryostat clamping nuts are made of silicon bronze. In the PC geometry their composition is considered to be 97% copper and 3% silicon. However there are known impurities in similar materials; most notably, some sources of silicon bronze are reported as containing up to 0.5% lead [SiB].

13. **Unknown if OFHC Cu or UGEFCu** As detailed in Sections 5.4 and 6.3, components are grouped during simulations and when comparing the PC background model to data. Components are only grouped together if they are expected to have the same activity; therefore the components made of OFHC Cu are grouped separately from those made of UGEFCu. The material and history of all parts in the DEMONSTRATOR can be found in the MAJORANA Parts Tracking Database (PTDB) [Abg15]. The PTDB was still under development during the building

and installation of the PC and therefore the material of several copper parts in the PC is unknown. It is assumed that these parts are made of OFHC Cu. Therefore some parts may be incorrectly considered to be OFHC Cu when they are in fact made from UGEFCu. This does not affect the simulations; the isotopic composition and density of the two materials are the same in the MaGe materials database, so for simulation purposes they are essentially the same. However this does affect how the components are grouped and therefore how the simulations are compared to data (Chapter 6).

5.4 Component Grouping in the Prototype Cryostat Background Model

To develop the background model of the PC, a simulation is done for each part to determine to what effect possible radioactivity in that part would have on the detectors of the PC. Each part inside of the passive shielding is simulated for possible ^{238}U and ^{232}Th activity. Additionally, parts made out of OFHC Cu and SS are simulated for possible ^{60}Co activity and the masses of solder in the temperature sensor assemblies are simulated for possible ^{210}Pb activity. The inner cavity volume of the PC is filled with nitrogen gas in the MaGe geometry and is only simulated for possible ^{222}Rn activity.

When simulating a single part for a single nuclide, the location of the primary vertex of the radioactive nuclide is randomly placed within the volume of the part and the nuclide is allowed to decay. Regardless of whether a particle from the decay deposits energy in a detector, this constitutes a single event. For a typical part in the PC, thousands to hundreds-of-thousands of events must be simulated for each part and for each nuclide to gather enough statistics for the detector's resulting energy spectrum. However rather than simulate each individual part of the PC, parts that are made of the same material, and are thus expected to have the same levels of radioactivity, are grouped together and simulated as one. For example, there are 24 cryostat clamping bolts in the PC geometry. In the PC these bolts are all made of SS and therefore

should have roughly the same ^{238}U, ^{232}Th and ^{60}Co activities. Furthermore each bolt is roughly the same radial distance from each detector and therefore all of the bolts should have a similar effect on the detector's energy spectrum and count rate. So rather than simulate each individual bolt on its own, the 24 bolts are grouped together and simulated as a whole. The feature to simulate a group of components was added to the MaGe framework as part of the work to create the PC background model. Therefore, the details on how the radioactive nuclides are distributed throughout the group of components is further explained in this work and can be found in Chapter A.4.

The groups used for the PC background model simulations can be found in Table 5.1. Table 5.1 also lists which radioactive nuclides are simulated for each group: "U" indicating ^{238}U, "Th" indicating ^{232}Th, "Co" indicating ^{60}Co, "Rn" indicating ^{222}Rn and "Pb" indicating ^{210}Pb. The masses reported in Table 5.1 are the total mass of the entire group as calculated by MaGe. As seen in Table 5.1, the copper parts for a string are split into two groups: one for the UGEFCu components of the string and one for the OFHC Cu components of the string. (Detailed lists of which parts in the strings are made of UGEFCu and OFHC Cu can be found in Tables C.6– C.11.) The same is generally true for the copper cryostat components, however the Cryostat Top Lid and Cryostat Bottom Lid are dealt with separately from the other copper components. This is due to the fact that the lids were fabricated via metal spinning and there is no known assay on the process; hence they are put into their own groups.

Table 5.1: The groups used for the PC background model simulations. The "Material" column refers to the actual material of the part(s) in the PC. The "Part(s)" column lists the parts in each group; the part names are the same as those found in Tables C.1–C.4. The "Total Mass" column is the total mass of the entire group. (For the masses of the individual parts see Tables C.1–C.4.)

Group	Nuclides Simulated	Material	Part(s)	Total Mass [kg]
1	Rn	Nitrogen Gas	Inner Cavity Volume	0.292
2	U/Th/Co	OFHC Cu	Thermosyphon Mount Plate Thermosyphon Tube Thermosyphon Hoop Adapter Thermosyphon Cold Plate Adapter Thermosyphon Bolts (×6)	5.05
3	U/Th/Co	OFHC Cu	Cryostat Hoop Cross Arm Tube Cryostat Clamping Rails (×16) Thermal Shield Annulus ColdPlate	32.1
4	U/Th/Co	OFHC Cu	Cryostat Top Lid†	7.01
5	U/Th/Co	OFHC Cu	Cryostat Bottom Lid†	21.2
6	U/Th/Co	OFHC Cu	String 1	0.516
7	U/Th/Co	OFHC Cu	String 2	0.299
8	U/Th/Co	OFHC Cu	String 3	0.753
9	U/Th	UGEFCu	Thermal Shield Can	3.23
10	U/Th	UGEFCu	String 1	0.285
11	U/Th	UGEFCu	String 2	0.033

12	U/Th	UGEFCu	String 3	0.172
13	U/Th/Co	SS	Cryostat Clamping Bolts (×24)	0.259
14	U/Th/Co	SS	Thermal Shield Screws (×14)	$2.21 \cdot 10^{-2}$
15	U/Th/Co	SS	Temperature Sensor Screw for S1D1	$2.99 \cdot 10^{-4}$
16	U/Th/Co	SS	Temperature Sensor Screw for S1D4	$2.99 \cdot 10^{-4}$
17	U/Th/Co	SS	Temperature Sensor Screw for S2D1	$2.99 \cdot 10^{-4}$
18	U/Th/Co	SS	Temperature Sensor Screw for S3D1	$2.99 \cdot 10^{-4}$
19	U/Th/Co	SS	Temperature Sensor Screw for S3D5	$2.99 \cdot 10^{-4}$
20	U/Th	Si-Bronze	Cryostat Clamping Nuts (×24)	$6.77 \cdot 10^{-2}$
21	U/Th	NXT-85	String 1 HV Nuts (×12)	$8.60 \cdot 10^{-3}$
22	U/Th	NXT-85	String 2 HV Nuts (×3)	$2.16 \cdot 10^{-3}$
23	U/Th	NXT-85	String 3 HV Nuts (×15)	$10.8 \cdot 10^{-3}$
24	U/Th	NXT-85	String 1 Crystal Insulators (×12)	$14.9 \cdot 10^{-3}$
25	U/Th	NXT-85	String 2 Crystal Insulators (×3)	$2.74 \cdot 10^{-3}$
26	U/Th	NXT-85	String 3 Crystal Insulators (×15)	$13.7 \cdot 10^{-3}$
27	U/Th	NXT-85	String 1 Center Bushings (×4)	$5.92 \cdot 10^{-4}$
28	U/Th	NXT-85	String 2 Center Bushings (×1)	$1.48 \cdot 10^{-4}$
29	U/Th	NXT-85	String 3 Center Bushings (×5)	$7.38 \cdot 10^{-4}$
30	U/Th	PEEK	Temperature Sensor Clamp for S1D1	$5.13 \cdot 10^{-4}$
31	U/Th	PEEK	Temperature Sensor Clamp for S1D4	$5.13 \cdot 10^{-4}$
32	U/Th	PEEK	Temperature Sensor Clamp for S2D1	$5.13 \cdot 10^{-4}$
33	U/Th	PEEK	Temperature Sensor Clamp for S3D1	$5.13 \cdot 10^{-4}$
34	U/Th	PEEK	Temperature Sensor Clamp for S3D5	$5.13 \cdot 10^{-4}$
35	U/Th	Silica with	String 1 LMFE Substrate (×4)	$4.22 \cdot 10^{-4}$

		Gold Traces	String 1 LMFE Traces (×4)	
36	U/Th	Silica with Gold Traces	String 2 LMFE Substrate (×1) String 2 LMFE Traces (×1)	$1.06{\cdot}10^{-4}$
37	U/Th	Silica with Gold Traces	String 3 LMFE Substrate (×5) String 3 LMFE Traces (×5)	$5.28{\cdot}10^{-4}$
38	Rn/Th/Pb	Solder	Temperature Sensor Solder for S1D1	$0.201{\cdot}10^{-4}$
39	Rn/Th/Pb	Solder	Temperature Sensor Solder for S1D4	$0.201{\cdot}10^{-4}$
40	Rn/Th/Pb	Solder	Temperature Sensor Solder for S2D1	$0.201{\cdot}10^{-4}$
41	Rn/Th/Pb	Solder	Temperature Sensor Solder for S3D1	$0.201{\cdot}10^{-4}$
42	Rn/Th/Pb	Solder	Temperature Sensor Solder for S3D5	$0.201{\cdot}10^{-4}$

5.5 Energy Resolution for MC-Generated Energy Spectra

For each nuclide and group of components that is simulated, an output file is generated by MaGe. Each file is then further processed with GAT. There are several GAT modules that can be used to process MaGe-generated files. A few key modules that are used for the PC background model are described below.

- `GATMCStepsWindower` - The user tells this module the digitization time used in the actual DAQ system for the experimental setup. From this information, the module determines which interactions to cluster into a single event. The digitization time used for the PC background model is 200 μs.

- `GATMCDeadLayerProcessor` - The user tells this module the detector and dead layer geometries. The module nulls the energy deposited from an interaction if it occurs within the dead layer of the crystal. The dead layer geometries are not modeled in the PC background model. Work is being perfomed by Majorana collaborations to make the dead layer geometries more accessible for post-processing with GAT.

- `GATMCEventEnergyCalculator` - The user tells this module the parameters that describe the detector's peak shape as a function of energy. The module takes the energy of the event and replaces it with a randomly chosen resolution-corrected energy. More details on this module are below.

The `GATMCEventEnergyCalculator` module was further developed as part of the work to create the PC background model and is therefore further described. The gamma peaks in the MaGe output do not take into account the detectors' response functions and are simply delta functions. After the `GATMCStepsWindower` module determines which interactions to cluster into a single event, the `GATMCEventEnergyCalculator` module takes the energy of the event (E_0) and replaces it with a resolution-corrected

energy (E). To calculate the resolution-corrected energy, the parameters that describe the detector's peak shape as a function of energy are needed; the user inputs these parameter. The parameters needed are the common parameters of the multi-peak fitting function: σ_0, σ_1, σ_2, b_τ, m_τ, b_H and m_H (Section 3.4). The parameters used for the PC background model are those found from the multi-peak fitting routine (Chapter 4) and are listed in Table 4.2. Using these common parameters, the resolution-corrected energy is calculated in the following way.

1. The original energy, E_0, is set to be M, the peak centroid of the multi-peak fitting function (Eq. 3.14). This is true regardless of whether or not the event contributes to an actual peak in the energy spectrum.

2. The parameters μ, σ, τ, H_{tail} and Σ are calculated using Eqs. 3.14, 3.16, 3.17, 3.18 and 3.15 respectively.

3. Using these parameters a PDF is created describing the energy at which the event is expected to be observed. This PDF is simply the signal of the peak-fitting function in Chapter 3. (i.e. $\frac{\text{Eq. 3.10}}{A} + \frac{\text{Eq. 3.11}}{A}$)

4. A random number is generated according to the distribution of the PDF. The random number that is generated is considered to be the resolution-corrected energy, E.

5. The original energy, E_0, is replaced by the resolution-corrected energy, E, in the GAT output.

5.6 Inaccuracies in the PC Background Model

5.6.1 The Decay of Protactinium-234m in Geant4

The ^{238}U decay chain is shown in Fig. 5.4. In simulations of the ^{238}U nuclide it is expected that nearly 100% of the time the ^{238}U will alpha decay to ^{234}Th and then

beta decay to ^{234m}Pa. (The notation ^{234m}Pa refers to the metastable state of ^{234}Pa.) And indeed, this is what is observed in MaGe/Geant4 simulations of ^{238}U. There is a problem however, with how the ^{234m}Pa isomer decays; 99.84% of the time it should beta decay directly to ^{234}U, and a mere 0.16% of the time it should transition to the ^{234}Pa ground state and then beta decay to ^{234}U. What is produced by the simulations however is the opposite; nearly every time the ^{234m}Pa isomer transitions to ^{234}Pa and then beta decays to ^{234}U. As a result, several gamma peaks from the beta decay of ^{234}Pa to ^{234}U are observed in the MC-generated energy spectra that should not be present.

This problem arises because in the particular version of Geant4 used here, the code mishandles the decays of metastable states. For the work presented here, Geant4 version 4.09.06.p03 is used which is not the most current version of Geant4. Currently, Majorana and Gerda collaborators are working to make MaGe compatible with the newest version of Geant4, which is expected to resolve this issue. In the meantime, all PC and Demonstrator simulations must break up ^{238}U simulations into – at the very least – two different portions of the decay chain: (1) ^{238}U up to ^{222}Rn and then for (2) ^{222}Rn to ^{206}Pb (i.e. the end of the ^{238}U decay chain). In fact, because equilibrium of the ^{238}U decay chain can be broken at several points in the decay chain, simulations of ^{238}U should actually be broken up further. This is further discussed in Section 5.6.3.

Simulations for possible ^{238}U activity in the solder were performed after this issue was discovered. Therefore rather than simulating the entire ^{238}U decay chain, the solder was only simulated for possible ^{222}Rn activity (i.e. the later portion of the ^{238}U decay chain). This is why the nuclides for "Temperature Sensor Solder" in Table 5.1 are listed as ^{222}Rn and ^{232}Th, rather than as ^{238}U and ^{232}Th as were the other groups.

However for all the other components, the ^{238}U decay chain was simulated in its entirety, resulting in several unphysical gamma peaks in the simulated spectra. As an example, Fig. 5.5 shows a select energy region of the MC-generated spectrum for the

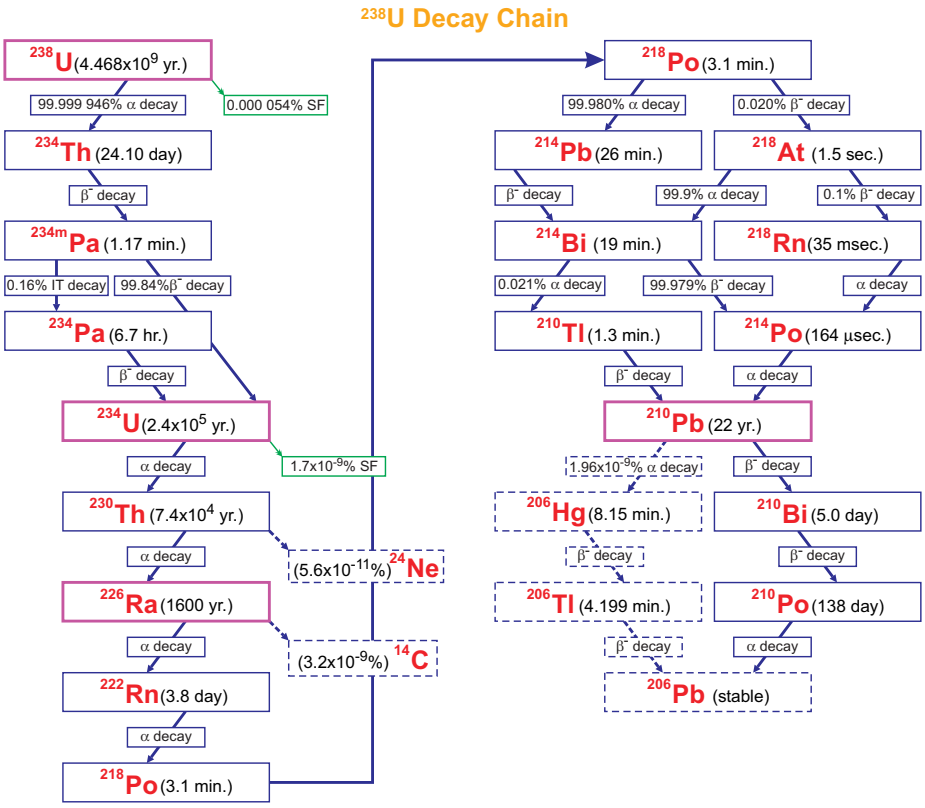

Figure 5.4: The ^{238}U decay chain. Figure taken from [INL].

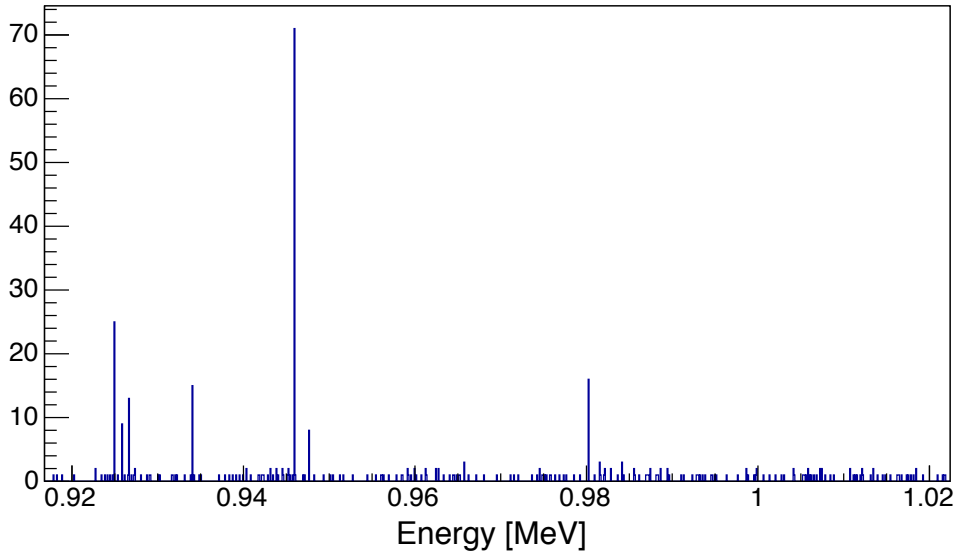

Figure 5.5: A select energy region of the MC-generated spectrum for the detectors' response to ^{238}U in String 3's crystal insulators. The spectrum shown is from the MaGe output and therefore the energy resolution of the detectors has not yet been taken into account.

detectors' response to ^{238}U in String 3's crystal insulators. The gamma peaks observed in Fig. 5.5 are identified in Table 5.2. Almost all of the peaks observed in this energy region are from the beta decay of ^{234}Pa to ^{234}U. It is not the observation of ^{234}Pa that is concerning, but rather the observation of ^{234}Pa *without* ^{234m}Pa that is concerning. This can be seen in Table 5.3, which lists all the gammas resulting from the decay of ^{234}Pa and ^{234m}Pa with an energy between 0.92 and 1.02 MeV. Also listed is the expected intensity of each gamma relative to the decay of ^{238}U (i.e. the branching ratio for ^{234m}Pa has been taken into account). The observed intensities of the gamma peaks associated with the decay of ^{234}Pa are much higher than expected. In fact, based on the fact that the 1001-keV peak from the decay of ^{234m}Pa is not statistically present, none of the ^{234}Pa peaks should even be present. It is of course undesirable to have unphysical peaks in the MC-generated energy spectra, and therefore – as described in the next section – a cut is performed on the simulated spectra in an attempt to remove the upper ^{238}U decay chain from the ^{238}U simulations.

Table 5.2: The gamma peaks identified in the simulated data shown in Fig. 5.5. The energies listed are the expected energies [NND].

Isotope	Energy [MeV]
^{234}Pa	0.9250 (1)
^{234}Pa	0.9260 (2)
^{234}Pa	0.92672 (15)
^{214}Bi	0.934056 (6)
^{234}Pa	0.94600 (3)
^{234}Pa	0.9477 (2)
^{234}Pa	0.9803 (1)

Table 5.3: With the observation of the ^{234}Pa gamma peaks identified in Fig. 5.5/Table 5.2, one would also expect to see several ^{234m}Pa peaks. Listed are the gammas associated with the decay of ^{234}Pa and ^{234m}Pa with an energy between 0.92 and 1.02 MeV [NND]. Also listed is the expected intensity of each gamma relative to the decay of ^{238}U (i.e. the branching ratio for ^{234m}Pa has been taken into account). The gammas that are identified in the spectrum are indicated as such.

Isotope	Energy [MeV]	Intensity	Status
^{234m}Pa	0.92172 (10)	$1.278{\cdot}10^{-2}$ % (16)	not seen
^{234}Pa	0.9250 (1)	$1.3{\cdot}10^{-2}$ % (1)	Identified
^{234}Pa	0.9260 (2)	$3{\cdot}10^{-3}$ % (2)	Identified
^{234}Pa	0.92672 (15)	$1.2{\cdot}10^{-2}$ % (2)	Identified
^{234m}Pa	0.92661 (10)	$1.24{\cdot}10^{-3}$ % (14)	not seen
^{234m}Pa	0.9363 (10)	$1.1{\cdot}10^{-3}$ % (3)	not seen
^{234m}Pa	0.94196 (10)	$2.52{\cdot}10^{-3}$ % (9)	not seen
^{234m}Pa	0.94594 (2)	$1.01{\cdot}10^{-2}$ % (8)	not seen
^{234}Pa	0.94600 (3)	$2.2{\cdot}10^{-2}$ % (2)	Identified
^{234}Pa	0.9477 (2)	$2.7{\cdot}10^{-3}$ % (3)	Identified
^{234m}Pa	0.9600 (10)	$8{\cdot}10^{-4}$ % (3)	not seen
^{234}Pa	0.9803 (1)	$4.5{\cdot}10^{-3}$ % (6)	Identified
^{234}Pa	0.9803 (1)	$2.9{\cdot}10^{-3}$ % (4)	
^{234m}Pa	0.9961 (20)	$5.6{\cdot}10^{-3}$ % (4)	not seen
^{234m}Pa	1.00103 (10)	0.842% (8)	not seen

5.6.2 Excluding the Upper Uranium-238 Decay Chain from Simulations

For a typical simulation of ^{238}U, thousands to hundreds-of-thousands of events are simulated for each group of parts. The decay of one ^{238}U nuclide constitutes a single event. For each event, a large amount of particles are created, and each particle is assigned a `trackID` by MaGe. The `trackID` starts at one and sequentially progresses from the start of the event. Therefore the `trackID` for the ^{238}U particle is always one. And if the ^{238}U particle alpha decays to ^{234}Th, then the alpha particle would be assigned a `trackID` of two and the ^{234}Th particle would be assigned a `trackID` of three (or vice versa). This continues on until the end of the decay chain.

The `trackID`s for all the particles in all the events are *not* recorded in the MaGe output. However, if a particle interacts with a sensitive volume (i.e. a detector), then the information for that particle is recorded in the MaGe output, and the `trackID` is included in that particle's information. Keeping this in mind, consider two gamma peaks in the ^{238}U decay chain: the 609-keV peak from the decay of ^{214}Bi and the 946-keV peak from the decay of ^{234}Pa. The ^{214}Bi nuclide is much further down the ^{238}U decay chain than the ^{234}Pa nuclide, and therefore many more particles will be created (and tracked by MaGe) before the decay of ^{214}Bi as compared to ^{234}Pa. Since the `trackID` progresses with the creation of each new particle, one would expect the `trackID`s of the detected events associated with the 609 keV peak to be significantly greater than those associated with the 946 keV peak. This can be seen in Fig. 5.6. In blue is a histogram of the `trackID`s for all of the detected events in three of the gamma peaks associated with the decay of ^{214}Bi. In red is a histogram of the `trackID`s for all of the detected events in four of the gamma peaks associated with the decay of ^{234}Pa. For the ^{214}Bi histogram the 609, 1120 and 1764-keV peaks are used, and for the ^{234}Pa histogram the 946, 980, 1353 and 1394-keV peaks are used. These particular peaks are chosen because they have a relatively high intensity and the gamma peaks sit on little

background.

From Fig. 5.6 it becomes clear that a lower threshold can be set so that the simulated energy spectrum only includes detected events with a `trackID` above the set threshold. To find the optimal value for the `trackID` threshold, a Cumulative Distribution Function (CDF) of the ^{234}Pa and ^{214}Bi `trackID`-histograms are created, as pictured in Fig. 5.7. From the ^{234}Pa CDF, the efficiency of rejecting the detected ^{234}Pa events can be directly obtained. For example, making a cut requiring the `trackID` to be greater than 20 would cut roughly 60% of all the detected ^{234}Pa events. The same is true of the ^{214}Bi CDF. The optimal value at which to set the `trackID` threshold will maximize the efficiency of rejecting the detected ^{234}Pa events while minimize the efficiency of rejecting the detected ^{214}Bi events. Or similarly, the optimal `trackID` threshold can be found by maximizing

$$\mathrm{CDF}_{Pa}\,(1-\mathrm{CDF}_{Bi})\,. \tag{5.1}$$

Equation 5.1 is shown in black in Fig. 5.7. The curve is maximized at a corresponding `trackID` value of 38. Therefore a cut is applied to all ^{238}U simulations requiring that a detected event have a `trackID` such that:

$$\texttt{trackID} \leq 38. \tag{5.2}$$

From this cut, the efficiency for rejecting detected ^{234}Pa events is $95.91 \pm 0.07\%$ and the efficiency for rejecting detected ^{214}Bi events is $0.98 \pm 0.02\%$. While the ^{214}Bi gamma peaks are used to set a `trackID` threshold and calculate the quoted efficiencies, it is assumed that the ^{214}Bi peaks are a good representation of all the nuclides of interest that occur in the later part of the ^{238}U decay chain. To account for the fact that some nuclides in the lower ^{238}U decay chain will be rejected by this cut (given that the rejection efficiency for ^{214}Bi is not zero), for all ^{238}U simulations the number of events

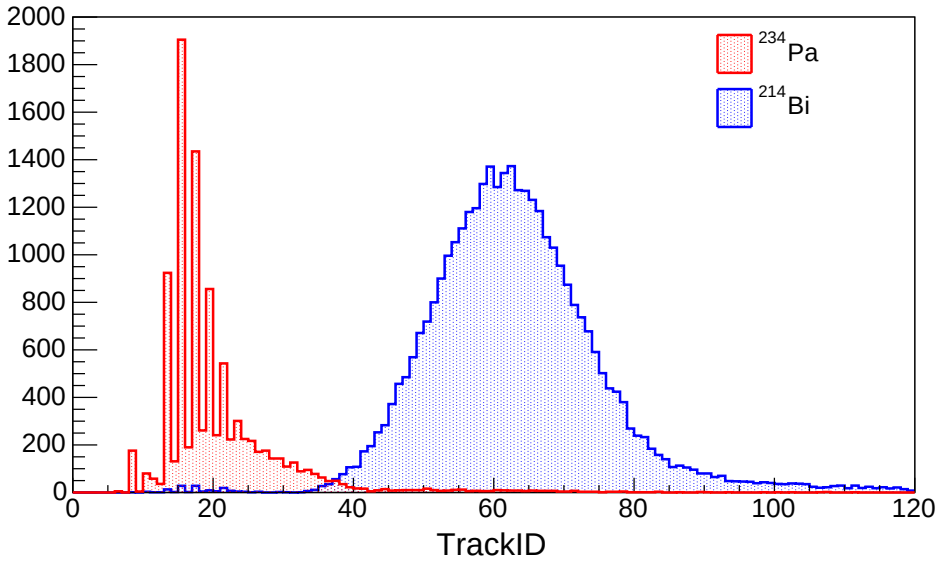

Figure 5.6: In blue (red) is a histogram of the `trackID`s for all of the detected events in three (four) of the gamma peaks associated with the decay of ^{214}Bi (^{234}Pa). For the ^{214}Bi histogram the 609, 1120 and 1764-keV peaks are used, and for the ^{234}Pa histogram the 946, 980, 1353 and 1394-keV peaks are used.

simulated for the group is adjusted such that

$$N = (1 - \epsilon_{Bi})\, N_0 \tag{5.3}$$

$$N = 0.9902\, N_0, \tag{5.4}$$

where N_0 is the actual number of events simulated for the group but N is the number used in further calculations.

5.6.3 Disequilibrium in the Uranium-238 and Thorium-232 Decay Chains

The ^{238}U and ^{232}Th decay chains were simulated in their entirety. By doing so, this assumes secular equilibrium which is almost certainly not true. To properly account for possible disequilibrium in the ^{238}U and ^{232}Th decay chains, portions of the decay chain should be simulated independently from one another [Sch12]. This is especially important given that the decay of ^{234m}Pa is incorrectly modeled in GEANT4 (Section 5.6.1). In future work, if disequilibrium is accounted for in the ^{238}U and ^{232}Th decay chains – as

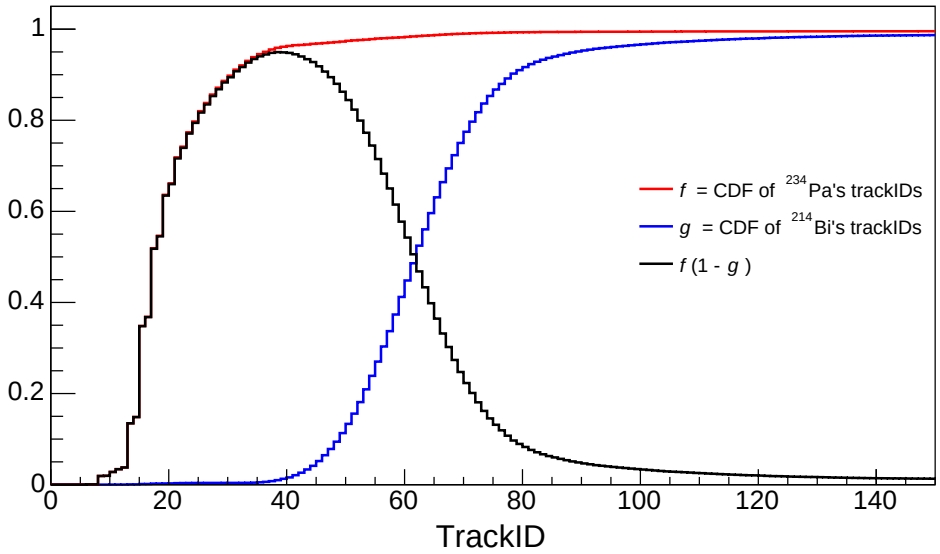

Figure 5.7: In blue (red) is a CDF of the ^{214}Bi (^{234}Pa) histogram in Fig. 5.6. The optimal value at which to set the `trackID` threshold will maximize the efficiency of rejecting the detected ^{234}Pa events while minimize the efficiency of rejecting the detected ^{214}Bi events; this is the black curve.

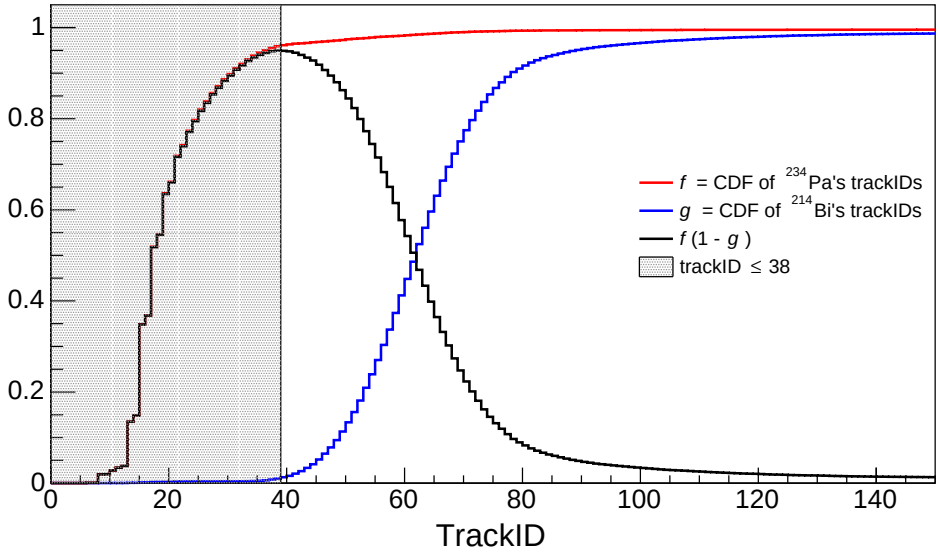

Figure 5.8: The `trackID` associated with the maximum of the black curve is the optimal value at which to set the `trackID` lower threshold. This `trackID` value is found to be 38. The detected events that will be cut with this `trackID` threshold are in the shaded gray region. See text and Fig. 5.7 for further details regarding the red, blue and black curves.

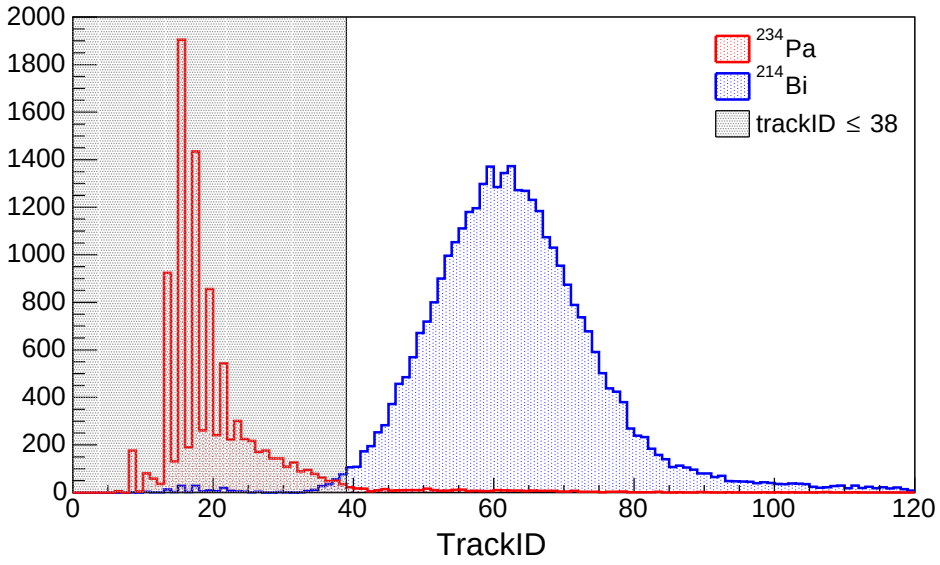

Figure 5.9: Figure 5.6 with the `trackID` lower threshold depicted. The detected events that will be cut with this `trackID` threshold are in the shaded gray region.

it should be – the subchain that contains the decay of ^{234m}Pa can be omitted from the simulations, thereby eliminating the need for the cut described in Section 5.6.2. This is of course preferred given that the cut is not 100% efficient at rejecting the ^{234m}Pa events and keeping the events associated with the later ^{238}U decay chain.

In future work the ^{238}U decay chain should be split into nine different subchains: (1) ^{238}U (2) ^{234}Th $\rightarrow$ ^{234}Pa (3) ^{234}U (4) ^{230}Th (5) ^{226}Ra (6) ^{222}Rn $\rightarrow$ ^{214}Po/^{210}Tl (7) ^{210}Pb $\rightarrow$ ^{206}Pb (8) ^{210}Pb $\rightarrow$ ^{206}Pb (9) ^{210}Po. Additionally, the ^{232}Th decay chain should be split into four different subchains: (1) ^{232}Th (2) ^{228}Ra $\rightarrow$ ^{228}Ac (3) ^{228}Th (4) ^{224}Ra $\rightarrow$ ^{208}Pb. The implementation of the splitting of the decay chains in MaGe is further discussed in Reference [Sch12].

5.6.4 Excluding Alphas from Simulations

In addition to the `trackID` cut, another modification is made to the output from the MaGe simulations. There is an unusually large number of high energy events in the simulated energy spectra; here, high energy refers to greater than 3 MeV. The detected high energy events come from alphas and high-energy gammas depositing energy in the

detectors.

The source of the alphas is due to the fact that the dead layer is not being correctly modeled for the detectors in the PC background model. The source of the high-energy gammas is from alphas – produced from the ^{238}U and ^{232}Th decay chain – capturing on the surrounding materials in the PC geometry. In the PC geometry, the alpha capture interactions observed in the simulations are:

- $^{16}\mathrm{O}\,(\alpha, N\gamma)^{20}\,\mathrm{Ne}$
- $^{28}\mathrm{Si}\,(\alpha, N\gamma)^{32}\,\mathrm{S}$
- $^{19}\mathrm{F}\,(\alpha, N\gamma)^{23}\,\mathrm{Na}$

where N is some natural number. The ^{16}O and ^{28}Si come from the LMFE boards which are made of SiO_2. The ^{19}F comes from the plastic components made of teflon: C_2F_4. The energies of the gammas produced in these interactions range up to 9 MeV. The rate at which these interactions occur is unphysically high; for simulations of the LMFE boards and teflon components, these interactions occur for roughly one out of every 2000 events simulated.

The problem lies with how GEANT4 calculates the inelastic cross sections for hadrons. The cross sections are derived from GHEISHA, a FORTRAN statistical model that was originally developed for collider physics studies [Fes85, Det15]. The energy ranges being investigated here are much lower than what the model was intended for, and are not so reliable. The inelastic cross sections for alphas used by GEANT4 are as follows [Det15].

$$\begin{cases} 0 & E < 6\mathrm{MeV} \\ 493\mathrm{mb} & E \geq 6\mathrm{MeV} \end{cases} \tag{5.5}$$

In an attempt to remove the alphas from the simulations, during the post-processing of the MAGE output, all detected alpha particles have their energy set to zero. This

removes the alphas from the spectra, however this does not completely rid the spectra of the high-energy gammas. Fortunately, the rate at which these interactions occur is low enough where the presence of the high-energy gammas does not hinder future analysis.

In future work the alphas should be removed during simulations so to remove the alphas themselves and the byproducts from their interactions. There is a command in MaGe that enables the user to do just that during runtime. This command was used for the ^{60}Co simulations and for the ^{222}Rn and ^{232}Th simulations with the temperature sensor solders. Therefore the removal of the alphas post-processing was considered unnecessary and was not performed on these simulations. However, during the analysis of the PC background model, a bug in MaGe has been discovered that makes the "killAlpha" command inactive. Therefore the alphas are *not* removed from all ^{60}Co spectra and from the ^{222}Rn and ^{232}Th spectra of the temperature sensor solders. Majorana collaborators are currently working to fix this bug in MaGe to thus allow its use in future simulations. In the mean time, all future work with the PC background model does not consider the higher-energy region, and one should not use the high energy portion of the background model to draw any conclusions.

5.6.5 Other Possible Sources of Background

The background model of the PC takes into account possible ^{238}U and ^{232}Th activities of the materials inside the passive shielding. It also takes into account the cosmogenically-activated ^{60}Co backgrounds from the OFHC Cu and SS components and backgrounds from ^{222}Rn in the nitrogen-purged volume inside of the shield. Other possible sources of background that are not included are as follows.

1. **^{40}K in All Materials** The 1461-keV gamma associated with the decay of ^{40}K is present in the PC data, however ^{40}K is not included in the background model.

2. **^{60}Co in the Crystals and in the UGEFCu**. Only components made from

SS and OFHC Cu are simulated for possible ^{60}Co activity, however it could be present in other materials. This should however be negligible compared to the ^{60}Co in the OFHC Cu and the SS.

3. **^{68}Ge in the Crystals** The 9 and 10-keV X-rays associated with the decay of ^{68}Ge are present in the PC data, however ^{68}Ge is not included in the background model.

4. **Depth-Dependent Backgrounds** No depth-dependent backgrounds are included in the PC background model. This however should be a negligible contribution to the PC background.

5. **Two-Neutrino Double-Beta Decay** The spectrum from the $2\nu\beta\beta$ of ^{76}Ge is not included in the PC background model.

CHAPTER 6: COMPARING THE PROTOTYPE CRYOSTAT BACKGROUND MODEL TO DATA

6.1 Introduction

As discussed in Chapter 5, the background model of the PC takes into account the naturally-occurring radioactivity of the materials used for the components inside of the passive shielding. It also takes into account the cosmogenically-activated backgrounds from the OFHC Cu and SS components and backgrounds from ^{222}Rn in the nitrogen-purged volume inside of the shield. For each nuclide and group of components that is simulated, a MC-generated energy spectrum for each detector of the PC can be predicted. The distinct features and general shape of the energy spectrum are known but unless the activity of the nuclide is known, the amplitude of the energy spectrum remains in question. For the materials used in the MAJORANA DEMONSTRATOR, either their activities are well known or a stringent upper limit has been placed on their activity. For some of the materials used in the PC this is true; mainly for parts of the PC that are made from materials that are present in the DEMONSTRATOR. However the activity of some materials (and hence, components) in the PC is unknown and therefore the contribution of these components to a detector's energy spectrum is unknown. Therefore to compare the PC background model to data, the amplitude of the MC-generated energy spectrum for each component of the background model is allowed to vary freely in a fit to each detector's energy spectrum.

6.2 Low-Background Data Used

The data used for the MC fit are from the low-background data set acquired from July 2014 to December 2014 (Section 2.2). Six of the PC detectors are used; the runtime

Table 6.1: The runtime of the low-background data set for each detector of the PC used for fitting the MC to data. Detectors with no runtime listed are not used in the fit; see text for more details.

Detector	Runtime (hrs)
S1D1	-
S1D2	1448.5
S1D3	1434.8
S1D4	-
S2D1	-
S3D1	826.16
S3D2	828.90
S3D3	-
S3D4	789.60
S3D5	777.72

for each detector during the low-background data set can be found in Table 6.1. The data quality cuts described in Chapter 2 are applied to the data set before the MC fit is performed, and therefore the runtimes listed in Table 6.1 are the effective runtimes after all DQ cuts are performed.

As discussed in Section 1.3, S1D1, S2D1 and S3D3 are not used for any analysis in this thesis and as discussed in Section 4.3.1, S1D4 is not included in analyses due to double peaking. Therefore these detectors are not included in the fit and their runtimes are not listed in Table 6.1.

6.3 Component Grouping for the Monte Carlo Fit to Data

To develop the background model of the PC certain parts are grouped together and simulated as one. For parts to be in the same simulation group they must satisfy two criteria. For one, parts in the same simulation group must be made of the same material. Secondly, their expected detection efficiency must be roughly the same. In other words, in a group, each part's radioactivity should be expected to have a comparable effect

on a detector's energy spectrum and count rate. Table 5.1 lists the 42 groups used during simulations. With one to three radioactive nuclide(s) simulated for each group, a total of 102 MC-generated energy spectra can be made for each detector. If the same grouping was used for fitting the MC to a single detector's data set this would result in a 102-parameter fit. To reduce the number of fit parameters a coarser, more optimized, grouping is chosen for fitting the MC to data. Parts in the same group still must be made of the same material but the detection efficiency criteria is more relaxed. This resulted in 23 different groups; these are listed in Table 6.2. A short description of each column in Table 6.2 is below; the columns are numbered 1–6 from left to right. An explanation of the color coding used in the table can be found in Section 6.4.

1. **Group Notation** The shorthand notation that is used to reference the group throughout this work. The notation references the parts in the group and/or the material of the parts, as well as the nuclide that is simulated in the group of parts.

2. **Nuclide** The nuclide that is simulated for possible radioactivity in the group of parts.

3. **N** The effective number of events simulated for the group. This is further discussed in Section 6.3.1.

4. **Mass [kg]** The mass of all the parts in the group. The masses are calculated with MaGe and the errors are taken to be 10%. Since some groups look at possible radioactivity in the same set of parts (but with different radioactive nuclides) the mass entry may be shared among multiple groups – the same is true of columns 5 and 6.

5. **Material** The material of the parts in the group.

6. **Part(s)** A short description of all the parts included in the group and which

simulation group(s) they correspond to (represented as SG #). The simulation groups with the actual part names can be found in Table 5.1.

Table 6.2: The groups used for fitting the MC-generated energy spectra to data. See Section 6.3 for a description of the column entries. See Section 6.4 for a description of the color coding.

Group Notation	Nuclide	N	Mass [kg]	Material	Part(s)
n2Vol_Rn	^{222}Rn	$1.50{\cdot}10^{7}$	0.292 (3)	Nitrogen Gas	Inner Cavity Volume (SG 1)
ofhc_U	^{238}U	$2.06\,(4){\cdot}10^{7}$	66.9 (7)	OFHC Cu	Thermosyphon and Hardware (SG 2)
ofhc_Th	^{232}Th	$8.89{\cdot}10^{6}$			Cross Arm, Cryostat Hoop,
ofhc_Co	^{60}Co	$8.33{\cdot}10^{6}$			ColdPlate, etc. (SG 3)
					Cryostat Top and Bottom Lids (SG 4 & 5)
					OFHC Cu in Strings (SG 6–8)
efcu_U	^{238}U	$1.14\,(2){\cdot}10^{7}$	3.72 (4)	UGEFCu	Thermal Shield Can (SG 9)
efcu_Th	^{232}Th	$1.30{\cdot}10^{6}$			Strings (SG 10–12)
ssCryo_U	^{238}U	$1.07\,(2){\cdot}10^{7}$	0.281 (3)	SS	Cryostat Clamping Bolts (SG 13)
ssCryo_Th	^{232}Th	$1.09{\cdot}10^{7}$			Thermal Shield Screws (SG 14)
ssCryo_Co	^{60}Co	$4.34{\cdot}10^{6}$			
siBr_U	^{238}U	$9.9\,(2){\cdot}10^{6}$	$6.77\ (7){\cdot}10^{-2}$	Si-Bronze	Cryostat Clamping Nuts (SG 20)
siBr_Th	^{232}Th	$1.0{\cdot}10^{7}$			
solder_Rn	^{222}Rn	$4.3{\cdot}10^{6}$	$1.00\ (1){\cdot}10^{-4}$	Solder	Temperature Sensor Solders (SG 38–42)
solder_Th	^{232}Th	$5.0{\cdot}10^{6}$			
solder_Pb	^{210}Pb	$5.0{\cdot}10^{6}$			
sensSc_U	^{238}U	$5.0\,(1){\cdot}10^{6}$	$1.49\ (1){\cdot}10^{-3}$	SS	Temperature Sensor Screws (SG 15–19)
sensSc_Th	^{232}Th	$5.0{\cdot}10^{6}$			
sensSc_Co	^{60}Co	$5.0{\cdot}10^{5}$			

peek_U	^{238}U	$5.0\,(1)\cdot10^{6}$	$2.57\ (3)\cdot10^{-3}$	PEEK	Temperature Sensor Clamps (SG 30–34)
peek_Th	^{232}Th	$5.0\cdot10^{6}$			
nxt85_U	^{238}U	$3.61\,(7)\cdot10^{6}$	$5.44\ (5)\cdot10^{-2}$	NXT-85	HV Nuts and Crystal Insulators (SG 21–29)
nxt85_Th	^{232}Th	$3.65\cdot10^{6}$			
lmfes_U	^{238}U	$1.98\,(4)\cdot10^{6}$	$1.06\ (1)\cdot10^{-3}$	Silica with Gold Traces	LMFEs (SG 35–37)
lmfes_Th	^{232}Th	$2.00\cdot10^{5}$			

6.3.1 The Effective Number of Events Simulated for a Group

To group components post-simulations, the MC-generated energy spectra of all the components are combined into one. However the components' energy histograms cannot simply be merged together; the mass of each component must be considered as well as the number of events simulated for that component. As detailed in Section A.4, if hypothetically simulating N' events for a group of components, approximately N'_i events are simulated in the i-th component, where N'_i is described by Eq. 6.1 (and the i-th component has a mass of m_i).

$$N'_i = \frac{m_i N'}{\sum_i m_i} \tag{6.1}$$

Therefore in this case, when combining energy histograms post-simulations, N_i^{eff} (Eq. 6.2) is the number of events that *would have* been simulated for the group of components given that N_i events were *actually* simulated for the i-th component.

$$N_i^{eff} = \frac{N_i \sum_i m_i}{m_i} \tag{6.2}$$

In order to maximize the statistics in the MC-generated energy spectra, it is desirable to find the maximum number of events that could have been simulated (had the components been simulated as a group). Therefore the maximum value of N possible, where N is the effective number of events simulated for the MC-fit group is

$$N = \min\left\{N_i^{eff} : \text{for all } i\right\}. \tag{6.3}$$

Thus to merge all the components into one fit group – and one energy spectrum –

the energy spectrum for the i-th component must be scaled by

$$k_i = \frac{N\, m_i}{N_i \sum\limits_i m_i}. \tag{6.4}$$

For example, suppose three groups are being combined post-simulations: groups A, B and C with masses of 1, 2 and 3 kg respectively. If each group had been simulated for 100 events, by Eq. 6.2, N_A^{eff} is equal to 600. This means that if groups A, B and C had been combined and simulated as one whole, one would have had to simulate a total of 600 events in order to have had 100 of the events come from group A. Similarly, N_B^{eff} is equal to 300 and N_C^{eff} is equal to 200. Therefore the maximum number of events that could have been simulated (had A, B and C been simulated as a group) is 200 (i.e. the minimum of 600, 300 and 200; Eq. 6.3). If groups A, B and C had been a single group and simulated for 200 events, by Eq. 6.1, $33\frac{1}{3}$ events would have been simulated in group A, $66\frac{2}{3}$ events in group B and 100 events in group C. Now, 100 events were actually simulated for each of the groups A, B and C. Therefore if combining the groups post-simulations, one would want to keep all of the events for group C, while only keeping $\frac{1}{3}$ of the events for group A and $\frac{2}{3}$ of the events for group B. Therefore – and as seen in Eq. 6.4 – the energy histograms of groups A, B and C must be scaled by $\frac{1}{3}$, $\frac{2}{3}$ and 1 respectively to be combined post-simulations.

The effective number of events simulated (Eq. 6.3) for each fit group can be found in Table 6.2. At this time it is important to recall the `trackID` cut discussed in Section 5.6.1. For any simulation of ^{238}U, the number of events simulated for the group is adjusted such that

$$0.9902 \cdot N \rightarrow N\ . \tag{6.5}$$

This is to account for the fact that the `trackID` cut is $0.98 \pm 0.02\%$ efficient at keeping the lower ^{238}U decay chain. This also gives the effective number of events, N, an

uncertainty as seen in Table 6.2.

6.4 Simultaneous Multi-Detector Fit

As seen in Table 6.2 all the components of the PC background model are arranged into the 23 MC-fit groups. If the PC background model comprehensively describes the backgrounds seen by the detectors of the PC then

$$d_j(E) = \sum_i p_{ji} \cdot s_{ji}(E) \tag{6.6}$$

for each j-th detector. Here, $d_j(E)$ is the j-th detector's energy spectrum from the low-background data set, $s_{j,i}(E)$ is the MC-generated energy spectrum for the i-th MC-fit group as seen by the j-th detector and $p_{j,i}$ is its associated fit parameter. The fit parameter, $p_{j,i}$, directly correlates with the nuclide's radioactivity in the group of components. For example, if $j = 0$ is detector S1D2 and $i = 0$ is the "n2Vol_Rn" group, then $p_{0,0}$ is directly proportional to the ^{222}Rn activity in the inner cavity volume as seen by S1D2. If instead $j = 1$ (and $j = 1$ is detector S1D3) then $p_{1,0}$ is directly proportional to the ^{222}Rn activity in the inner cavity volume as seen by S1D3.

Sticking with this example, $p_{0,0}$ and $p_{1,0}$ are expected to be the same. In fact, $p_{j,0}$ is expected to be the same for all j; any ^{222}Rn in the inner cavity volume should be (roughly) homogeneously distributed and therefore each detector of the PC is expected to measure the same level of radioactivity. This is true for the $p_{j,0}$ parameters as well as for several others. These parameters that are expected to be detector-independent are referred to as the common parameters; they are the fit groups in blue in Table 6.2 and include the following.

- ^{222}Rn in the inner cavity volume
- ^{238}U, ^{232}Th and ^{60}Co in the OFHC Cu
- ^{238}U and ^{232}Th in the UGEFCu

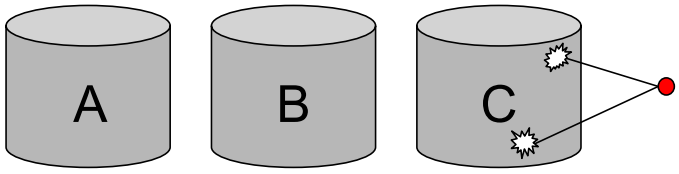

Figure 6.1: A toy drawing of three detectors (designated A, B and C) in a row with a mass of solder (red) in front of detector C. The solder is a very localized source and therefore certain detectors (in this example, A and B) are shielded from any radioactivity in the solder.

- ^{238}U, ^{232}Th and ^{60}Co in the cryostat's SS components
- ^{238}U and ^{232}Th in the silicon bronze.

On the other hand, consider the "solder_Pb" fit group; this is the MC-generated energy spectrum for possible ^{210}Pb in the temperature sensor solders. The solders are small and very close to the detectors, making them a very localized source. Certain detectors are shielded from any radioactivity in the solder by other detectors and by surrounding strings parts. For example, consider the toy drawing of detectors A, B and C in Fig. 6.1; each detector is in front of the other with a mass of solder in front of detector C.

For this example, assume that the efficiency – for detectors C, B and A – of detecting any ^{210}Pb activity in the solder is 1, $1/50$, and $1/100$ respectively. If ten events are simulated, on average the MC-generated energy spectra for detector C will have ten events while the spectra for detectors A and B will have zero events. In this example

it would be incorrect to conclude that detectors A and B have the same efficiency; rather, due to the geometry and the number of events simulated, the MC-generated energy spectra are not sensitive to the differences in the efficiencies of the two detectors. Therefore in this example, detector C is able to measure the ^{210}Pb activity in the solder while detectors B and A are only able to place an upper limit on the activity (with the upper limit from detector A being less-stringent than that from detector B). To take this into account, during the fitting routine each detector is assigned its own fit parameter for the "solder_Pb" fit group.

This is true for several other parameters as well; these detector-dependent parameters are referred to as the unique parameters. They are the fit groups in pink in Table 6.2. Because they are detector-dependent, the shorthand notation that is used to reference these group throughout this work is "SxDy_ZZZ" where ZZZ is the group notation in Table 6.2 and SxDy is the string and detector number (e.g. "S1D2_solder_Pb" refers to the ^{210}Pb activity in the temperature sensor solder as seen by S1D2). The detector-dependent fit groups include the following.

- ^{222}Rn, ^{232}Th and ^{210}Pb in the temperature sensors' solder
- ^{238}U, ^{232}Th and ^{60}Co in the SS temperature sensor screws
- ^{238}U and ^{232}Th in the PEEK temperature sensor clamps
- ^{238}U and ^{232}Th in the NXT-85 string parts
- ^{238}U and ^{232}Th in the LMFEs

To take into account that some fit parameters are expected to be detector-independent, all the detectors are fit at the same time and the common parameters are set to be the same for all detectors. Meanwhile, in this simulatenous-fit, the unique parameters for

each detector are independent of one another. In other words, Eq. 6.6 becomes

$$d_j(E) = \sum_{\substack{i \in \\ \text{common}}} p_i \cdot t_j \cdot s_{ji}(E) + \sum_{\substack{i \in \\ \text{unique}}} p_{ji} \cdot t_j \cdot s_{ji}(E) \ . \tag{6.7}$$

The first term takes into account the common parameters (notice the fit parameter p_i loses its detector-dependent index) and the second term takes into account the unique parameters. There is now an additional parameter, t_j; this is the runtime for the j-th detector's low-background data set.

A multi-detector fit with common parameters ensures that certain parts have consistent activities across all of the detectors while reducing the number of fit parameters. In the absence of common parameters, each detector needs its own set of fit parameters for each fit group; with 23 fit groups and 6 detectors that would be a total of 138 parameters. With the inclusion of the 11 common parameters the number of fit parameters reduces to 83.

6.4.1 Minimization Function

To fit the MC-generated energy spectra to the data, a Negative Log-Likelihood (NLL) function is minimized, where the likelihood function used is an extended likelihood function with binned data. If the k-th bin of a single detector's energy histogram has a bin content equal to ν_k, then the extended likelihood function (Eq. 6.8) assumes that the content of the k-th bin is a Poisson random variable with a mean value of $\sum_i p_i f_{ik}$ [Cow98].

$$L\left(\nu_k; \sum_i p_i f_{ik}\right) = \prod_k \frac{\left[\sum_i p_i f_{ik}\right]^{\nu_k} exp\left[-\sum_i p_i f_{ik}\right]}{\nu_k!} \tag{6.8}$$

In Eq. 6.8, the index k ranges over the energy bins and the index i is summed over

all of the MC-fit groups (Table 6.2). The f_{ik} is the content of the k-th bin of the MC-generated energy spectrum for the i-th fit group and p_i is its associated fit parameter. Taking the negative log of the likelihood function and rearranging terms gives the NLL function to be Eq. 6.9.

$$-logL = -\sum_k \nu_k \, log\left[\sum_i p_i f_{ik}\right] + \sum_k \sum_i p_i f_{ik} + \sum_k log(\nu_k!) \tag{6.9}$$

To aid the minimizing processor in finding a best fit, two modifications are made to the standard NLL function in Eq. 6.9. First, the last term ($\sum_k log(\nu_k!)$) does not depend on the fitting parameters and therefore it is dropped in the NLL function. Secondly, it is unphysical to have a negative fit parameter as it would result in a negative energy spectrum, so the absolute value is taken of the fit parameters: $p_i \rightarrow \mathrm{Abs}\,(p_i)$. With these modifications Eq. 6.9 becomes Eq. 6.10.

$$-logL = -\sum_k \nu_k \, log\left[\sum_i \mathrm{Abs}\,(p_i)\, f_{ik}\right] + \sum_k \sum_i \mathrm{Abs}\,(p_i)\, f_{ik} \tag{6.10}$$

Equation 6.10 is the NLL function that would be minimized if fitting the MC-generated energy spectra to one detector's data. However, the PC has multiple detectors and it is desirable to fit all of them at the same time with common fit parameters between the detectors. Therefore the NLL that is minimized for fitting the detectors of the PC is Eq. 6.11.

$$\begin{aligned}\mathrm{NLL} = \sum_j \Bigg[&-\sum_k \nu_{jk} \, log\left[\sum_{\substack{i \in \\ \text{common}}} \mathrm{Abs}\,(p_i)\, t_j f_{jik} + \sum_{\substack{i \in \\ \text{unique}}} \mathrm{Abs}\,(p_{ji})\, t_j f_{jik}\right] \\ &+ \sum_k \left[\sum_{\substack{i \in \\ \text{common}}} \mathrm{Abs}\,(p_i)\, t_j f_{jik} + \sum_{\substack{i \in \\ \text{unique}}} \mathrm{Abs}\,(p_{ji})\, t_j f_{jik}\right]\Bigg]\end{aligned} \tag{6.11}$$

The index j is summed over all detectors and t_j is the runtime for the j-th detector's low-background data set. During the fit a 5-keV binning is used for both the data and MC spectra and the index k is summed over the bins in the fit range: 100–1674 keV. The best fit is the parameter values for which the NLL (Eq. 6.11) is minimized. The NLL function is minimized with MINOS, one of the the MINUIT processors, and is further described in Section 3.2.

6.5 Low-Background Data Fit Results

The radioactivity of the PC materials can be calculated from the parameter values which yield the best fit. If p_i is the fit parameter associated with the i-th MC-fit group, then the corresponding activity is

$$A = \frac{\mathrm{Abs}\,(p_i)\,N_i}{m_i} \tag{6.12}$$

where N_i is the effective number of events simulated and m_i is the total mass of the parts in the group, as listed in Table 6.2. The activities calculated from the best fit can be found in Tables 6.3–6.5. The activity uncertainties are calculated using the standard technique of propagation of uncertainties. Table 6.3 contains the common parameters of the fit. The common parameters are the same for all of the detectors and therefore for each common parameter there is only one activity. Tables 6.4 and 6.5 contain the unique parameters of the fit. The unique parameters are detector-dependent and therefore for each unique parameter there are six activities – one for each detector.

The activities from the best fit can be compared to the expected values in two ways. First, they can be compared with the activity values obtained from assay. These values are in the "Expected Activity" columns in Tables 6.3–6.5. There are a few caveats worth mentioning with regards to the "Expected Activity" columns.

1. A DURRIDGE RAD7 is used to continuously monitor the amount of ^{222}Rn inside

the shielding of the PC. At almost all times the amount of ^{222}Rn in the inner cavity volume is below the detection limits of the RAD7. The detection range of the RAD7 is 4 – 750,000 Bq/m^3 [Rad]. Therefore the expected activity of the n2Vol_Rn group is given as an upper limit of 4 Bq/m^3.

2. The "Expected Activity" for ^{60}Co in the OFHC Cu (in Table 6.3) assumes that the OFHC Cu is fully saturated at 200 decays/kg/day [Lau09]. However several of the OFHC Cu parts had been underground prior to and therefore the ^{60}Co activity is expected to be lower than the saturation value quoted in Table 6.3. Hence the "Expected Activity" for ^{60}Co in the OFHC Cu is quoted as an upper limit.

3. The ^{238}U and ^{232}Th activities for SS that are quoted in Tables 6.3–6.3 are obtained from an assay of a SS vacuum component [Abgon]. The ^{238}U and ^{232}Th activities in SS are known to vary greatly and therefore the quoted values should be considered an approximation.

4. As a reminder, not all of the materials of the PC have been assayed by the MAJORANA collaboration, hence some parameters have no assigned value for an expected activity.

5. The ^{210}Pb activity in the temperature sensor solder is taken from literature [Bun85].

6. For the remaining groups, the expected activities are are obtained from assays performed by the MAJORANA collaboration. The materials in Tables 6.3–6.3 that have been assayed by MAJORANA are the: OFHC Cu, UGEFCu, PEEK, NXT-85 and the LMFEs [Abgon].

Table 6.3: The activities obtained from the best fit of the MC to the low-background data. See text for more details.

MC Fit Group	Activity from Fit to Low-Background Data [Bq/kg]	Expected Activity [Bq/kg]
n2Vol_Rn [Bq/m^3]†	0.28 ± 0.02	< 4
ofhc_U	$3{\cdot}10^{-9} \pm 1{\cdot}10^{-6}$	$(1.25 \pm 0.24){\cdot}10^{-6}$
ofhc_Th	$2{\cdot}10^{-9} \pm 7{\cdot}10^{-7}$	$(1.1 \pm 0.21){\cdot}10^{-6}$
ofhc_Co	$(3 \pm 1){\cdot}10^{-5}$	$< 2 \cdot 10^{-3}$
efcu_U	$10{\cdot}10^{-9} \pm 2{\cdot}10^{-6}$	$(0.17 \pm 0.03){\cdot}10^{-6}$
efcu_Th	$5{\cdot}10^{-9} \pm 1{\cdot}10^{-6}$	$(0.06 \pm 0.02){\cdot}10^{-6}$
ssCryo_U	0.104 ± 0.006	$< 5 \cdot 10^{-3}$
ssCryo_Th	0.061 ± 0.005	$(13 \pm 4){\cdot}10^{-3}$
ssCryo_Co	0.056 ± 0.005	-
siBr_U	0.45 ± 0.03	-
siBr_Th	0.14 ± 0.02	-

† The conversion from Bq/kg to Bq/m^3 uses the density of nitrogen gas as in MaGe: 1.251 mg/cm^3.

Table 6.4: The activities obtained from the best fit of the MC to the low-background data. See text for more details.

MC Fit Group	Activity from Fit to Low-Background Data [Bq/kg] S1D2	S1D3	S3D1	Expected Activity [Bq/kg]
solder_Rn	$7{\cdot}10^{-5} \pm 5{\cdot}10^{0}$	$2{\cdot}10^{-2} \pm 1{\cdot}10^{1}$	$2{\cdot}10^{-6} \pm 1{\cdot}10^{-1}$	-
solder_Th	30 ± 5	96 ± 8	$4{\cdot}10^{-4} \pm 2{\cdot}10^{-1}$	-
solder_Pb	2300 ± 300	7100 ± 900	$2{\cdot}10^{-2} \pm 5{\cdot}10^{0}$	500–57,000
sensSc_U	$5{\cdot}10^{-5} \pm 5{\cdot}10^{-2}$	$2{\cdot}10^{-4} \pm 1{\cdot}10^{-1}$	$3{\cdot}10^{-6} \pm 9{\cdot}10^{-4}$	$< 5 \cdot 10^{-3}$
sensSc_Th	$9{\cdot}10^{-6} \pm 5{\cdot}10^{-3}$	$1{\cdot}10^{-4} \pm 4{\cdot}10^{-2}$	$7{\cdot}10^{-6} \pm 3{\cdot}10^{-3}$	$(13 \pm 4){\cdot}10^{-3}$
sensSc_Co	1.0 ± 0.3	1.6 ± 0.4	$4{\cdot}10^{-5} \pm 1{\cdot}10^{-2}$	-
peek_U	$3{\cdot}10^{-5} \pm 2{\cdot}10^{-2}$	4.4 ± 0.4	$6{\cdot}10^{-6} \pm 2{\cdot}10^{-3}$	$< 63 \cdot 10^{-3}$
peek_Th	$6{\cdot}10^{-5} \pm 2{\cdot}10^{-2}$	$1{\cdot}10^{-4} \pm 7{\cdot}10^{-2}$	$6{\cdot}10^{-6} \pm 2{\cdot}10^{-3}$	$< 16 \cdot 10^{-4}$
nxt85_U	0.019 ± 0.005	$10{\cdot}10^{-7} \pm 3{\cdot}10^{-4}$	$4{\cdot}10^{-8} \pm 2{\cdot}10^{-4}$	$< 5 \cdot 10^{-6}$
nxt85_Th	$2{\cdot}10^{-7} \pm 1{\cdot}10^{-4}$	$5{\cdot}10^{-7} \pm 3{\cdot}10^{-4}$	$4{\cdot}10^{-7} \pm 1{\cdot}10^{-4}$	$(0.10 \pm 0.01){\cdot}10^{-6}$
lmfes_U	$2{\cdot}10^{-5} \pm 8{\cdot}10^{-3}$	$2{\cdot}10^{-5} \pm 6{\cdot}10^{-3}$	$3{\cdot}10^{-7} \pm 9{\cdot}10^{-3}$	$(10.570 \pm 0.370){\cdot}10^{-3}$
lmfes_Th	$4{\cdot}10^{-6} \pm 7{\cdot}10^{-3}$	$5{\cdot}10^{-6} \pm 2{\cdot}10^{-2}$	$10{\cdot}10^{-6} \pm 3{\cdot}10^{-3}$	$(6.530 \pm 0.120){\cdot}10^{-3}$

Table 6.5: The activities obtained from the best fit of the MC to the low-background data. See text for more details.

MC Fit Group	Activity from Fit to Low-Background Data [Bq/kg] S3D2	S3D4	S3D5	Expected Activity [Bq/kg]
solder_Rn	$7{\cdot}10^{-4} \pm 3{\cdot}10^{-1}$	$3{\cdot}10^{-3} \pm 2{\cdot}10^{0}$	$10{\cdot}10^{-4} \pm 4{\cdot}10^{-1}$	-
solder_Th	$3{\cdot}10^{-6} \pm 2{\cdot}10^{-1}$	21 ± 5	$5{\cdot}10^{-4} \pm 8{\cdot}10^{-1}$	-
solder_Pb	530 ± 100	3700 ± 500	720 ± 80	500–57,000
sensSc_U	$6{\cdot}10^{-5} \pm 3{\cdot}10^{-2}$	$4{\cdot}10^{-5} \pm 2{\cdot}10^{-1}$	$2{\cdot}10^{-5} \pm 5{\cdot}10^{-2}$	$< 5 \cdot 10^{-3}$
sensSc_Th	$2{\cdot}10^{-5} \pm 4{\cdot}10^{-3}$	$3{\cdot}10^{-5} \pm 1{\cdot}10^{-2}$	$4{\cdot}10^{-6} \pm 9{\cdot}10^{-2}$	$(13 \pm 4){\cdot}10^{-3}$
sensSc_Co	$1{\cdot}10^{-5} \pm 1{\cdot}10^{-2}$	0.8 ± 0.3	0.1 ± 0.1	-
peek_U	$4{\cdot}10^{-5} \pm 3{\cdot}10^{-2}$	0.7 ± 0.2	$4{\cdot}10^{-5} \pm 2{\cdot}10^{-2}$	$< 63 \cdot 10^{-3}$
peek_Th	$9{\cdot}10^{-6} \pm 7{\cdot}10^{-3}$	$10{\cdot}10^{-5} \pm 3{\cdot}10^{-2}$	$3{\cdot}10^{-5} \pm 2{\cdot}10^{-2}$	$< 16 \cdot 10^{-4}$
nxt85_U	$(3 \pm 7){\cdot}10^{-3}$	$6{\cdot}10^{-8} \pm 5{\cdot}10^{-3}$	0.049 ± 0.008	$< 5 \cdot 10^{-6}$
nxt85_Th	$2{\cdot}10^{-7} \pm 8{\cdot}10^{-5}$	$1{\cdot}10^{-6} \pm 5{\cdot}10^{-4}$	0.024 ± 0.006	$(0.10 \pm 0.01){\cdot}10^{-6}$
lmfes_U	$4{\cdot}10^{-6} \pm 1{\cdot}10^{-1}$	$7{\cdot}10^{-5} \pm 2{\cdot}10^{-2}$	$6{\cdot}10^{-5} \pm 2{\cdot}10^{-2}$	$(10.570 \pm 0.370){\cdot}10^{-3}$
lmfes_Th	$1{\cdot}10^{-6} \pm 2{\cdot}10^{-2}$	$6{\cdot}10^{-6} \pm 2{\cdot}10^{-3}$	$4{\cdot}10^{-7} \pm 1{\cdot}10^{-3}$	$(6.530 \pm 0.120){\cdot}10^{-3}$

Table 6.6: The count rates in the fit region (100–1674 keV) as seen in: (1) each detector's low-background energy spectrum and (2) the sum of each detector's activity-scaled MC-generated energy spectra.

Detector	Count Rate in Fit Region [cts/ton/yr]	
	Data	MC
S1D2	5.67 (7)·10^7	5.62 (7)·10^7
S1D3	4.34 (5)·10^7	4.32 (5)·10^7
S3D1	5.18 (9)·10^7	5.38 (10)·10^7
S3D2	5.02 (9)·10^7	5.01 (9)·10^7
S3D4	4.15 (9)·10^7	4.13 (9)·10^7
S3D5	4.12 (9)·10^7	4.09 (9)·10^7

A second way the best fit can be compared to expectations is that – as referenced in Eq. 6.7 – the activity-scaled MC-generated energy spectra should sum to each detector's low-background data. Table 6.6 gives the count rates in the fit region (100–1674 keV) as seen in: (1) each detector's low-background energy spectrum and (2) the sum of each detector's activity-scaled MC-generated energy spectra.

To visually compare the fit results across all of the detectors, Fig. 6.2 shows the count rate in the fit region for each activity-scaled MC-fit group – as seen by each detector. Fit groups with the same parts (but different radioactive nuclide) are grouped together. Fit groups whose associated fit parameters are detector-dependent are annotated with an asterisk. The other fit groups are those whose associated fit parameters are detector-independent. For each detector-independent fit group the associated activity is set to be equal across all of the detectors and therefore the count rates are expected to be fairly consistent for all detectors. Any differences between the count rates of the detector-independent parameters in Fig. 6.2 are due to the fact that each detector has a unique efficiency of detecting radiation in a part.

The best fit to each detector's low-background data can be seen in Section D.2. As

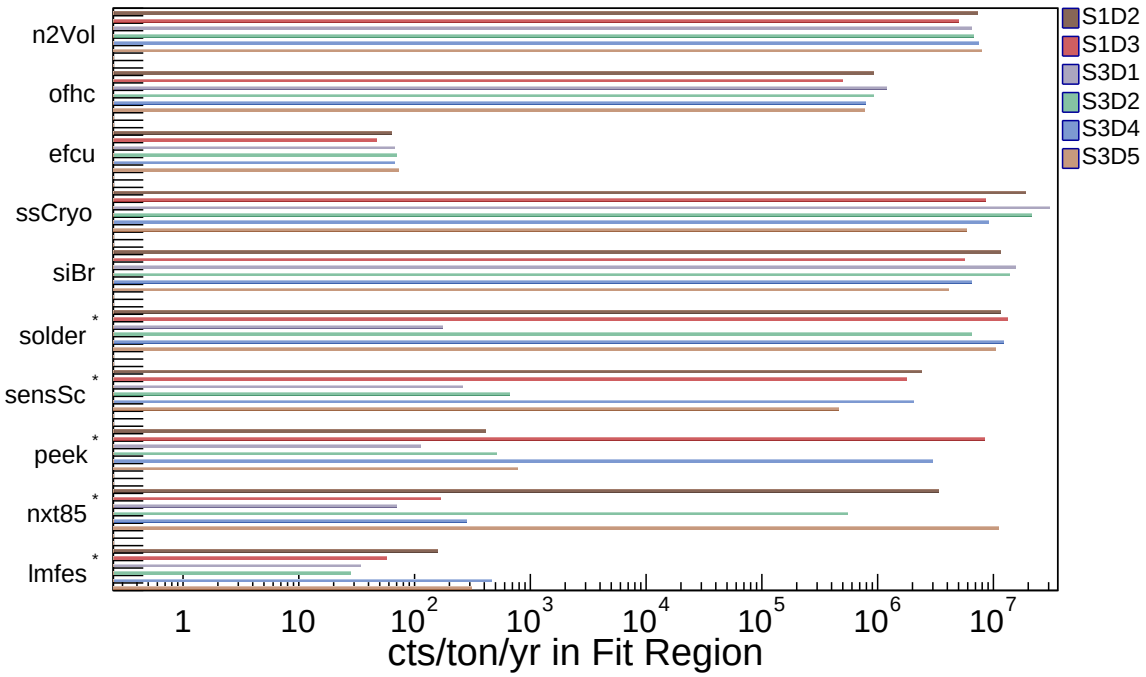

Figure 6.2: The count rate in the fit region (100–1674 keV) for each MC-fit group, as seen by each detector. To calculate the count rate, each MC-generated energy spectrum is scaled by the activity which resulted in the best fit to the low-background data. Fit groups with the same parts (but different radioactive nuclide) are grouped together. Fit groups whose associated fit parameters are detector-dependent are annotated with an asterisk. See text for more details.

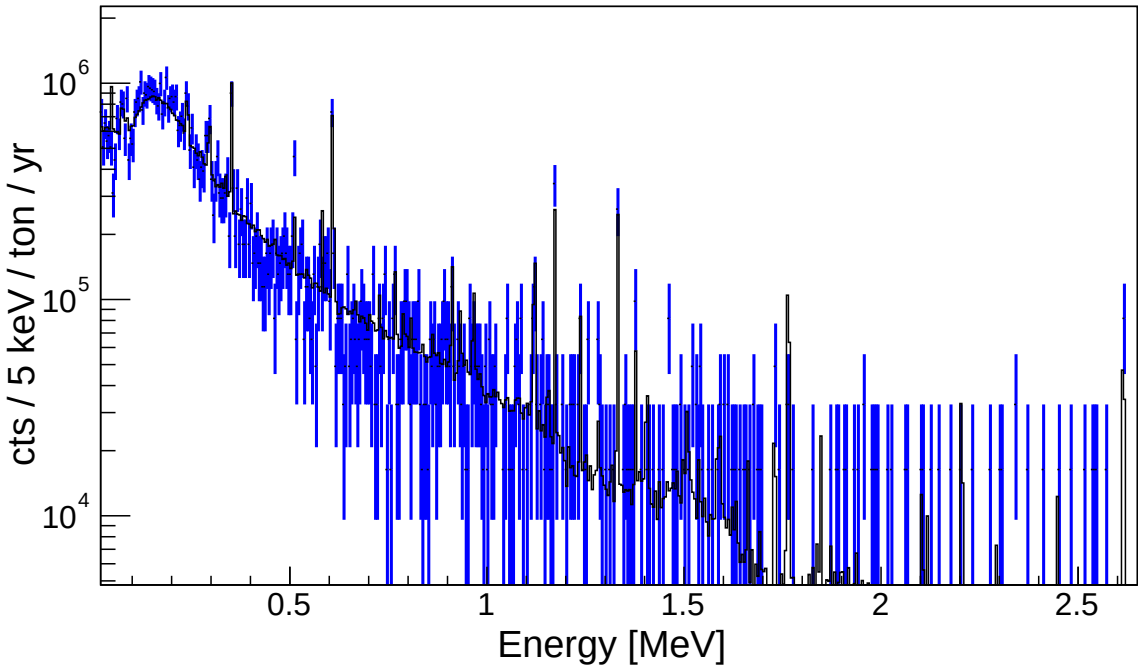

Figure 6.3: The low-background energy spectrum of S3D2 (blue) and the fit to S3D2's data (black).

an example, the fit to the energy spectrum for S3D2 is shown in Fig. 6.3. (Note, even though this example is for only one detector, this fit is found from fitting all of the detectors at the same time.) Figure 6.3 shows the low-background energy spectrum for S3D2 (blue) and the fit to S3D2's data (black). The fit shown is the "total" fit: the sum of the 23 MC-fit groups as seen by S3D2 (i.e. the right-hand side of Eq. 6.7).

The top portion of Fig. 6.4 shows the final fit to the data as well as each of the 23 MC-fit groups that contribute to the total fit. In the accompanying legend, the MC-fit groups are listed in decreasing order (from top to bottom, left to right) by their contribution to the total fit in the fit region of 100–1674 keV. As a reminder, the naming convention used is outlined in Table 6.2 and the prefix "S3D2_" is an indication that the fit parameter is detector-dependent. The bottom portion of Fig. 6.4 shows the pull resulting from the fit to the data. The pull of the k-th bin is defined by Eq. 6.13 where Data_k is the content of the k-th bin in the low-background energy spectrum and Fit_k

is the content of the k-th bin in the total fit.

$$\text{pull}_k = \begin{cases} \frac{\text{Data}_k - \text{Fit}_k}{\sqrt{\text{Data}_k}}, & \text{Data}_k \neq 0 \\ \frac{\text{Data}_k - \text{Fit}_k}{1}, & \text{Data}_k = 0 \end{cases} \tag{6.13}$$

To better comprehend the distribution of the pull, Fig. 6.5 is a histogram of the pull values shown in the bottom portion of Fig. 6.4 with a red line indicating the average of the pull values. The histogram should be roughly Gaussian in shape and the average of the pull should be approximately zero. The histogram of each detector's pull can be found in Section D.2.7.

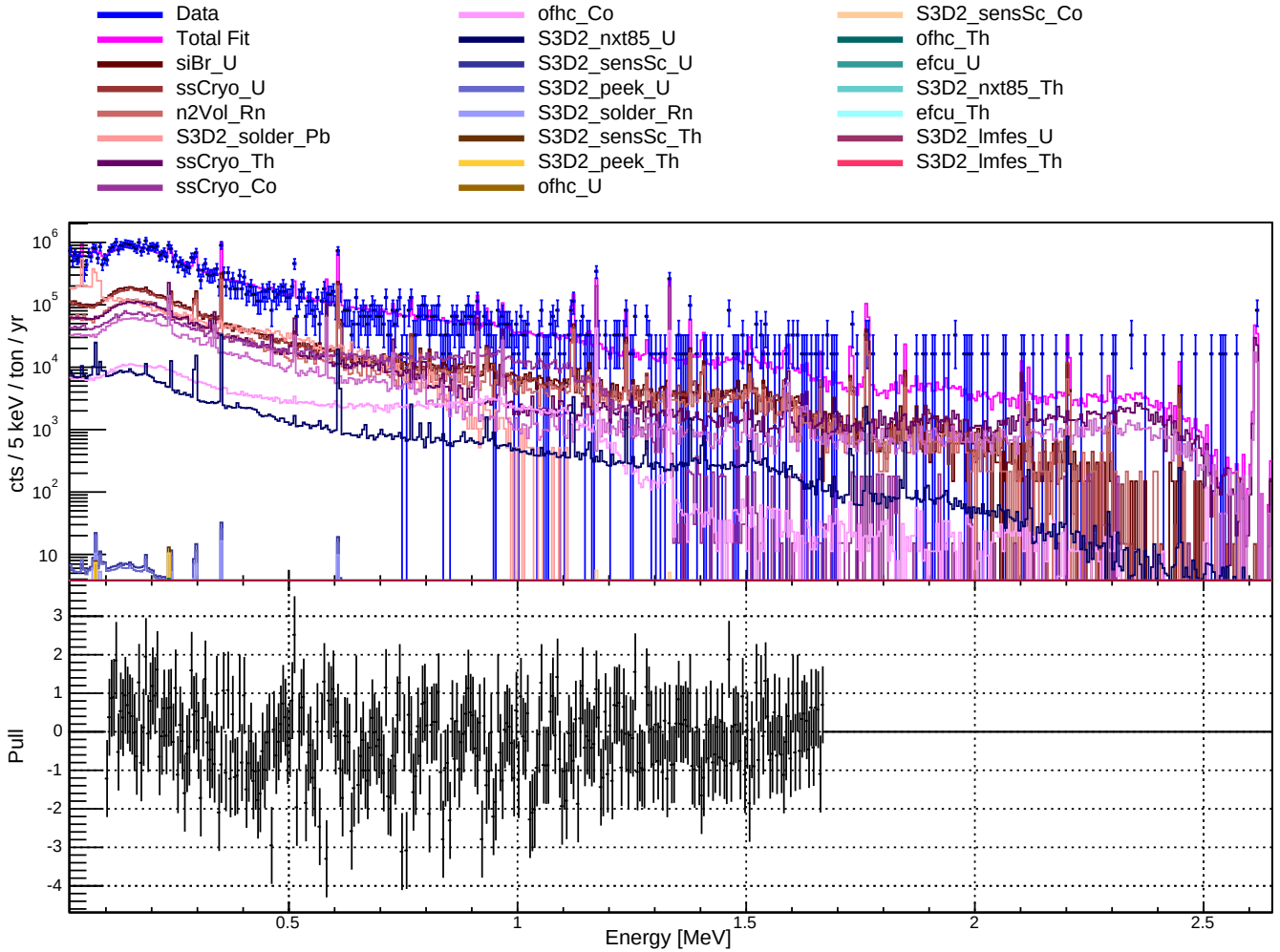

Figure 6.4: (Top) The low-background energy spectrum of S3D2 (blue) and the fit to S3D2's data (pink). Also shown is each of the 23 MC-fit groups and the contribution they make to the total fit. In the accompanying legend, the MC-fit groups are listed in decreasing order (from top to bottom, left to right) by their contribution to the total fit. (Bottom) The pull resulting from the fit to the data.

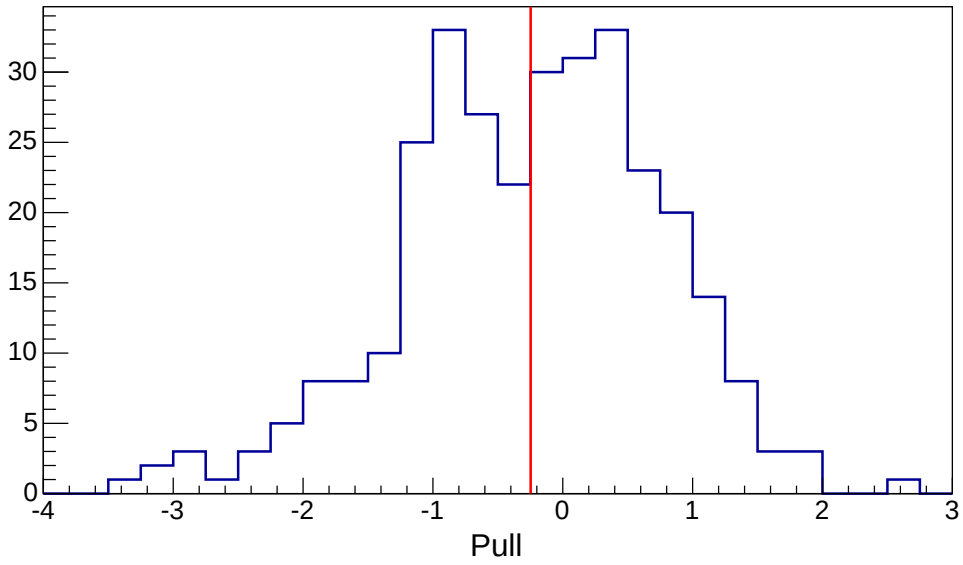

Figure 6.5: A histogram of the pull values resulting from the fit to the low-background data for S3D2.

In the top portion of Fig. 6.4 only the MC-fit groups that are the top contributors can be seen as the other fit groups' contribution to the total fit is order of magnitudes less. Therefore to better compare the relative contribution from all of the MC-fit groups, Fig 6.6 is a bar graph of the count rate (in the fit region) for each of the 23 fit groups. Also shown are the rates from the data and the total fit (which are also listed in Table 6.6).

Figures 6.3–6.6 for each of the six detectors can be found in Section D.2.

6.6 A Systematics Test

The following study was done to understand the systematics associated with the MC-fitting routine and in particular, fitting multiple detectors simultaneously with common parameters. For roughly 20 hours (on April 7^{th} 2015) the ^{222}Rn-purge system for the PC was turned off. A DURRIDGE RAD7 is used to continuously monitor the amount of ^{222}Rn inside the shielding of the PC and – as expected – an increase in ^{222}Rn was seen during this time. This can be seen in Fig. 6.7, which shows the amount of ^{222}Rn inside of the shield of the PC from April 6^{th} to the 8^{th}. At nearly all

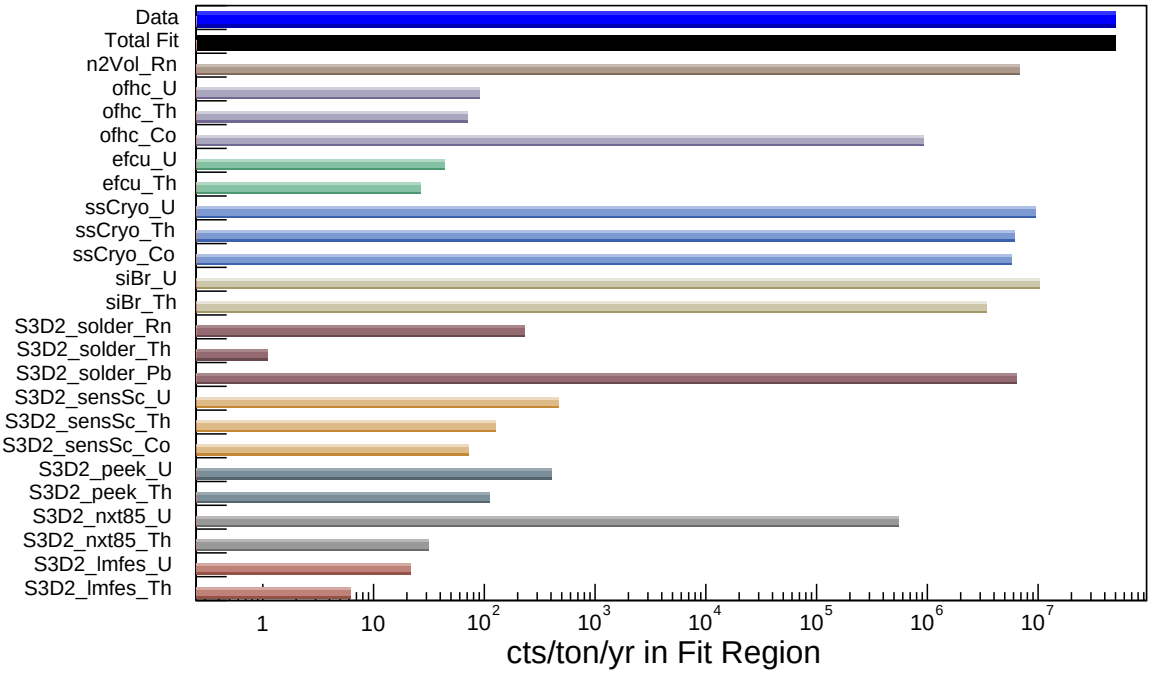

Figure 6.6: The count rate in the fit region (100–1674 keV) for each MC-fit group, as seen by S3D2. To calculate the count rate, each MC-generated energy spectrum is scaled by the activity which resulted in the best fit to the low-background data.

times the amount of ^{222}Rn inside of the shield of the PC is consistent with 0 pCi/L, however during the time when the ^{222}Rn-purge system was turned off the amount of ^{222}Rn increased to as much as 7 pCi/L.

While the data collected during this 20-hour time period is not included in the low-background data set it is used for the study described in this section. (The same series of data selection criteria that are performed on the low-background data set are performed on the high-Rn data set.)

Given that the ^{222}Rn-purge system was off, the backgrounds in this high-Rn data set should come almost exclusively from ^{222}Rn in the inner cavity volume. Therefore the high-Rn data is fit with a simplified NLL function; one that only takes into account the "n2Vol_Rn" fit group. The parameter associated with the "n2Vol_Rn" fit group is detector-independent and therefore each of the six detectors of the PC are simultaneously fit with one common parameter.

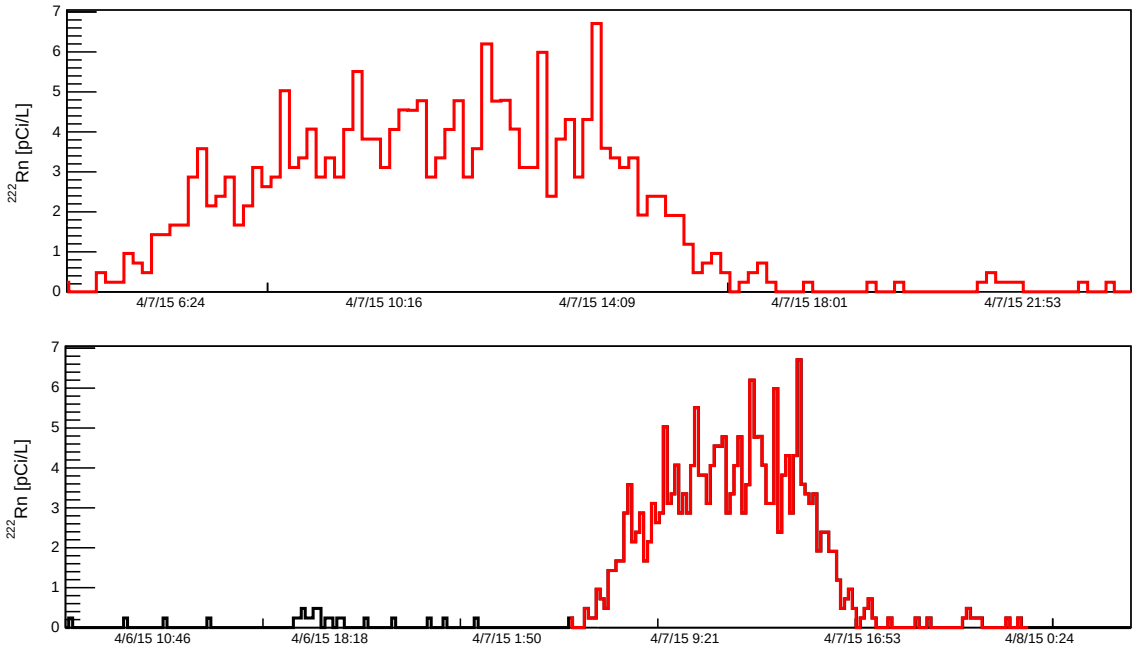

Figure 6.7: The bottom graph shows the amount of ^{222}Rn inside of the shield of the PC from April 6^{th} to the 8^{th}. For roughly 20 hours (on April 7^{th} 2015) the ^{222}Rn-purge system for the PC was turned off and therefore an increase in ^{222}Rn was seen during this time. This 20-hour time period is shown in red in the bottom graph and is exclusively shown in the top graph.

In addition to this one-parameter fit, the high-Rn data set is also fit using the standard 83-parameter NLL function. (i.e. The same fit that is performed on the low-background data set is performed on the high-Rn data set.) By comparing the results of the two fits several observations can be made.

- How does the fit parameter associated with the MC-fit group "n2Vol_Rn" compare between the two fits? The parameters are expected to be in agreement with one another.

- How do the other fit parameters behave in the 83-parameter fit to the high-Rn data? The parameter values that result in the best fit are expected to at least roughly agree with those from the fit to the low-background data.

These questions and the results of the two fits are discussed below.

6.6.1 High-Radon Data Fit Results

The best 1-parameter fit to each detector's high-Rn data can be seen in Section D.3. The best 83-parameter fit to each detector's high-Rn data can be seen in Section D.4. The same figures that are pictured for the low-background fit are pictured for the high-Rn fits.

In the same way the activities of the materials can be extracted from the MC-fit to the low-background data, the activities can be extracted from the fit to the high-Rn data. Tables 6.7–6.9 contain the activities from the 83-parameter fit. In the "Expected Activities" column all of the values are the same as in the low-background tables (Tables 6.3–6.5) except for the expected activity associated with the n2Vol_Rn group. For the low-background data, any amount of ^{222}Rn in the inner cavity volume is below the detection limits of the RAD7 and therefore the expected activity is quoted as an upper limit of 4 Bq/m^3. However for the high-Rn data, the amount of ^{222}Rn was measurable and therefore the expected activity is found by averaging the amount of

measured ^{222}Rn over the 20-hour time period shown in Fig. 6.7. This average is found to be 67 Bq/m^3 (1.8 pCi/L). Only one activity can be calculated for the 1-parameter fit – the activity of ^{222}Rn in the inner cavity volume – and it is found to be 112 ± 2 Bq/m^3 (90 ± 1 Bq/kg).

Furthermore, as with the low-background fit, the activity-scaled MC-generated energy spectra should sum to each detector's high-Rn data. Table 6.10 gives the count rates in the fit region (100–1674 keV) as seen in: (1) each detector's high-Rn energy spectrum and (2 & 3) the sum of each detector's scaled MC-generated energy spectra. Each MC-generated energy spectrum is scaled by the activity which resulted in the best fit to the high-Rn data with (2) the 83-parameter fit and (3) the 1-parameter. Since the 83-parameter NLL and 1-parameter NLL are fit to the same high-Rn data their minimization functions are directly comparable and are included in Table 6.10.

To visually compare the fit results across all of the detectors in the 83-parameter fit, Fig. 6.8 shows the count rate in the fit region for each activity-scaled MC-fit group – as seen by each detector. To calculate the count rates in Fig. 6.8 each MC-generated energy spectrum is scaled by the activity which resulted in the best 83-parameter fit to the high-Rn data. Fit groups with the same parts (but different radioactive nuclide) are grouped together. Fit groups whose associated fit parameters are detector-dependent are annotated with an asterisk.

Table 6.7: The activities obtained from the best 83-parameter fit of the MC to the high-Rn data. See Section 6.5 for more details.

MC Fit Group	Activity from Fit to High-Rn Data [Bq/kg]	Expected Activity [Bq/kg]
n2Vol_Rn [Bq/m^3]†	30 ± 8	67
ofhc_U	$3{\cdot}10^{-7} \pm 3{\cdot}10^{-3}$	$(1.25 \pm 0.24){\cdot}10^{-6}$
ofhc_Th	$1{\cdot}10^{-7} \pm 1{\cdot}10^{-3}$	$(1.1 \pm 0.21){\cdot}10^{-6}$
ofhc_Co	$(5 \pm 7){\cdot}10^{-4}$	$< 2 \cdot 10^{-3}$
efcu_U	$9{\cdot}10^{-8} \pm 1{\cdot}10^{-2}$	$(0.17 \pm 0.03){\cdot}10^{-6}$
efcu_Th	$7{\cdot}10^{-7} \pm 7{\cdot}10^{-3}$	$(0.06 \pm 0.02){\cdot}10^{-6}$
ssCryo_U	2 ± 3	$< 5 \cdot 10^{-3}$
ssCryo_Th	$1 \cdot 10^{-4} \pm 6 \cdot 10^{-1}$	$(13 \pm 4){\cdot}10^{-3}$
ssCryo_Co	$5 \cdot 10^{-4} \pm 3 \cdot 10^{-1}$	-
siBr_U	5 ± 1	-
siBr_Th	$8 \cdot 10^{-4} \pm 3 \cdot 10^{0}$	-

† The conversion from Bq/kg to Bq/m^3 uses the density of nitrogen gas as in MaGe: 1.251 mg/cm^3.

Table 6.8: The activities obtained from the best 83-parameter fit of the MC to the high-Rn data. See Section 6.5 for more details.

MC Fit Group	Activity from Fit to High-Rn Data [Bq/kg]			Expected Activity [Bq/kg]
	S1D2	S1D3	S3D1	
solder_Rn	$(5 \pm 2)\cdot 10^{3}$	$(1.6 \pm 0.6)\cdot 10^{4}$	$3 \cdot 10^{2} \pm 2 \cdot 10^{3}$	-
solder_Th	$3 \cdot 10^{-1} \pm 6 \cdot 10^{2}$	$4 \cdot 10^{-1} \pm 9 \cdot 10^{2}$	$3 \cdot 10^{-3} \pm 2 \cdot 10^{2}$	-
solder_Pb	$(2 \pm 5)\cdot 10^{4}$	$2 \cdot 10^{4} \pm 1 \cdot 10^{5}$	$2 \cdot 10^{-2} \pm 1 \cdot 10^{4}$	500–57,000
sensSc_U	$2 \cdot 10^{-2} \pm 6 \cdot 10^{1}$	$(2 \pm 4)\cdot 10^{2}$	$9 \cdot 10^{-3} \pm 2 \cdot 10^{1}$	$< 5 \cdot 10^{-3}$
sensSc_Th	$3 \cdot 10^{-2} \pm 3 \cdot 10^{1}$	$3 \cdot 10^{-2} \pm 7 \cdot 10^{1}$	$1 \cdot 10^{-4} \pm 8 \cdot 10^{0}$	$(13 \pm 4)\cdot 10^{-3}$
sensSc_Co	$4 \cdot 10^{0} \pm 1 \cdot 10^{1}$	10 ± 20	$3 \cdot 10^{-4} \pm 6 \cdot 10^{0}$	-
peek_U	$4 \cdot 10^{-2} \pm 4 \cdot 10^{1}$	$6 \cdot 10^{-3} \pm 8 \cdot 10^{1}$	$1 \cdot 10^{-3} \pm 2 \cdot 10^{1}$	$< 63 \cdot 10^{-3}$
peek_Th	$2 \cdot 10^{0} \pm 9 \cdot 10^{1}$	$6 \cdot 10^{-2} \pm 4 \cdot 10^{1}$	$8 \cdot 10^{-5} \pm 6 \cdot 10^{0}$	$< 16 \cdot 10^{-4}$
nxt85_U	$4 \cdot 10^{-4} \pm 9 \cdot 10^{-1}$	$1 \cdot 10^{-4} \pm 1 \cdot 10^{0}$	$3 \cdot 10^{-4} \pm 1 \cdot 10^{0}$	$< 5 \cdot 10^{-6}$
nxt85_Th	$2 \cdot 10^{-3} \pm 5 \cdot 10^{-1}$	0.4 ± 0.8	$6 \cdot 10^{-6} \pm 4 \cdot 10^{-1}$	$(0.10 \pm 0.01)\cdot 10^{-6}$
lmfes_U	$6 \cdot 10^{-3} \pm 2 \cdot 10^{1}$	$4 \cdot 10^{-3} \pm 6 \cdot 10^{1}$	$3 \cdot 10^{1} \pm 1 \cdot 10^{2}$	$(10.570 \pm 0.370)\cdot 10^{-3}$
lmfes_Th	10 ± 50	$9 \cdot 10^{-4} \pm 3 \cdot 10^{1}$	$7 \cdot 10^{-4} \pm 1 \cdot 10^{1}$	$(6.530 \pm 0.120)\cdot 10^{-3}$

Table 6.9: The activities obtained from the best 83-parameter fit of the MC to the high-Rn data. See Section 6.5 for more details.

MC Fit Group	Activity from Fit to High-Rn Data [Bq/kg]			Expected Activity [Bq/kg]
	S3D2	S3D4	S3D5	
solder_Rn	$(2.4 \pm 0.8)\cdot10^{3}$	$(3 \pm 3)\cdot10^{3}$	$(2 \pm 10)\cdot10^{2}$	-
solder_Th	$1 \cdot 10^{-2} \pm 2 \cdot 10^{2}$	$(2 \pm 6)\cdot10^{2}$	$(1 \pm 3)\cdot10^{2}$	-
solder_Pb	$(1.7 \pm 1.0)\cdot10^{4}$	$2 \cdot 10^{0} \pm 3 \cdot 10^{4}$	$(1.6 \pm 0.8)\cdot10^{4}$	500–57,000
sensSc_U	$2 \cdot 10^{-3} \pm 2 \cdot 10^{1}$	$2 \cdot 10^{-2} \pm 6 \cdot 10^{1}$	$5 \cdot 10^{-3} \pm 3 \cdot 10^{1}$	$< 5 \cdot 10^{-3}$
sensSc_Th	$3 \cdot 10^{-3} \pm 9 \cdot 10^{0}$	$5 \cdot 10^{-4} \pm 3 \cdot 10^{1}$	$2 \cdot 10^{-2} \pm 1 \cdot 10^{1}$	$(13 \pm 4)\cdot10^{-3}$
sensSc_Co	2 ± 4	$6 \cdot 10^{0} \pm 1 \cdot 10^{1}$	$2 \cdot 10^{-1} \pm 6 \cdot 10^{0}$	-
peek_U	$2 \cdot 10^{-3} \pm 2 \cdot 10^{1}$	$(2 \pm 1)\cdot10^{2}$	$2 \cdot 10^{-2} \pm 2 \cdot 10^{1}$	$< 63 \cdot 10^{-3}$
peek_Th	$2 \cdot 10^{-3} \pm 6 \cdot 10^{0}$	$6 \cdot 10^{-2} \pm 2 \cdot 10^{1}$	$2 \cdot 10^{-2} \pm 8 \cdot 10^{0}$	$< 16 \cdot 10^{-4}$
nxt85_U	$4 \cdot 10^{-4} \pm 1 \cdot 10^{0}$	$2 \cdot 10^{-4} \pm 8 \cdot 10^{-1}$	5 ± 3	$< 5 \cdot 10^{-6}$
nxt85_Th	$2 \cdot 10^{-4} \pm 4 \cdot 10^{-1}$	$10 \cdot 10^{-6} \pm 4 \cdot 10^{-1}$	$3 \cdot 10^{-4} \pm 6 \cdot 10^{-1}$	$(0.10 \pm 0.01)\cdot10^{-6}$
lmfes_U	$6 \cdot 10^{-4} \pm 3 \cdot 10^{1}$	$2 \cdot 10^{-3} \pm 2 \cdot 10^{1}$	$8 \cdot 10^{-3} \pm 2 \cdot 10^{1}$	$(10.570 \pm 0.370)\cdot10^{-3}$
lmfes_Th	$2 \cdot 10^{-3} \pm 10 \cdot 10^{0}$	$5 \cdot 10^{-4} \pm 10 \cdot 10^{0}$	$2 \cdot 10^{-2} \pm 1 \cdot 10^{1}$	$(6.530 \pm 0.120)\cdot10^{-3}$

Table 6.10: The count rates in the fit region (100–1674 keV) as seen in: (1) each detector's high-Rn energy spectrum and (2 & 3) the sum of each detector's scaled MC-generated energy spectra. Each MC-generated energy spectrum is scaled by the activity which resulted in the best fit to the high-Rn data with the (2) 83-parameter fit and (3) the 1-parameter.

Detector	Count Rate in Fit Region [cts/ton/yr]		
	Data	83-par MC	1-par MC
S1D2	2.86 (5)$\cdot 10^9$	2.86 (5)$\cdot 10^9$	2.94 (5)$\cdot 10^9$
S1D3	2.46 (4)$\cdot 10^9$	2.46 (4)$\cdot 10^9$	2.01 (3)$\cdot 10^9$
S3D1	2.45 (4)$\cdot 10^9$	2.48 (4)$\cdot 10^9$	2.58 (4)$\cdot 10^9$
S3D2	3.16 (5)$\cdot 10^9$	3.15 (5)$\cdot 10^9$	2.70 (4)$\cdot 10^9$
S3D4	2.84 (5)$\cdot 10^9$	2.84 (5)$\cdot 10^9$	3.00 (5)$\cdot 10^9$
S3D5	2.39 (4)$\cdot 10^9$	2.38 (4)$\cdot 10^9$	3.16 (5)$\cdot 10^9$
Value of Minimized NLL		-56,003	-55,555

6.7 Discussion of Results and Future Work

At this time it is important to recall the differences between the PC and the DEMONSTRATOR as listed in Section 1.3. These differences are expected to account for the majority of the backgrounds seen by the detectors of the PC. Section 1.3 lists the differences between the PC and the DEMONSTRATOR. The following is a (repeated) list of the differences and how they are accounted for in the PC background model and the subsequent MC-fitting routine(s).

1. **Temperature Sensor Assemblies** Five temperature sensors are installed in the PC (and are not installed in the DEMONSTRATOR). The temperature sensors are soldered to their cabling. A clamp made of PEEK and a stainless steel screw are used to clamp the sensor to the string to monitor temperature stability and cooling. The temperature sensors, solder, cabling and SS screws are all un-assayed. The material PEEK – which is what the clamps are made of – has been assayed

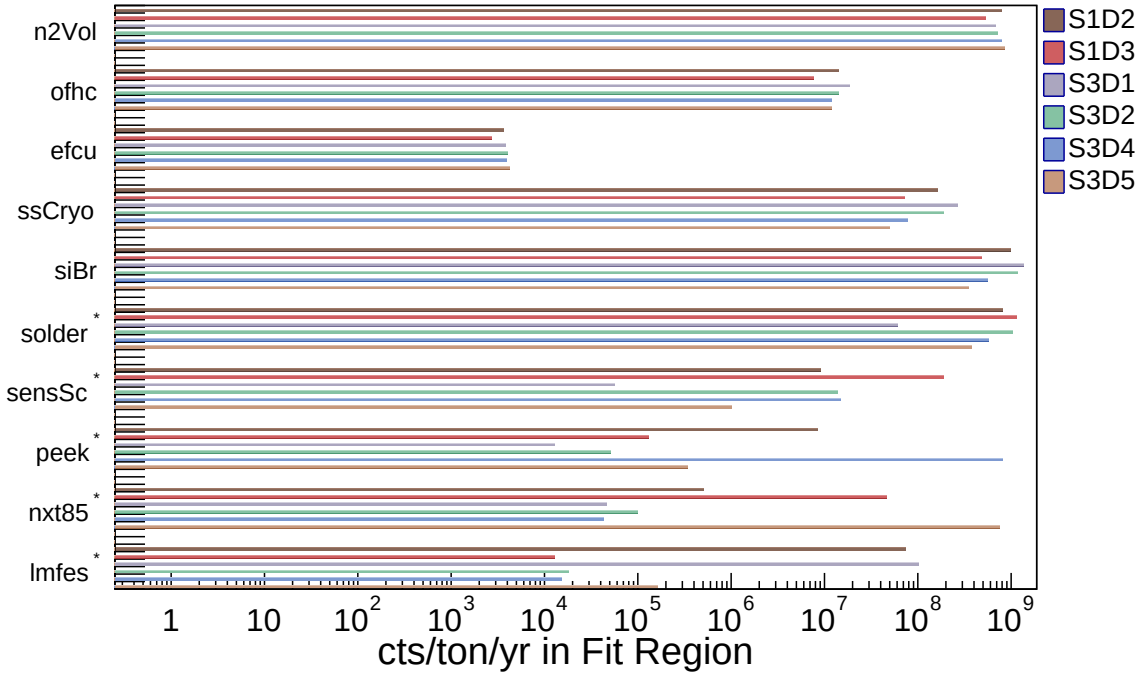

Figure 6.8: The count rate in the fit region (100–1674 keV) for each MC-fit group, as seen by each detector. To calculate the count rate, each MC-generated energy spectrum is scaled by the activity which resulted in the best 83-parameter fit to the high-Rn data. Fit groups with the same parts (but different radioactive nuclide) are grouped together. Fit groups whose associated fit parameters are detector-dependent are annotated with an asterisk. See text for more details.

and is known to have a relatively high amount of natural radioactivity compared to the preferred polymer, NXT-85, that are being used in the DEMONSTRATOR.

- **PC Bkgd Model** Three components of the temperature sensor assemblies are in the PC background model: the PEEK clamp, the SS screws and the solder.
- **MC Fit to Data** Each of these components has its own detector-dependent MC-fit group.

2. **OFHC Cu** Several parts in the PC are made of OFHC Cu, while their DEMONSTRATOR counterparts are made of UGEFCu. Also, the time that the OFHC Cu parts spent above ground was not tightly controlled and therefore the cosmogenically-induced radioactivity (e.g. ^{60}Co) in the OFHC Cu is expected to be higher.

   - **PC Bkgd Model** In MAGE there is no difference between UGEFCu and OFHC Cu, Therefore all copper components are modeled as the same material: OFHC Cu.
   - **MC Fit to Data** The OFHC Cu parts have their own detector-independent MC-fit group (as do the UGEFCu parts). One of the fit groups is for possible ^{60}Co activity in the OFHC Cu.

3. **SS** Several parts in the PC are made of SS, while their DEMONSTRATOR counterparts are made of UGEFCu. These SS parts include some of the cryostat clamping hardware and some of the outer copper shield fasteners.

   - **PC Bkgd Model** Only the SS parts of the cryostat clamping hardware are included in the background model.
   - **MC Fit to Data** These cryostat SS parts have their own detector-independent MC-fit group.

4. **Silicon Bronze** Some parts of the PC cryostat clamping hardware are made of silicon bronze, while their DEMONSTRATOR counterparts are made of UGEFCu.

    - **PC Bkgd Model** The parts made of silicon bronze are included in the PC background model.
    - **MC Fit to Data** These parts have their own detector-independent MC-fit group.

5. **Metal Spinning** The top and bottom cryostat lids of the PC were fabricated via metal spinning. The top and bottom cryostat lids of the DEMONSTRATOR were not fabricated this way as there is no known assay on the procedure.

    - **PC Bkgd Model** The top and bottom lids of the PC are modeled like all other copper parts.
    - **MC Fit to Data** The top and bottom lids are included in the MC-fit group for OFHC Cu. This is not ideal; since there is no assay on their fabrication process they could have a higher activity than the other OFHC Cu components, so they should have their own MC-fit group.

6. **Radon Purge** The radon purge system is not in its final state and therefore higher levels of ^{222}Rn are expected in the inner cavity volume (than for the DEMONSTRATOR).

    - **PC Bkgd Model** The nitrogen gas in the inner cavity volume is modeled for possible ^{222}Rn activity.
    - **MC Fit to Data** The inner cavity volume has its own detector-independent MC-fit group.

7. **Passive Shielding** The inner copper shield is not installed in the PC. The poly shield and muon veto are only partially installed. Additional shielding is required

where the cross arm tube penetrates the passive shielding and is not installed in the PC. Additionally there is SS hardware in the outer copper shield of the PC.

- **PC Bkgd Model** The relevant components of the poly shield and muon veto are removed from the PC geometry in MaGe, as well as the additional shielding at the cross arm tube. The inner copper shield is also removed and the inner cavity volume is expanded to account for the missing shield. Only components inside of the passive shield are included in the PC background model so the effect that the missing passive shielding has on the detectors' backgrounds is not included in the model. The SS hardware in the outer copper shield is not included in the PC background model.
- **MC Fit to Data** n/a

8. **Gasket** The PC cryostat is vacuum-sealed with a Viton gasket rather than with a cleaner parylene film that is being used in the Demonstrator.

   - **PC Bkgd Model** The gasket is not included in the PC background model.
   - **MC Fit to Data** n/a

9. **Cables** The signal cables in the PC are known to be higher in radioactivity than the cables in the Demonstrator.

   - **PC Bkgd Model** The cables are not included in the PC background model.
   - **MC Fit to Data** n/a

10. **Thermosyphon Supports** The thermosyphon supports are made of PEEK, while their Demonstrator counterparts are made of a cleaner polymer.

    - **PC Bkgd Model** The support are not included in the PC background model.

- **MC Fit to Data** n/a

11. **Detector Cosmogenics** Unlike the detectors of the DEMONSTRATOR, the time that the detectors of the PC spent above ground was not tightly controlled. Therefore the cosmogenically-induced radioactivity in the detectors is expected to be higher than for the detectors of the DEMONSTRATOR.

    - **PC Bkgd Model** Possible cosmogonies in the detectors are not included in the PC background model.
    - **MC Fit to Data** n/a

It is no coincidence that many of the MC-fit groups are a reflection of the differences between the PC and the DEMONSTRATOR. The PC background model focuses on the key differences between the PC and the DEMONSTRATOR since it is these differences that are expected to contribute the most to the backgrounds. There are six MC-fit groups that correspond to materials that are also used in the DEMONSTRATOR: efcu_U, efcu_Th, nxt85_U, nxt85_Th, lmfes_U and lmfes_Th. These fit groups are expected to have a negligible contribution to the PC backgrounds because the parts in the groups are made of radio-pure materials. Furthermore, while PEEK is known to not be as radio-pure as its polymer counterpart, NXT-85, it is still relatively clean. The PEEK parts that are included in the background model are the temperature sensor clamps. The clamps are in close proximity to the temperature sensor screws (made of SS) and the solder, which are expected to have much higher levels of radioactivity than the PEEK. Therefore, the PEEK MC-fit groups (peek_U, peek_Th) are also expected to have a negligible contribution to the PC backgrounds. Indeed, many of these MC-fit groups do have associated activities that are consistent with zero (as seen in Tables 6.3–6.5; 6.7–6.9). This can be better seen in Tables 6.11–6.13 where – for better comprehension

– those activities that are consistent with zero for both the low-background and high-Rn fits are omitted. At times, the activity from one of the fits is consistent with zero while the other is not; for these cases, the activity that is consistent with zero is taken to be an upper limit where the value of the upper limit is the activity error. Table 6.11 contains the activities associated with the detector-independent parameters and Tables 6.12 and 6.13 contain the activities associated with the detector-dependent parameters. The 1-parameter fit to the high-Rn data only has one fit group and is therefore only listed in Table 6.11. The detector-dependent activities are split into two tables; Table 6.13 contains the activities for fit groups that are expected to contribute a negligible amount to the background and Table 6.12 contains the activities for the other fit groups. In the detector-dependent tables the detectors are no longer listed in the standard order that is used throughout this work. They are listed in decreasing order by their efficiency for detecting radioactivity in the temperature sensor solders. The expected activity for ^{210}Pb in the solder is much greater than the other expected activities, therefore it is desirable to compare detector-dependent activities with respect to this efficiency. As a reminder to the location of the temperature sensors, Fig. 6.9 is a visualization of the PC strings as built in MaGe with the temperature sensor assemblies circled in yellow.

There are several things to note regarding Tables 6.11–6.13. The first thing to note is with regards to the ^{222}Rn in the inner cavity volume (i.e. MC-fit group n2Vol_Rn). For the 1-parameter high-Rn fit it is assumed that all of the backgrounds observed from the PC come from ^{222}Rn in the inner cavity volume. This is of course an exaggeration and therefore, when comparing the 1-parameter and 83-parameter high-Rn fits, a slight difference is expected between the activities for the n2Vol_Rn fit group. However the activities in Table 6.11 differ greatly. While that is concerning, what is truly troublesome is that the ^{222}Rn is clearly being distributed throughout the other components in the

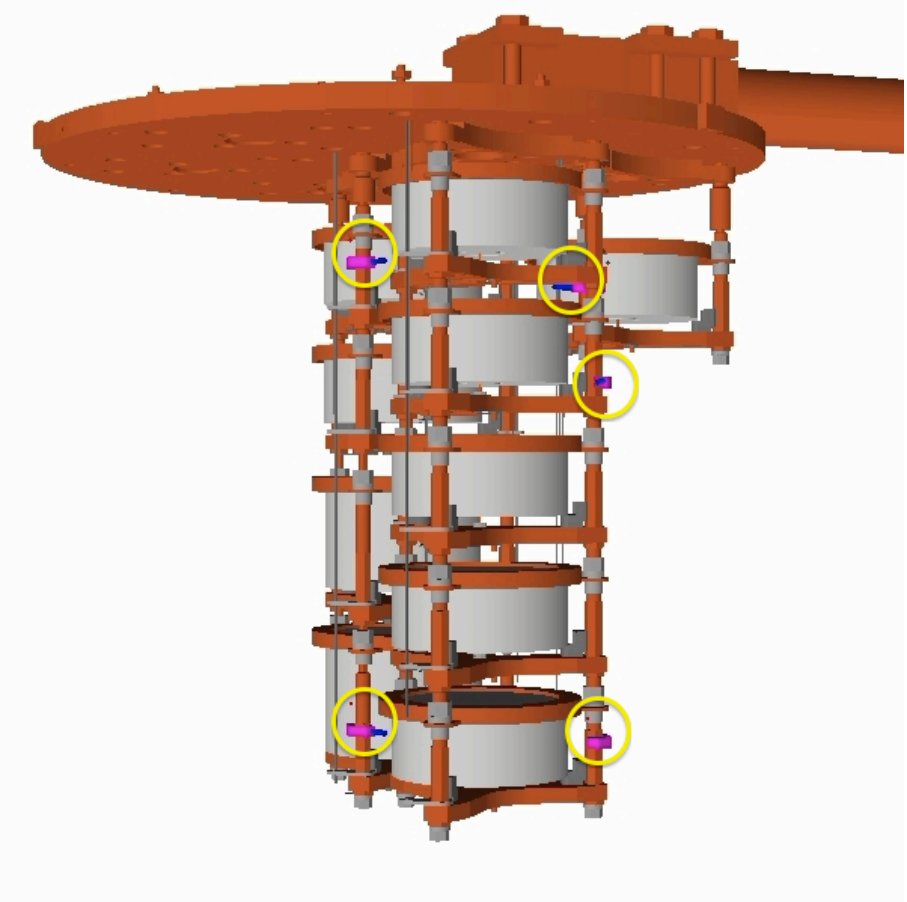

Figure 6.9: A visualization of the PC detectors as built in the MaGe geometry with the temperature sensor assemblies circled in yellow. The PEEK clamps are colored pink and the SS screws are colored blue. The solder masses are colored red but are barely visible as they are extremely small in size; they are located above the clamps. In the foreground is String 3 which contains five detectors. In the background to the left is String 1 which contains four detectors. In the background to the right is String 2 which contains one detector. The detectors in the strings are numbered in increasing value as one moves away from the coldplate, with SxD1 being the detector closest to the coldplate.

Table 6.11: The activities obtained from the best fit of the MC to the low-background and high-Rn data. A fit group is not listed if its associated activity is consistent with zero for both of the fits. The detectors are listed in decreasing order by their efficiency for detecting radioactivity in the temperature sensor solders. Also listed is the total counts in the fit region in the low-background and high-Rn data. See text for more details.

MC Fit Group	Activity [Bq/kg] (Low-Background)	Activity [Bq/kg] (83-par; High-Rn)	Activity [Bq/m^3] (1-par; High-Rn)
n2Vol_Rn [Bq/m^3]†	0.28 ± 0.02	30 ± 8	112 ± 2
ofhc_Co	$(3 \pm 1)\cdot 10^{-5}$	$(5 \pm 7) \cdot 10^{-4}$	n/a
ssCryo_U	0.104 ± 0.006	2 ± 3	n/a
ssCryo_Th	0.061 ± 0.005	< 0.6	n/a
ssCryo_Co	0.056 ± 0.005	< 0.3	n/a
siBr_U	0.45 ± 0.03	5 ± 1	n/a
siBr_Th	0.14 ± 0.02	< 3	n/a
Cts in Data	24055	23119	23119

† The conversion from Bq/kg to Bq/m^3 uses the density of nitrogen gas as in MaGe: 1.251 mg/cm^3.

Table 6.12: The activities obtained from the best fit of the MC to the low-background and high-Rn data. A fit group is not listed if its associated activity is consistent with zero for both of the fits. The detectors are listed in decreasing order by their efficiency for detecting radioactivity in the temperature sensor solders. Also listed is the total counts in the fit region in the low-background and high-Rn data. See text for more details.

MC Fit Group	Activity [Bq/kg] (Low-Background)	Activity [Bq/kg] (83-par; High-Rn)
S3D5_solder_Pb	720 ± 80	$(1.6 \pm 0.8) \cdot 10^4$
S3D2_solder_Pb	530 ± 100	$(1.7 \pm 1.0) \cdot 10^4$
S3D1_solder_Pb	< 5	$< 1 \cdot 10^4$
S1D2_solder_Pb	2300 ± 300	$(2 \pm 5) \cdot 10^4$
S3D4_solder_Pb	3700 ± 500	$< 3 \cdot 10^4$
S1D3_solder_Pb	7100 ± 900	$< 1 \cdot 10^5$
S3D5_solder_Rn	< 0.4	$(2 \pm 10) \cdot 10^2$
S3D2_solder_Rn	< 0.3	$(2.4 \pm 0.8) \cdot 10^3$
S1D2_solder_Rn	< 5	$(5 \pm 2) \cdot 10^3$
S3D4_solder_Rn	< 2	$(3 \pm 3) \cdot 10^3$
S1D3_solder_Rn	< 10	$(1.6 \pm 0.6) \cdot 10^4$
S3D5_solder_Th	< 0.8	$(1 \pm 3) \cdot 10^2$
S1D2_solder_Th	30 ± 5	< 600
S3D4_solder_Th	21 ± 5	$(2 \pm 6) \cdot 10^2$
S1D3_solder_Th	96 ± 8	< 900
S1D3_sensSc_U		$(2 \pm 4) \cdot 10^2$
S3D5_sensSc_Co	0.1 ± 0.1	< 6
S3D2_sensSc_Co	< 0.01	2 ± 4
S3D1_sensSc_Co	< 0.01	< 6
S1D2_sensSc_Co	1.0 ± 0.3	< 10
S3D4_sensSc_Co	0.8 ± 0.3	< 10
S1D3_sensSc_Co	1.6 ± 0.4	10 ± 20
Cts in Data	24055	23119

Table 6.13: The activities obtained from the best fit of the MC to the low-background and high-Rn data. A fit group is not listed if its associated activity is consistent with zero for both of the fits. Also listed is the total counts in the fit region in the low-background and high-Rn data. See text for more details.

MC Fit Group	Activity [Bq/kg] (Low-Background)	Activity [Bq/kg] (83-par; High-Rn)
S3D4_peek_U	0.7 ± 0.2	$(2 \pm 1) \cdot 10^2$
S1D3_peek_U	4.4 ± 0.4	< 80
S3D5_nxt85_U	0.049 ± 0.008	5 ± 3
S3D2_nxt85_U	$(3 \pm 7) \cdot 10^{-3}$	< 1
S1D2_nxt85_U	0.019 ± 0.005	< 0.9
S3D5_nxt85_Th	0.024 ± 0.006	< 0.6
S1D3_nxt85_Th	$< 3 \cdot 10^{-4}$	0.4 ± 0.8
S1D2_lmfe_Th		10 ± 50
Cts in Data	24055	23119

background model. This can be seen in Tables 6.11–6.13 if one compares the ^{238}U and ^{222}Rn activities between the low-background fit and the 83-parameter high-Rn fit. The effect is especially noticeable with the activities associated with the detector-dependent solder_Rn fit groups. The reason this is concerning is that if an increase in the activity of n2Vol_Rn causes an increase in the other ^{238}U and ^{222}Rn groups, it is reasonable to imagine that if there was a "hot spot" in the PC that the activity associated with the hot spot would erroneously distribute itself amongst the other components in the geometry. (The term "hot spot" refers to a part – or a group of parts – that might be significantly higher in activity than the other components of the geometry.) What one concludes from this is that there is a degeneracy between the MC-generated energy spectra for the different fit groups. Section D.1 contains the MC-generated energy spectra for S3D2. To better compare the spectrum from one fit group to another, the

spectra are normalized so that the sum of their bin contents (in the fig range of 100–1674 keV) equals one. There is clearly some degeneracy between some of the fit groups' spectra. In future work, the MC-fit groups should be carefully considered and possibly rearranged. The MC-fit groups for this work are chosen so that all parts in a group are made of the same material and their detection efficiencies are roughly the same. The criteria that all parts in a group must be the same material must be true to satisfy the equations in Section A.4, so in future work that must not change. However rather than group parts by their efficiency, components could be grouped post-simulations so that there is not too much degeneracy between the MC-generated energy spectra of the fit groups. Possible degeneracy between two spectra could even be determined quantitatively through the implementation of a Kolmogorov-Smirnov test (KS test) on the MC-generated energy spectra.

A further issue that can be seen in Tables 6.11–6.13 is with regards to the activity uncertainties. At the bottom of each of the three tables the total counts in the fit region in the low-background and high-Rn data are listed. The total counts in the low-background and high-Rn data are roughly the same, and therefore one might expect that the activity uncertainties from the 83-parameter low-background fit should be comparable to those from the 83-parameter high-Rn fit. However this is not the case. For example, the ^{222}Rn activity from the low-background fit is 0.28 ± 0.02 Bq/m^3, giving a 7% uncertainty. However, the ^{222}Rn activity from the 83-parameter high-Rn fit is 30 ± 8 Bq/m^3, giving a 27% uncertainty. Given that the parameter uncertainties are inconsistent, it is reasonable to question the interpretation of the quoted activity uncertainties in Tables 6.11–6.13. It is possible that these inconsistencies are both degeneracies in the spectral shape of the materials being simulated and inadequacies in the overall model. Regardless, in future work the activity uncertainties should be carefully considered and a similar systematics test should be done to test the reliability

of the uncertainties.

Another point of concern with the results presented in Tables 6.12 and 6.13 is with regards to the ^{210}Pb in the temperature sensor solders. The ^{210}Pb activities, as listed in Tables 6.12 and 6.13 should be the same for all of the detectors. However that is not what is being observed, and in fact one might conclude that they are instead increasing. Now, the efficiencies are calculated based on the assumption that the ^{210}Pb activity in each of the temperature sensor solders is the same, which is not necessarily true. To determine if the activities from the fit are consistent with one (or more) temperature sensor solders having a higher (or lower) activity than the others, consider the following. If one assumes that each of the five temperature sensor solders has a unique ^{210}Pb activity then

$$A_j = \frac{\sum\limits_{\alpha} n_{j,\alpha} A_\alpha}{\sum\limits_{\alpha} n_{j,\alpha}} \tag{6.14}$$

where A_j is the activity of ^{210}Pb in the temperature sensor solders as found from the fit to the j-th detector's energy spectrum, $n_{j,\alpha}$ is the number of events seen by the j-th detector from ^{210}Pb activity in the α-th temperature sensor solder and A_α is the actual ^{210}Pb activity of the α-th temperature sensor solder. The activities from the fit, A_j, are known and are listed in Table 6.12. Therefore to find the actual ^{210}Pb activities in the temperature sensor solders (based on the activities that yielded the best MC-fit to the data), the augmented matrix Λ (Eq. 6.15) must simply be row reduced. In matrix Λ the entries in the right-most column are the activities from the best MC-fit to the low-background data and the coefficients are the ratio $n_{j,\alpha}/\sum_\alpha n_{j,\alpha}$. Detector S3D1 is not included in the matrix since its ^{210}Pb activity of the solder found from the fit is an

upper limit rather than a value.

$$\Lambda = \left[\begin{array}{ccccc|c} 0.177 & 0.048 & 0.305 & 0.447 & 0.023 & 2300 \\ 0.085 & 0.247 & 0.146 & 0.409 & 0.113 & 7100 \\ 0.039 & 0.010 & 0.087 & 0.856 & 0.009 & 530 \\ 0.039 & 0.350 & 0.054 & 0.083 & 0.474 & 3700 \\ 0.004 & 0.083 & 0.004 & 0.007 & 0.902 & 720 \end{array}\right] \tag{6.15}$$

Matrix Λ reduces to

$$\Lambda = \left[\begin{array}{ccccc|c} 1 & 0 & 0 & 0 & 0 & -2.1 \cdot 10^6 \\ 0 & 1 & 0 & 0 & 0 & 5.9 \cdot 10^4 \\ 0 & 0 & 1 & 0 & 0 & 1.3 \cdot 10^6 \\ 0 & 0 & 0 & 1 & 0 & -3.3 \cdot 10^4 \\ 0 & 0 & 0 & 0 & 1 & -5.9 \cdot 10^2 \end{array}\right]. \tag{6.16}$$

Equation 6.16 implies that three of the five temperature sensor solders have a negative ^{210}Pb activity. This is of course unphysical and therefore the ^{210}Pb activities found from the low-background fit are inconsistent with one another.

In future work the activities of the temperature sensor solders can be forced to be consistent with one another, and in fact this can be done for all the detector-dependent parameters. To understand how this can be implemented, consider the MC-fit group for ^{210}Pb activity in the temperature sensor solders. In this work, the parameters corresponding to this fit group are made detector-dependent to account for the fact that the solders are localized point-like sources and therefore each detector's efficiency for detecting activity in the solders varies greatly. However, as seen in Eq. 6.16, by making the parameters detector-dependent the resulting activities are inconsistent. In future work, rather than make all of the temperature sensor solders one fit group, each

mass of solder could be its own fit group. There are five temperature sensors, so this would result in five solder fit groups (per nuclide). Then, these fit groups could be made common parameters to force consistency throughout all the detectors. As stated before, this could be done for all the detector-dependent parameters in future fitting.

There are numerous inaccuracies with the geometry of the PC in MaGe 5.3.1. Any of these inaccuracies could greatly affect the fit results presented here. The accuracy of the MaGe geometry and its effect on the fitting routine could be tested. Simulations could be done of the ^{228}Th line source in the PC. Then the data taken from the line source could be fit with the MC-generated energy spectra from the simulations. From the fit, the activity of the ^{228}Th line source could be found and compared to the known activity. This would validate not only the PC geometry in MaGe but the MC-fitting routine described in this work. Furthermore, similar to the systematics test done with the high-Rn data, the ^{228}Th data could be fit twice. One fit could be done where there would just be one common parameter that would be associated with the activity of the line source. And then another fit could be done that would include all the components of the PC background model in addition to the components involving the line source. This test was not in the scope of this work as the calibration system geometry in MaGe was not compatible with the PC geometry at the time. However recent updates have been made to the calibration system geometry in MaGe for the Demonstrator and therefore it could be implemented into the PC geometry with little effort. This test could prove to be extremely valuable in diagnosing the issues with the PC background model and the fitting routine presented in this work.

Lastly, Table 6.13 contains the activities for the fit groups which are expected to have a negligible contribution to the observed backgrounds. If there truly was a part that was contaminated with higher levels of radioactivity than expected, an increased level of both the ^{238}U and ^{232}Th activities is expected. This is true for only one fit

group in Table 6.13: S3D5_nxt85_U/Th. As a reminder, the parts made from NXT-85 are the center bushings, crystal insulators and HV Nuts. S3D5 sits the lowest (with respect to the coldplate) of all the detectors in the PC. The center bushing for S3D5 sits directly below the detector and therefore no other detector has a direct line-of-sight to the part. Therefore it is possible that the bushing has an increased amount of natural radioactivity which is only visible to S3D5. This could also be plausible for S3D5's crystal insulators and/or HV Nuts, however given that one or two detectors have a direct line-of-sight to these parts it is not as likely of a scenario. All other activities listed in Table 6.13 are most likely erroneous given that the ^{238}U (^{232}Th) fit groups in the table are not accompanied by their associated ^{232}Th (^{238}U) fit group.

CHAPTER 7: CONCLUSIONS

In conclusion, this dissertation has identified several issues with the PC background model and fitting its MC-generated energy spectra to data. MAJORANA collaborators will continue to work on the PC background model and aim to address these issues in the near future. On a positive note, the failures and successes of the PC background model have helped the MAJORANA collaboration identify possible future issues with the DEMONSTRATOR background model. Furthermore, through the development of the PC background model many simulation and analysis tools were developed that will be used and extended for work with the DEMONSTRATOR. The PC has now been decommissioned and partially disassembled, thereby giving MAJORANA collaborators an opportunity to assay the components that are predicted to have been dominant contributions to the PC backgrounds (e.g. the temperature sensors and the SS and silicon bronze components). This should prove to be extremely valuable in validating the PC background model and the fitting routine. The data used in this thesis are a small subset of the entire data taken with the PC. It would most certainly be beneficial to extend upon the data set used here to gain better statistics for comparing the background model to data. Furthermore, there have been additional calibration runs with the ^{228}Th line source. It would be beneficial to use the multi-peak fitting routine with these ^{228}Th data sets to further investigate how the energy response function of the detectors might change over time. Furthermore, Chapters 3 and 6 discuss in detail suggested future work based on the results of this dissertation.

The first cryostat of the DEMONSTRATOR is currently taking data and the second cryostat is well on its way. The coming period will be an exciting time for the

MAJORANA collaboration and the $0\nu\beta\beta$ community.

APPENDIX A: RELEVANT CALCULATIONS

A.1 For the case of Fitting a Single Peak

A.1.1 Peak Centroid

The peak's centroid depends, not only on the centroid of the gaussian, but also the centroid of the tail. By definition, the peak's centroid — the expectation value of the signal — is

$$M = \int_{-\infty}^{+\infty} x \, \mathrm{PDF}_{\mathrm{signal}} \, dx = \frac{\int_{-\infty}^{+\infty} x \ (\mathrm{gaus} + \mathrm{tail}) \ dx}{\int_{-\infty}^{+\infty} (\mathrm{gaus} + \mathrm{tail}) \ dx} \, . \tag{A.1}$$

Similarly, the centroid of the gaussian and tail component is

$$M_f = \frac{\int_{-\infty}^{+\infty} x \, f(x) \, dx}{\int_{-\infty}^{+\infty} f(x) \, dx} = \frac{\int_{-\infty}^{+\infty} x \, f(x) \, dx}{A_f} \, , \tag{A.2}$$

where $f(x)$ is the gaussian or tail component, M_f is the centroid of the component, and A_f is the area of the component. Substituting Eq. A.2 into Eq. A.1, Eq. A.1 simplifies to

$$M = \frac{M_{\mathrm{gaus}} \cdot A_{\mathrm{gaus}} + M_{\mathrm{tail}} \cdot A_{\mathrm{tail}}}{A_{\mathrm{gaus}} + A_{\mathrm{tail}}} \, . \tag{A.3}$$

The centroid of the gaussian is μ, as seen in Eq. A.4.

$$\begin{aligned} M_{\mathrm{gaus}} &= \int_{-\infty}^{+\infty} x \, \mathrm{PDF}_{\mathrm{gaus}} \, dx \\ &= \int_{-\infty}^{+\infty} \frac{x}{\sigma\sqrt{2\pi}} \, \exp\left[-\left(\frac{x-\mu}{\sigma\sqrt{2}} \right)^2 \right] dx \\ &= \left[\frac{\mu}{2} \, \mathrm{erf}\left(\frac{x-\mu}{\sigma\sqrt{2}} \right) - \frac{\sigma}{\sqrt{2\pi}} \, \exp\left[-\left(\frac{x-\mu}{\sigma\sqrt{2}} \right)^2 \right] \right]_{-\infty}^{+\infty} \\ &= \left(\frac{\mu}{2} - 0 \right) - \left(-\frac{\mu}{2} - 0 \right) \\ &= \mu \end{aligned} \tag{A.4}$$

The centroid of the tail is $(\mu - \tau)$, as seen in Eq. A.5.

$$\begin{aligned}
M_{\text{tail}} &= \int_{-\infty}^{+\infty} x \, \text{PDF}_{\text{tail}} \, dx \\
&= \int_{-\infty}^{+\infty} \frac{x}{2\tau} \exp\left(\frac{x-\mu}{\tau} + \frac{\sigma^2}{2\tau^2}\right) \text{erfc}\left(\frac{x-\mu}{\sigma\sqrt{2}} + \frac{\sigma}{\tau\sqrt{2}}\right) dx \\
&= \left[\frac{1}{2} \text{erf}\left(\frac{x-\mu}{\sigma\sqrt{2}}\right)(\mu - \tau) - \frac{\sigma}{\sqrt{2\pi}} \exp\left[-\left(\frac{x-\mu}{\sigma\sqrt{2}}\right)^2\right]\right. \\
&\qquad \left. + \frac{x-\tau}{2} \exp\left(\frac{x-\mu}{\tau} + \frac{\sigma^2}{2\tau^2}\right) \text{erfc}\left(\frac{x-\mu}{\sigma\sqrt{2}} + \frac{\sigma}{\tau\sqrt{2}}\right)\right]_{-\infty}^{+\infty} \\
&= \left(\frac{1}{2}(\mu - \tau) - 0 + 0\right) - \left(-\frac{1}{2}(\mu - \tau) - 0 + 0\right) \\
&= \mu - \tau \, . \qquad \text{(A.5)}
\end{aligned}$$

The area of the gaussian is $(1 - H_{\text{tail}})$ and the area of the tail is H_{tail}. Thus the peak centroid is

$$M = \mu - \tau H_{\text{tail}} \, . \qquad \text{(A.6)}$$

A.1.2 Peak Variance

Like the centroid, the peak's variance depends on the variance of the gaussian and the variance of the tail. The peak's variance, by definition, is

$$\begin{aligned}
\Sigma^2 &= \int_{-\infty}^{+\infty} (x - M)^2 \, \text{PDF}_{\text{signal}} \, dx \\
&= \left(\int_{-\infty}^{+\infty} x^2 \, \text{PDF}_{\text{signal}} \, dx\right) - M^2
\end{aligned} \qquad \text{(A.7)}$$

To calculate the peak's variance first consider only the integral of the gaussian

portion of the PDF.

$$
\begin{aligned}
&\int_{-\infty}^{+\infty} x^2 \, \mathrm{PDF}_{\mathrm{gaus}} \, dx \\
&= \int_{-\infty}^{+\infty} \frac{x^2}{\sigma\sqrt{2\pi}} \exp\left[-\left(\frac{x-\mu}{\sigma\sqrt{2}}\right)^2\right] dx \\
&= \left[\frac{1}{2}\left(\mu^2+\sigma^2\right)\mathrm{erf}\left(\frac{x-\mu}{\sigma\sqrt{2}}\right) - \frac{\sigma\left(\mu+x\right)}{\sqrt{2\pi}} \exp\left[-\left(\frac{x-\mu}{\sigma\sqrt{2}}\right)^2\right]\right]_{-\infty}^{+\infty} \\
&= \left(\frac{1}{2}\left(\mu^2+\sigma^2\right)-0\right) - \left(-\frac{1}{2}\left(\mu^2+\sigma^2\right)-0\right) \\
&= \mu^2+\sigma^2 \qquad \text{(A.8)}
\end{aligned}
$$

Similarly, the integral of the tail portion of the PDF is as follows.

$$
\begin{aligned}
&\int_{-\infty}^{+\infty} x^2 \,\mathrm{PDF}_{\mathrm{tail}}\, dx \\
&= \int_{-\infty}^{+\infty} \frac{x^2}{2\tau} \exp\left(\frac{x-\mu}{\tau} + \frac{\sigma^2}{2\tau^2}\right) \operatorname{erfc}\left(\frac{x-\mu}{\sigma\sqrt{2}} + \frac{\sigma}{\tau\sqrt{2}}\right) dx \\
&= \left[\frac{1}{2}\left(\mu^2 - 2\mu\tau + \sigma^2 + 2\tau^2\right) \operatorname{erf}\left(\frac{x-\mu}{\sigma\sqrt{2}}\right) - \frac{\sigma}{\sqrt{2\pi}}\left(\mu - 2\tau + x\right) \exp\left[-\left(\frac{x-\mu}{\sigma\sqrt{2}}\right)^2\right]\right. \\
&\qquad \left. + \frac{1}{2}\left(2\tau^2 + x^2 - 2\tau x\right) \exp\left(\frac{x-\mu}{\tau} + \frac{\sigma^2}{2\tau^2}\right) \operatorname{erfc}\left(\frac{x-\mu}{\sigma\sqrt{2}} + \frac{\sigma}{\tau\sqrt{2}}\right)\right]_{-\infty}^{+\infty} \\
&= \left(\frac{1}{2}\left(\mu^2 - 2\mu\tau + \sigma^2 + 2\tau^2\right) - 0 + 0\right) - \left(-\frac{1}{2}\left(\mu^2 - 2\mu\tau + \sigma^2 + 2\tau^2\right) - 0 + 0\right) \\
&= \mu^2 - 2\mu\tau + \sigma^2 + 2\tau^2
\end{aligned}
\tag{A.9}
$$

By substituting Eqs. A.8 and A.9 into Eq. A.7 the peak's variance can be found.

$$
\begin{aligned}
\Sigma^2 &= \left(\int_{-\infty}^{+\infty} x^2 \,\mathrm{PDF}_{\mathrm{signal}}\, dx\right) - M^2 \\
&= (1 - H_{\mathrm{tail}}) \int_{-\infty}^{+\infty} x^2 \,\mathrm{PDF}_{\mathrm{gaus}}\, dx \; + H_{\mathrm{tail}} \int_{-\infty}^{+\infty} x^2 \,\mathrm{PDF}_{\mathrm{tail}}\, dx \; - \; M^2 \\
&= (1 - H_{\mathrm{tail}})\left(\mu^2 + \sigma^2\right) + H_{\mathrm{tail}}\left(\mu^2 - 2\mu\tau + \sigma^2 + 2\tau^2\right) - \left(\mu - \tau H_{\mathrm{tail}}\right)^2 \\
&= \sigma^2 - \tau^2 H_{\mathrm{tail}}^2 + 2\tau^2 H_{\mathrm{tail}}
\end{aligned}
\tag{A.10}
$$

A.1.3 Uncertainty of Peak Centroid

The peak centroid, as defined in Eq 3.14, is

$$
M = \mu - \tau H_{\mathrm{tail}}\,. \tag{A.11}
$$

Thus, the uncertainty of the peak centroid is

$$\Delta M = \sqrt{(\Delta\mu)^2 + (\tau\,\Delta H_{\text{tail}})^2 + (H_{\text{tail}}\,\Delta\tau)^2}\,. \tag{A.12}$$

A.1.4 Uncertainty of Peak Variance

The peak variance, as defined in Eq 3.15, is

$$\Sigma^2 = \sigma^2 - \tau^2 H_{\text{tail}}^2 + 2\tau^2 H_{\text{tail}}\,. \tag{A.13}$$

Thus, the uncertainty of the peak variance is

$$\Delta\Sigma = \sqrt{\left(\frac{\sigma}{\Sigma}\,\Delta\sigma\right)^2 + \left(\frac{\tau H_{\text{tail}}\,(2 - H_{\text{tail}})}{\Sigma}\,\Delta\tau\right)^2 + \left(\frac{\tau^2\,(1 - H_{\text{tail}})}{\Sigma}\,\Delta H_{\text{tail}}\right)^2}\,. \tag{A.14}$$

A.2 For the case of Fitting Muliple Peaks

A.2.1 Uncertainty of Peak Centroid

The peak centroid, as defined in Eq 3.19, is

$$M = \frac{-\,(1 + b_\tau\,m_H + m_\tau\,b_H) + \sqrt{(1 + b_\tau\,m_H + m_\tau\,b_H)^2 - 4\,m_\tau\,m_H\,(b_\tau\,b_H - \mu)}}{2\,m_\tau\,m_H}\,. \tag{A.15}$$

Thus, the uncertainty of the peak centroid is

$$\Delta M = \sqrt{\sum_i \left(\frac{\partial M}{\partial i}\Delta i\right)^2 + \sum_i \sum_{\substack{j,\\ i\neq j}} \text{cov}_{ij}\,\frac{\partial M}{\partial i}\,\frac{\partial M}{\partial j}}\,, \tag{A.16}$$

where $i = j = [\, b_\tau,\, b_H,\, m_\tau,\, m_H,\, \mu\,]$. The relevant partial derivatives are below.

$$\frac{\partial M}{\partial b_\tau} = \frac{1}{2\, m_\tau\, m_H} \left(-m_H + \frac{m_H\ (1 + b_\tau\, m_H + m_\tau\, b_H) - 2\, m_\tau\, m_H\, b_H}{\sqrt{(1 + b_\tau\, m_H + m_\tau\, b_H)^2 - 4\, m_\tau\, m_H\, (b_\tau\, b_H - \mu)}} \right) \tag{A.17}$$

$$\frac{\partial M}{\partial b_H} = \frac{1}{2\, m_\tau\, m_H} \left(-m_\tau + \frac{m_\tau\ (1 + b_\tau\, m_H + m_\tau\, b_H) - 2\, m_\tau\, m_H\, b_\tau}{\sqrt{(1 + b_\tau\, m_H + m_\tau\, b_H)^2 - 4\, m_\tau\, m_H\, (b_\tau\, b_H - \mu)}} \right) \tag{A.18}$$

$$\frac{\partial M}{\partial m_\tau} = \frac{m_\tau \frac{\partial N}{\partial m_\tau} - N}{2\, m_\tau^2\, m_H} \tag{A.19}$$

$$\frac{\partial M}{\partial m_H} = \frac{m_H \frac{\partial N}{\partial m_H} - N}{2\, m_\tau\, m_H^2} \tag{A.20}$$

$$\frac{\partial M}{\partial \mu} = \frac{1}{\sqrt{(1 + b_\tau\, m_H + m_\tau\, b_H)^2 - 4\, m_\tau\, m_H\, (b_\tau\, b_H - \mu)}} \tag{A.21}$$

In Eqs. A.19 and A.20, the variables N, $\frac{\partial N}{\partial m_\tau}$ and $\frac{\partial N}{\partial m_H}$ are defined as follows.

$$N = -\,(1 + b_\tau\, m_H + m_\tau\, b_H) + \sqrt{(1 + b_\tau\, m_H + m_\tau\, b_H)^2 - 4\, m_\tau\, m_H\, (b_\tau\, b_H - \mu)} \tag{A.22}$$

$$\frac{\partial N}{\partial m_\tau} = -b_H + \frac{b_H\ (1 + b_\tau\, m_H + m_\tau\, b_H) - 2\, m_H\, (b_\tau\, b_H - \mu)}{\sqrt{(1 + b_\tau\, m_H + m_\tau\, b_H)^2 - 4\, m_\tau\, m_H\, (b_\tau\, b_H - \mu)}} \tag{A.23}$$

$$\frac{\partial N}{\partial m_H} = -b_\tau + \frac{b_\tau\ (1 + b_\tau\, m_H + m_\tau\, b_H) - 2\, m_\tau\, (b_\tau\, b_H - \mu)}{\sqrt{(1 + b_\tau\, m_H + m_\tau\, b_H)^2 - 4\, m_\tau\, m_H\, (b_\tau\, b_H - \mu)}} \tag{A.24}$$

A.2.2 Uncertainty of Peak Variance

The peak variance, as defined in Eq. 3.15, is

$$\Sigma^2 = \sigma^2 - \tau^2 H_{\text{tail}}^2 + 2\tau^2 H_{\text{tail}} \tag{A.25}$$

where $\sigma = \sigma\,(\sigma_0,\, \sigma_1,\, \sigma_2,\, b_\tau,\, b_H,\, m_\tau,\, m_H,\, \mu)$, and τ and $\mathrm{H_{tail}}$ are functions of b_τ, b_H, m_τ, m_H, and μ.

So the uncertainty of the peak variance is

$$\Delta\Sigma = \sqrt{\sum_i \left(\frac{\partial\Sigma}{\partial i}\Delta i\right)^2 + \sum_i \sum_{\substack{j,\\ i\neq j}} \mathrm{cov}_{ij} \frac{\partial\Sigma}{\partial i}\frac{\partial\Sigma}{\partial j}} \tag{A.26}$$

where $i = j = [\,\sigma_0,\, \sigma_1,\, \sigma_2,\, b_\tau,\, b_H,\, m_\tau,\, m_H,\, \mu\,]$. The relevant partial derivates are below.

$$\frac{\partial\Sigma}{\partial\sigma_0} = \frac{\partial\Sigma}{\partial\sigma}\cdot\frac{\partial\sigma}{\partial\sigma_0} = \left(\frac{\sigma}{\Sigma}\right)\left(\frac{\sigma_0}{\sigma}\right) = \frac{\sigma_0}{\Sigma} \tag{A.27}$$

$$\frac{\partial\Sigma}{\partial\sigma_1} = \frac{\partial\Sigma}{\partial\sigma}\cdot\frac{\partial\sigma}{\partial\sigma_1} = \left(\frac{\sigma}{\Sigma}\right)\left(\frac{\sigma_1\, M}{\sigma}\right) = \frac{\sigma_1\, M}{\Sigma} \tag{A.28}$$

$$\frac{\partial\Sigma}{\partial\sigma_2} = \frac{\partial\Sigma}{\partial\sigma}\cdot\frac{\partial\sigma}{\partial\sigma_2} = \left(\frac{\sigma}{\Sigma}\right)\left(\frac{\sigma_2\, M^2}{\sigma}\right) = \frac{\sigma_2\, M^2}{\Sigma} \tag{A.29}$$

$$
\begin{aligned}
\frac{\partial \Sigma}{\partial b_\tau} &= \frac{\partial \Sigma}{\partial \sigma} \cdot \frac{\partial \sigma}{\partial b_\tau} + \frac{\partial \Sigma}{\partial \tau} \cdot \frac{\partial \tau}{\partial b_\tau} + \frac{\partial \Sigma}{\partial H_{\text{tail}}} \cdot \frac{\partial H_{\text{tail}}}{\partial b_\tau} \\
&= \left(\frac{\sigma}{\Sigma}\right) \cdot \frac{\partial \sigma}{\partial b_\tau} + \frac{\tau H_{\text{tail}} \left(2 - H_{\text{tail}}\right)}{\Sigma} \cdot \frac{\partial \tau}{\partial b_\tau} + \frac{\tau^2 \left(1 - H_{\text{tail}}\right)}{\Sigma} \cdot \frac{\partial H_{\text{tail}}}{\partial b_\tau} \\
&= \left(\frac{\sigma}{\Sigma}\right) \cdot \frac{\partial \sigma}{\partial M} \cdot \frac{\partial M}{\partial b_\tau} + \frac{\tau H_{\text{tail}} \left(2 - H_{\text{tail}}\right)}{\Sigma} \cdot \left(1 + m_\tau \frac{\partial M}{\partial b_\tau}\right) + \frac{\tau^2 \left(1 - H_{\text{tail}}\right)}{\Sigma} \cdot \frac{\partial M}{\partial b_\tau} \\
&= \frac{\tau H_{\text{tail}} \left(2 - H_{\text{tail}}\right)}{\Sigma} + \frac{1}{\Sigma} \frac{\partial M}{\partial b_\tau} \left[\frac{1}{2} \sigma_1^2 + \sigma_2^2 M + m_\tau \tau H_{\text{tail}} \left(2 - H_{\text{tail}}\right) + \tau^2 \left(1 - H_{\text{tail}}\right)\right]
\end{aligned}
\tag{A.30}
$$

where $\frac{\partial M}{\partial b_\tau}$ is defined in Eq. A.17. Similarly,

$$
\frac{\partial \Sigma}{\partial b_{H_{\text{tail}}}} = \frac{\tau^2 \left(1 - H_{\text{tail}}\right)}{\Sigma} + \frac{1}{\Sigma} \frac{\partial M}{\partial b_{H_{\text{tail}}}} \left[\frac{1}{2} \sigma_1^2 + \sigma_2^2 M + \tau H_{\text{tail}} \left(2 - H_{\text{tail}}\right) + m_{H_{\text{tail}}} \tau^2 \left(1 - H_{\text{tail}}\right)\right]
\tag{A.31}
$$

where $\frac{\partial M}{\partial b_{H_{\text{tail}}}}$ is defined in Eq. A.18.

$$
\begin{aligned}
\frac{\partial \Sigma}{\partial m_\tau} &= \frac{\partial \Sigma}{\partial \sigma} \cdot \frac{\partial \sigma}{\partial m_\tau} + \frac{\partial \Sigma}{\partial \tau} \cdot \frac{\partial \tau}{\partial m_\tau} + \frac{\partial \Sigma}{\partial H_{\text{tail}}} \cdot \frac{\partial H_{\text{tail}}}{\partial m_\tau} \\
&= \left(\frac{\sigma}{\Sigma}\right) \cdot \frac{\partial \sigma}{\partial m_\tau} + \frac{\tau H_{\text{tail}} \left(2 - H_{\text{tail}}\right)}{\Sigma} \cdot \frac{\partial \tau}{\partial m_\tau} + \frac{\tau^2 \left(1 - H_{\text{tail}}\right)}{\Sigma} \cdot \frac{\partial H_{\text{tail}}}{\partial m_\tau} \\
&= \left(\frac{\sigma}{\Sigma}\right) \cdot \frac{\partial \sigma}{\partial M} \cdot \frac{\partial M}{\partial m_\tau} + \frac{\tau H_{\text{tail}} \left(2 - H_{\text{tail}}\right)}{\Sigma} \cdot \left(M + m_\tau \frac{\partial M}{\partial m_\tau}\right) + \frac{\tau^2 \left(1 - H_{\text{tail}}\right)}{\Sigma} \cdot \frac{\partial M}{\partial m_\tau} \\
&= \frac{M \tau H_{\text{tail}} \left(2 - H_{\text{tail}}\right)}{\Sigma} + \frac{1}{\Sigma} \frac{\partial M}{\partial m_\tau} \left[\frac{1}{2} \sigma_1^2 + \sigma_2^2 M + m_\tau \tau H_{\text{tail}} \left(2 - H_{\text{tail}}\right) + \tau^2 \left(1 - H_{\text{tail}}\right)\right]
\end{aligned}
\tag{A.32}
$$

where $\frac{\partial M}{\partial m_\tau}$ is defined in Eq. A.19. Similarly,

$$\frac{\partial \Sigma}{\partial m_{H_{\text{tail}}}} = \frac{M\tau^2\,(1-H_{\text{tail}})}{\Sigma} + \frac{1}{\Sigma}\,\frac{\partial M}{\partial m_{H_{\text{tail}}}}\left[\frac{1}{2}\,\sigma_1^2 + \sigma_2^2\,M + \tau\,H_{\text{tail}}\,(2-H_{\text{tail}}) + m_{H_{\text{tail}}}\,\tau^2\,(1-H_{\text{tail}})\right] \tag{A.33}$$

And lastly,

$$\begin{aligned}
\frac{\partial \Sigma}{\partial \mu} &= \frac{\partial \Sigma}{\partial \sigma}\cdot\frac{\partial \sigma}{\partial M}\cdot\frac{\partial M}{\partial \mu} + \frac{\partial \Sigma}{\partial \tau}\cdot\frac{\partial \tau}{\partial M}\cdot\frac{\partial M}{\partial \mu} + \frac{\partial \Sigma}{\partial H_{\text{tail}}}\cdot\frac{\partial H_{\text{tail}}}{\partial M}\cdot\frac{\partial M}{\partial \mu} \\
&= \frac{\partial M}{\partial \mu}\left[\left(\frac{\sigma}{\Sigma}\right)\cdot\left(\frac{\frac{1}{2}\sigma_1^2 + \sigma_2^2 M}{\sigma}\right) + \left(\frac{\tau H_{\text{tail}}\,(2-H_{\text{tail}})}{\Sigma}\right)\cdot(m_\tau) + \left(\frac{\tau^2\,(1-H_{\text{tail}})}{\Sigma}\right)\cdot(m_{H_{\text{tail}}})\right] \\
&= \frac{1}{\Sigma}\,\frac{\partial M}{\partial \mu}\left[\frac{1}{2}\sigma_1^2 + \sigma_2^2 M + m_\tau\,\tau\,H_{\text{tail}}\,(2-H_{\text{tail}}) + m_{H_{\text{tail}}}\,\tau^2\,(1-H_{\text{tail}})\right]
\end{aligned} \tag{A.34}$$

where $\frac{\partial M}{\partial \mu}$ is defined in Eq. A.21.

A.2.3 Uncertainty of Sigma

$$\begin{aligned}
(\Delta\sigma)^2 = \left(\frac{\sigma_0}{\sigma}\,\Delta\sigma_0\right)^2 + \left(\frac{\sigma_1\,M}{\sigma}\,\Delta\sigma_1\right)^2 + \left(\frac{\sigma_2\,M^2}{\sigma}\,\Delta\sigma_2\right)^2 + \left(\frac{\frac{1}{2}\sigma_1^2 + \sigma_2^2 M}{\sigma}\right)^2 \Bigg[\left(\frac{\partial M}{\partial b_\tau}\,\Delta b_\tau\right)^2 \\
+ \left(\frac{\partial M}{\partial b_H}\,\Delta b_H\right)^2 + \left(\frac{\partial M}{\partial m_\tau}\,\Delta m_\tau\right)^2 + \left(\frac{\partial M}{\partial m_H}\,\Delta m_H\right)^2 + \left(\frac{\partial M}{\partial \mu}\,\Delta\mu\right)^2 \Bigg]
\end{aligned} \tag{A.35}$$

The partial derivatives of M with respect to b_τ, b_H, m_τ, m_H and μ can be found in Eqs. A.17 – A.21.

A.2.4 Uncertainty of Tau

$$(\Delta\tau)^2 = \left(\left(1 + m_\tau \frac{\partial M}{\partial b_\tau}\right) \Delta b_\tau\right)^2 + \left(\frac{\partial M}{\partial b_H} \Delta b_H\right)^2 + \left(\left(m_\tau \frac{\partial M}{\partial m_\tau} + M\right) \Delta m_\tau\right)^2 + \left(\frac{\partial M}{\partial m_H} \Delta m_H\right)^2 + \left(\frac{\partial M}{\partial \mu} \Delta \mu\right)^2 \quad \text{(A.36)}$$

The partial derivatives of M with respect to b_τ, b_H, m_τ, m_H and μ can be found in Eqs. A.17 – A.21.

A.2.5 Uncertainty of Htail

$$(\Delta H_{\text{tail}})^2 = \left(\left(1 + m_H \frac{\partial M}{\partial b_H}\right) \Delta b_H\right)^2 + \left(\frac{\partial M}{\partial b_\tau} \Delta b_\tau\right)^2 + \left(\left(m_H \frac{\partial M}{\partial m_H} + M\right) \Delta m_H\right)^2 + \left(\frac{\partial M}{\partial m_\tau} \Delta m_\tau\right)^2 + \left(\frac{\partial M}{\partial \mu} \Delta \mu\right)^2 \quad \text{(A.37)}$$

The partial derivatives of M with respect to b_τ, b_H, m_τ, m_H and μ can be found in Eqs. A.17 – A.21.

A.3 Estimation of the Contribution from Missing Components in the PC Background Model

A.3.1 Gasket

The Viton gasket is not in the PC geometry and therefore is not included in the PC background model. The PC cryostat is vacuum-sealed with two Viton gaskets rather than with the cleaner parylene film that is being used in the DEMONSTRATOR. The ^{238}U and ^{232}Th activities of the gasket material are 0.42 and 0.36 Bq/kg respectively. To estimate the contribution the gaskets have to the PC background model, it is assumed the efficiencies for detecting radioactivity in the cryostat top lid are roughly the same as

for the gaskets. Therefore the number of counts the gaskets are expected to contribute to the fit region are

$$cts_{\text{gasket}} = A_{\text{gasket}}\, m_{\text{gasket}}\, \epsilon_{\text{Top Lid}} \tag{A.38}$$

Therefore the rate at which the gaskets are expected to contribute to the PC background is: 29 cts/ROI/ton/yr from the ^{238}U activity, and 27 cts/ROI/ton/yr from the ^{232}Th activity.

A.3.2 Outer Copper Shield

The outer copper shield is not included in the PC background model. Since the inner copper shield is not installed in the PC, to estimate the outer Cu shield's contribution to the PC background model, it is assumed that the efficiencies for detecting radioactivity in the DEMONSTRATOR's inner Cu shield are roughly the same as for the PC's outer Cu shield. Therefore

$$\frac{R_{out}}{A_{out}\, m_{out}} = \frac{R_{in}}{A_{in}\, m_{in}} \tag{A.39}$$

where R_{out} (R_{in}) is the rate at which the outer (inner) Cu shield contributes to the PC (DEMONSTRATOR) background and A_{out} and m_{out} (A_{in} and m_{in}) are the activity and mass of the outer (inner) Cu shield respectively. The DEMONSTRATOR's inner Cu shield is made of UGEFCu and the PC's outer Cu shield is made of OFHC; therefore both A_{in} and A_{out} are known. Furthermore m_{out} is known from the PC background model and m_{in} and R_{in} are known from the DEMONSTRATOR background model.

Therefore the rate at which the inner Cu shield is expected to contribute to the PC background is:

$$R_{in} = \frac{0.033\,\text{cts}}{\text{ROI-ton-yr}} \cdot \frac{1380\,\text{kg}}{1000\,\text{kg}} \cdot \frac{1.25\,\text{Bq/kg}}{0.17\,\text{Bq/kg}} = \frac{0.33\,\text{cts}}{\text{ROI-ton-yr}} \tag{A.40}$$

from the ^{238}U activity. And similarly:

$$R_{in} = \frac{0.259\,\text{cts}}{\text{ROI-ton-yr}} \cdot \frac{1380\,\text{kg}}{1000\,\text{kg}} \cdot \frac{1.1\,\text{Bq/kg}}{0.06\,\text{Bq/kg}} = \frac{6.55\,\text{cts}}{\text{ROI-ton-yr}} \tag{A.41}$$

from the ^{232}Th activity.

A.3.3 Cables

The signal and HV cables are not included in the PC background model. The PC cable geometry in MaGe is outdated; so much so that certain portions of cable conflict with other components in the PC geometry. Therefore several portions of the cable geometry have been removed from the PC geometry and no simulations have been done with what is remaining. The signal cables in the PC are known to be higher in radioactivity than the cables in the Demonstrator; while the ^{238}U and ^{232}Th activities of the cables used in the Demonstrator are 145 and 2.2 μBq/kg respectively, the activities of the cables used in the PC are 12,000 (^{238}U) and 900 (^{232}Th) μBq/kg. To estimate the cables' contribution to the PC background model it is assumed that the efficiencies for detecting radioactivity in the Demonstrator's cables are roughly the same as for the PC's cables. Therefore

$$\frac{R_{PC}}{A_{PC}\,m_{PC}} = \frac{R_{Demo}}{A_{Demo}\,m_{Demo}} \tag{A.42}$$

where R_{PC} (R_{Demo}) is the rate at which the cables contribute to the PC (Demonstrator) background and A_{PC} and m_{PC} (A_{Demo} and m_{Demo}) are the activity and mass of the PC's (Demonstrator's) cables respectively. The ^{238}U and ^{232}Th activities are known for the cables in both the PC and Demonstrator and R_{Demo} is known from the Demonstrator background model. The exact mass of the cables in the PC is not known, however the mass of the cables in the Demonstrator is known from the Demonstrator background model. Since the Demonstrator background

model contains 60 detectors while the PC background model contains 10 detectors, the mass of the cables in the PC is approximated to be one-sixth of the mass in the DEMONSTRATOR.

Therefore the rate at which the cables are expected to contribute to the PC background is:

$$R_{PC} = \frac{0.081\,\text{cts}}{\text{ROI-ton-yr}} \cdot \frac{1}{6} \cdot \frac{12000}{145} = \frac{1.1\,\text{cts}}{\text{ROI-ton-yr}} \tag{A.43}$$

from the ^{238}U activity. And similarly:

$$R_{PC} = \frac{0.004\,\text{cts}}{\text{ROI-ton-yr}} \cdot \frac{1}{6} \cdot \frac{900}{2.2} = \frac{0.3\,\text{cts}}{\text{ROI-ton-yr}} \tag{A.44}$$

from the ^{232}Th activity.

A.4 Technique Used to Simulate Radioactivity in a Group of Components in MaGe

Rather than simulate each individual component of the PC, components that are made of the same material, and are thus expected to have the same levels of radioactivity, are grouped together and simulated as one. When simulating an individual component the location of the primary vertex of the radioactive nuclide is randomly placed within the volume of the component. When simulating a group of components it is first decided in which component to place the primary vertex, and then the location of the primary vertex is decided. To determine which component to use, an array is created that contains the fractional masses of each component in the group. This can be seen in Eq. A.46, where m_i is the mass of the i-th component and m is the total mass of all the components (i.e. $m = \sum_{i=1}^{n} m_i$).

$$array[0] = 0$$

$$array[1] = \frac{m_1}{m}$$

$$array[2] = \frac{m_1 + m_2}{m}$$

$$\ldots$$

$$array[n-1] = \frac{m_1 + m_2 + \ldots + m_{n-1}}{m}$$

$$array[n] = 1 \tag{A.45}$$

$$\tag{A.46}$$

A random number, k, between zero and one is then generated. For any random number it will be true that $array[j-1] < k \leq array[j]$, for some value of j. The component with mass m_j is the component in which the primary vertex of that event will be located. For each new event simulated, a new vertex location is found. In summary, if simulating N events for a group of components, approximately N_i events are simulated in the i-th component, where N_i is described by Eq. A.47.

$$N_i = \frac{m_i N}{m} \tag{A.47}$$

Because of this fact, the detection efficiency from simulating a group of components scales appropriately as compared to the detection efficiencies from simulating each component individually and summing their expected contributions. The proof of this follows. The number of decays from one radioactive nuclide in a single component that

a detector is expected to detect is

$$D_i = A_i \, m_i \, \epsilon_i \, t \, . \tag{A.48}$$

As before, m_i is the mass of the component, A_i is the component's radioactivity for the nuclide of interest (in Bq/kg), ϵ_i is the detector's efficiency to detect the radioactivity from the given component, and t is the livetime of the detector. The efficiency, ϵ_i is obtained from the simulation as follows.

$$\epsilon_i = \frac{\chi_i}{N_i} \tag{A.49}$$

As before, N_i is the number of events simulated in the individual component, and χ_i is the number of events seen by the detector in the radioactive nuclide's signature gamma-peak. Equations A.48 and A.49 reduce to

$$D_i = A_i \, m_i \, \frac{\chi_i}{N_i} \, t \, , \tag{A.50}$$

and therefore the number of decays from one radioactive nuclide in several component that the detector is expected to detect is

$$D = \sum_{i=1}^{n} A_i \, m_i \, \frac{\chi_i}{N_i} \, t \, . \tag{A.51}$$

If all the components are composed of the same material and expected to have the same radioactivity Eq. A.51 reduces to

$$D = A \, t \sum_{i=1}^{n} m_i \, \frac{\chi_i}{N_i} \, . \tag{A.52}$$

If the several components are simulated as a single group and the number of events

simulated in the i-th component is as given by Eq. A.47, the number of decays detected is

$$\begin{aligned} D &= A\,t \sum_{i=1}^{n} m_i \frac{\chi_i m}{m_i N} \\ &= A\,t\,m \frac{1}{N} \sum_{i=1}^{n} \chi_i \\ &= A\,t\,m \frac{\chi}{N}\,. \end{aligned} \tag{A.53}$$

Here, N is the number of events simulated in the entire group of components and χ is the number of events seen by the detector in the radioactive nuclide's signature gamma-peak (from the simulated group of components). Thus, the detection efficiency from simulating a group of components is simply

$$\epsilon = \frac{\chi}{N} \tag{A.54}$$

and can be directly obtained from the simulated energy spectrum of the detector.

APPENDIX B: DETECTOR PEAK SHAPE CHARACTERIZATION

The multi-peak fitting function is used to classify the response function for six of the detectors in the PC. The multi-peak fitting routine performs best with higher statistics and therefore is used on binned data taken with a ^{228}Th line source. The routine is used on a total of five calibration sets in order to investigate how the peak fitting parameters change over time. The five calibration sets that are used in this analysis are referred to as calibration data sets: A, B, C, D and E. They are listed in chronological order and their relative timing with respect to one another can be found in Fig. 2.2. For each detector in each calibration data set, the multi-peak fitting routine is used to fit five gamma peaks, which are listed in Table 4.1.

All fitting is done on binned data with a bin width of 0.1 keV. For each peak, a fit range corresponding to $(M \pm 10\Sigma)$ is used for the multi-peak fitting routine. More details on the multi-peak fitting function can be found in Chapter 3. More details on the multi-peak fitting routine can be found in Chapter 4.

The results of the multi-peak fitting routine for each detector during each data set are below; it includes, for each detector, the following.

1. The common parameters for each of the calibration data sets (σ_0, σ_1 and σ_2 and when applicable b_τ, m_τ, b_H and m_H). These are presented first as a series of figures (of the parameters plotted over time) ...

2. ... and then in tabular form.

3. In tabular form, the parameters resulting in the best fit for each calibration data set for gamma peak #1. Immediately following is a figure of the centroid of the peak plotted over time.

4. And then for gamma peak #2, ...

5. ... gamma peak #3 ...

6. ... gamma peak #4 ...

7. ... and gamma peak #5.

8. A comparison of the peak rates for all of the calibration data sets.

9. The fits to each of the gamma peaks in all of the calibration data sets and the residuals of the fits.

B.1 S1D2 of the PC (Detector B8717)

All five gamma-peaks in S1D2 of the PC can be fit in all five of the calibration data sets. As discussed in Chapter 4, data set E is not used when fitting any of the common parameters over time. Additionally, the best fit for data sets B and D yield unphysical values for parameters b_τ and m_H. In both data sets b_τ is negative and in data set B m_H is negative. These negative parameters do not affect the peak shape in the energy range that is investigated here and therefore the fit is accepted. However these negative values are not used when fitting the common parameters over time.

B.1.1 Summary of Fit Results

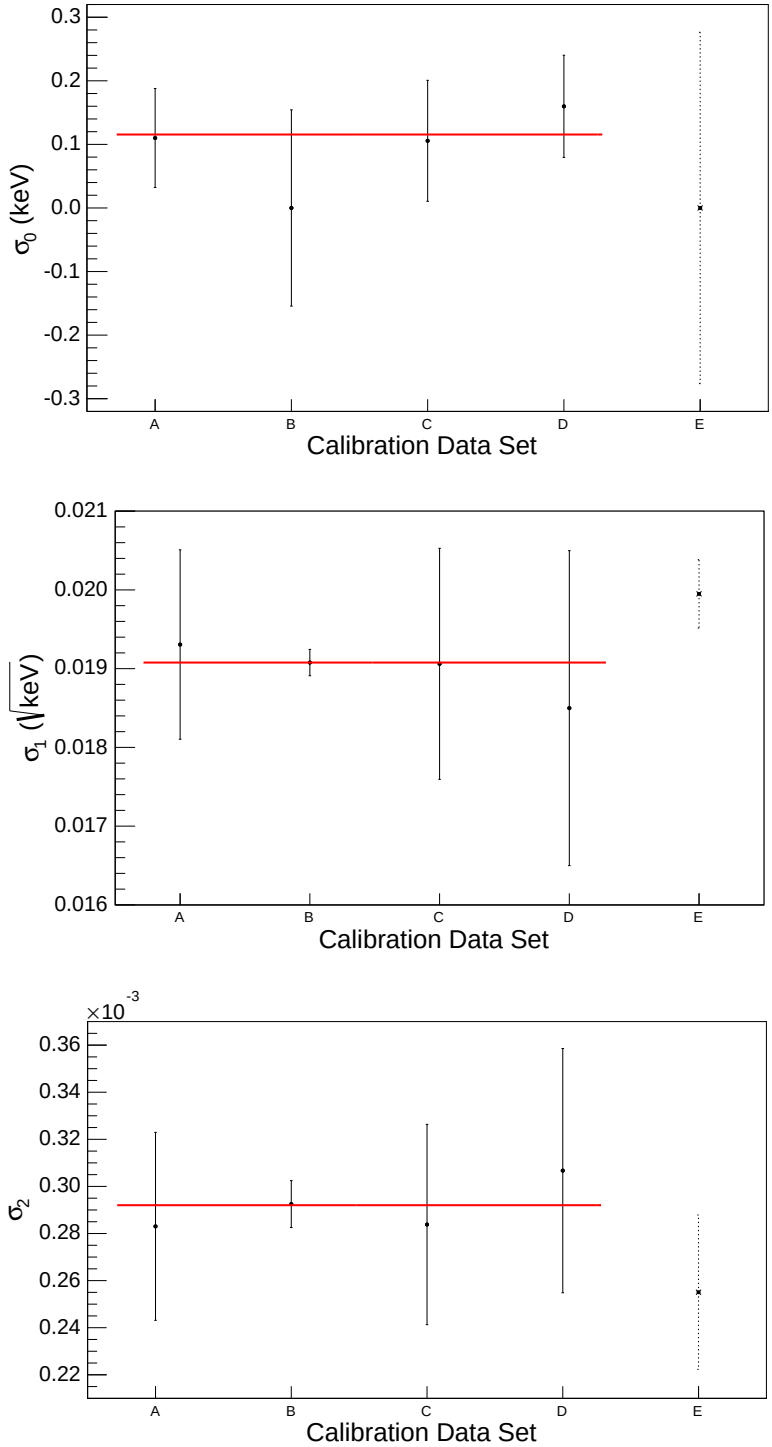

Figure B.1: Parameter σ_0 (top), σ_1 (middle) and σ_2 (bottom) for S1D2 over time. Data with solid error bars are fit with a constant over time. The best fits result in average values of: $\sigma_0 = 0.12$ (5) keV, $\sigma_1 = 1.91$ (2)$\cdot 10^{-2}$ keV$^{1/2}$ and $\sigma_2 = 2.92$ (9)$\cdot 10^{-4}$.

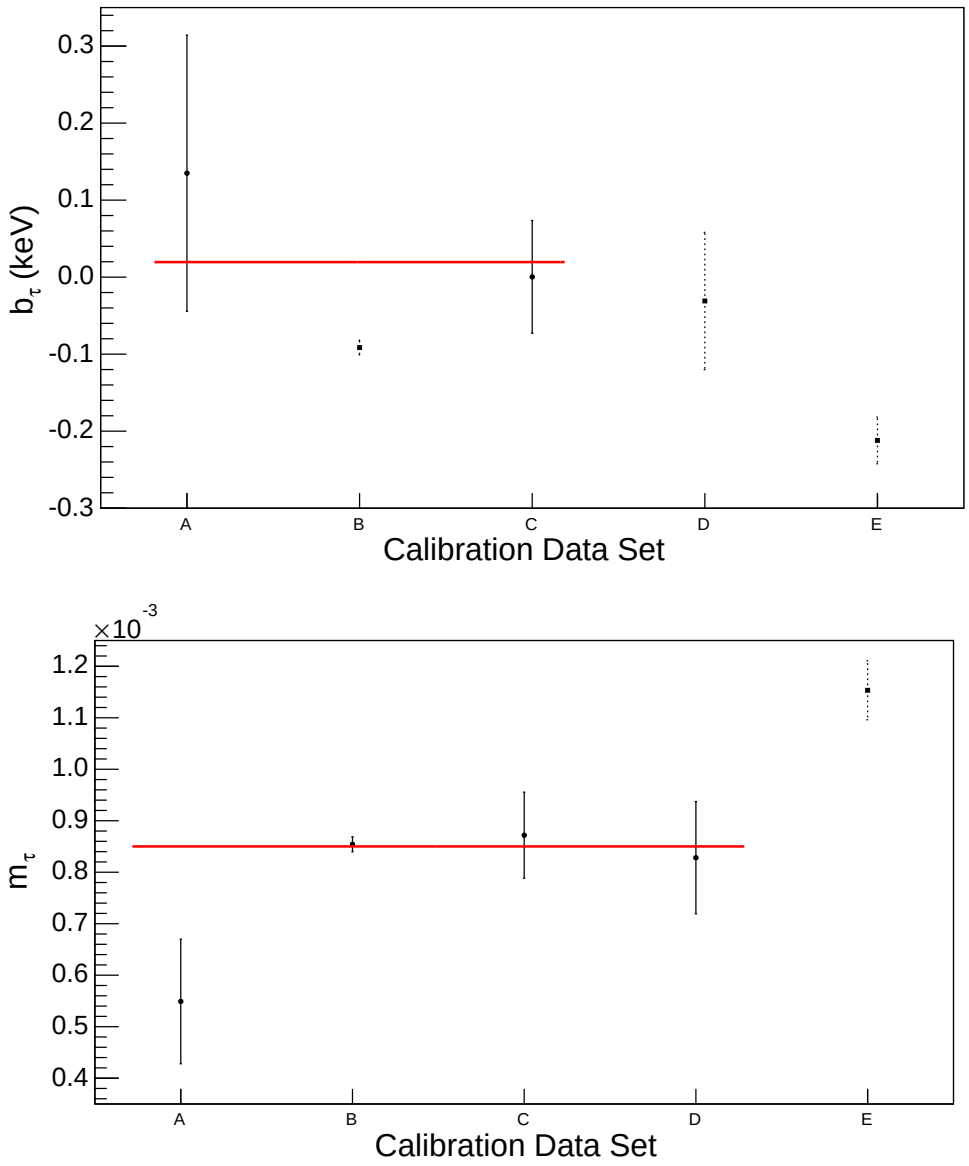

Figure B.2: Parameter b_τ (top) and m_τ (bottom) for S1D2 over time. Data with solid error bars are fit with a constant over time. The best fits result in average values of: $b_\tau = 2\ (7)\cdot 10^{-2}$ keV and $m_\tau = 8.5\ (1)\cdot 10^{-4}$.

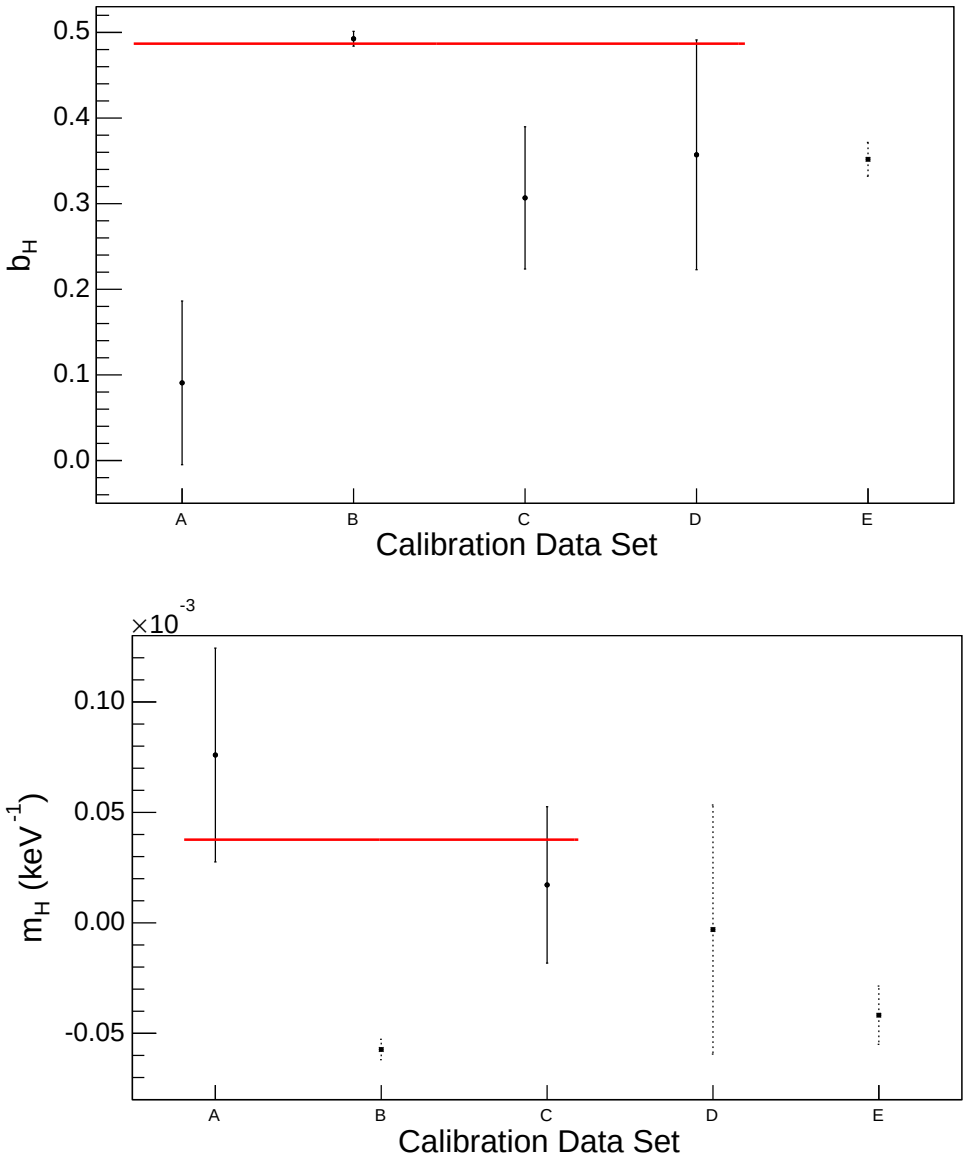

Figure B.3: Parameter b_H (top) and m_H (bottom) for S1D2 over time. Data with solid error bars are fit with a constant over time. The best fits result in average values of: $b_H = 0.487\ (9)$ and $m_H = 4\ (3) \cdot 10^{-5}$ keV^{-1}.

Table B.1: Common parameters of S1D2 for all calibration data.

	Calibration Data Set				
	A	B	C	D	E
σ_0 [keV]	0.11 (8)	0.0 (2)	0.11 (10)	0.16 (8)	0.0 (3)
$\sigma_1/10^{-2}$ [keV$^{1/2}$]	1.9 (1)	1.91 (2)	1.9 (1)	1.8 (2)	1.99 (4)
$\sigma_2/10^{-4}$	2.8 (4)	2.92 (10)	2.8 (4)	3.1 (5)	2.6 (3)
b_τ [keV]	0.1 (2)	-0.091 (9)	0.00 (7)	-0.03 (9)	-0.21 (3)
$m_\tau/10^{-3}$	0.5 (1)	0.85 (1)	0.87 (8)	0.8 (1)	1.15 (6)
b_H	0.09 (10)	0.493 (9)	0.31 (8)	0.4 (1)	0.35 (2)
$m_H/10^{-4}$ [keV^{-1}]	0.8 (5)	-0.57 (5)	0.2 (4)	0.0 (6)	-0.4 (1)
Runtime [hrs]	4.300	5.155	4.232	3.361	0.871
Fixed Parameters	-	-	-	-	-

Table B.2: Peak #1 parameters of S1D2 for all calibration data.

	Calibration Data Set				
	A	B	C	D	E
μ [keV]	277.34 (2)	277.39 (1)	277.24 (2)	277.23 (2)	277.16 (4)
A/t $[cts/hr]$	53 (2)	49 (2)	51 (2)	50 (2)	44 (4)
H_{step}	0.02 (2)	0.3 (5)$\cdot 10^{-2}$	1.1 (9)$\cdot 10^{-2}$	0.02 (1)	0 (7)$\cdot 10^{-4}$
σ [keV]	0.35 (1)	0.328 (3)	0.34 (1)	0.36 (1)	0.340 (7)
τ [keV]	0.3 (2)	0.15 (2)	0.24 (7)	0.20 (8)	0.11 (5)
H_{tail}	0.1 (1)	0.48 (2)	0.31 (10)	0.4 (2)	0.34 (5)
M	277.30 (2)	277.32 (1)	277.16 (2)	277.16 (2)	277.12 (4)
Σ [keV]	0.37 (2)	0.351 (4)	0.39 (2)	0.39 (2)	0.349 (8)
FWHM [keV]	0.84 (4)	0.809 (9)	0.85 (4)	0.88 (4)	0.82 (2)
Runtime [hrs]	4.300	5.155	4.232	3.361	0.871
Fixed Parameters	-	-	-	-	-

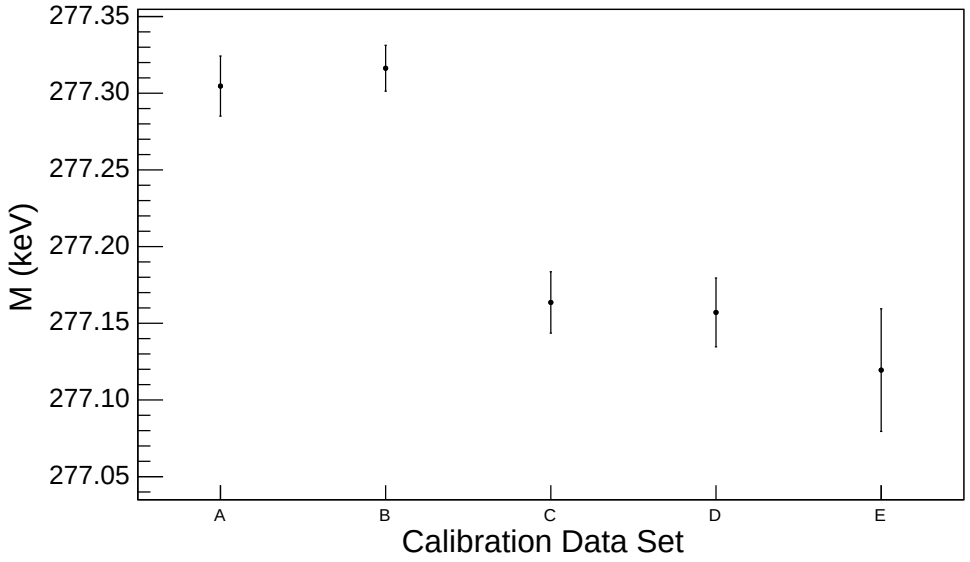

Figure B.4: The centroid (M) of peak #1 for S1D2 over time.

Table B.3: Peak #2 parameters of S1D2 for all calibration data.

	Calibration Data Set				
	A	B	C	D	E
μ [keV]	300.10 (2)	300.17 (1)	299.97 (2)	299.95 (2)	299.86 (3)
A/t $[cts/hr]$	71 (2)	69 (2)	69 (2)	68 (3)	67 (4)
H_{step}	0.02 (1)	0 (1)$\cdot 10^{-3}$	1.3 (6)$\cdot 10^{-2}$	1.2 (6)$\cdot 10^{-2}$	0 (5)$\cdot 10^{-4}$
σ [keV]	0.36 (1)	0.342 (3)	0.36 (1)	0.37 (1)	0.354 (7)
τ [keV]	0.3 (2)	0.16 (2)	0.26 (7)	0.22 (8)	0.13 (5)
H_{tail}	0.1 (1)	0.48 (2)	0.31 (10)	0.4 (2)	0.34 (4)
M	300.06 (2)	300.09 (1)	299.89 (2)	299.87 (2)	299.81 (3)
Σ [keV]	0.39 (2)	0.370 (4)	0.40 (2)	0.41 (2)	0.368 (9)
FWHM [keV]	0.87 (4)	0.848 (9)	0.89 (4)	0.92 (4)	0.86 (2)
Runtime [hrs]	4.300	5.155	4.232	3.361	0.871
Fixed Parameters	-	-	-	-	-

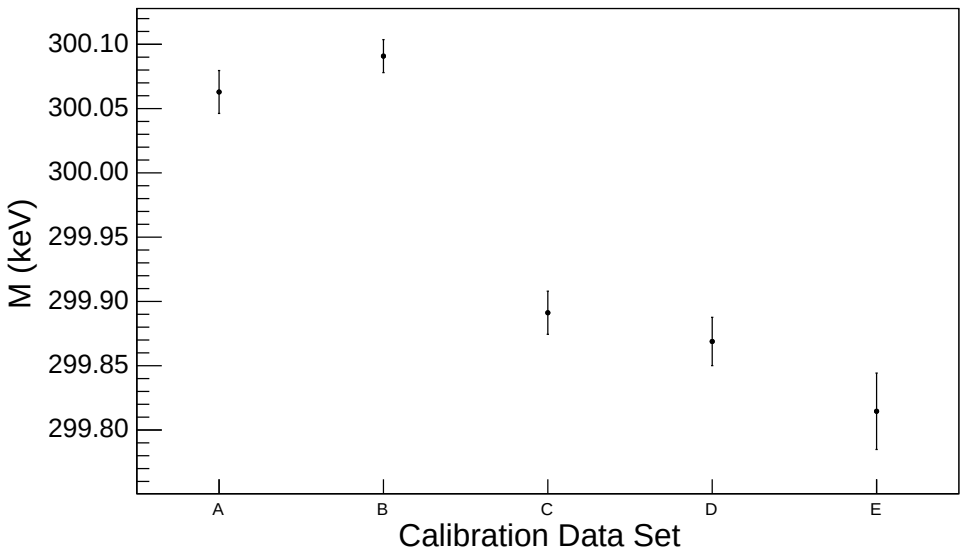

Figure B.5: The centroid (M) of peak #2 for S1D2 over time.

Table B.4: Peak #3 parameters of S1D2 for all calibration data.

	Calibration Data Set				
	A	B	C	D	E
μ [keV]	583.27 (2)	583.272 (5)	582.82 (2)	582.74 (3)	582.73 (1)
A/t $[cts/hr]$	470 (5)	461 (4)	454 (5)	437 (5)	430 (10)
H_{step}	0.2 (1)$\cdot 10^{-2}$	1.4 (2)$\cdot 10^{-3}$	1.2 (4)$\cdot 10^{-3}$	0.6 (4)$\cdot 10^{-3}$	0 (2)$\cdot 10^{-4}$
σ [keV]	0.507 (9)	0.491 (4)	0.500 (9)	0.51 (1)	0.50 (1)
τ [keV]	0.5 (1)	0.41 (1)	0.51 (6)	0.45 (7)	0.46 (5)
H_{tail}	0.1 (1)	0.46 (1)	0.3 (1)	0.4 (2)	0.33 (3)
M	583.204 (8)	583.086 (8)	582.662 (8)	582.579 (9)	582.58 (2)
Σ [keV]	0.56 (1)	0.599 (6)	0.62 (2)	0.61 (2)	0.61 (2)
FWHM [keV]	1.23 (3)	1.27 (1)	1.27 (4)	1.29 (5)	1.27 (3)
Runtime [hrs]	4.300	5.155	4.232	3.361	0.871
Fixed Parameters	-	-	-	-	-

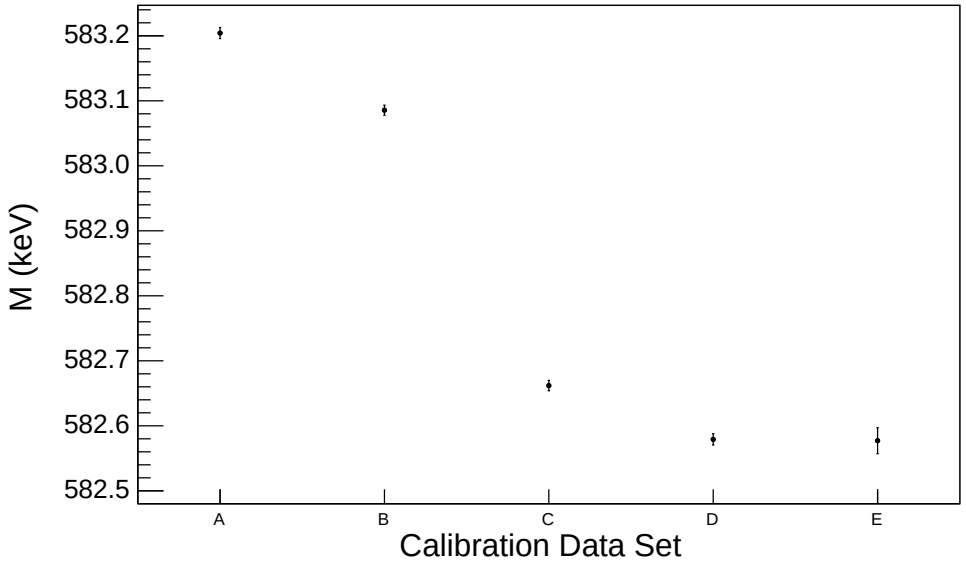

Figure B.6: The centroid (M) of peak #3 for S1D2 over time.

Table B.5: Peak #4 parameters of S1D2 for all calibration data.

	Calibration Data Set				
	A	B	C	D	E
μ [keV]	860.47 (3)	860.89 (2)	860.25 (4)	860.13 (5)	860.05 (6)
A/t $[cts/hr]$	55 (2)	54 (2)	55 (2)	52 (2)	50 (4)
H_{step}	0.4 (6)$\cdot 10^{-2}$	0 (2)$\cdot 10^{-4}$	0.4 (1)$\cdot 10^{-2}$	0.3 (1)$\cdot 10^{-2}$	0 (4)$\cdot 10^{-6}$
σ [keV]	0.63 (1)	0.614 (6)	0.62 (1)	0.62 (2)	0.62 (1)
τ [keV]	0.6 (1)	0.64 (3)	0.75 (7)	0.68 (8)	0.78 (8)
H_{tail}	0.2 (1)	0.44 (2)	0.3 (1)	0.4 (2)	0.32 (6)
M	860.37 (3)	860.61 (2)	860.01 (3)	859.89 (3)	859.81 (6)
Σ [keV]	0.71 (1)	0.814 (7)	0.83 (2)	0.81 (3)	0.84 (2)
FWHM [keV]	1.52 (3)	1.61 (1)	1.58 (4)	1.60 (5)	1.59 (4)
Runtime [hrs]	4.300	5.155	4.232	3.361	0.871
Fixed Parameters	-	-	-	-	-

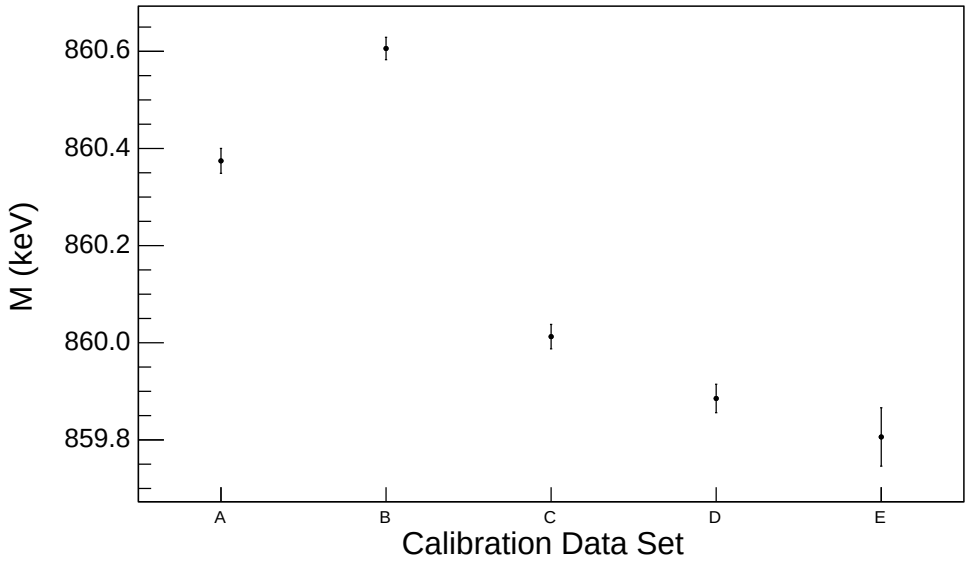

Figure B.7: The centroid (M) of peak #4 for S1D2 over time.

Table B.6: Peak #5 parameters of S1D2 for all calibration data.

	Calibration Data Set				
	A	B	C	D	E
μ [keV]	2614.94 (7)	2615.47 (1)	2613.64 (5)	2613.15 (7)	2613.21 (6)
A/t $[cts/hr]$	212 (3)	203 (3)	201 (3)	194 (4)	193 (7)
H_{step}	0 (3)$\cdot 10^{-5}$	0 (2)$\cdot 10^{-6}$	0 (4)$\cdot 10^{-6}$	0 (2)$\cdot 10^{-6}$	0 (2)$\cdot 10^{-5}$
σ [keV]	1.24 (3)	1.24 (2)	1.23 (3)	1.25 (4)	1.22 (5)
τ [keV]	1.6 (3)	2.14 (5)	2.3 (2)	2.1 (3)	2.8 (2)
H_{tail}	0.3 (2)	0.34 (3)	0.4 (1)	0.3 (2)	0.24 (10)
M	2614.49 (3)	2614.74 (3)	2612.84 (4)	2612.40 (5)	2612.5 (1)
Σ [keV]	1.66 (3)	2.04 (1)	2.13 (2)	2.05 (3)	2.20 (5)
FWHM [keV]	3.14 (6)	3.22 (2)	3.20 (3)	3.25 (5)	3.05 (7)
Runtime [hrs]	4.300	5.155	4.232	3.361	0.871
Fixed Parameters	-	-	-	-	-

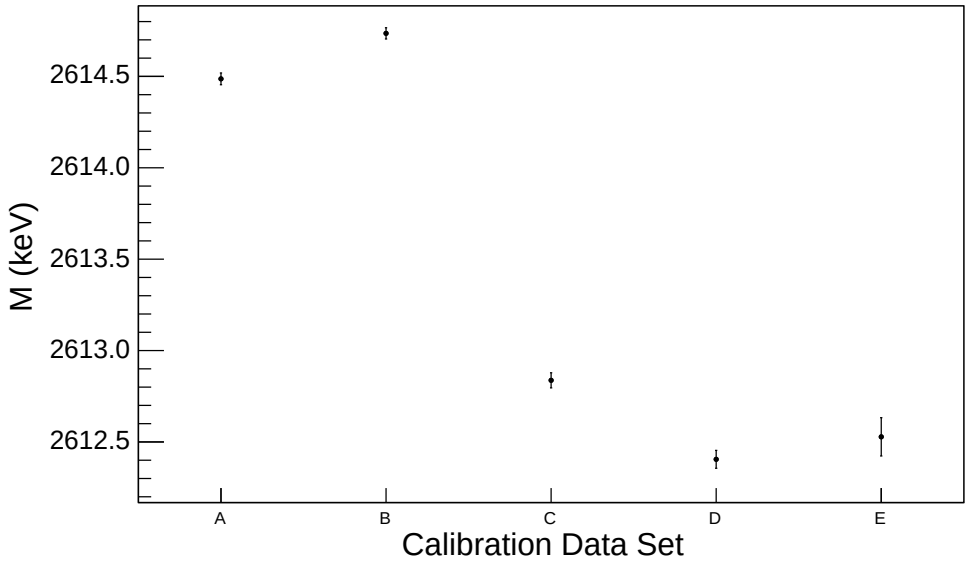

Figure B.8: The centroid (M) of peak #5 for S1D2 over time.

Table B.7: The peak rate for each of the five peaks during each of the five calibration data sets for S1D2. The peak rate is the area parameter divided by the runtime divided by the bin width (0.1 keV). Also shown is the ratio of each peak's rate to the 583-keV peak rate (i.e. Pk #3).

		Calibration Data Set				
		A	B	C	D	E
Pk Rate $\left[\frac{cts}{hr}\right]$	Pk #1	530 (20)	490 (20)	510 (20)	500 (20)	440 (40)
	Pk #2	710 (20)	690 (20)	690 (20)	680 (30)	670 (40)
	Pk #3	4700 (50)	4610 (40)	4540 (50)	4370 (50)	4300 (100)
	Pk #4	550 (20)	540 (20)	550 (20)	520 (20)	500 (40)
	Pk #5	2120 (30)	2030 (30)	2010 (30)	1940 (40)	1930 (70)
$\frac{\text{Pk \#}n\text{ Rate}}{\text{Pk \#3 Rate}}$	$n = 1$	0.112 (5)	0.107 (4)	0.112 (5)	0.115 (6)	0.101 (9)
	$n = 2$	0.150 (5)	0.149 (4)	0.151 (5)	0.156 (6)	0.15 (1)
	$n = 3$	1.	1.	1.	1.	1.
	$n = 4$	0.118 (4)	0.118 (3)	0.120 (4)	0.120 (5)	0.115 (9)
	$n = 5$	0.450 (9)	0.441 (7)	0.443 (9)	0.44 (1)	0.45 (2)

B.1.2 Individual Peak Fits

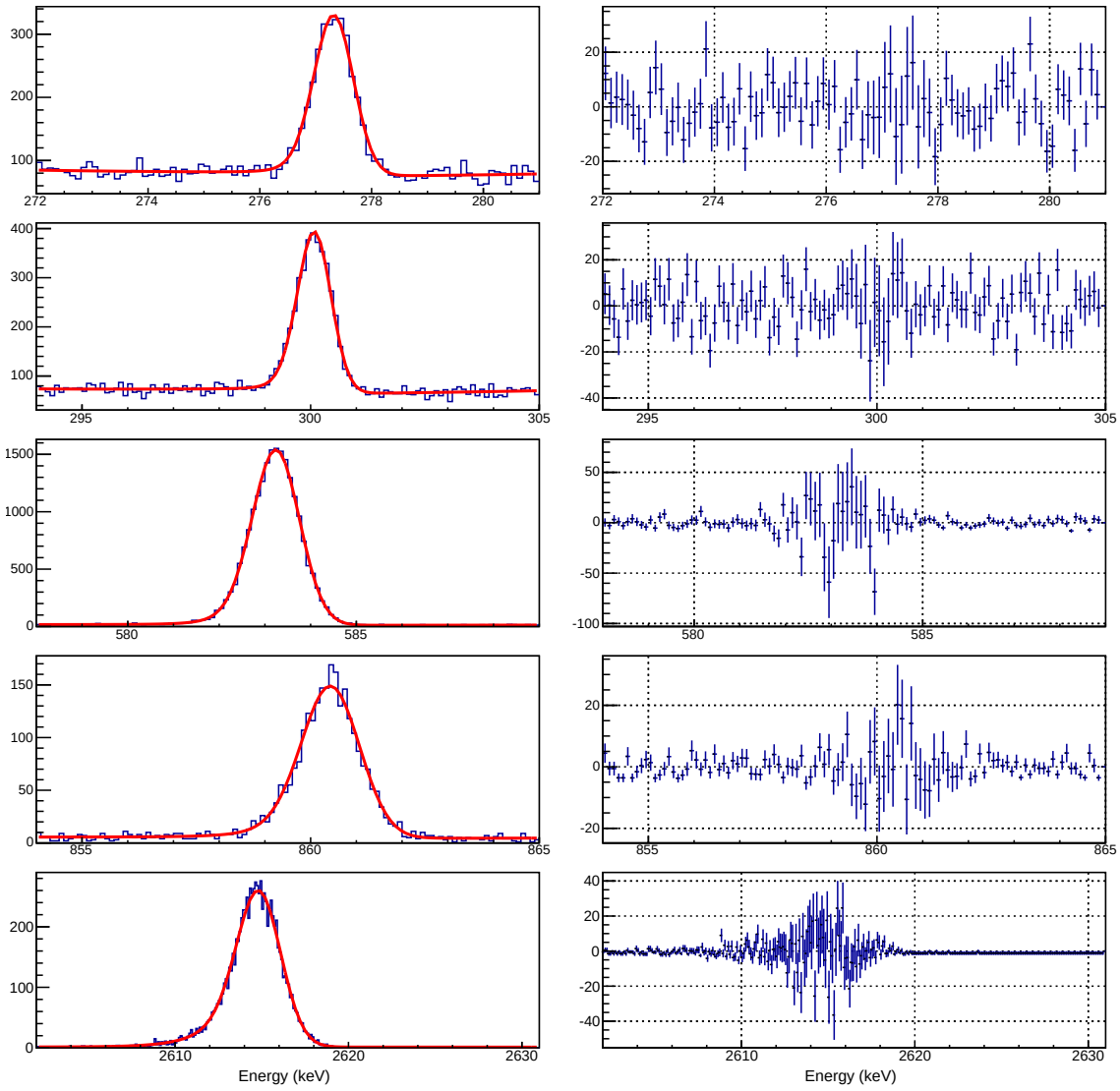

Figure B.9: The five gamma peaks of S1D2 in calibration data set A that are fit with the multi-peak fitting routine. Shown on the left is each of the five peaks with the best fit of the multi-peak fitting function shown in red. Shown on the right is the residual of the fit for each peak.

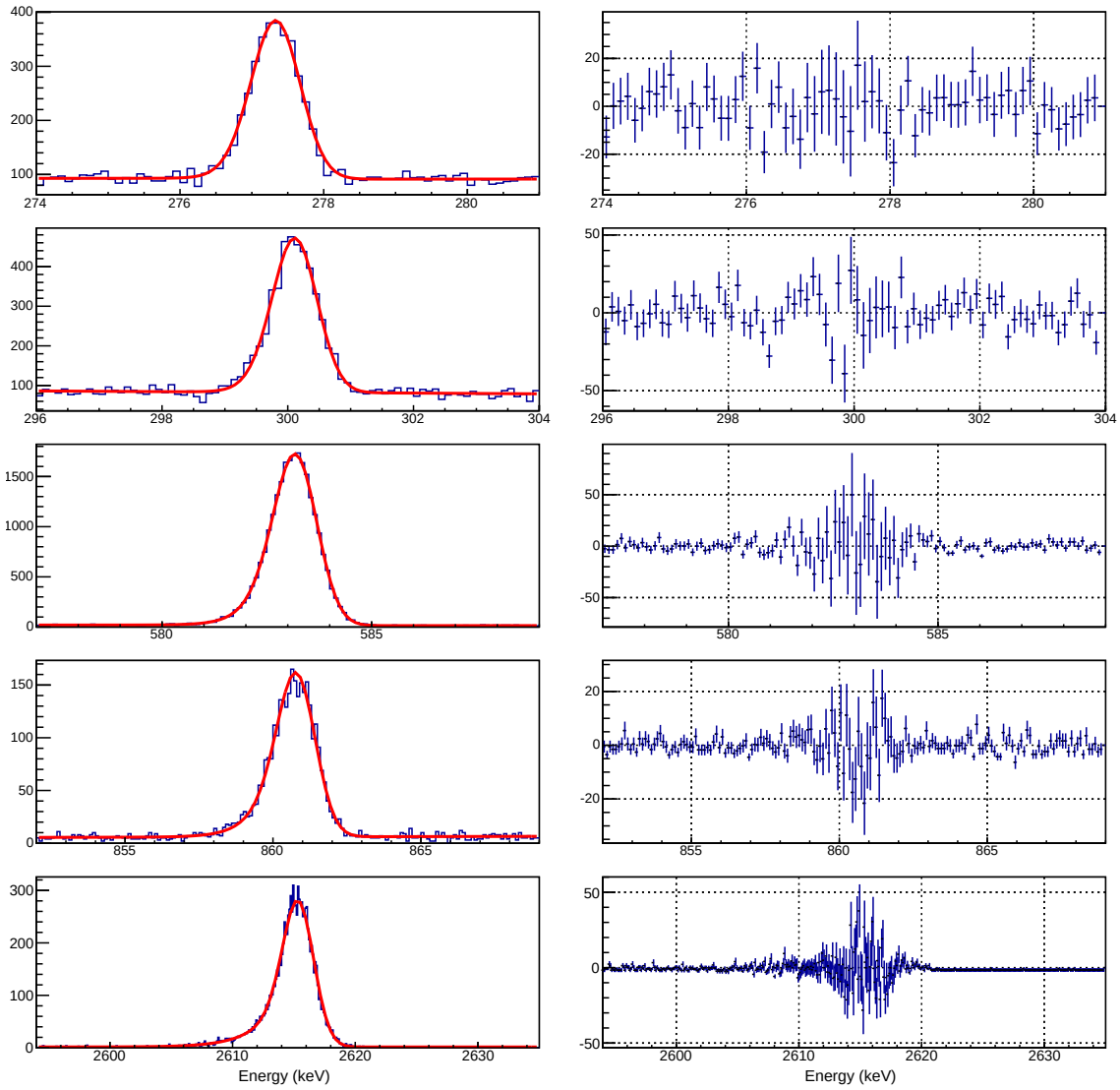

Figure B.10: The five gamma peaks of S1D2 in calibration data set B that are fit with the multi-peak fitting routine. Shown on the left is each of the five peaks with the best fit of the multi-peak fitting function shown in red. Shown on the right is the residual of the fit for each peak.

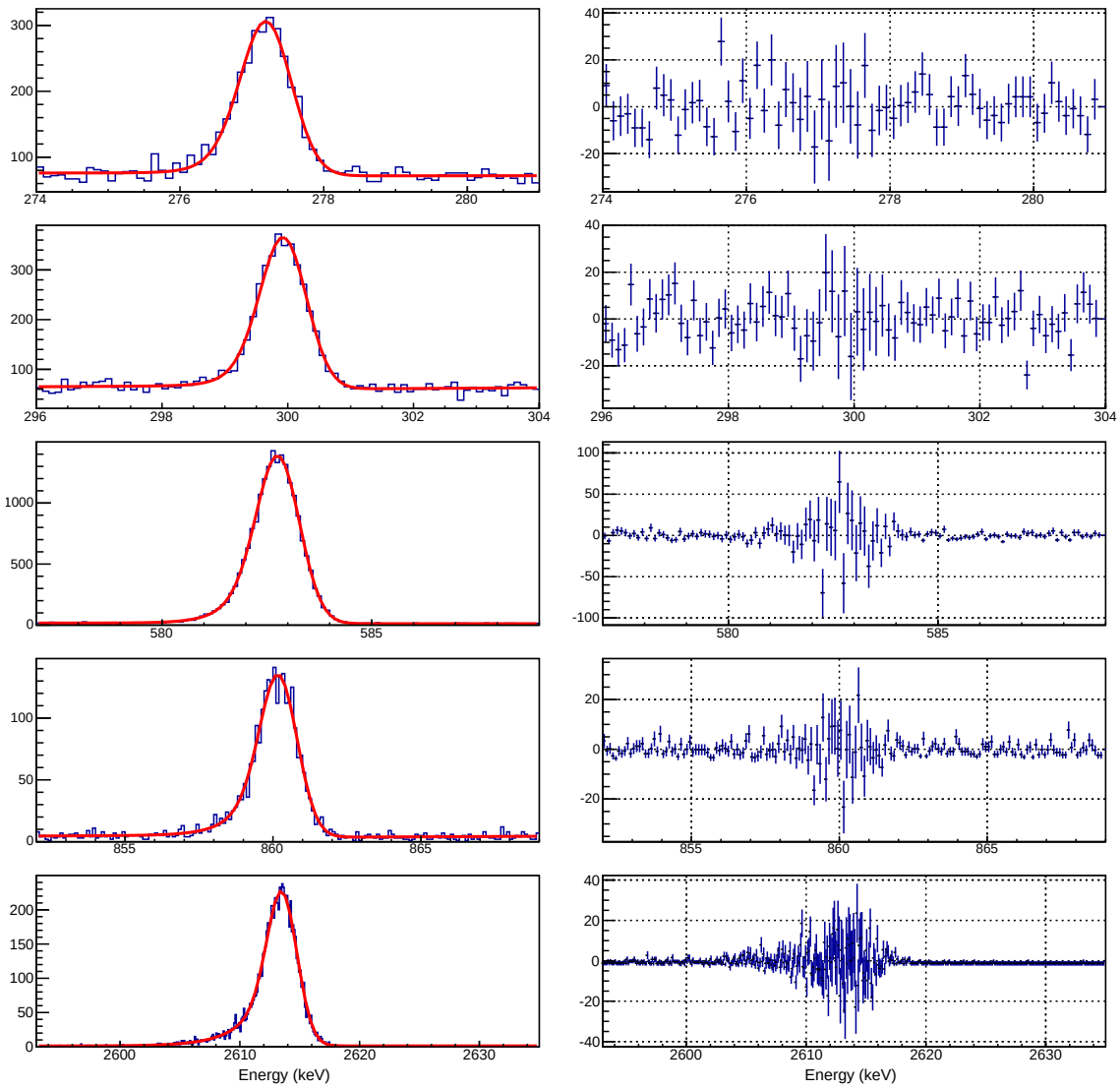

Figure B.11: The five gamma peaks of S1D2 in calibration data set C that are fit with the multi-peak fitting routine. Shown on the left is each of the five peaks with the best fit of the multi-peak fitting function shown in red. Shown on the right is the residual of the fit for each peak.

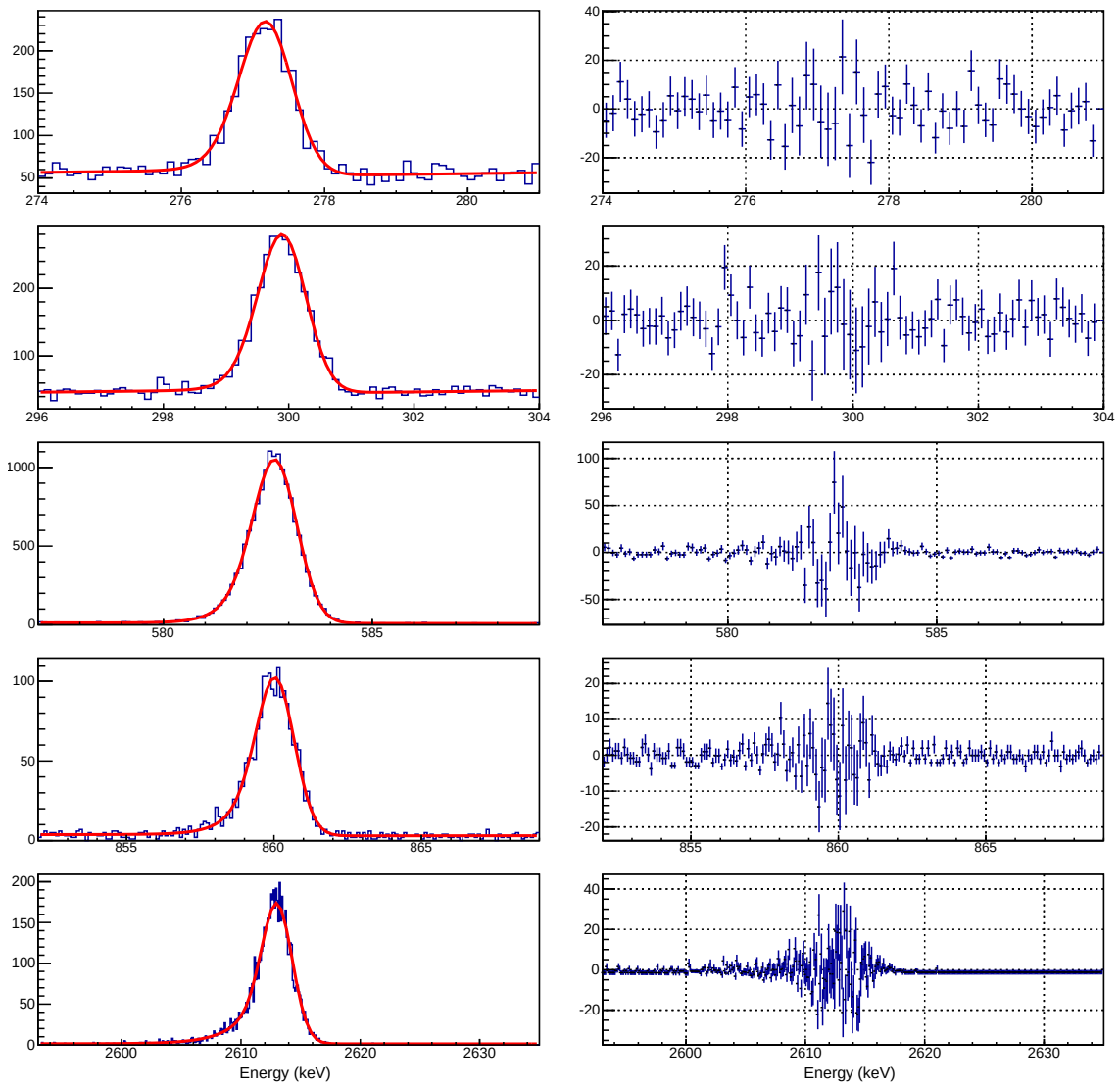

Figure B.12: The five gamma peaks of S1D2 in calibration data set D that are fit with the multi-peak fitting routine. Shown on the left is each of the five peaks with the best fit of the multi-peak fitting function shown in red. Shown on the right is the residual of the fit for each peak.

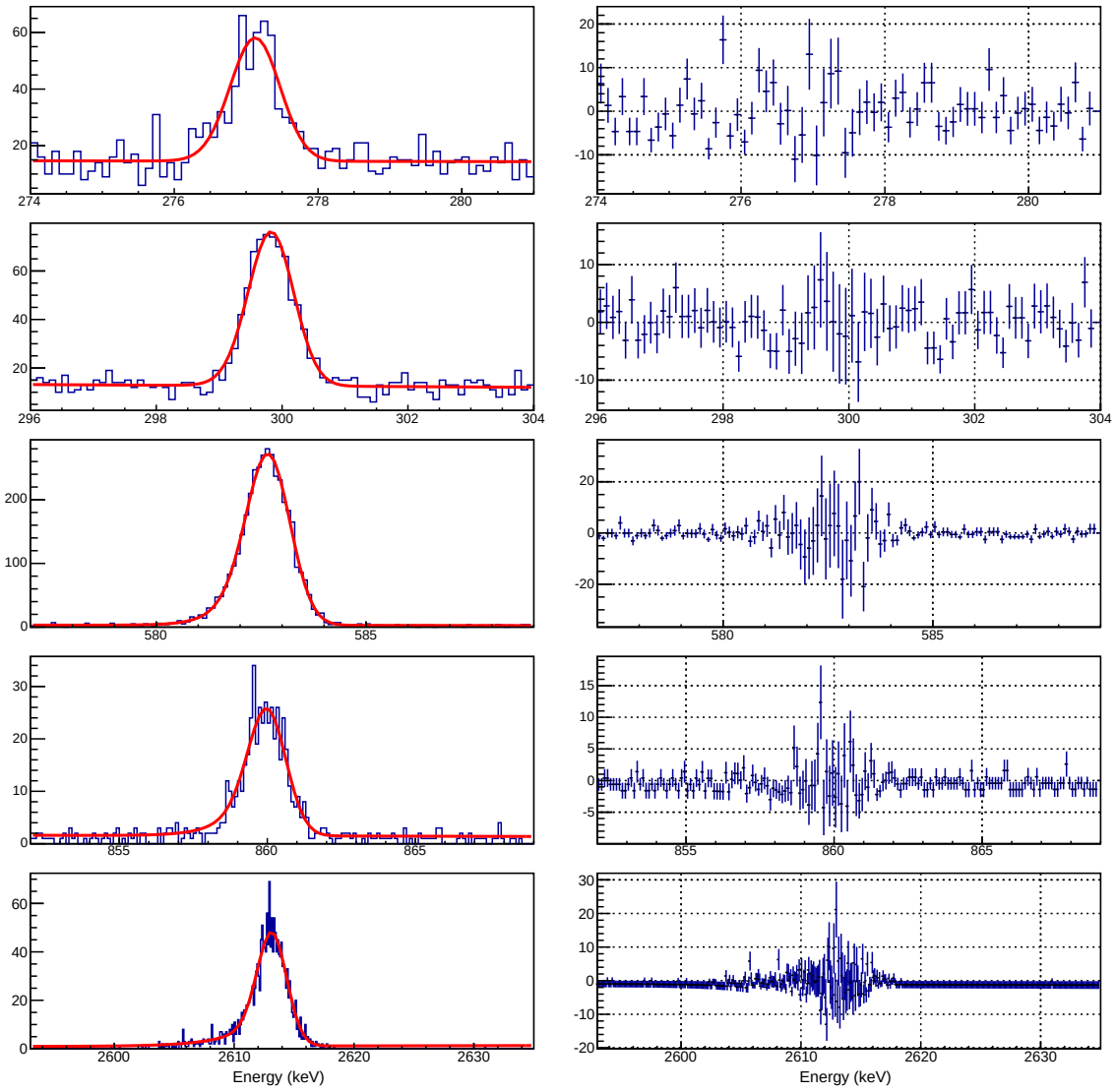

Figure B.13: The five gamma peaks of S1D2 in calibration data set E that are fit with the multi-peak fitting routine. Shown on the left is each of the five peaks with the best fit of the multi-peak fitting function shown in red. Shown on the right is the residual of the fit for each peak.

Table B.8: Common parameters of S1D3 for all calibration data.

	Calibration Data Set				
	A	B	C	D	E
σ_0 [keV]	0.0 (1)	0.00 (1)	0.27 (8)	0.0 (3)	-
$\sigma_1/10^{-2}$ [keV$^{1/2}$]	2.11 (10)	2.0 (1)	1.5 (5)	2.3 (1)	-
$\sigma_2/10^{-4}$	4.6 (5)	5.1 (5)	5.7 (6)	4.7 (5)	-
b_τ [keV]	0.00 (6)	-0.15 (5)	-0.24 (5)	-0.05 (7)	-
$m_\tau/10^{-3}$	2.05 (9)	2.53 (8)	2.63 (8)	2.5 (1)	-
b_H	0.64 (6)	0.77 (6)	0.8 (1)	0.69 (6)	-
$m_H/10^{-4}$ [keV^{-1}]	0.5 (3)	0.2 (3)	-0.2 (4)	0.3 (3)	-
Runtime [hrs]	4.300	5.155	4.232	3.204	0.871
Fixed Parameters	-	-	-	-	-

B.2 S1D3 of the PC (Detector Ponama II)

All five gamma-peaks in S1D2 of the PC can be fit in four of the five calibration data sets. Data set E is the only data set in which S1D3 cannot be fit but as discussed in Chapter 4, data set E is not used when fitting any of the common parameters over time regardless. Additionally, the best fit for data sets B, C and D yield unphysical values for parameters b_τ and m_H. In all three data sets b_τ is negative and in data set C m_H is negative. These negative parameters do not affect the peak shape in the energy range that is investigated here and therefore the fit is accepted. However these negative values are not used when fitting the common parameters over time.

B.2.1 Summary of Fit Results

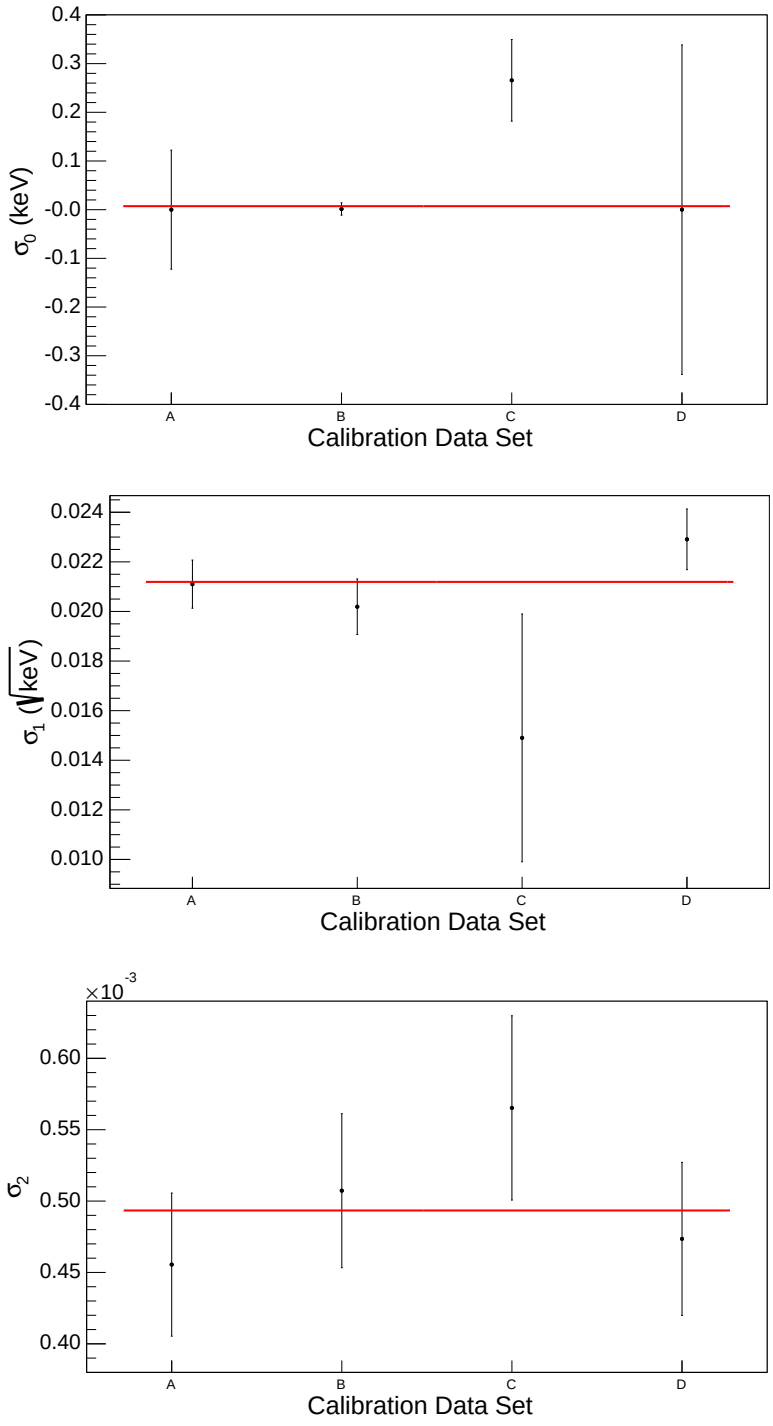

Figure B.14: Parameter σ_0 (top), σ_1 (middle) and σ_2 (bottom) for S1D3 over time. Data with solid error bars are fit with a constant over time. The best fits result in average values of: $\sigma_0 = 0.01\ (1)$ keV, $\sigma_1 = 2.12\ (6)\cdot 10^{-2}$ keV$^{1/2}$ and $\sigma_2 = 4.9\ (3)\cdot 10^{-4}$.

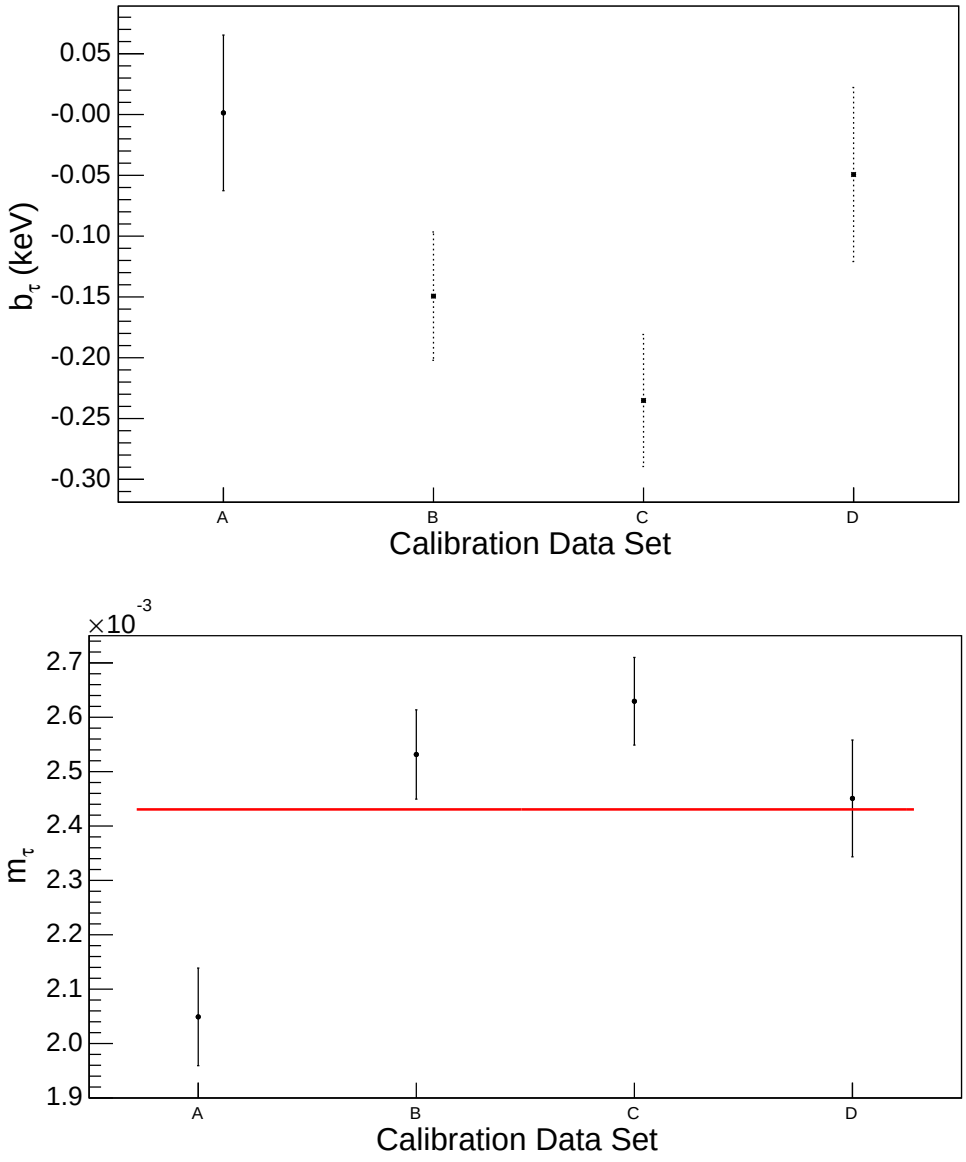

Figure B.15: Parameter b_τ (top) and m_τ (bottom) for S1D3 over time. Data with solid error bars are fit with a constant over time. The best fits result in average values of: $b_\tau = 0\ (6)\cdot 10^{-2}$ keV and $m_\tau = 2.43\ (4)\cdot 10^{-3}$.

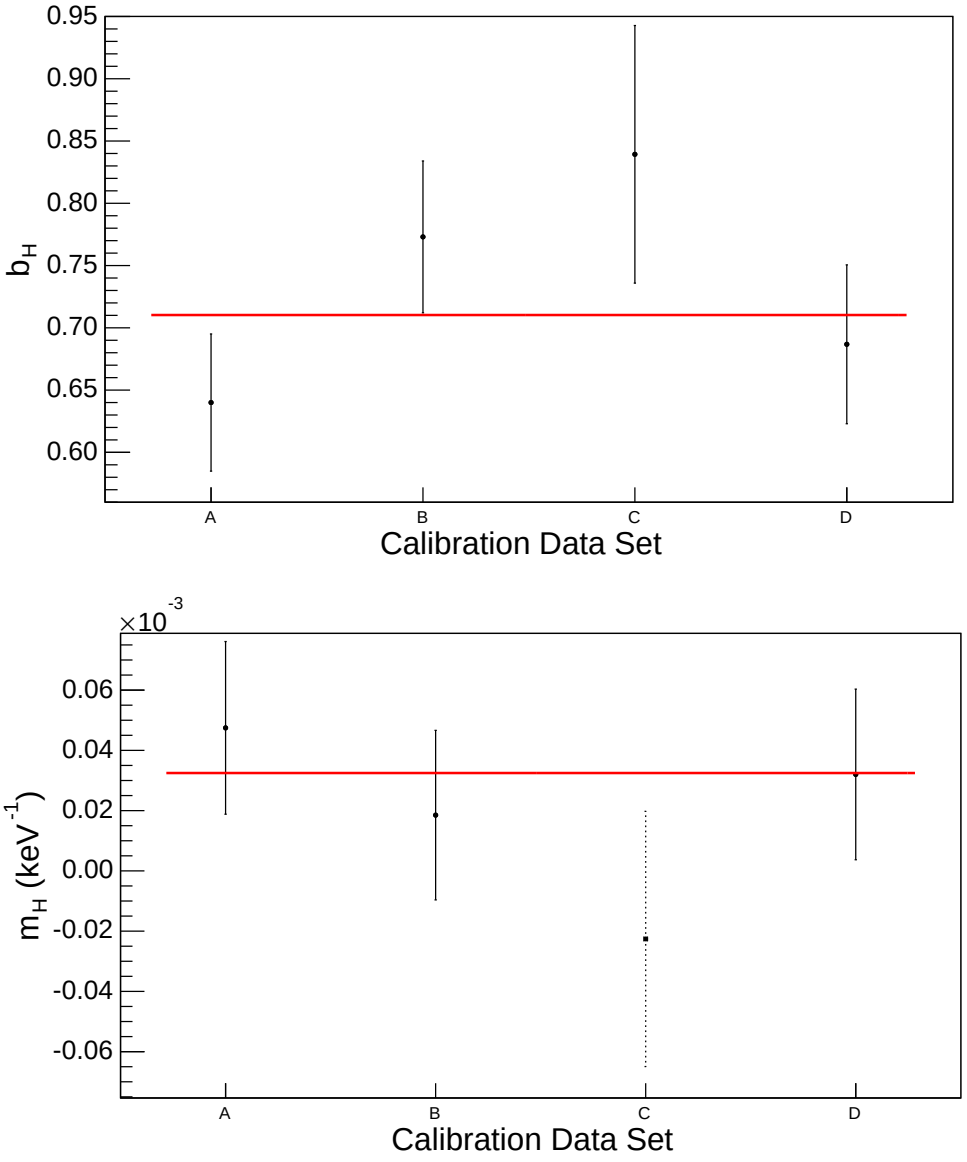

Figure B.16: Parameter b_H (top) and m_H (bottom) for S1D3 over time. Data with solid error bars are fit with a constant over time. The best fits result in average values of: $b_H = 0.71\ (3)$ and $m_H = 3\ (2)\cdot 10^{-5}$ keV^{-1}.

Table B.9: Peak #1 parameters of S1D3 for all calibration data.

	Calibration Data Set				
	A	B	C	D	E
μ [keV]	277.35 (3)	277.97 (3)	277.59 (5)	277.54 (4)	-
A/t $[cts/hr]$	73 (3)	65 (3)	64 (3)	72 (3)	-
H_{step}	0 (1)$\cdot 10^{-2}$	0 (5)$\cdot 10^{-4}$	0 (3)$\cdot 10^{-3}$	0 (1)$\cdot 10^{-5}$	-
σ [keV]	0.37 (1)	0.36 (1)	0.40 (2)	0.40 (2)	-
τ [keV]	0.57 (6)	0.55 (5)	0.49 (6)	0.63 (7)	-
H_{tail}	0.65 (9)	0.78 (10)	0.8 (1)	0.7 (1)	-
M	276.98 (3)	277.54 (3)	277.18 (3)	277.11 (4)	-
Σ [keV]	0.65 (4)	0.65 (4)	0.63 (5)	0.72 (5)	-
FWHM [keV]	1.11 (7)	1.14 (8)	1.19 (9)	1.22 (9)	-
Runtime [hrs]	4.300	5.155	4.232	3.204	0.871
Fixed Parameters	-	-	-	-	-

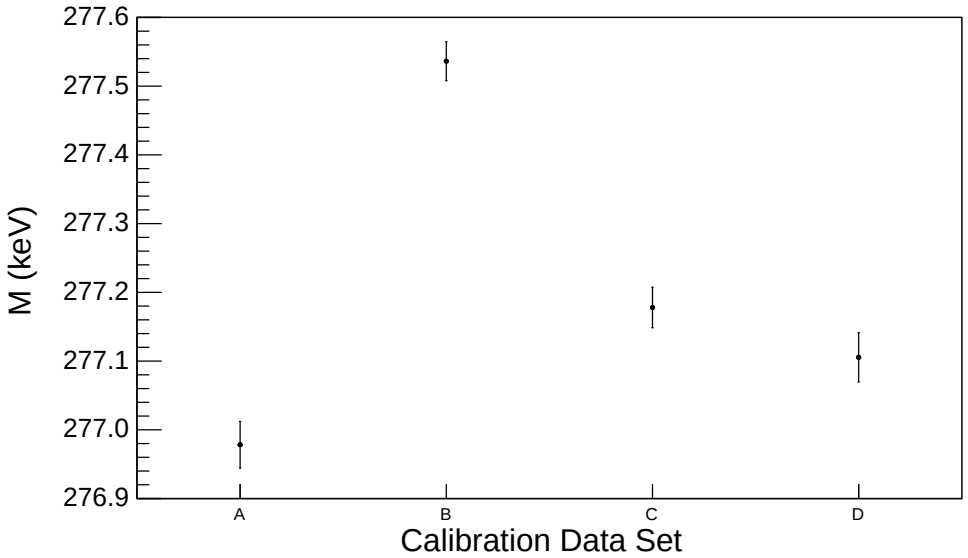

Figure B.17: The centroid (M) of peak #1 for S1D3 over time.

Table B.10: Peak #2 parameters of S1D3 for all calibration data.

Parameter	Calibration Data Set				
	A	B	C	D	E
μ [keV]	300.18 (3)	300.69 (3)	300.28 (5)	300.25 (4)	-
A/t $[cts/hr]$	103 (3)	96 (3)	94 (3)	100 (4)	-
H_{step}	0.5 (9)$\cdot 10^{-2}$	1.4 (9)$\cdot 10^{-2}$	0.1 (3)$\cdot 10^{-2}$	1.3 (6)$\cdot 10^{-2}$	-
σ [keV]	0.39 (1)	0.38 (1)	0.41 (2)	0.42 (2)	-
τ [keV]	0.62 (5)	0.61 (4)	0.55 (5)	0.69 (6)	-
H_{tail}	0.65 (9)	0.8 (1)	0.8 (2)	0.7 (1)	-
M	299.77 (3)	300.21 (3)	299.82 (3)	299.77 (4)	-
Σ [keV]	0.70 (4)	0.71 (5)	0.68 (5)	0.78 (5)	-
FWHM [keV]	1.16 (7)	1.21 (8)	1.25 (10)	1.29 (9)	-
Runtime [hrs]	4.300	5.155	4.232	3.204	0.871
Fixed Parameters	-	-	-	-	-

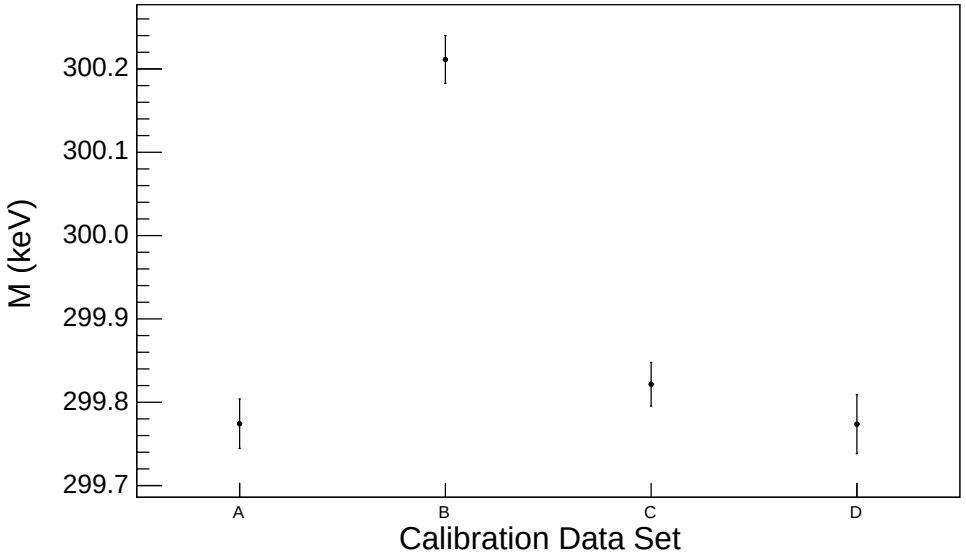

Figure B.18: The centroid (M) of peak #2 for S1D3 over time.

Table B.11: Peak #3 parameters of S1D3 for all calibration data.

Parameter	Calibration Data Set				
	A	B	C	D	E
μ [keV]	583.37 (4)	583.75 (5)	583.10 (9)	582.87 (5)	-
A/t $[cts/hr]$	709 (6)	695 (6)	657 (6)	655 (7)	-
H_{step}	3.5 (5)$\cdot 10^{-3}$	3.6 (4)$\cdot 10^{-3}$	5.7 (2)$\cdot 10^{-3}$	3.6 (3)$\cdot 10^{-3}$	-
σ [keV]	0.57 (1)	0.57 (2)	0.56 (3)	0.62 (2)	-
τ [keV]	1.20 (5)	1.33 (4)	1.30 (4)	1.38 (6)	-
H_{tail}	0.67 (10)	0.8 (1)	0.8 (2)	0.7 (1)	-
M	582.57 (2)	582.72 (2)	582.03 (2)	581.90 (2)	-
Σ [keV]	1.26 (5)	1.41 (7)	1.4 (1)	1.45 (7)	-
FWHM [keV]	1.80 (7)	2.00 (9)	2.0 (1)	2.02 (9)	-
Runtime [hrs]	4.300	5.155	4.232	3.204	0.871
Fixed Parameters	-	-	-	-	-

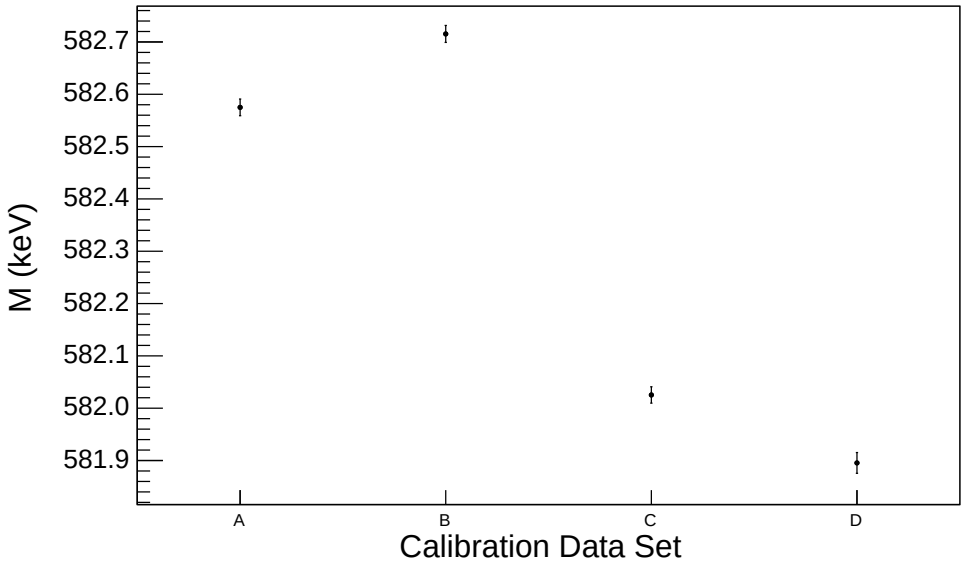

Figure B.19: The centroid (M) of peak #3 for S1D3 over time.

Table B.12: Peak #4 parameters of S1D3 for all calibration data.

Parameter	Calibration Data Set				
	A	B	C	D	E
μ [keV]	861.08 (6)	861.30 (8)	860.3 (1)	860.02 (8)	-
A/t $[cts/hr]$	85 (2)	82 (2)	81 (2)	80 (3)	-
H_{step}	3 (2)$\cdot 10^{-3}$	2 (1)$\cdot 10^{-3}$	3.7 (5)$\cdot 10^{-3}$	5.9 (9)$\cdot 10^{-3}$	-
σ [keV]	0.73 (2)	0.74 (2)	0.70 (3)	0.78 (2)	-
τ [keV]	1.76 (7)	2.03 (6)	2.02 (7)	2.05 (9)	-
H_{tail}	0.7 (1)	0.8 (1)	0.8 (2)	0.7 (1)	-
M	859.88 (4)	859.71 (4)	858.65 (4)	858.55 (5)	-
Σ [keV]	1.82 (6)	2.11 (9)	2.1 (1)	2.12 (8)	-
FWHM [keV]	2.37 (8)	2.7 (1)	2.7 (2)	2.7 (1)	-
Runtime [hrs]	4.300	5.155	4.232	3.204	0.871
Fixed Parameters	-	-	-	-	-

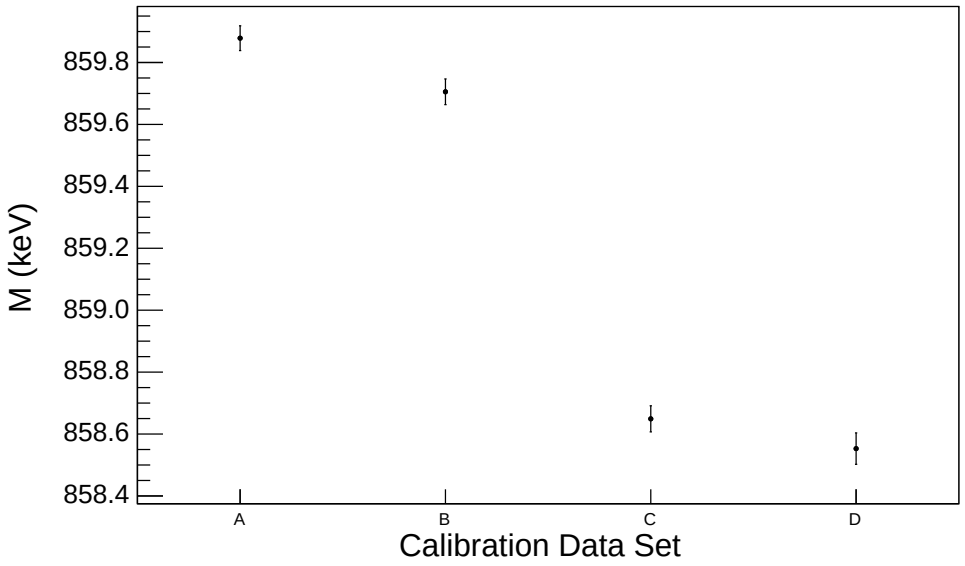

Figure B.20: The centroid (M) of peak #4 for S1D3 over time.

Table B.13: Peak #5 parameters of S1D3 for all calibration data.

Parameter	Calibration Data Set				
	A	B	C	D	E
μ [keV]	2616.6 (2)	2617.0 (2)	2613.9 (2)	2613.4 (2)	-
A/t $[cts/hr]$	347 (5)	344 (4)	334 (4)	323 (6)	-
H_{step}	1.1 (3)$\cdot 10^{-3}$	0.8 (2)$\cdot 10^{-3}$	0.65 (8)$\cdot 10^{-3}$	0.9 (3)$\cdot 10^{-3}$	-
σ [keV]	1.61 (8)	1.68 (9)	1.68 (8)	1.70 (8)	-
τ [keV]	5.4 (2)	6.5 (2)	6.6 (2)	6.3 (3)	-
H_{tail}	0.8 (3)	0.8 (4)	0.8 (3)	0.8 (3)	-
M	2612.5 (1)	2611.7 (1)	2608.7 (1)	2608.6 (2)	-
Σ [keV]	5.4 (2)	6.6 (3)	6.7 (2)	6.4 (2)	-
FWHM [keV]	6.1 (2)	7.2 (3)	6.8 (2)	6.6 (2)	-
Runtime [hrs]	4.300	5.155	4.232	3.204	0.871
Fixed Parameters	-	-	-	-	-

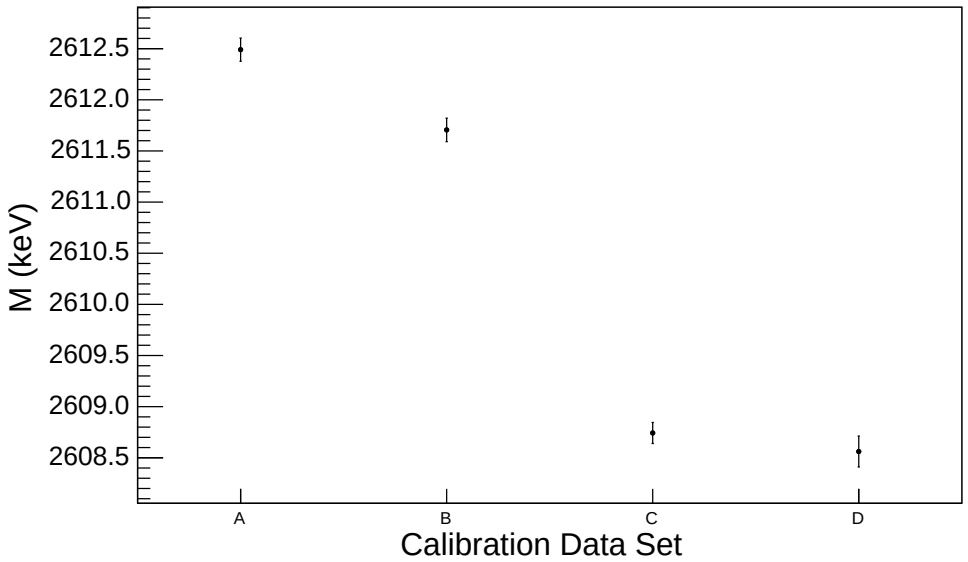

Figure B.21: The centroid (M) of peak #5 for S1D3 over time.

Table B.14: The peak rate for each of the five peaks during each of the four calibration data sets for S1D3. The peak rate is the area parameter divided by the runtime divided by the bin width (0.1 keV). Also shown is the ratio of each peak's rate to the 583-keV peak rate (i.e. Pk #3).

		Calibration Data Set				
		A	B	C	D	E
Pk Rate $\left[\frac{cts}{hr}\right]$	Pk #1	730 (30)	650 (30)	640 (30)	720 (30)	-
	Pk #2	1030 (30)	960 (30)	940 (30)	1000 (40)	-
	Pk #3	7090 (60)	6950 (60)	6570 (60)	6550 (70)	-
	Pk #4	850 (20)	820 (20)	810 (20)	800 (30)	-
	Pk #5	3470 (50)	3440 (40)	3340 (40)	3230 (60)	-
$\frac{\text{Pk } \#n \text{ Rate}}{\text{Pk } \#3 \text{ Rate}}$	$n = 1$	0.103 (4)	0.093 (4)	0.097 (4)	0.110 (5)	-
	$n = 2$	0.145 (5)	0.138 (5)	0.143 (5)	0.153 (6)	-
	$n = 3$	1.	1.	1.	1.	-
	$n = 4$	0.120 (3)	0.118 (3)	0.123 (3)	0.122 (4)	-
	$n = 5$	0.489 (8)	0.496 (8)	0.508 (8)	0.49 (1)	-

B.2.2 Individual Peak Fits

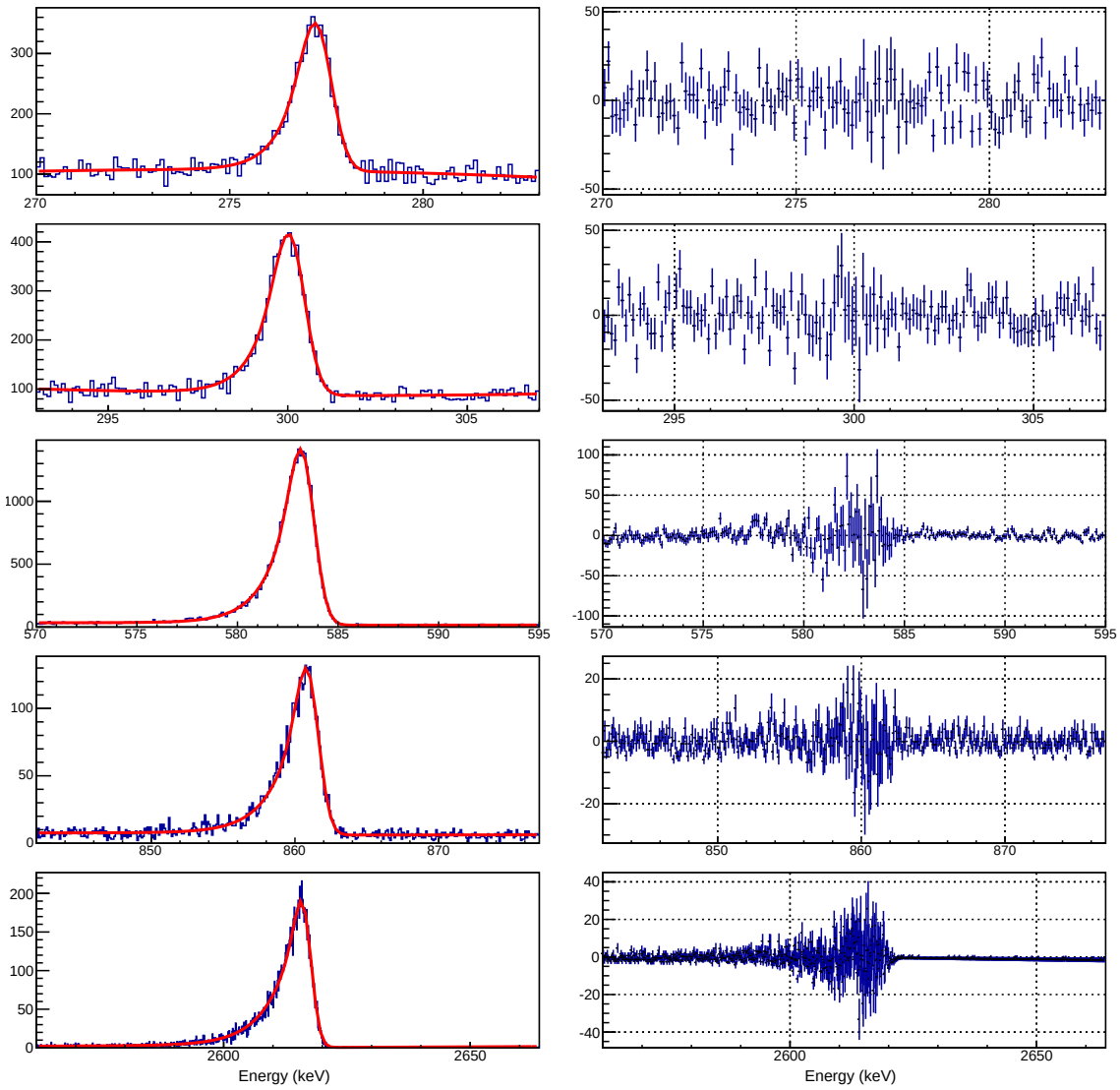

Figure B.22: The five gamma peaks of S1D3 in calibration data set A that are fit with the multi-peak fitting routine. Shown on the left is each of the five peaks with the best fit of the multi-peak fitting function shown in red. Shown on the right is the residual of the fit for each peak.

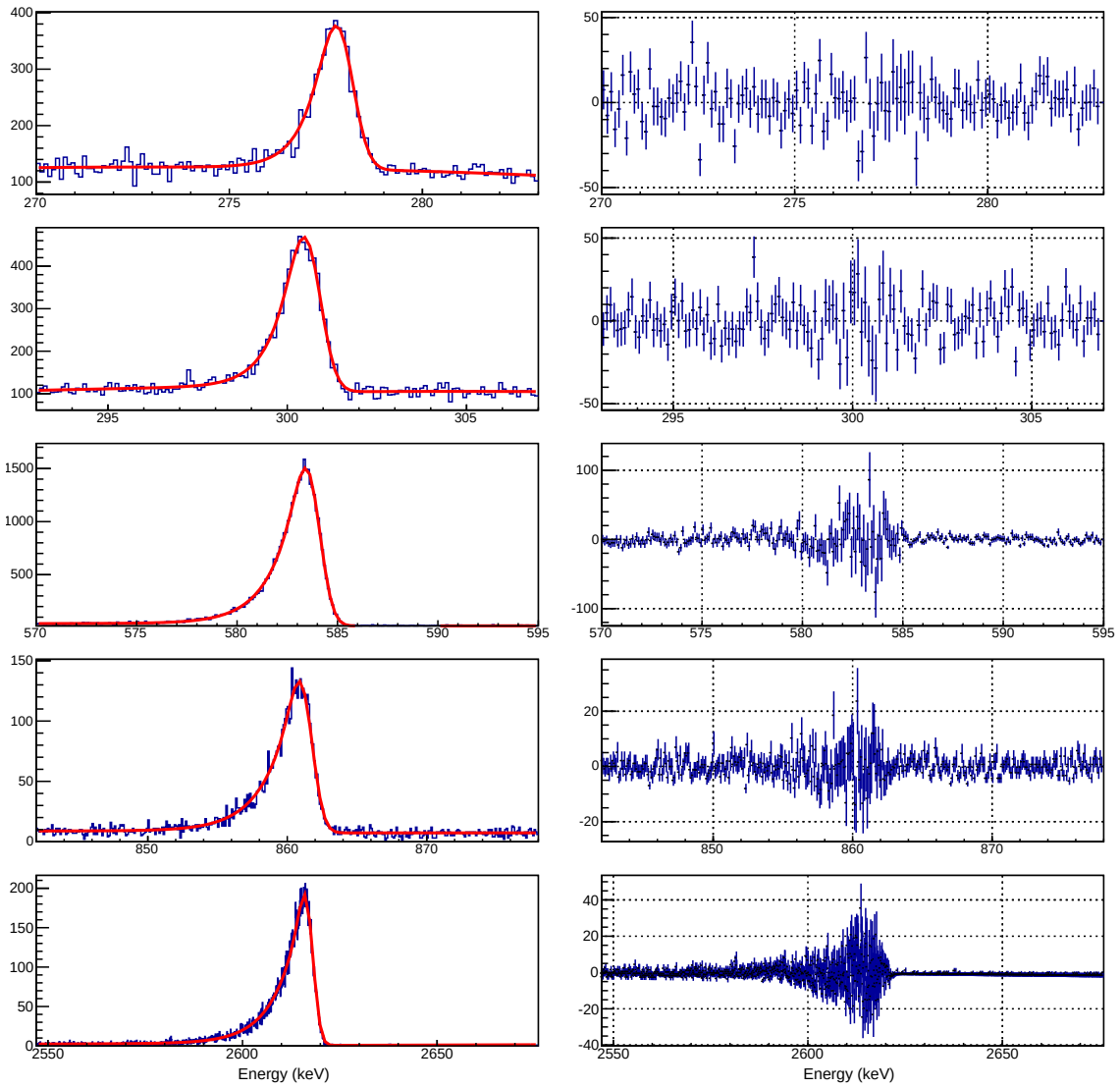

Figure B.23: The five gamma peaks of S1D3 in calibration data set B that are fit with the multi-peak fitting routine. Shown on the left is each of the five peaks with the best fit of the multi-peak fitting function shown in red. Shown on the right is the residual of the fit for each peak.

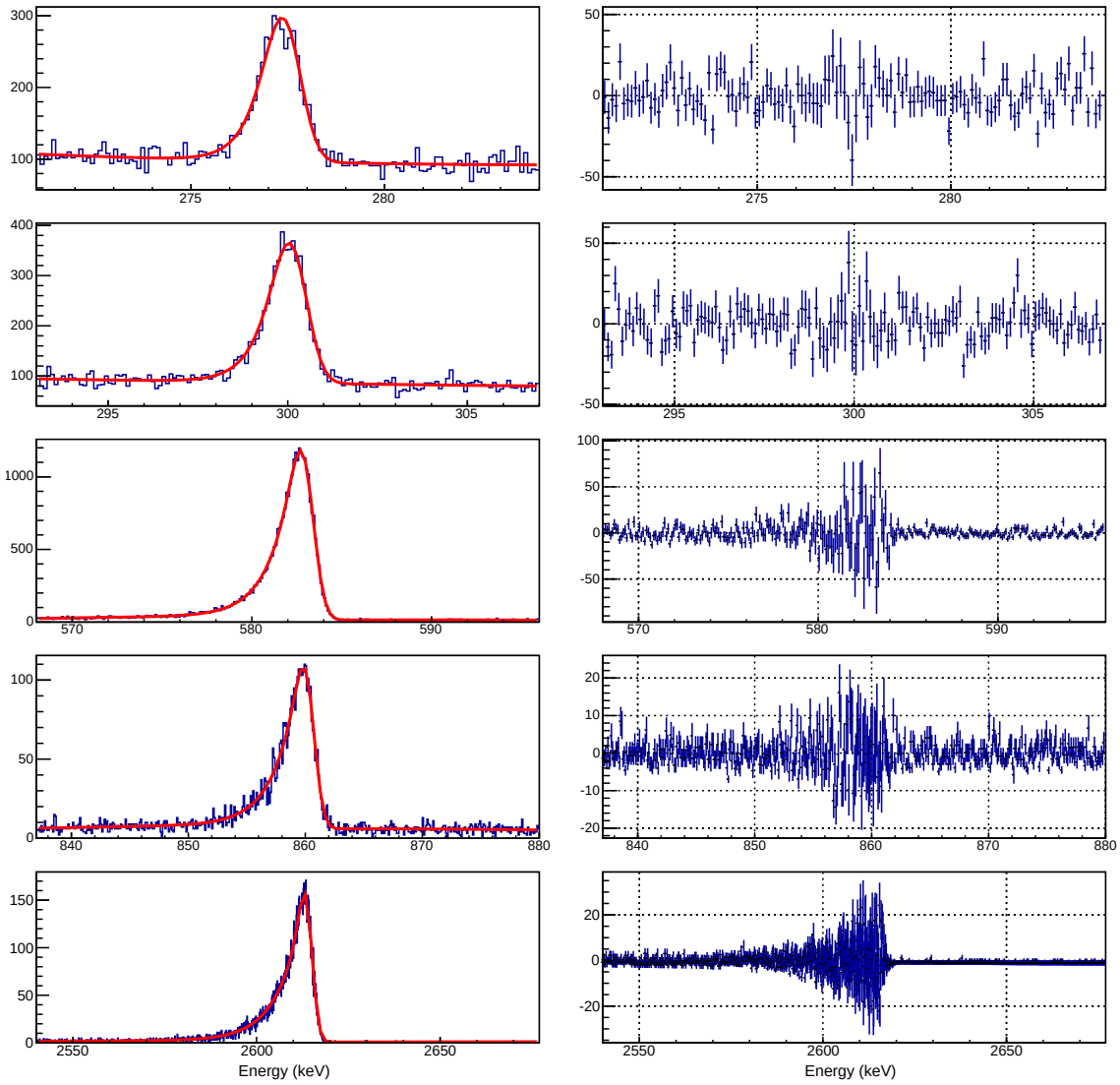

Figure B.24: The five gamma peaks of S1D3 in calibration data set C that are fit with the multi-peak fitting routine. Shown on the left is each of the five peaks with the best fit of the multi-peak fitting function shown in red. Shown on the right is the residual of the fit for each peak.

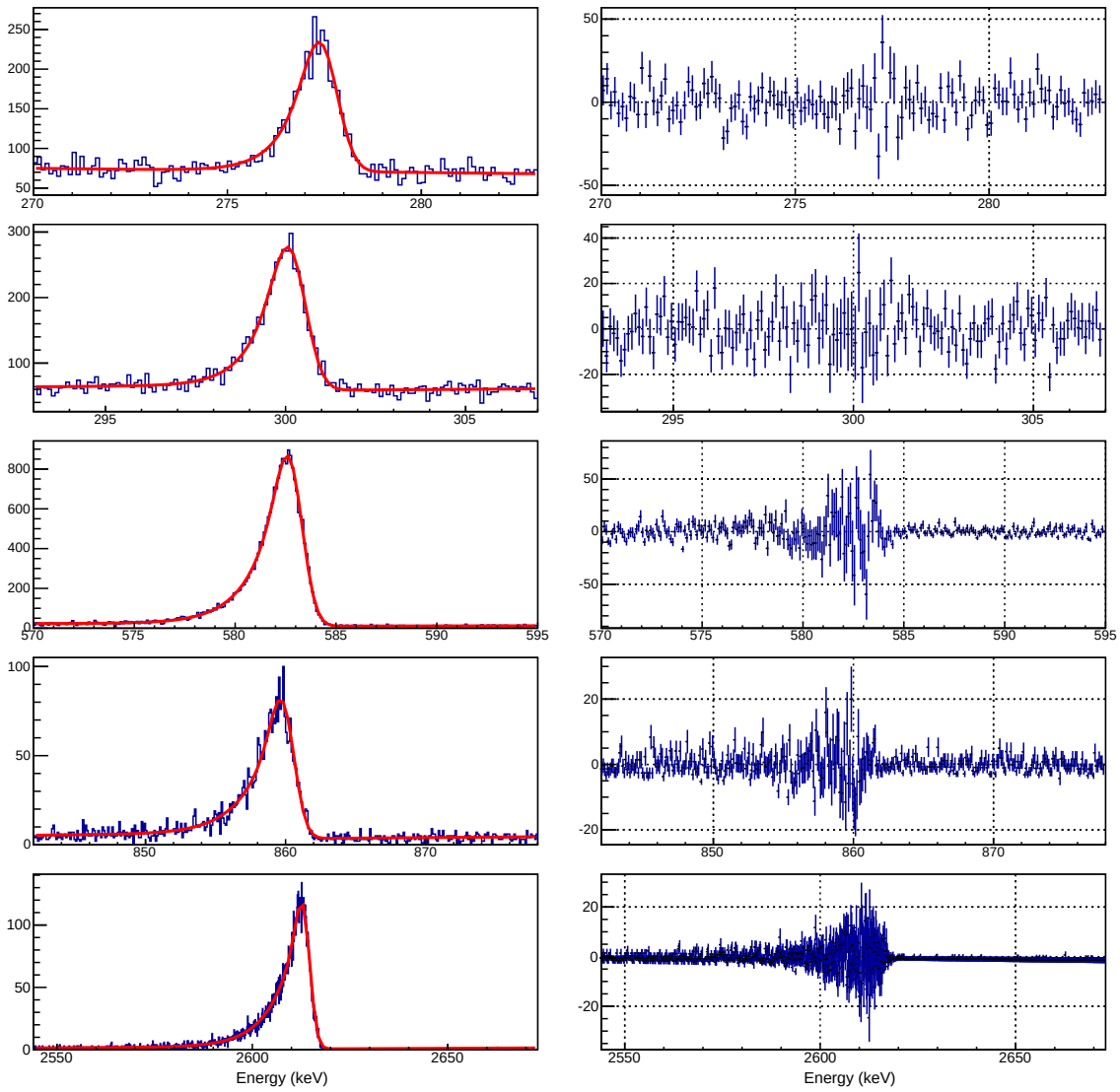

Figure B.25: The five gamma peaks of S1D3 in calibration data set D that are fit with the multi-peak fitting routine. Shown on the left is each of the five peaks with the best fit of the multi-peak fitting function shown in red. Shown on the right is the residual of the fit for each peak.

B.3 S3D1 of the PC (Detector B8607)

All five gamma-peaks in S3D1 of the PC can be fit in four of the five calibration data sets. Data set E is the only data set in which S3D1 cannot be fit but as discussed in Chapter 4, data set E is not used when fitting any of the common parameters over time regardless.

B.3.1 Summary of Fit Results

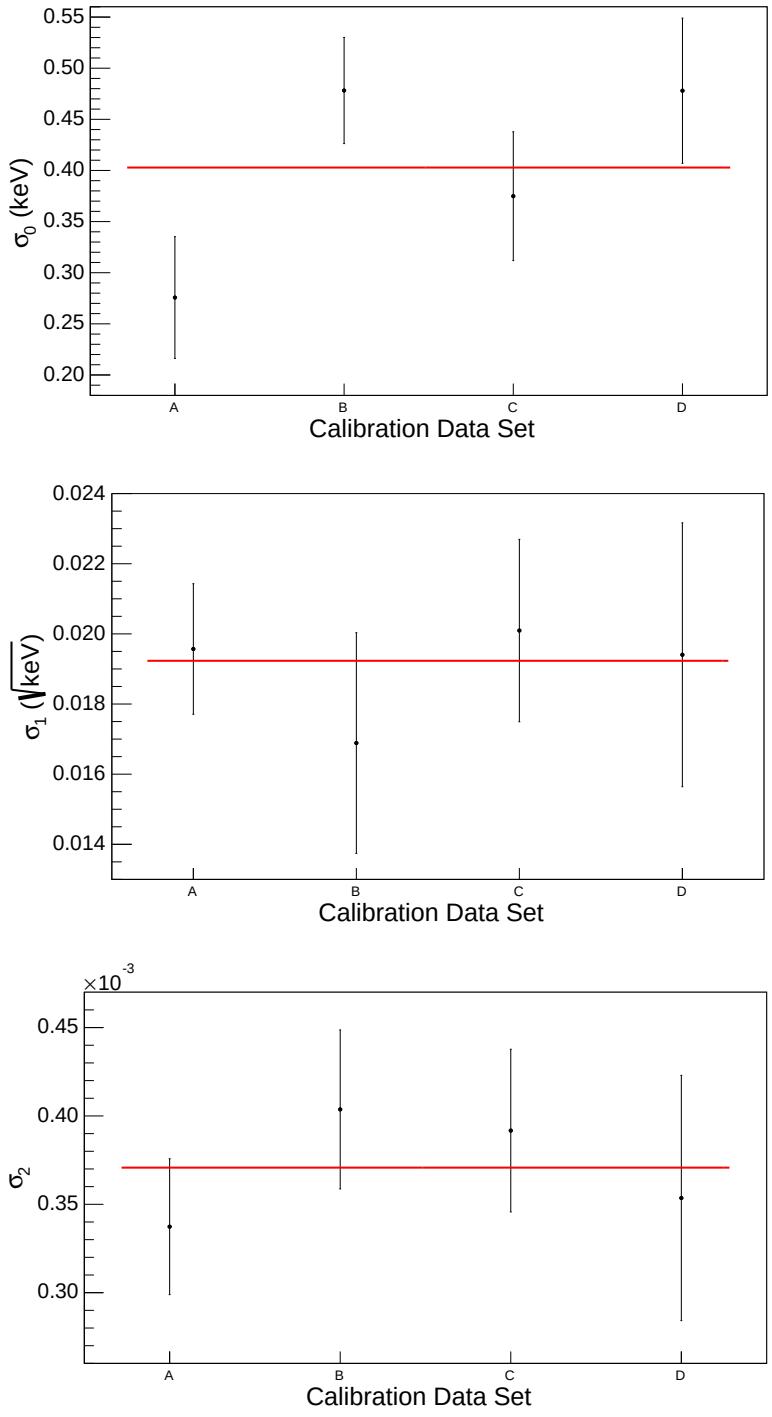

Figure B.26: Parameter σ_0 (top), σ_1 (middle) and σ_2 (bottom) for S3D1 over time. Data with solid error bars are fit with a constant over time. The best fits result in average values of: $\sigma_0 = 0.40\ (3)$ keV, $\sigma_1 = 1.9\ (1)\cdot 10^{-2}$ keV$^{1/2}$ and $\sigma_2 = 3.7\ (2)\cdot 10^{-4}$.

Table B.15: Common parameters of S3D1 for all calibration data.

	Calibration Data Set				
	A	B	C	D	E
σ_0 [keV]	0.28 (6)	0.48 (5)	0.37 (6)	0.48 (7)	-
$\sigma_1/10^{-2}$ [keV$^{1/2}$]	2.0 (2)	1.7 (3)	2.0 (3)	1.9 (4)	-
$\sigma_2/10^{-4}$	3.4 (4)	4.0 (4)	3.9 (5)	3.5 (7)	-
b_τ [keV]	0†	0†	0†	0†	-
m_τ	0†	0†	0†	0†	-
b_H	0†	0†	0†	0†	-
m_H [keV^{-1}]	0†	0†	0†	0†	-
Runtime [hrs]	4.303	5.155	4.383	3.361	0.871
Fixed Parameters	$m_H = b_H = 0$ $m_\tau = b_\tau = 0$				-

† The best fit results in the parameter b_H being consistent with zero. Therefore the final fit is performed with b_τ, m_τ, b_H and m_H fixed to be zero.

Table B.16: Peak #1 parameters of S3D1 for all calibration data.

	Calibration Data Set				
	A	B	C	D	E
μ [keV]	277.34 (3)	277.63 (4)	277.51 (4)	277.72 (5)	-
A/t $[cts/hr]$	32 (2)	31 (2)	27 (2)	29 (2)	-
H_{step}	0 (1)$\cdot 10^{-2}$	2.0 (8)$\cdot 10^{-2}$	0 (3)$\cdot 10^{-3}$	4 (1)$\cdot 10^{-2}$	-
σ [keV]	0.44 (2)	0.57 (2)	0.51 (2)	0.59 (3)	-
τ [keV]	0†	0†	0†	0†	-
H_{tail}	0†	0†	0†	0†	-
M	277.34 (3)	277.63 (4)	277.51 (4)	277.72 (5)	-
Σ [keV]	0.44 (2)	0.57 (2)	0.51 (2)	0.59 (3)	-
FWHM [keV]	1.03 (4)	1.33 (5)	1.21 (5)	1.38 (6)	-
Runtime [hrs]	4.303	5.155	4.383	3.361	0.871
Fixed Parameters	$m_H = b_H = 0$ $m_\tau = b_\tau = 0$				-

† The best fit results in the parameter b_H being consistent with zero. Therefore the final fit is performed with b_τ, m_τ, b_H and m_H fixed to be zero.

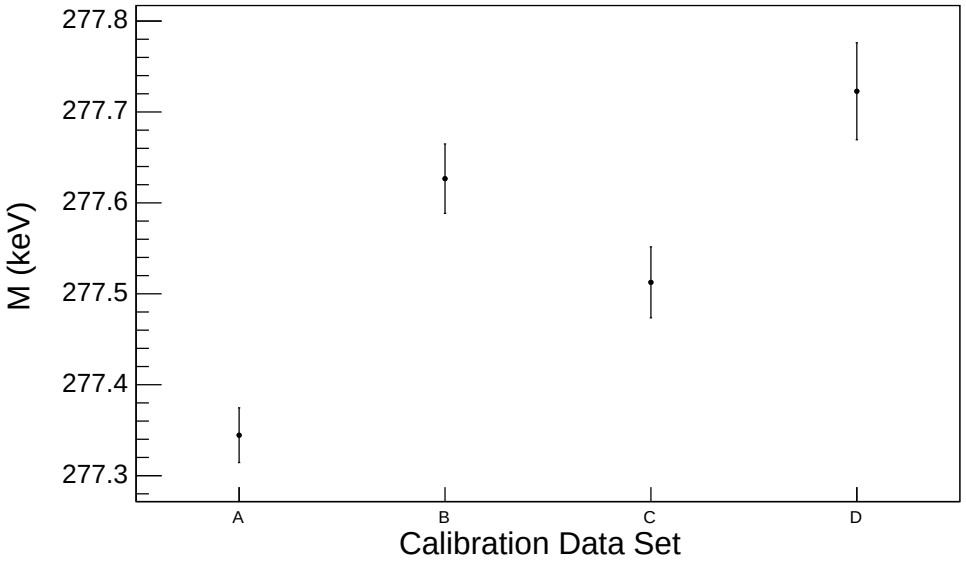

Figure B.27: The centroid (M) of peak #1 for S3D1 over time.

Table B.17: Peak #2 parameters of S3D1 for all calibration data.

	Calibration Data Set				
	A	B	C	D	E
μ [keV]	300.03 (2)	300.29 (3)	300.28 (3)	300.39 (4)	-
A/t $[cts/hr]$	42 (2)	44 (2)	43 (2)	39 (2)	-
H_{step}	0 (3)$\cdot 10^{-4}$	6 (6)$\cdot 10^{-3}$	0 (4)$\cdot 10^{-4}$	1.8 (9)$\cdot 10^{-2}$	-
σ [keV]	0.45 (2)	0.57 (2)	0.52 (2)	0.59 (2)	-
τ [keV]	0†	0†	0†	0†	-
H_{tail}	0†	0†	0†	0†	-
M	300.03 (2)	300.29 (3)	300.28 (3)	300.39 (4)	-
Σ [keV]	0.45 (2)	0.57 (2)	0.52 (2)	0.59 (2)	-
FWHM [keV]	1.06 (4)	1.35 (4)	1.24 (4)	1.40 (6)	-
Runtime [hrs]	4.303	5.155	4.383	3.361	0.871
Fixed Parameters	$m_H = b_H = 0$ $m_\tau = b_\tau = 0$				-

† The best fit results in the parameter b_H being consistent with zero. Therefore the final fit is performed with b_τ, m_τ, b_H and m_H fixed to be zero.

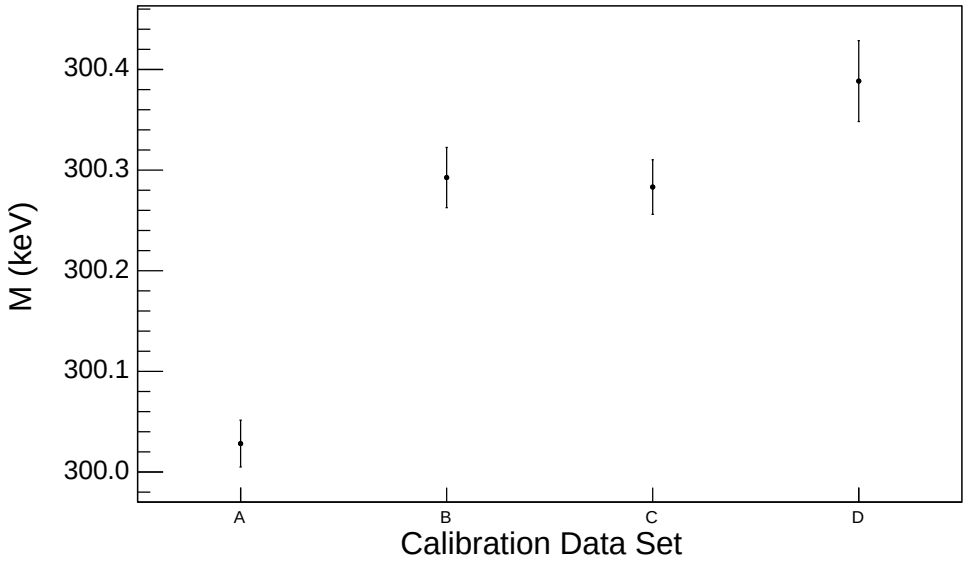

Figure B.28: The centroid (M) of peak #2 for S3D1 over time.

Table B.18: Peak #3 parameters of S3D1 for all calibration data.

Parameter	Calibration Data Set				
	A	B	C	D	E
μ [keV]	583.278 (8)	583.171 (8)	583.205 (9)	583.31 (1)	-
A/t [cts/hr]	317 (4)	309 (3)	303 (4)	293 (4)	-
H_{step}	1.1 (8)$\cdot 10^{-3}$	2 (1)$\cdot 10^{-3}$	1 (1)$\cdot 10^{-3}$	3.1 (5)$\cdot 10^{-3}$	-
σ [keV]	0.581 (6)	0.671 (6)	0.654 (7)	0.700 (8)	-
τ [keV]	$0^{\dagger}$	$0^{\dagger}$	$0^{\dagger}$	$0^{\dagger}$	-
H_{tail}	$0^{\dagger}$	$0^{\dagger}$	$0^{\dagger}$	$0^{\dagger}$	-
M	583.278 (8)	583.171 (8)	583.205 (9)	583.31 (1)	-
Σ [keV]	0.581 (6)	0.671 (6)	0.654 (7)	0.700 (8)	-
FWHM [keV]	1.37 (1)	1.58 (1)	1.54 (2)	1.65 (2)	-
Runtime [hrs]	4.303	5.155	4.383	3.361	0.871
Fixed Parameters	$m_H = b_H = 0$ $m_\tau = b_\tau = 0$				-

† The best fit results in the parameter b_H being consistent with zero. Therefore the final fit is performed with b_τ, m_τ, b_H and m_H fixed to be zero.

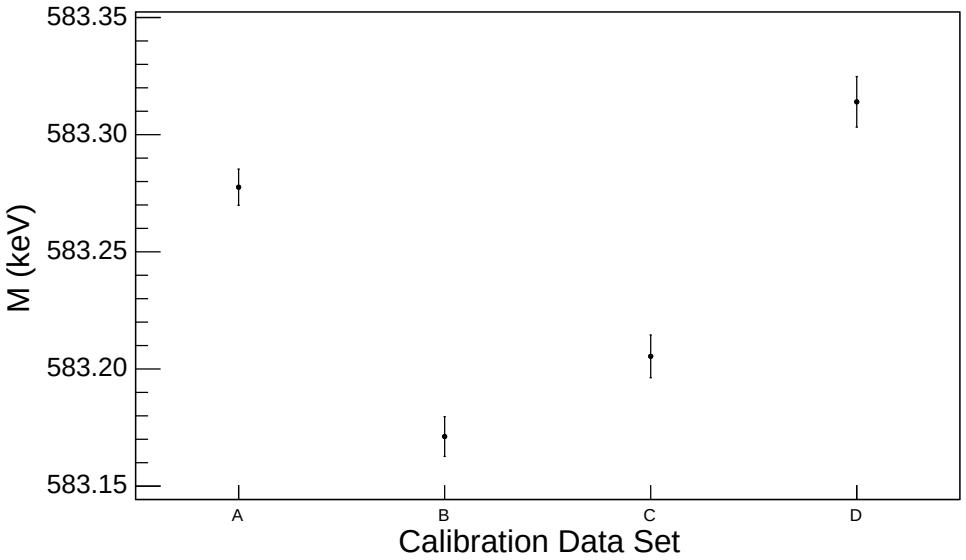

Figure B.29: The centroid (M) of peak #3 for S3D1 over time.

Table B.19: Peak #4 parameters of S3D1 for all calibration data.

Parameter	Calibration Data Set				
	A	B	C	D	E
μ [keV]	860.83 (3)	860.61 (3)	860.67 (3)	860.84 (4)	-
A/t $[cts/hr]$	39 (1)	38 (1)	38 (1)	36 (2)	-
H_{step}	0 (2)$\cdot 10^{-3}$	0 (2)$\cdot 10^{-6}$	0 (5)$\cdot 10^{-5}$	1.0 (2)$\cdot 10^{-2}$	-
σ [keV]	0.70 (1)	0.77 (1)	0.78 (1)	0.80 (2)	-
τ [keV]	0†	0†	0†	0†	-
H_{tail}	0†	0†	0†	0†	-
M	860.83 (3)	860.61 (3)	860.67 (3)	860.84 (4)	-
Σ [keV]	0.70 (1)	0.77 (1)	0.78 (1)	0.80 (2)	-
FWHM [keV]	1.65 (2)	1.82 (3)	1.83 (3)	1.89 (4)	-
Runtime [hrs]	4.303	5.155	4.383	3.361	0.871
Fixed Parameters	$m_H = b_H = 0$				-
	$m_\tau = b_\tau = 0$				

† The best fit results in the parameter b_H being consistent with zero. Therefore the final fit is performed with b_τ, m_τ, b_H and m_H fixed to be zero.

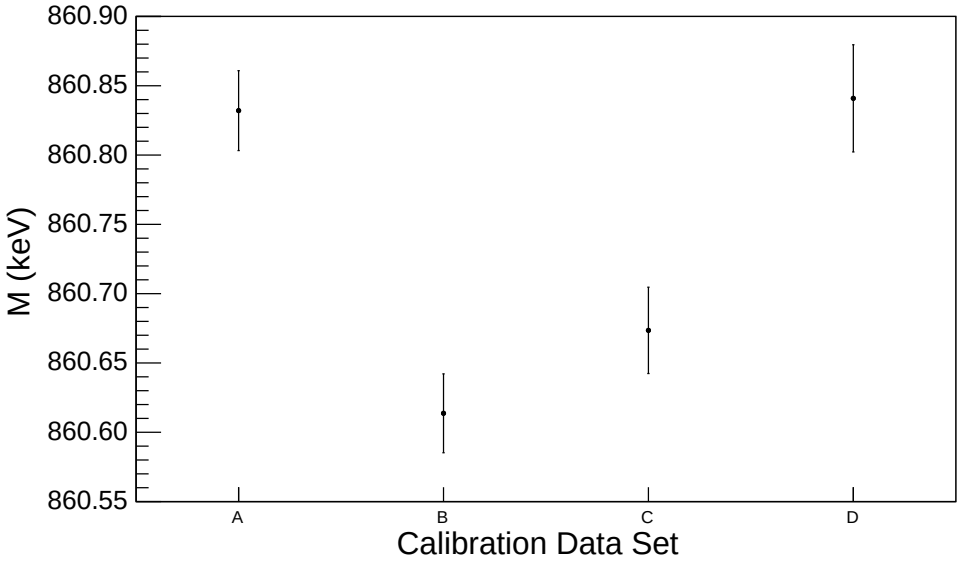

Figure B.30: The centroid (M) of peak #4 for S3D1 over time.

Table B.20: Peak #5 parameters of S3D1 for all calibration data.

Parameter	Calibration Data Set				
	A	B	C	D	E
μ [keV]	2615.30 (3)	2614.72 (3)	2615.23 (3)	2615.26 (3)	-
A/t [cts/hr]	153 (3)	149 (2)	146 (3)	138 (3)	-
H_{step}	1 (5)$\cdot 10^{-8}$	2.0 (3)$\cdot 10^{-3}$	1.4 (9)$\cdot 10^{-3}$	2.1 (6)$\cdot 10^{-3}$	-
σ [keV]	1.36 (2)	1.45 (2)	1.50 (2)	1.44 (3)	-
τ [keV]	$0^{\dagger}$	$0^{\dagger}$	$0^{\dagger}$	$0^{\dagger}$	-
H_{tail}	$0^{\dagger}$	$0^{\dagger}$	$0^{\dagger}$	$0^{\dagger}$	-
M	2615.30 (3)	2614.72 (3)	2615.23 (3)	2615.26 (3)	-
Σ [keV]	1.36 (2)	1.45 (2)	1.50 (2)	1.44 (3)	-
FWHM [keV]	3.21 (5)	3.40 (5)	3.53 (6)	3.39 (7)	-
Runtime [hrs]	4.303	5.155	4.383	3.361	0.871
Fixed Parameters	$m_H = b_H = 0$ $m_\tau = b_\tau = 0$				-

† The best fit results in the parameter b_H being consistent with zero. Therefore the final fit is performed with b_τ, m_τ, b_H and m_H fixed to be zero.

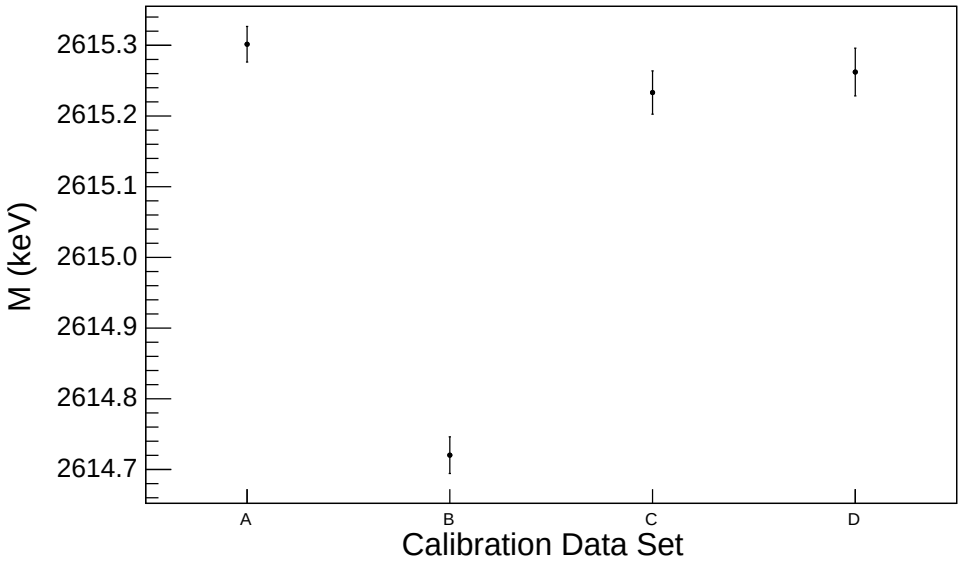

Figure B.31: The centroid (M) of peak #5 for S3D1 over time.

Table B.21: The peak rate for each of the five peaks during each of the four calibration data sets for S3D1. The peak rate is the area parameter divided by the runtime divided by the bin width (0.1 keV). Also shown is the ratio of each peak's rate to the 583-keV peak rate (i.e. Pk #3).

		Calibration Data Set				
		A	B	C	D	E
Pk Rate $\left[\frac{cts}{hr}\right]$	Pk #1	320 (20)	310 (20)	270 (20)	290 (20)	-
	Pk #2	420 (20)	440 (20)	430 (20)	390 (20)	-
	Pk #3	3170 (40)	3090 (30)	3030 (40)	2930 (40)	-
	Pk #4	390 (10)	380 (10)	380 (10)	360 (20)	-
	Pk #5	1530 (30)	1490 (20)	1460 (30)	1380 (30)	-
$\frac{\text{Pk } \#n \text{ Rate}}{\text{Pk } \#3 \text{ Rate}}$	$n = 1$	0.102 (6)	0.101 (6)	0.088 (6)	0.099 (7)	-
	$n = 2$	0.133 (6)	0.141 (6)	0.141 (7)	0.133 (8)	-
	$n = 3$	1.	1.	1.	1.	-
	$n = 4$	0.123 (5)	0.123 (4)	0.124 (5)	0.123 (6)	-
	$n = 5$	0.48 (1)	0.480 (10)	0.48 (1)	0.47 (1)	-

B.3.2 Individual Peak Fits

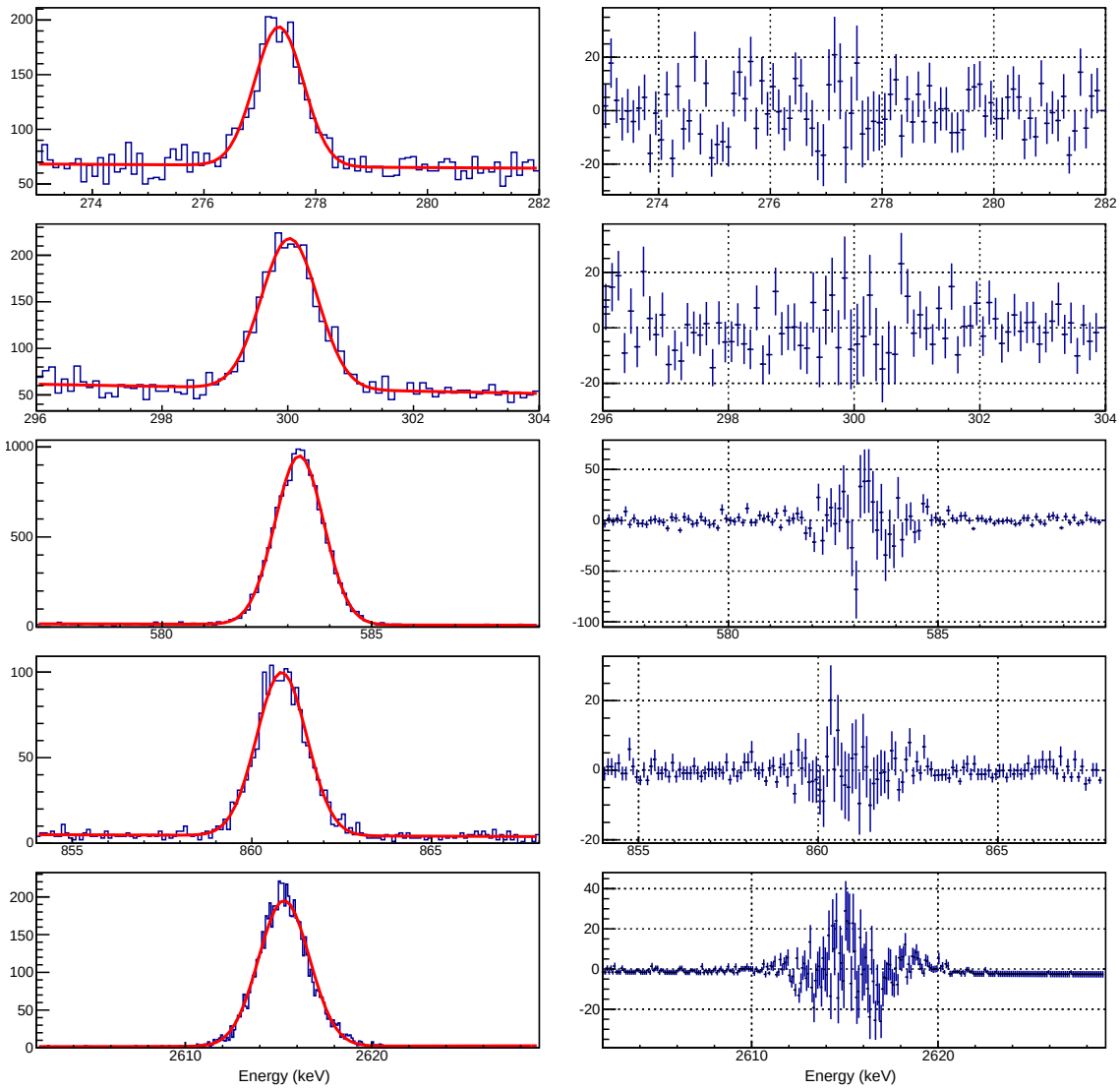

Figure B.32: The five gamma peaks of S3D1 in calibration data set A that are fit with the multi-peak fitting routine. Shown on the left is each of the five peaks with the best fit of the multi-peak fitting function shown in red. Shown on the right is the residual of the fit for each peak.

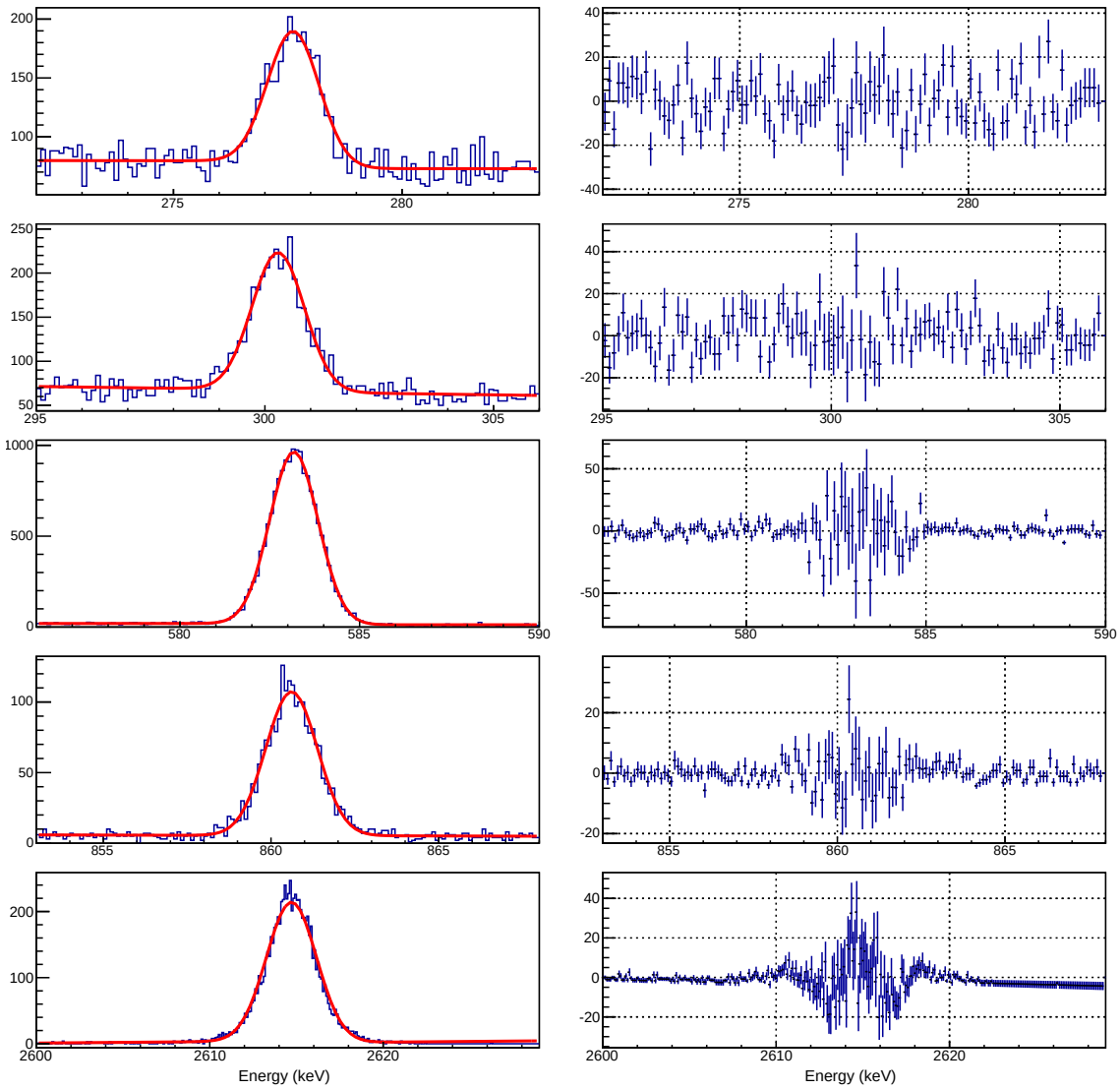

Figure B.33: The five gamma peaks of S3D1 in calibration data set B that are fit with the multi-peak fitting routine. Shown on the left is each of the five peaks with the best fit of the multi-peak fitting function shown in red. Shown on the right is the residual of the fit for each peak.

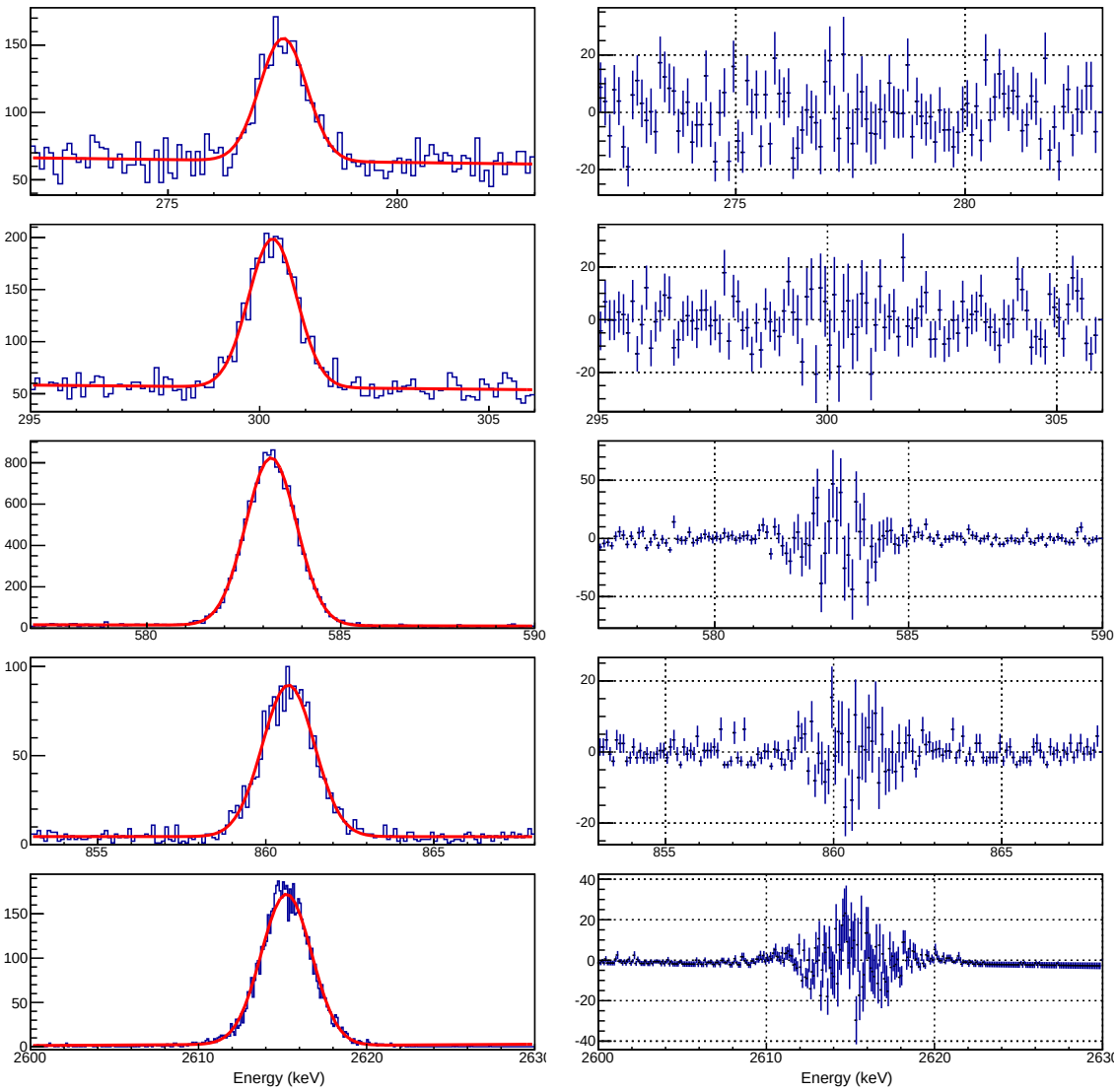

Figure B.34: The five gamma peaks of S3D1 in calibration data set C that are fit with the multi-peak fitting routine. Shown on the left is each of the five peaks with the best fit of the multi-peak fitting function shown in red. Shown on the right is the residual of the fit for each peak.

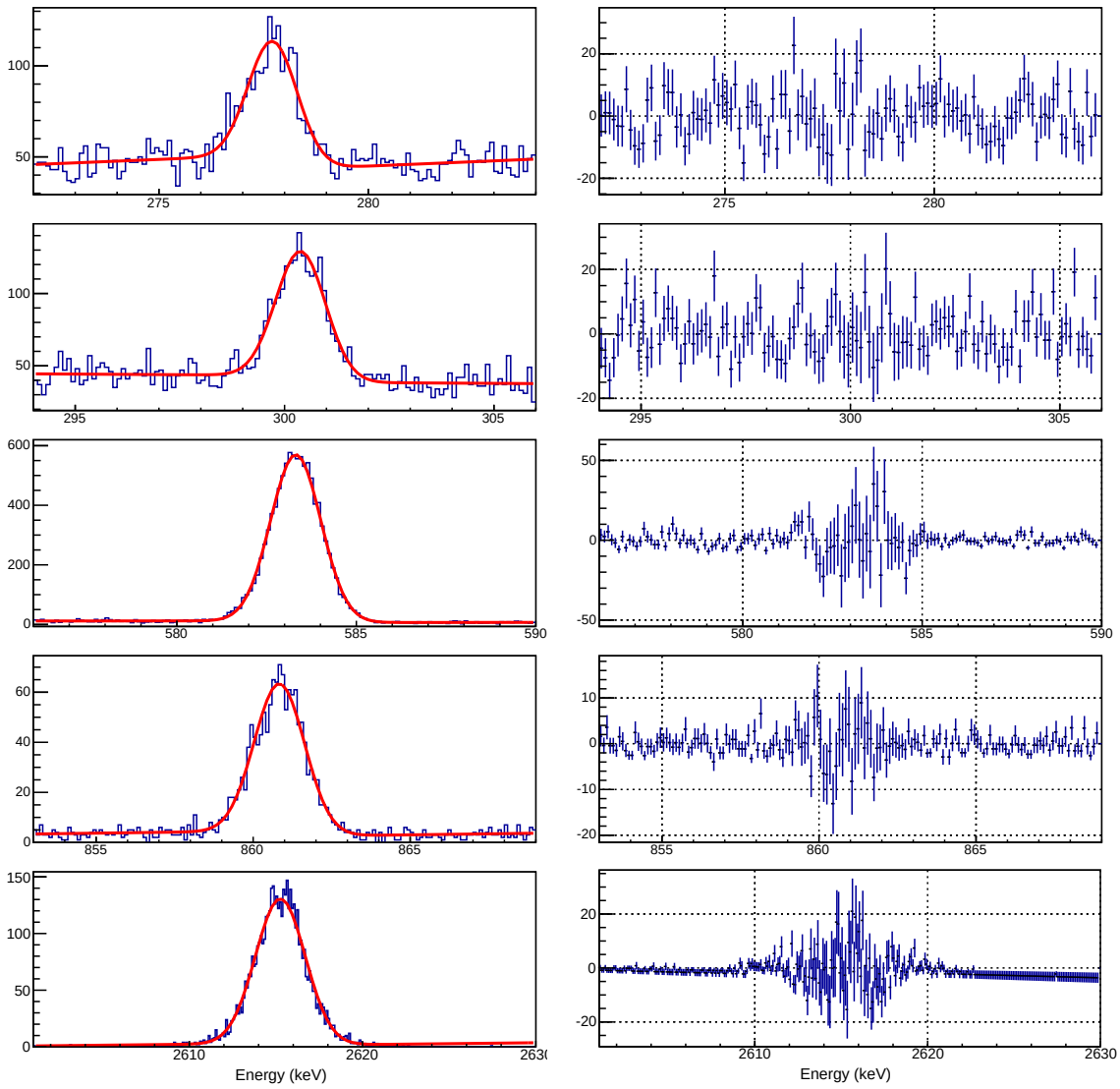

Figure B.35: The five gamma peaks of S3D1 in calibration data set D that are fit with the multi-peak fitting routine. Shown on the left is each of the five peaks with the best fit of the multi-peak fitting function shown in red. Shown on the right is the residual of the fit for each peak.

Table B.22: Common parameters of S3D2 for all calibration data.

	Calibration Data Set				
	A	B	C	D	E
σ_0 [keV]	0.34 (4)	0.38 (4)	0.34 (4)	0.48 (5)	0.21 (6)
$\sigma_1/10^{-2}$ [keV$^{1/2}$]	1.7 (2)	2.0 (2)	2.1 (2)	1.8 (3)	2.42 (9)
$\sigma_2/10^{-4}$	2.8 (4)	1.9 (7)	1.8 (7)	2.3 (8)	0 (5)
b_τ [keV]	0.0 (2)	0.2 (2)	0.5 (2)	0.4 (3)	0†
$m_\tau/10^{-3}$	0.9 (2)	0.6 (1)	0.6 (1)	0.5 (2)	0†
b_H	0.12 (7)	0.18 (9)	0.10 (4)	0.2 (1)	0†
$m_H/10^{-4}$ [keV^{-1}]	0.1 (3)	0.3 (4)	0.6 (3)	0.4 (6)	0†
Runtime [hrs]	4.471	5.155	4.383	3.361	0.871
Fixed Parameters	-	-	-	-	$m_H = b_H = 0$ $m_\tau = b_\tau = 0$

† The best fit results in the parameter b_H being consistent with zero. Therefore the final fit is performed with b_τ, m_τ, b_H and m_H fixed to be zero.

B.4 S3D2 of the PC (Detector B8456)

All five gamma-peaks in S3D2 of the PC can be fit in all five of the calibration data sets. As discussed in Chapter 4, data set E is not used when fitting any of the common parameters over time. Additionally, the best fit for data set A yields an unphysical, negative value for parameter b_τ. The negative parameter does not affect the peak shape in the energy range that is investigated here and when the parameter's error is considered it is consistent with zero; therefore the fit is accepted. However this negative value is not used with fitting the parameter over time.

B.4.1 Summary of Fit Results

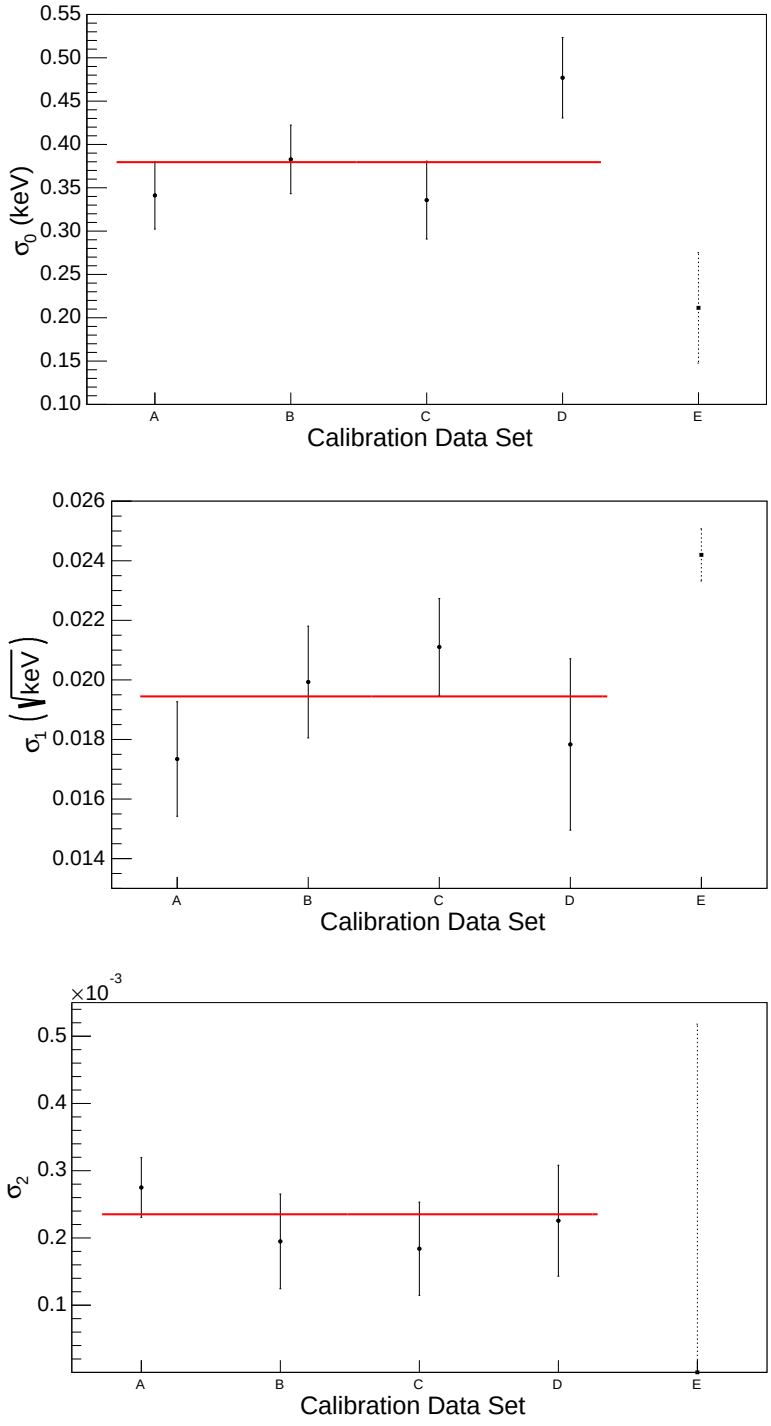

Figure B.36: Parameter σ_0 (top), σ_1 (middle) and σ_2 (bottom) for S3D2 over time. Data with solid error bars are fit with a constant over time. The best fits result in average values of: $\sigma_0 = 0.38\ (2)$ keV, $\sigma_1 = 1.94\ (10)\cdot 10^{-2}$ keV$^{1/2}$ and $\sigma_2 = 2.4\ (3)\cdot 10^{-4}$.

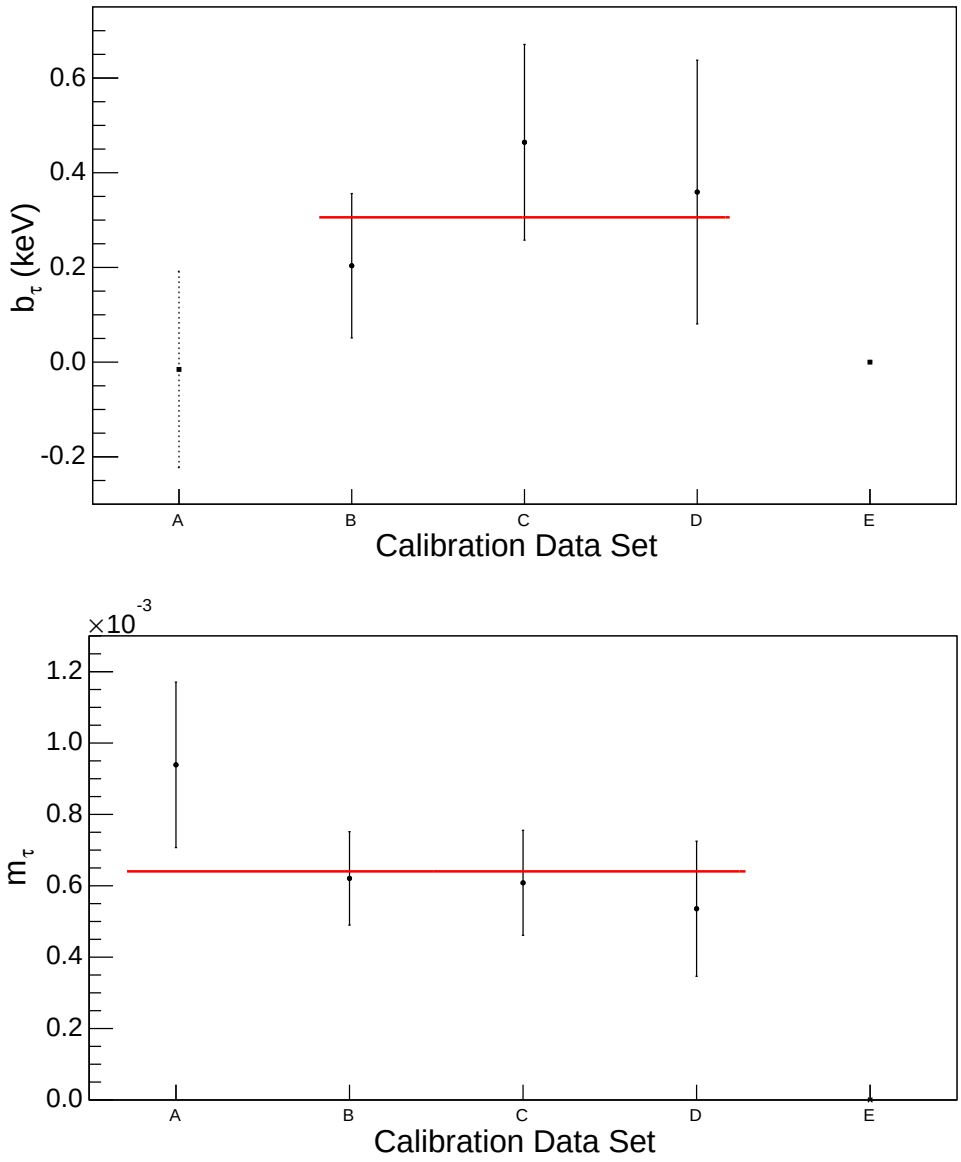

Figure B.37: Parameter b_τ (top) and m_τ (bottom) for S3D2 over time. Data with solid error bars are fit with a constant over time. The best fits result in average values of: $b_\tau = 0.3\ (1)$ keV and $m_\tau = 6.4\ (8) \cdot 10^{-4}$.

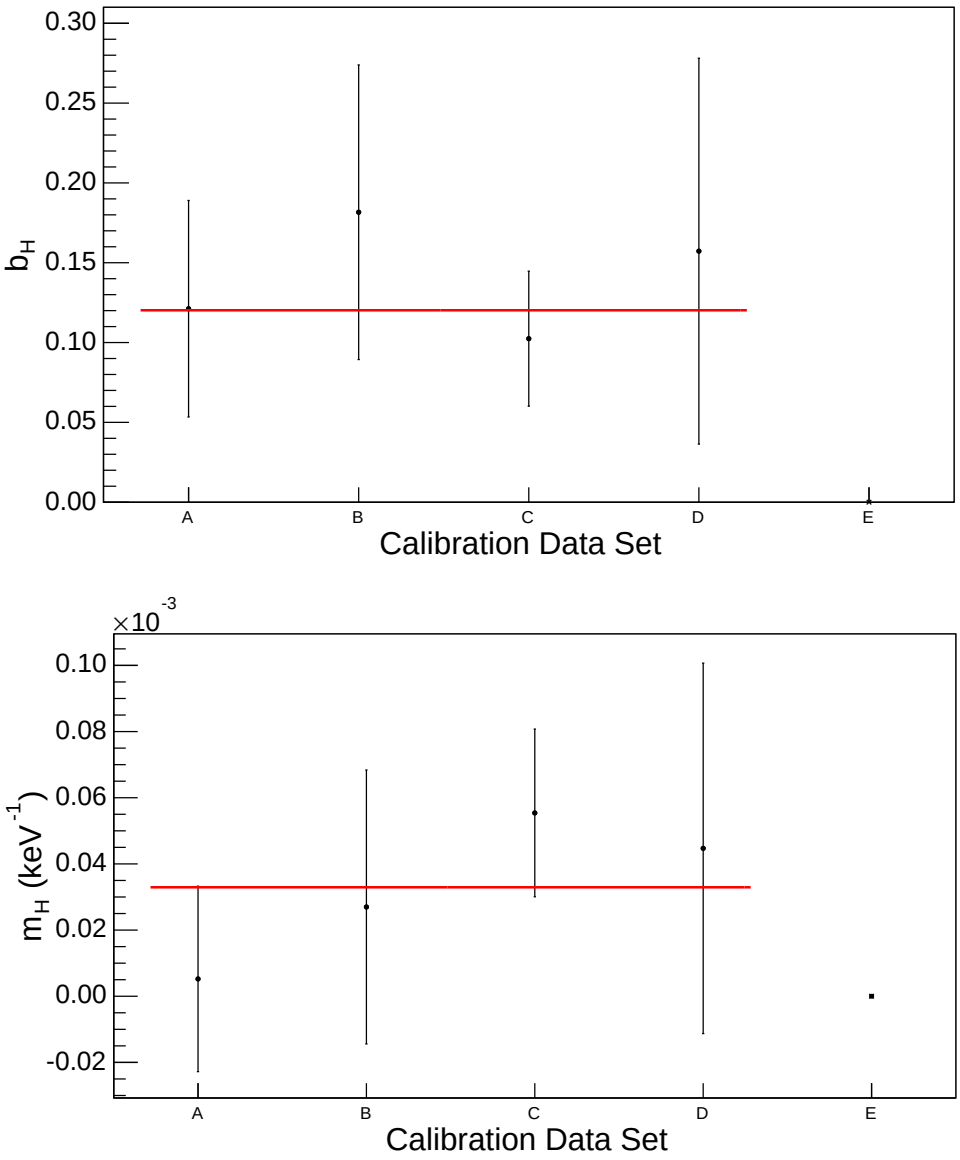

Figure B.38: Parameter b_H (top) and m_H (bottom) for S3D2 over time. Data with solid error bars are fit with a constant over time. The best fits result in average values of: $b_H = 0.12\ (3)$ and $m_H = 3\ (2)\cdot 10^{-5}$ keV^{-1}.

Table B.23: Peak #1 parameters of S3D2 for all calibration data.

	Calibration Data Set				
	A	B	C	D	E
μ [keV]	277.38 (2)	277.42 (3)	277.41 (3)	277.46 (5)	277.41 (5)
A/t [cts/hr]	59 (2)	60 (2)	58 (2)	57 (3)	55 (5)
H_{step}	2.4 (4)$\cdot 10^{-2}$	0 (3)$\cdot 10^{-4}$	0 (1)$\cdot 10^{-4}$	0.01 (2)	0.02 (2)
σ [keV]	0.45 (1)	0.51 (1)	0.49 (2)	0.57 (2)	0.46 (2)
τ [keV]	0.2 (2)	0.4 (1)	0.6 (2)	0.5 (3)	0†
H_{tail}	0.12 (8)	0.2 (1)	0.12 (7)	0.2 (2)	0†
M	277.35 (2)	277.35 (2)	277.34 (3)	277.38 (4)	277.41 (5)
Σ [keV]	0.47 (1)	0.55 (2)	0.57 (2)	0.63 (3)	0.46 (2)
FWHM [keV]	1.09 (3)	1.24 (5)	1.18 (5)	1.38 (7)	1.07 (4)
Runtime [hrs]	4.471	5.155	4.383	3.361	0.871
Fixed Parameters	-	-	-	-	$m_H = b_H = 0$ $m_\tau = b_\tau = 0$

† The best fit results in the parameter b_H being consistent with zero. Therefore the final fit is performed with b_τ, m_τ, b_H and m_H fixed to be zero.

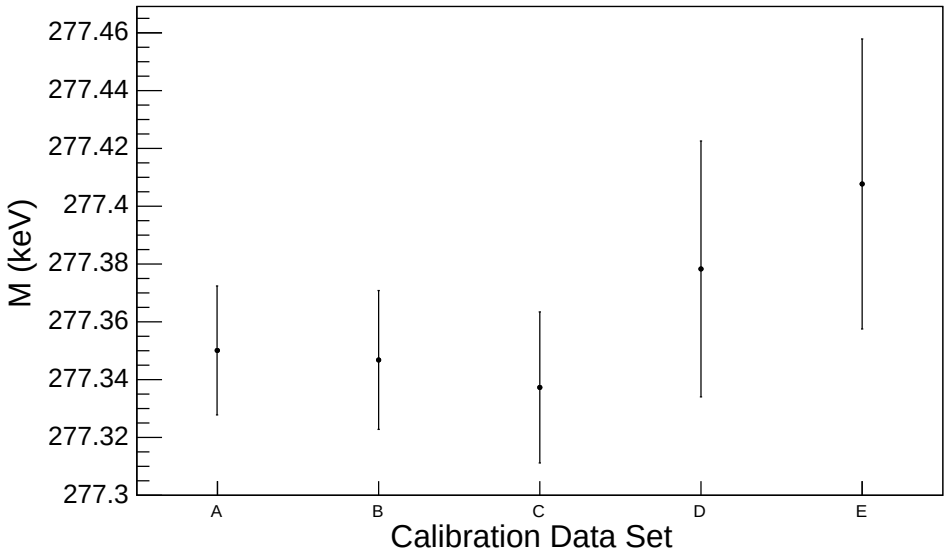

Figure B.39: The centroid (M) of peak #1 for S3D2 over time.

Table B.24: Peak #2 parameters of S3D2 for all calibration data.

Parameter	Calibration Data Set				
	A	B	C	D	E
μ [keV]	300.10 (2)	300.10 (2)	300.08 (2)	300.09 (4)	300.07 (4)
A/t $[cts/hr]$	86 (2)	86 (3)	80 (3)	79 (3)	74 (5)
H_{step}	0 (1)$\cdot 10^{-4}$	0 (1)$\cdot 10^{-4}$	0.7 (5)$\cdot 10^{-2}$	0 (1)$\cdot 10^{-2}$	0.03 (1)
σ [keV]	0.46 (1)	0.52 (1)	0.50 (1)	0.57 (2)	0.47 (2)
τ [keV]	0.3 (2)	0.4 (1)	0.6 (2)	0.5 (3)	0†
H_{tail}	0.12 (8)	0.2 (1)	0.12 (7)	0.2 (2)	0†
M	300.07 (2)	300.02 (2)	300.00 (2)	300.00 (4)	300.07 (4)
Σ [keV]	0.48 (1)	0.57 (2)	0.59 (2)	0.64 (3)	0.47 (2)
FWHM [keV]	1.11 (3)	1.26 (4)	1.21 (4)	1.39 (7)	1.11 (4)
Runtime [hrs]	4.471	5.155	4.383	3.361	0.871
Fixed Parameters	-	-	-	-	$m_H = b_H = 0$ $m_\tau = b_\tau = 0$

† The best fit results in the parameter b_H being consistent with zero. Therefore the final fit is performed with b_τ, m_τ, b_H and m_H fixed to be zero.

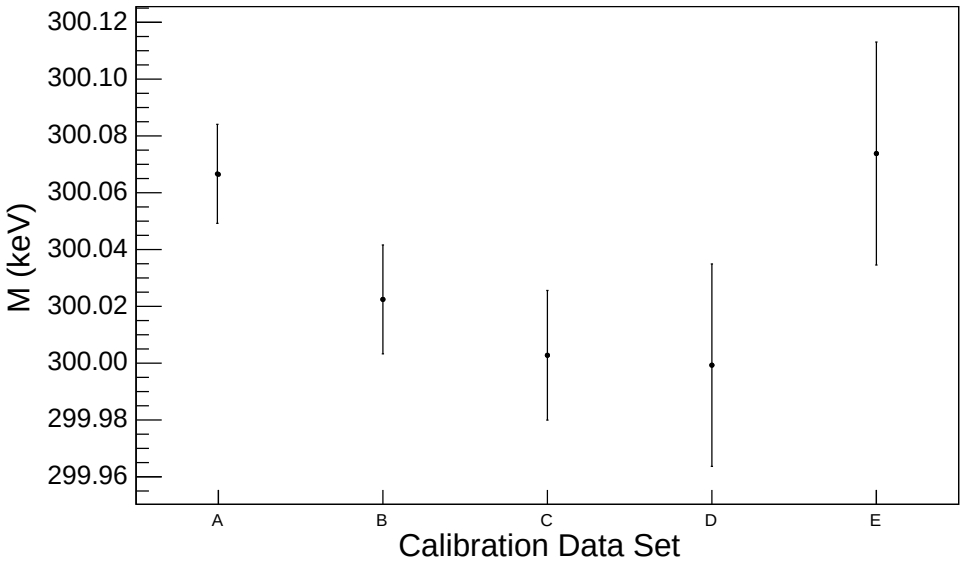

Figure B.40: The centroid (M) of peak #2 for S3D2 over time.

Table B.25: Peak #3 parameters of S3D2 for all calibration data.

Parameter	Calibration Data Set				
	A	B	C	D	E
μ [keV]	583.12 (2)	583.10 (3)	583.09 (1)	583.13 (4)	583.12 (1)
A/t $[cts/hr]$	558 (5)	549 (5)	550 (5)	523 (6)	520 (10)
H_{step}	$1.7\ (3)\cdot10^{-3}$	$0.9\ (10)\cdot10^{-3}$	$0.1\ (4)\cdot10^{-3}$	$0.1\ (1)\cdot10^{-2}$	$7.3\ (8)\cdot10^{-3}$
σ [keV]	0.563 (7)	0.63 (1)	0.620 (8)	0.66 (1)	0.621 (10)
τ [keV]	0.5 (1)	0.6 (1)	0.8 (2)	0.7 (2)	$0^{\dagger}$
H_{tail}	0.12 (8)	0.2 (1)	0.13 (6)	0.2 (2)	$0^{\dagger}$
M	583.051 (8)	582.992 (9)	582.98 (1)	583.01 (2)	583.12 (1)
Σ [keV]	0.62 (1)	0.71 (2)	0.74 (2)	0.76 (3)	0.621 (10)
FWHM [keV]	1.36 (2)	1.53 (3)	1.50 (3)	1.61 (5)	1.46 (2)
Runtime [hrs]	4.471	5.155	4.383	3.361	0.871
Fixed Parameters	-	-	-	-	$m_H = b_H = 0$ $m_\tau = b_\tau = 0$

† The best fit results in the parameter b_H being consistent with zero. Therefore the final fit is performed with b_τ, m_τ, b_H and m_H fixed to be zero.

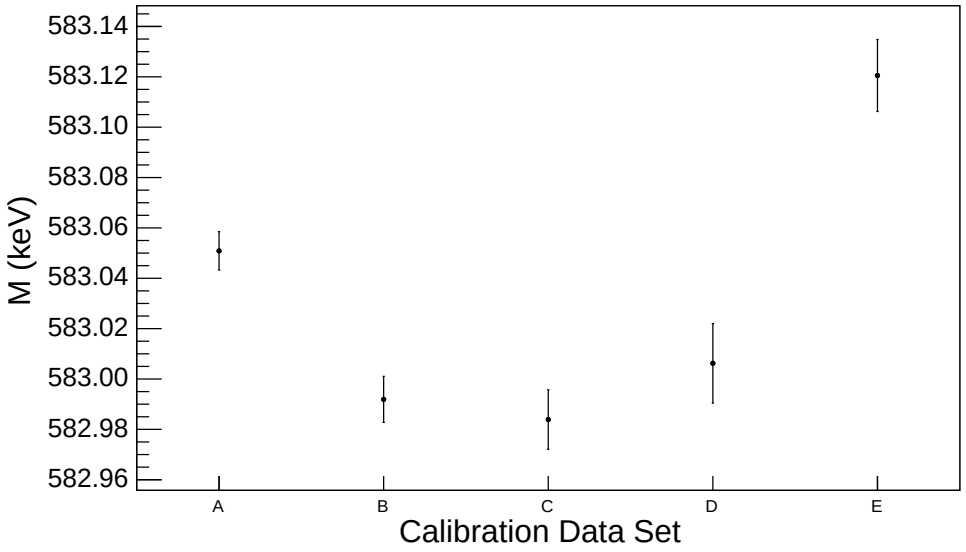

Figure B.41: The centroid (M) of peak #3 for S3D2 over time.

Table B.26: Peak #4 parameters of S3D2 for all calibration data.

Parameter	Calibration Data Set				
	A	B	C	D	E
μ [keV]	860.32 (3)	860.86 (4)	860.86 (3)	860.88 (5)	860.93 (5)
A/t $[cts/hr]$	68 (2)	63 (2)	67 (2)	65 (2)	58 (4)
H_{step}	1.9 (10)$\cdot 10^{-3}$	0.4 (3)$\cdot 10^{-2}$	0.4 (1)$\cdot 10^{-2}$	0.1 (4)$\cdot 10^{-2}$	0.5 (4)$\cdot 10^{-2}$
σ [keV]	0.66 (1)	0.72 (1)	0.72 (1)	0.73 (2)	0.74 (1)
τ [keV]	0.8 (1)	0.7 (1)	1.0 (1)	0.8 (2)	0†
H_{tail}	0.13 (8)	0.2 (1)	0.15 (6)	0.2 (2)	0†
M	860.22 (2)	860.71 (3)	860.71 (3)	860.72 (3)	860.93 (5)
Σ [keV]	0.76 (1)	0.85 (1)	0.89 (1)	0.88 (2)	0.74 (1)
FWHM [keV]	1.59 (2)	1.77 (3)	1.76 (3)	1.81 (5)	1.74 (3)
Runtime [hrs]	4.471	5.155	4.383	3.361	0.871
Fixed Parameters	-	-	-	-	$m_H = b_H = 0$ $m_\tau = b_\tau = 0$

† The best fit results in the parameter b_H being consistent with zero. Therefore the final fit is performed with b_τ, m_τ, b_H and m_H fixed to be zero.

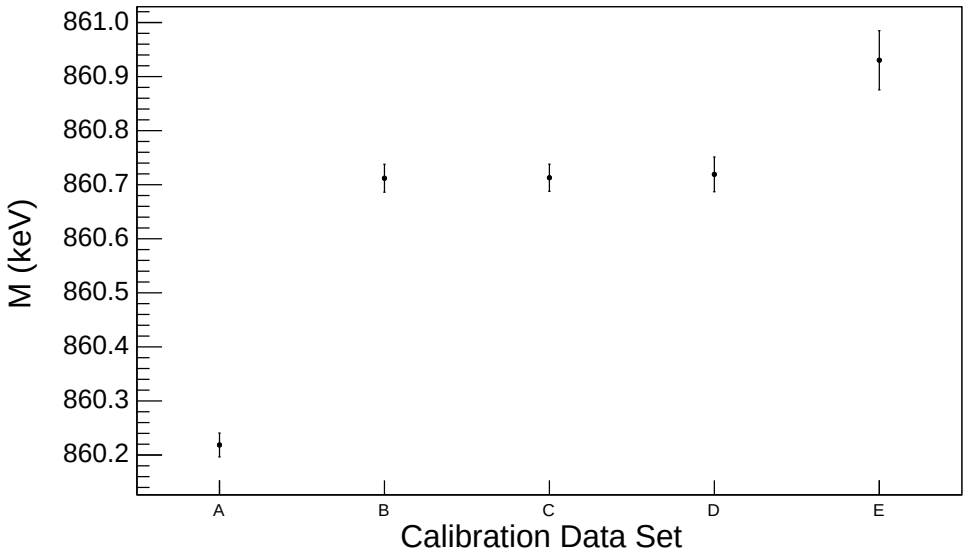

Figure B.42: The centroid (M) of peak #4 for S3D2 over time.

Table B.27: Peak #5 parameters of S3D2 for all calibration data.

Parameter	Calibration Data Set				
	A	B	C	D	E
μ [keV]	2613.53 (3)	2615.44 (4)	2615.59 (5)	2615.73 (7)	2615.95 (5)
A/t $[cts/hr]$	269 (4)	257 (4)	253 (4)	244 (5)	224 (8)
H_{step}	$0.1\ (2)\cdot10^{-3}$	$0.8\ (7)\cdot10^{-3}$	$0.3\ (2)\cdot10^{-3}$	$0.1\ (1)\cdot10^{-2}$	$0.9\ (1)\cdot10^{-2}$
σ [keV]	1.19 (2)	1.20 (2)	1.23 (3)	1.19 (3)	1.26 (4)
τ [keV]	2.4 (5)	1.8 (3)	2.1 (3)	1.8 (3)	$0^{\dagger}$
H_{tail}	0.1 (1)	0.3 (1)	0.2 (1)	0.3 (2)	$0^{\dagger}$
M	2613.20 (5)	2614.98 (4)	2615.08 (4)	2615.25 (6)	2615.95 (5)
Σ [keV]	1.71 (6)	1.71 (2)	1.83 (1)	1.70 (3)	1.26 (4)
FWHM [keV]	2.89 (10)	3.02 (3)	3.08 (2)	3.00 (6)	2.96 (8)
Runtime [hrs]	4.471	5.155	4.383	3.361	0.871
Fixed Parameters	-	-	-	-	$m_H = b_H = 0$ $m_\tau = b_\tau = 0$

† The best fit results in the parameter b_H being consistent with zero. Therefore the final fit is performed with b_τ, m_τ, b_H and m_H fixed to be zero.

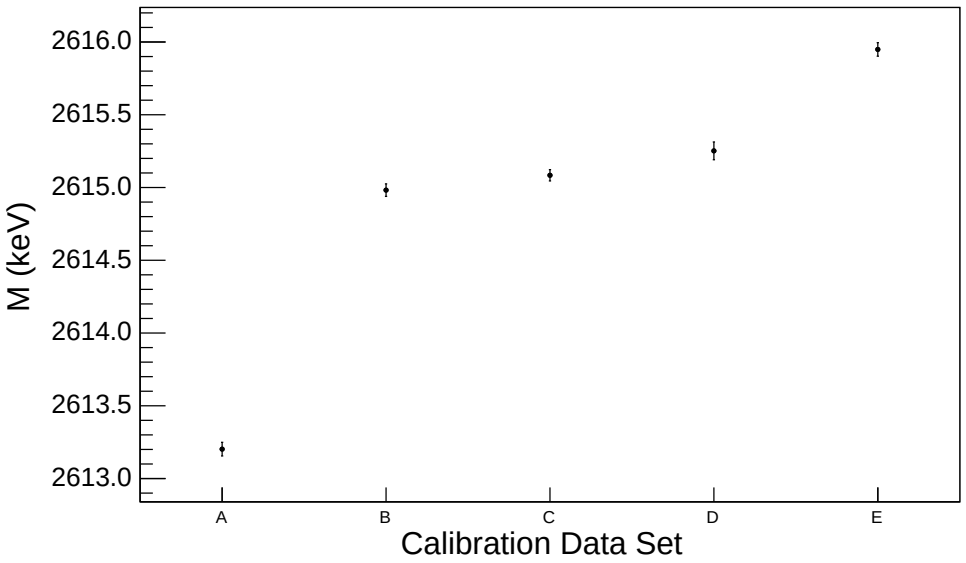

Figure B.43: The centroid (M) of peak #5 for S3D2 over time.

Table B.28: The peak rate for each of the five peaks during each of the five calibration data sets for S3D2. The peak rate is the area parameter divided by the runtime divided by the bin width (0.1 keV). Also shown is the ratio of each peak's rate to the 583-keV peak rate (i.e. Pk #3).

		Calibration Data Set				
		A	B	C	D	E
Pk Rate $\left[\frac{cts}{hr}\right]$	Pk #1	590 (20)	600 (20)	580 (20)	570 (30)	550 (50)
	Pk #2	860 (20)	860 (30)	800 (30)	790 (30)	740 (50)
	Pk #3	5580 (50)	5490 (50)	5500 (50)	5230 (60)	5200 (100)
	Pk #4	680 (20)	630 (20)	670 (20)	650 (20)	580 (40)
	Pk #5	2690 (40)	2570 (40)	2530 (40)	2440 (50)	2240 (80)
$\frac{\text{Pk \#}n\text{ Rate}}{\text{Pk \#3 Rate}}$	$n = 1$	0.106 (5)	0.109 (4)	0.105 (5)	0.108 (6)	0.107 (10)
	$n = 2$	0.154 (5)	0.157 (5)	0.145 (5)	0.151 (7)	0.14 (1)
	$n = 3$	1.	1.	1.	1.	1.
	$n = 4$	0.122 (3)	0.115 (3)	0.123 (5)	0.124 (4)	0.113 (8)
	$n = 5$	0.482 (8)	0.468 (8)	0.460 (8)	0.47 (1)	0.43 (2)

B.4.2 Individual Peak Fits

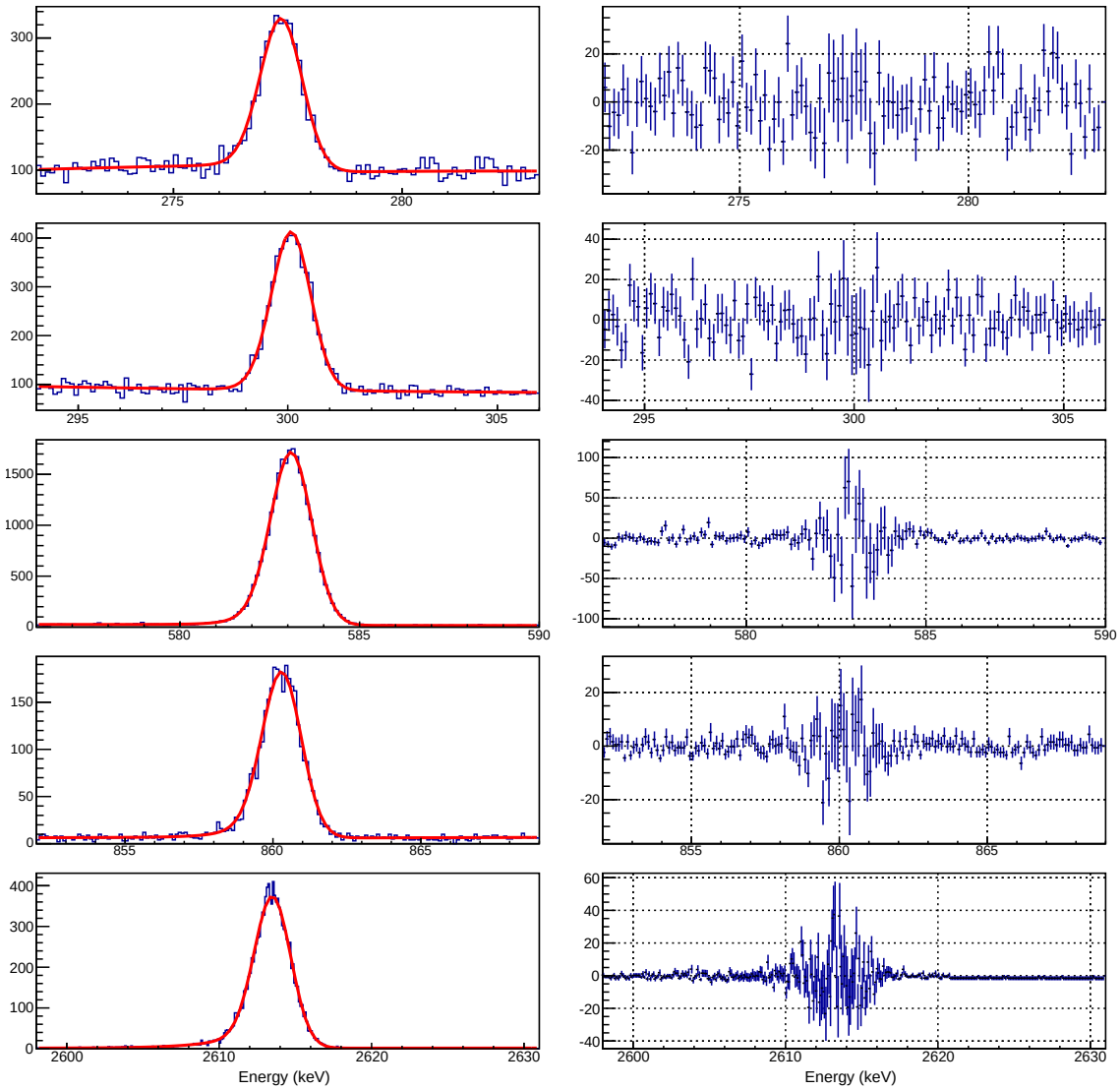

Figure B.44: The five gamma peaks of S3D2 in calibration data set A that are fit with the multi-peak fitting routine. Shown on the left is each of the five peaks with the best fit of the multi-peak fitting function shown in red. Shown on the right is the residual of the fit for each peak.

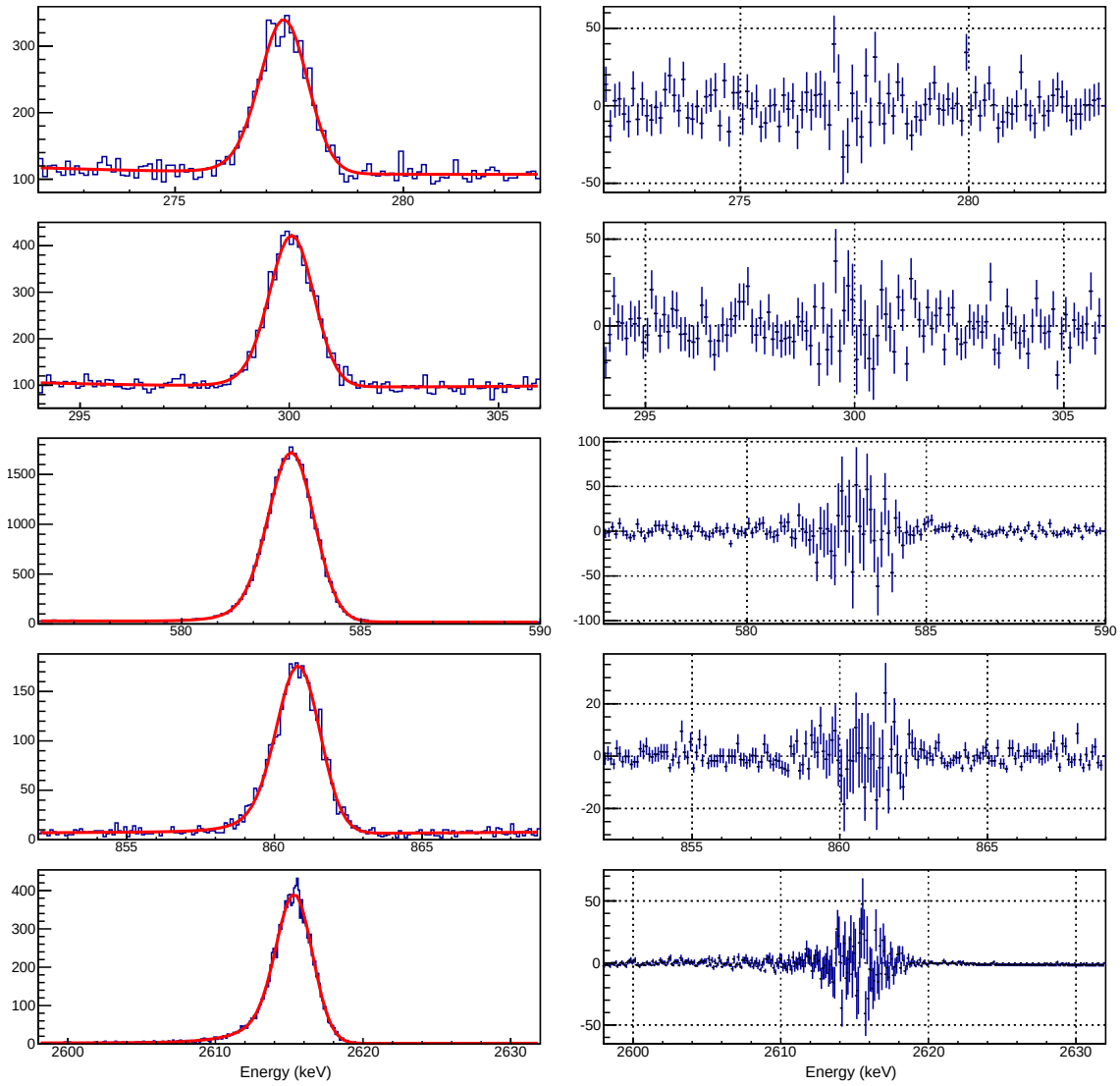

Figure B.45: The five gamma peaks of S3D2 in calibration data set B that are fit with the multi-peak fitting routine. Shown on the left is each of the five peaks with the best fit of the multi-peak fitting function shown in red. Shown on the right is the residual of the fit for each peak.

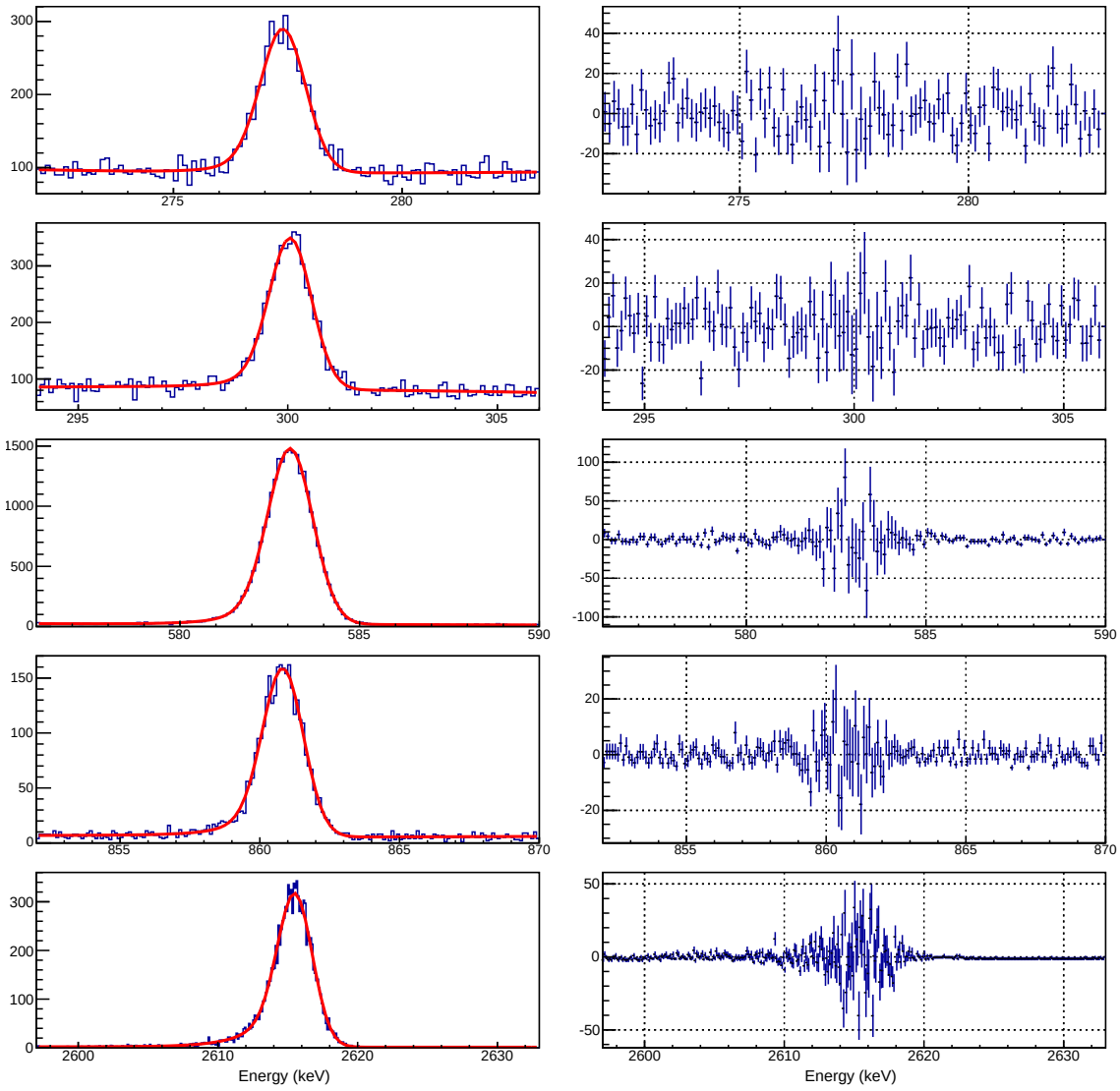

Figure B.46: The five gamma peaks of S3D2 in calibration data set C that are fit with the multi-peak fitting routine. Shown on the left is each of the five peaks with the best fit of the multi-peak fitting function shown in red. Shown on the right is the residual of the fit for each peak.

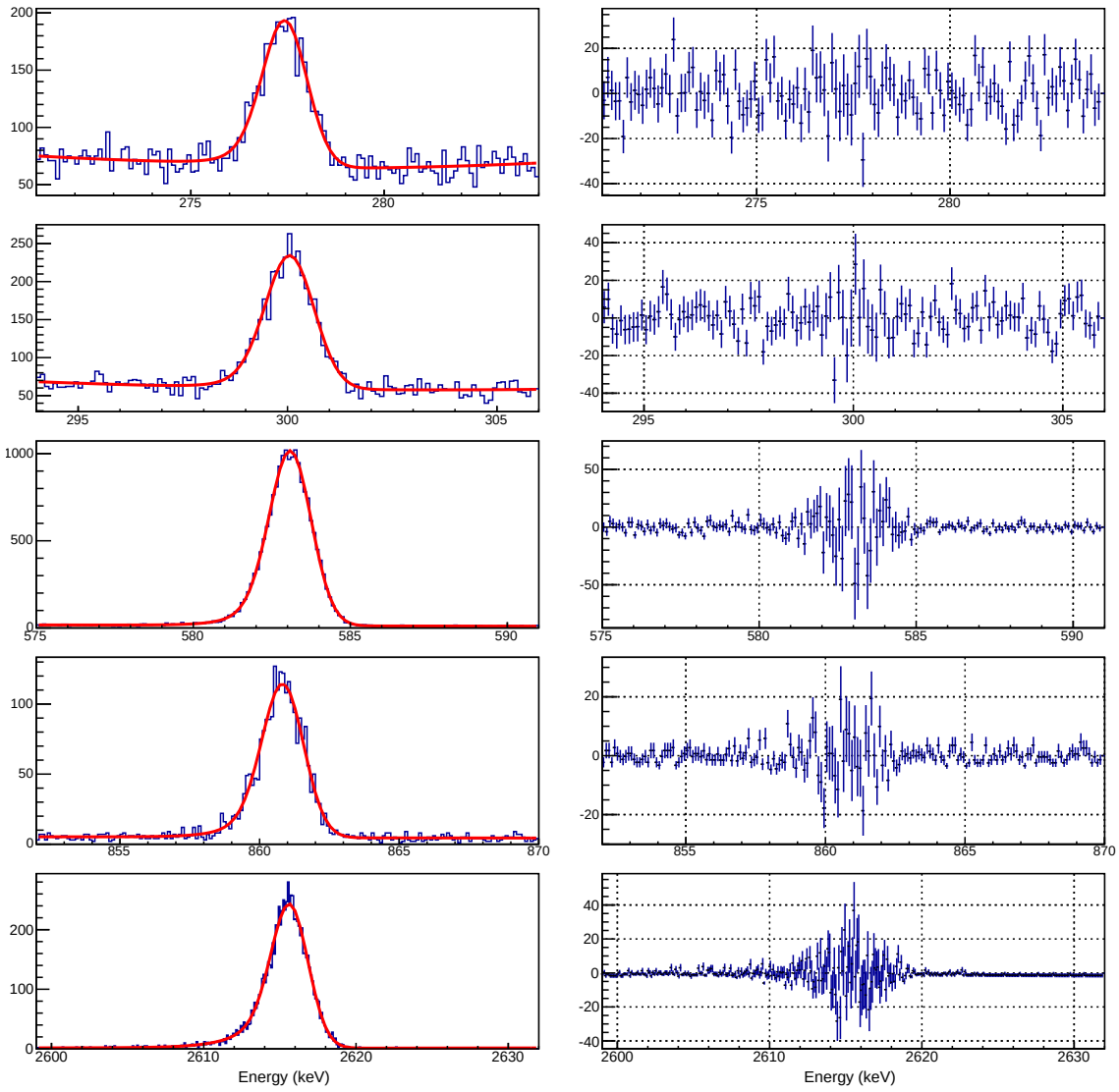

Figure B.47: The five gamma peaks of S3D2 in calibration data set D that are fit with the multi-peak fitting routine. Shown on the left is each of the five peaks with the best fit of the multi-peak fitting function shown in red. Shown on the right is the residual of the fit for each peak.

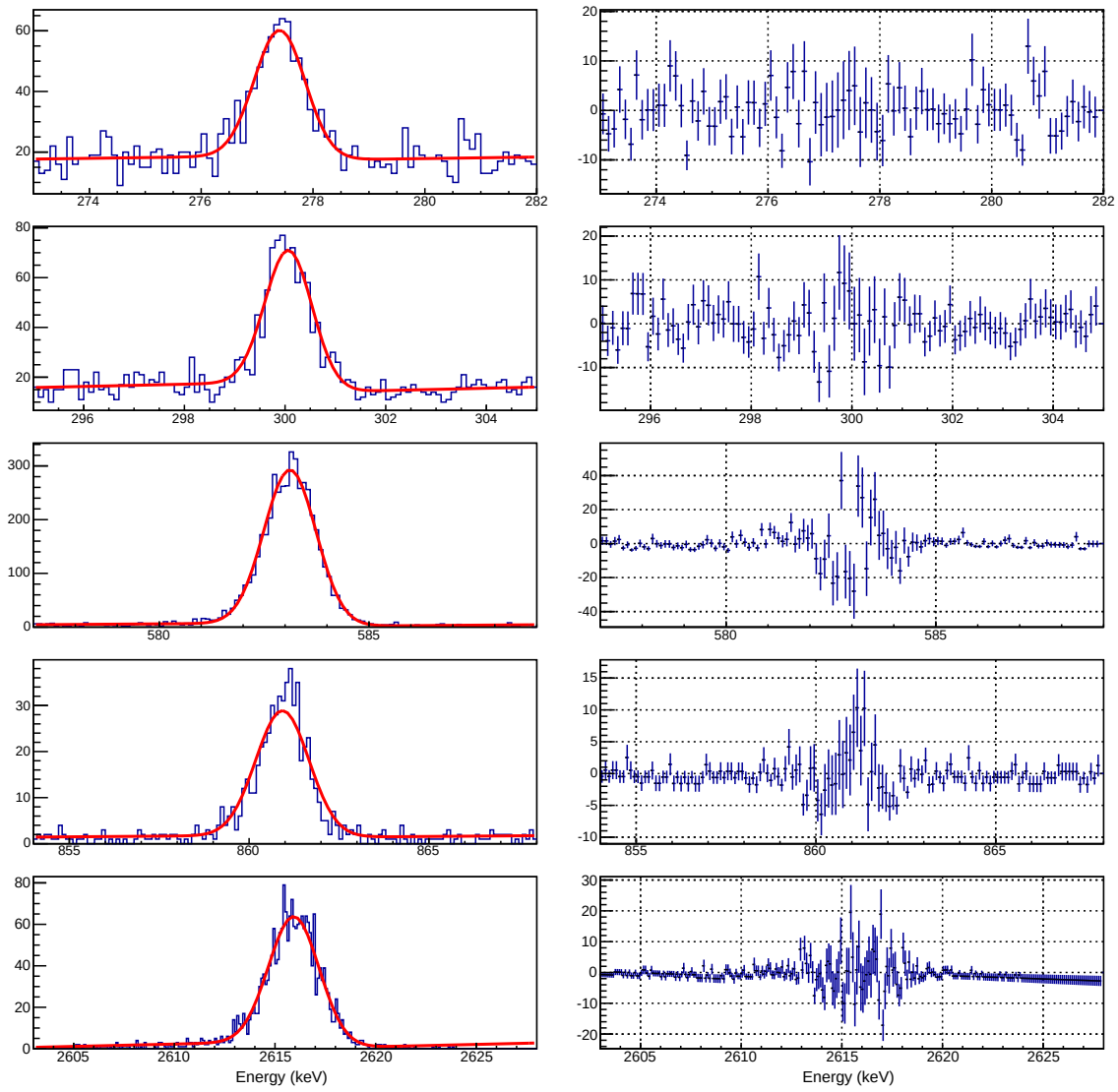

Figure B.48: The five gamma peaks of S3D2 in calibration data set E that are fit with the multi-peak fitting routine. Shown on the left is each of the five peaks with the best fit of the multi-peak fitting function shown in red. Shown on the right is the residual of the fit for each peak.

Table B.29: Common parameters of S3D4 for all calibration data.

	Calibration Data Set				
	A	B	C	D	E
σ_0 [keV]	0.27 (4)	0.40 (4)	0.46 (4)	0.44 (5)	0.3 (1)
$\sigma_1/10^{-2}$ [keV$^{1/2}$]	2.0 (1)	2.0 (2)	1.8 (2)	2.1 (2)	2.5 (3)
$\sigma_2/10^{-4}$	3.5 (3)	3.9 (3)	4.2 (3)	3.5 (4)	2 (2)
b_τ [keV]	0†	0†	0†	0†	0†
m_τ	0†	0†	0†	0†	0†
b_H	0†	0†	0†	0†	0†
m_H [keV^{-1}]	0†	0†	0†	0†	0†
Runtime [hrs]	4.471	5.000	4.383	3.361	0.871
Fixed Parameters	$m_H = b_H = 0$				
	$m_\tau = b_\tau = 0$				

† The best fit results in the parameter b_H being consistent with zero. Therefore the final fit is performed with b_τ, m_τ, b_H and m_H fixed to be zero.

B.5 S3D4 of the PC (Detector B8466)

All five gamma-peaks in S3D4 of the PC can be fit in all five of the calibration data sets. As discussed in Chapter 4, data set E is not used when fitting any of the common parameters over time.

B.5.1 Summary of Fit Results

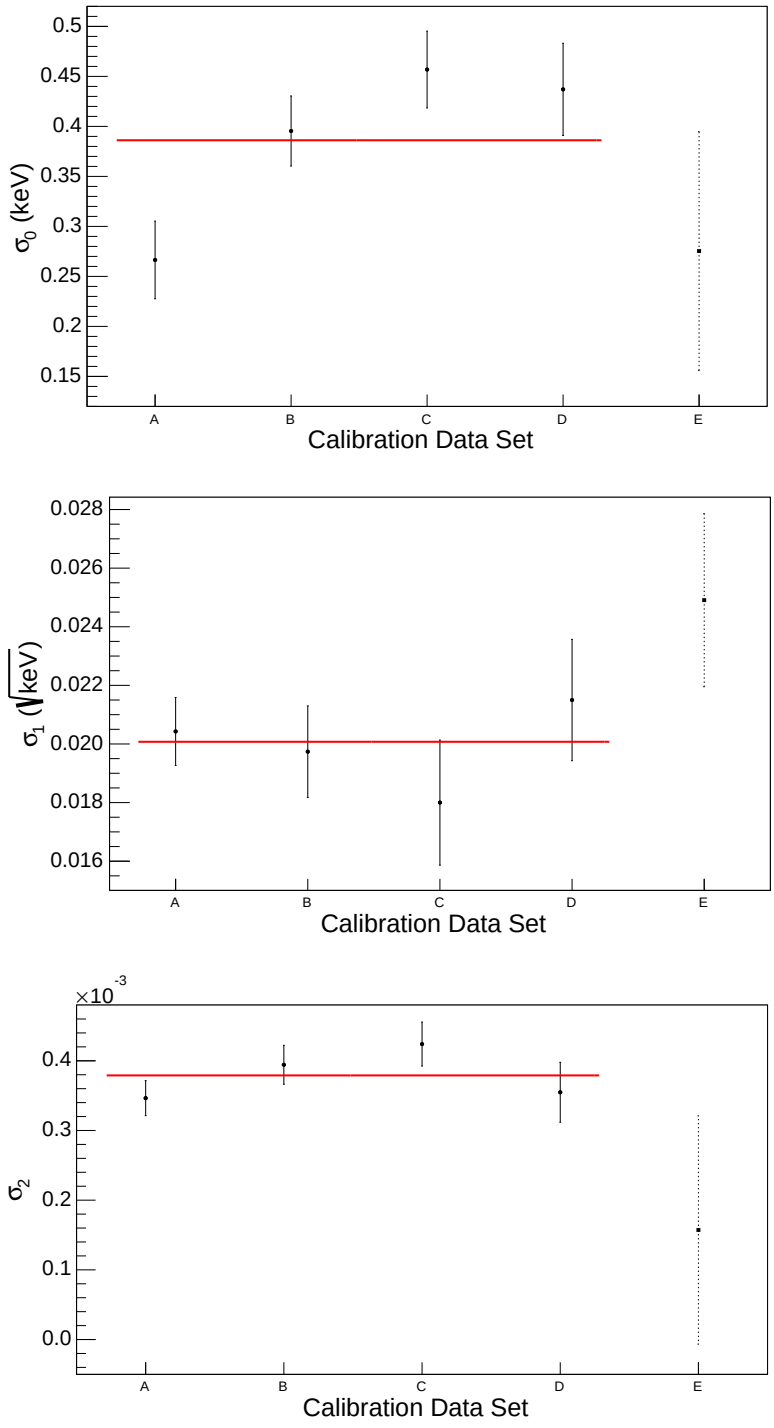

Figure B.49: Parameter σ_0 (top), σ_1 (middle) and σ_2 (bottom) for S3D4 over time. Data with solid error bars are fit with a constant over time. The best fits result in average values of: $\sigma_0 = 0.39\ (2)$ keV, $\sigma_1 = 2.01\ (8)\cdot 10^{-2}$ keV$^{1/2}$ and $\sigma_2 = 3.8\ (2)\cdot 10^{-4}$.

Table B.30: Peak #1 parameters of S3D4 for all calibration data.

	Calibration Data Set				
	A	B	C	D	E
μ [keV]	277.45 (2)	277.61 (2)	277.61 (3)	277.49 (3)	277.43 (6)
A/t $[cts/hr]$	68 (2)	68 (3)	64 (3)	59 (3)	58 (5)
H_{step}	0 (2)$\cdot 10^{-2}$	2 (1)$\cdot 10^{-2}$	2 (8)$\cdot 10^{-3}$	0 (3)$\cdot 10^{-4}$	2 (4)$\cdot 10^{-2}$
σ [keV]	0.44 (1)	0.53 (1)	0.56 (1)	0.57 (2)	0.50 (3)
τ [keV]	0†	0†	0†	0†	0†
H_{tail}	0†	0†	0†	0†	0†
M	277.45 (2)	277.61 (2)	277.61 (3)	277.49 (3)	277.43 (6)
Σ [keV]	0.44 (1)	0.53 (1)	0.56 (1)	0.57 (2)	0.50 (3)
FWHM [keV]	1.04 (3)	1.24 (3)	1.32 (3)	1.35 (4)	1.18 (7)
Runtime [hrs]	4.471	5.000	4.383	3.361	0.871
Fixed Parameters	$m_H = b_H = 0$				
	$m_\tau = b_\tau = 0$				

† The best fit results in the parameter b_H being consistent with zero. Therefore the final fit is performed with b_τ, m_τ, b_H and m_H fixed to be zero.

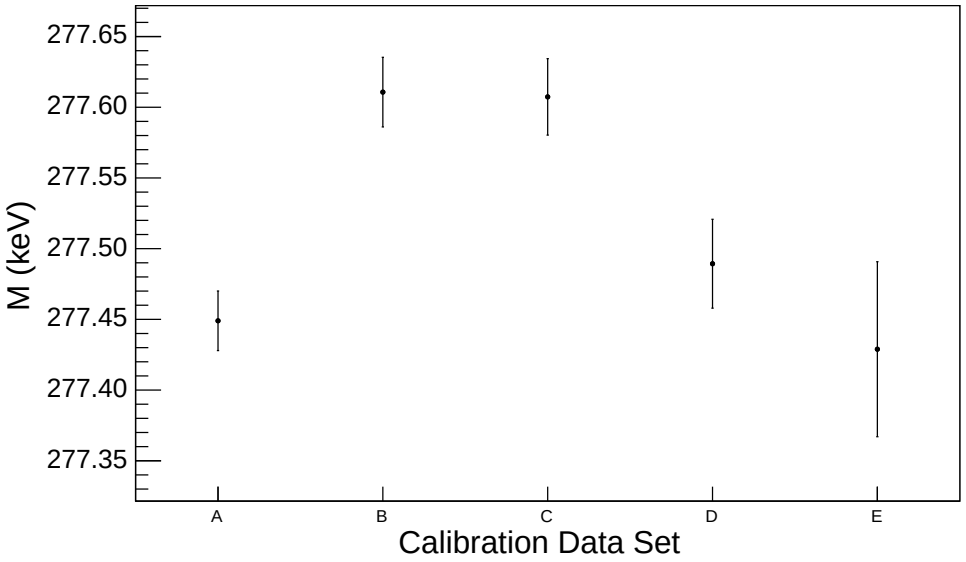

Figure B.50: The centroid (M) of peak #1 for S3D4 over time.

Table B.31: Peak #2 parameters of S3D4 for all calibration data.

Parameter	Calibration Data Set				
	A	B	C	D	E
μ [keV]	300.15 (2)	300.31 (2)	300.29 (2)	300.24 (2)	300.15 (4)
A/t $[cts/hr]$	93 (3)	92 (3)	88 (3)	87 (3)	83 (6)
H_{step}	9 (4)$\cdot 10^{-3}$	9 (9)$\cdot 10^{-3}$	0 (3)$\cdot 10^{-5}$	0 (2)$\cdot 10^{-4}$	0 (4)$\cdot 10^{-4}$
σ [keV]	0.455 (10)	0.54 (1)	0.57 (1)	0.58 (1)	0.51 (3)
τ [keV]	0†	0†	0†	0†	0†
H_{tail}	0†	0†	0†	0†	0†
M	300.15 (2)	300.31 (2)	300.29 (2)	300.24 (2)	300.15 (4)
Σ [keV]	0.455 (10)	0.54 (1)	0.57 (1)	0.58 (1)	0.51 (3)
FWHM [keV]	1.07 (2)	1.26 (3)	1.34 (3)	1.38 (3)	1.21 (6)
Runtime [hrs]	4.471	5.000	4.383	3.361	0.871
Fixed Parameters	$m_H = b_H = 0$				
	$m_\tau = b_\tau = 0$				

† The best fit results in the parameter b_H being consistent with zero. Therefore the final fit is performed with b_τ, m_τ, b_H and m_H fixed to be zero.

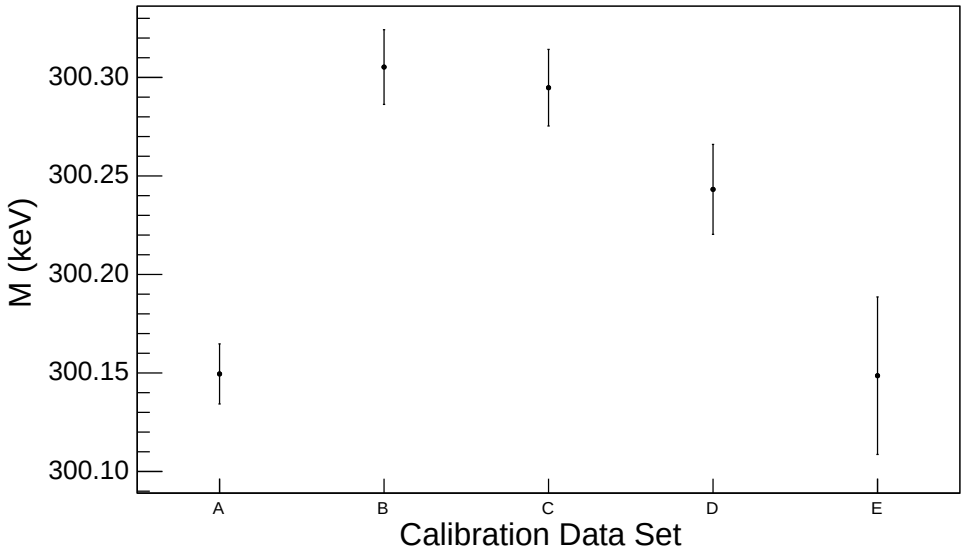

Figure B.51: The centroid (M) of peak #2 for S3D4 over time.

Table B.32: Peak #3 parameters of S3D4 for all calibration data.

Parameter	Calibration Data Set				
	A	B	C	D	E
μ [keV]	583.200 (5)	583.283 (6)	583.263 (6)	583.170 (8)	583.19 (1)
A/t $[cts/hr]$	631 (5)	613 (5)	588 (5)	583 (6)	580 (10)
H_{step}	2.1 (4)$\cdot 10^{-3}$	1.3 (7)$\cdot 10^{-3}$	1.7 (3)$\cdot 10^{-3}$	2.2 (9)$\cdot 10^{-3}$	3.7 (6)$\cdot 10^{-3}$
σ [keV]	0.596 (4)	0.661 (4)	0.677 (5)	0.709 (6)	0.67 (1)
τ [keV]	0†	0†	0†	0†	0†
H_{tail}	0†	0†	0†	0†	0†
M	583.200 (5)	583.283 (6)	583.263 (6)	583.170 (8)	583.19 (1)
Σ [keV]	0.596 (4)	0.661 (4)	0.677 (5)	0.709 (6)	0.67 (1)
FWHM [keV]	1.403 (9)	1.556 (10)	1.60 (1)	1.67 (1)	1.57 (2)
Runtime [hrs]	4.471	5.000	4.383	3.361	0.871
Fixed Parameters			$m_H = b_H = 0$ $m_\tau = b_\tau = 0$		

† The best fit results in the parameter b_H being consistent with zero. Therefore the final fit is performed with b_τ, m_τ, b_H and m_H fixed to be zero.

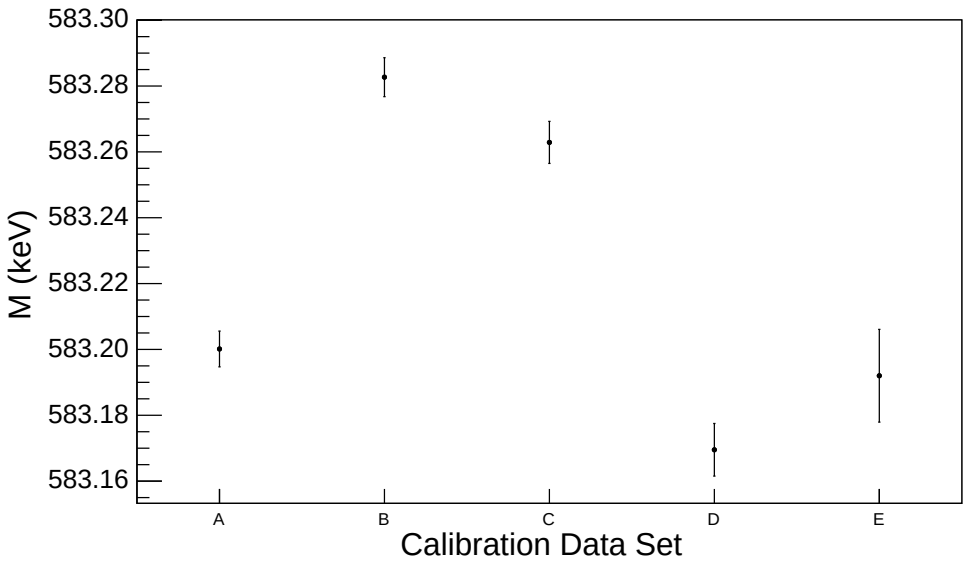

Figure B.52: The centroid (M) of peak #3 for S3D4 over time.

Table B.33: Peak #4 parameters of S3D4 for all calibration data.

Parameter	Calibration Data Set				
	A	B	C	D	E
μ [keV]	860.42 (2)	860.50 (2)	860.47 (2)	860.39 (3)	860.44 (6)
A/t $[cts/hr]$	76 (2)	75 (2)	71 (2)	70 (2)	66 (4)
H_{step}	0 (1)$\cdot 10^{-4}$	1 (3)$\cdot 10^{-3}$	0 (2)$\cdot 10^{-4}$	0 (5)$\cdot 10^{-5}$	1.0 (7)$\cdot 10^{-2}$
σ [keV]	0.720 (7)	0.779 (8)	0.788 (9)	0.83 (1)	0.79 (2)
τ [keV]	0†	0†	0†	0†	0†
H_{tail}	0†	0†	0†	0†	0†
M	860.42 (2)	860.50 (2)	860.47 (2)	860.39 (3)	860.44 (6)
Σ [keV]	0.720 (7)	0.779 (8)	0.788 (9)	0.83 (1)	0.79 (2)
FWHM [keV]	1.70 (2)	1.83 (2)	1.86 (2)	1.94 (3)	1.87 (4)
Runtime [hrs]	4.471	5.000	4.383	3.361	0.871
Fixed Parameters	$m_H = b_H = 0$				
	$m_\tau = b_\tau = 0$				

† The best fit results in the parameter b_H being consistent with zero. Therefore the final fit is performed with b_τ, m_τ, b_H and m_H fixed to be zero.

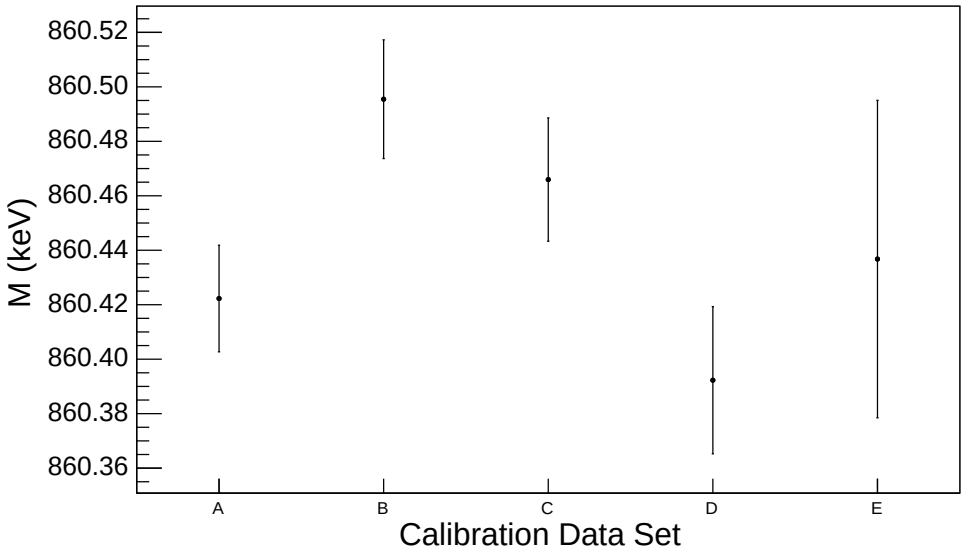

Figure B.53: The centroid (M) of peak #4 for S3D4 over time.

Table B.34: Peak #5 parameters of S3D4 for all calibration data.

Parameter	Calibration Data Set				
	A	B	C	D	E
μ [keV]	2613.35 (2)	2614.34 (2)	2614.38 (2)	2614.30 (3)	2614.72 (5)
A/t [cts/hr]	285 (4)	273 (3)	268 (4)	262 (4)	246 (8)
H_{step}	1 (6)$\cdot 10^{-8}$	1.5 (4)$\cdot 10^{-3}$	1.6 (2)$\cdot 10^{-3}$	2.6 (7)$\cdot 10^{-3}$	2 (2)$\cdot 10^{-3}$
σ [keV]	1.41 (1)	1.50 (2)	1.51 (2)	1.50 (2)	1.37 (4)
τ [keV]	0†	0†	0†	0†	0†
H_{tail}	0†	0†	0†	0†	0†
M	2613.35 (2)	2614.34 (2)	2614.38 (2)	2614.30 (3)	2614.72 (5)
Σ [keV]	1.41 (1)	1.50 (2)	1.51 (2)	1.50 (2)	1.37 (4)
FWHM [keV]	3.31 (3)	3.52 (4)	3.56 (4)	3.54 (5)	3.22 (9)
Runtime [hrs]	4.471	5.000	4.383	3.361	0.871
Fixed Parameters	$m_H = b_H = 0$ $m_\tau = b_\tau = 0$				

† The best fit results in the parameter b_H being consistent with zero. Therefore the final fit is performed with b_τ, m_τ, b_H and m_H fixed to be zero.

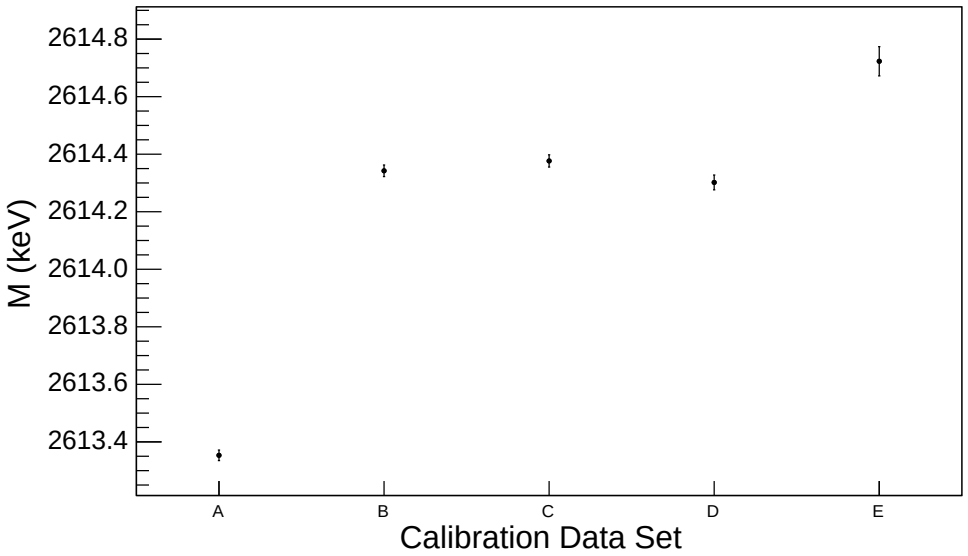

Figure B.54: The centroid (M) of peak #5 for S3D4 over time.

Table B.35: The peak rate for each of the five peaks during each of the five calibration data sets for S3D4. The peak rate is the area parameter divided by the runtime divided by the bin width (0.1 keV). Also shown is the ratio of each peak's rate to the 583-keV peak rate (i.e. Pk #3).

		Calibration Data Set				
		A	B	C	D	E
Pk Rate $\left[\frac{cts}{hr}\right]$	Pk #1	680 (20)	680 (30)	640 (30)	590 (30)	580 (50)
	Pk #2	930 (30)	920 (30)	880 (30)	870 (30)	830 (60)
	Pk #3	6310 (50)	6130 (50)	5880 (50)	5830 (60)	5800 (100)
	Pk #4	760 (20)	750 (20)	710 (20)	700 (20)	660 (40)
	Pk #5	2850 (40)	2730 (30)	2680 (40)	2620 (40)	2460 (80)
$\frac{\text{Pk } \#n \text{ Rate}}{\text{Pk } \#3 \text{ Rate}}$	$n = 1$	0.108 (4)	0.112 (4)	0.108 (4)	0.102 (5)	0.100 (9)
	$n = 2$	0.147 (4)	0.149 (4)	0.150 (5)	0.150 (5)	0.14 (1)
	$n = 3$	1.	1.	1.	1.	1.
	$n = 2$	0.121 (3)	0.122 (3)	0.120 (3)	0.120 (4)	0.114 (7)
	$n = 2$	0.451 (7)	0.444 (7)	0.456 (7)	0.448 (9)	0.42 (2)

B.5.2 Individual Peak Fits

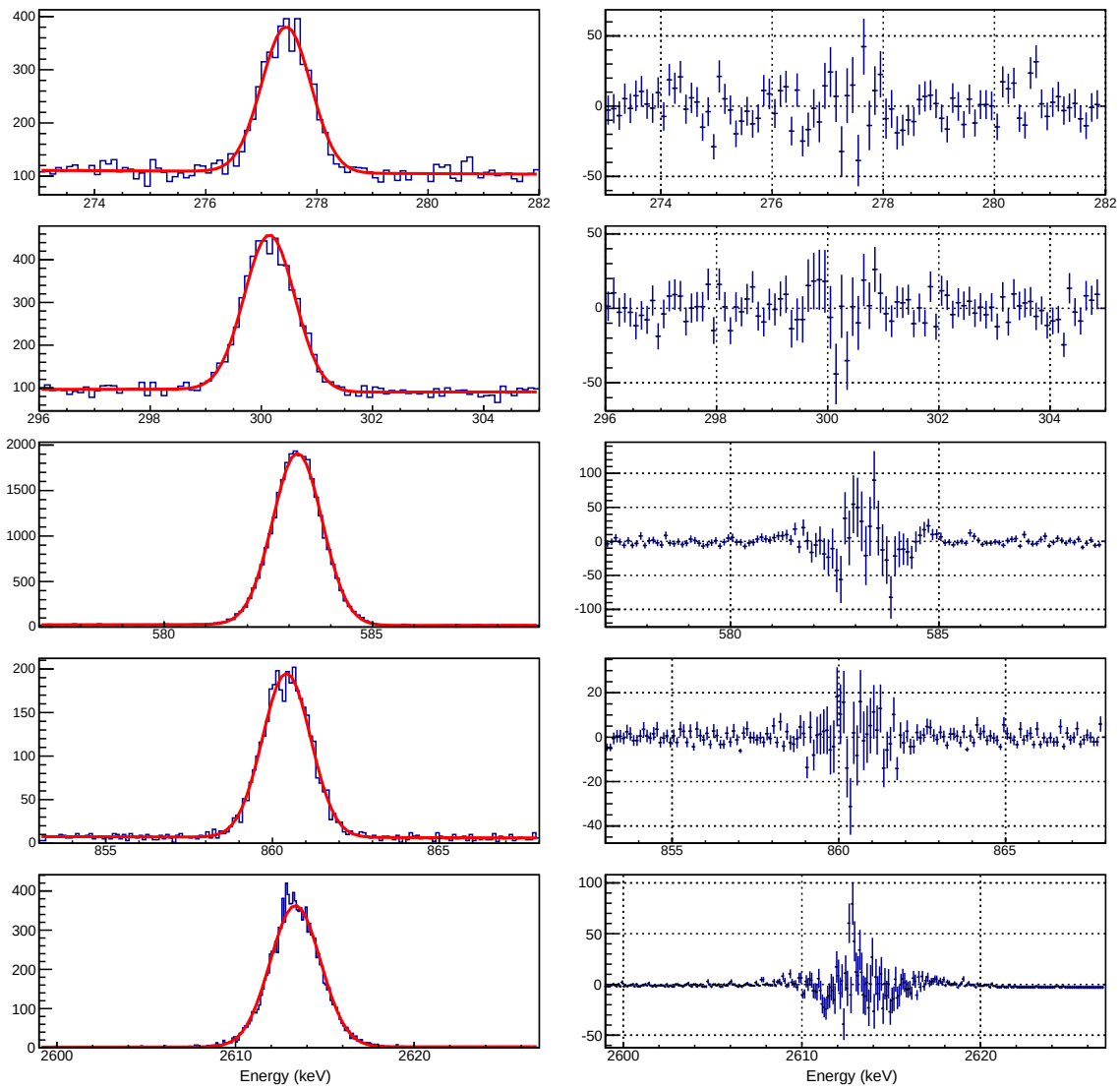

Figure B.55: The five gamma peaks of S3D4 in calibration data set A that are fit with the multi-peak fitting routine. Shown on the left is each of the five peaks with the best fit of the multi-peak fitting function shown in red. Shown on the right is the residual of the fit for each peak.

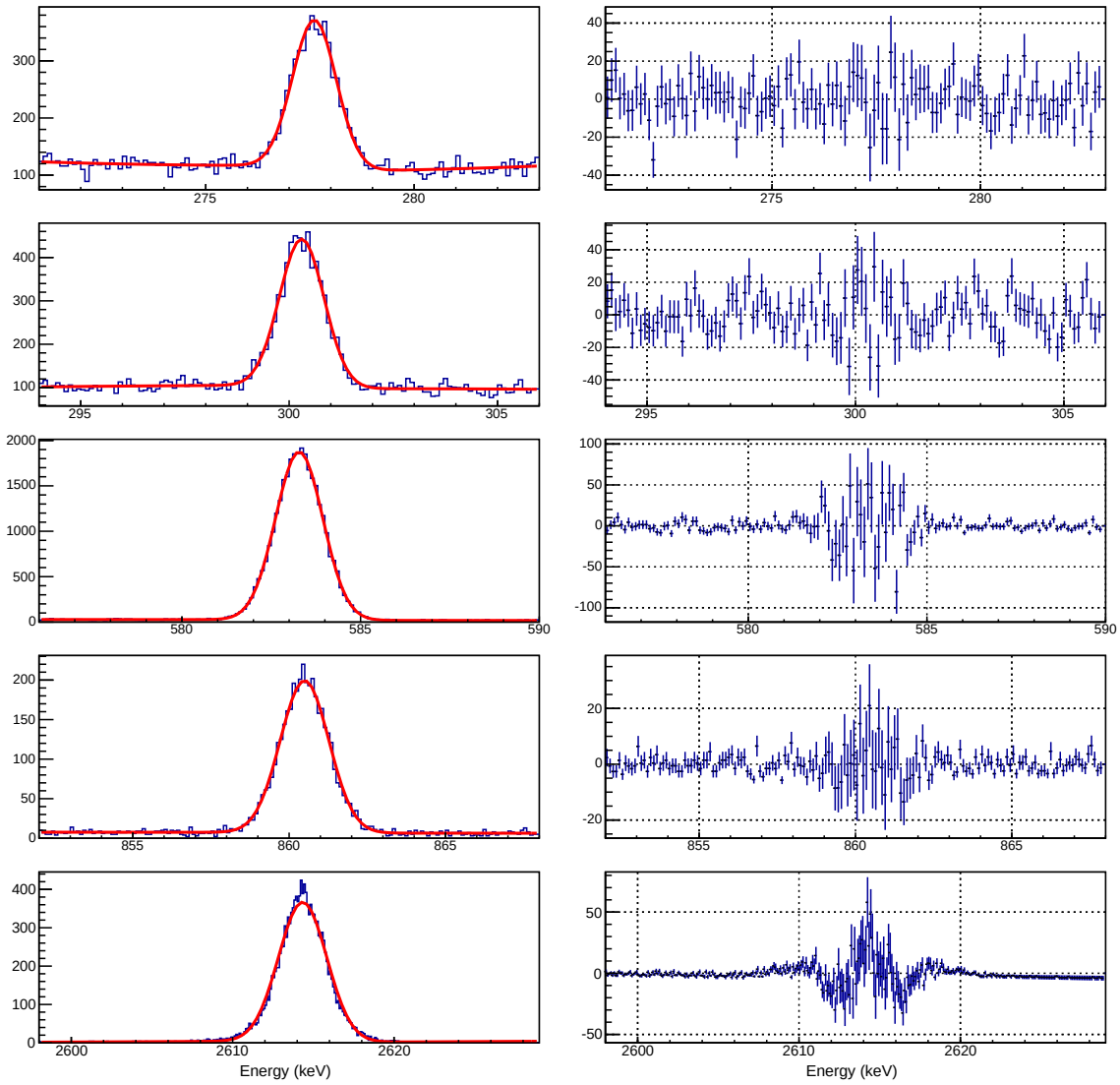

Figure B.56: The five gamma peaks of S3D4 in calibration data set B that are fit with the multi-peak fitting routine. Shown on the left is each of the five peaks with the best fit of the multi-peak fitting function shown in red. Shown on the right is the residual of the fit for each peak.

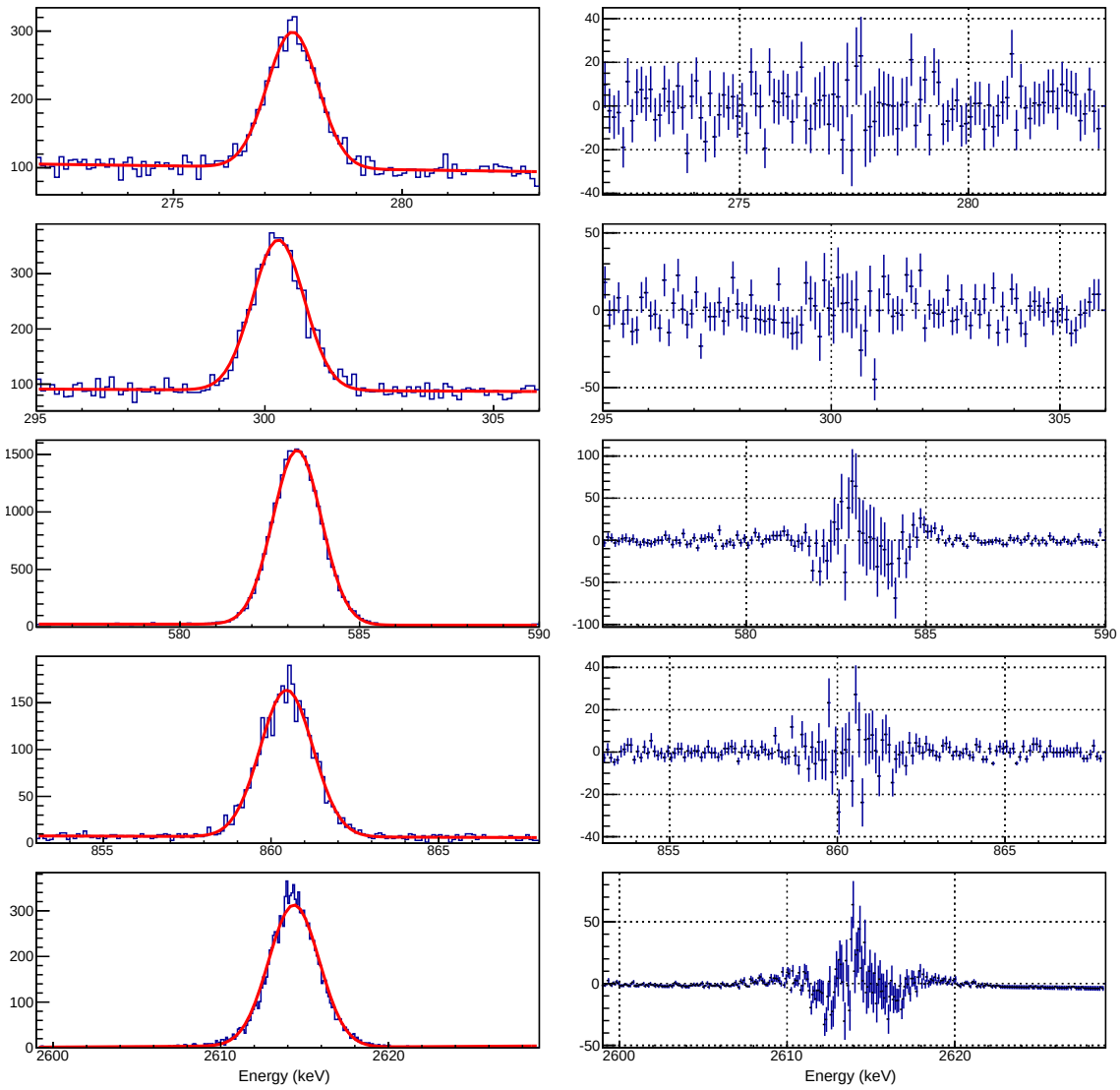

Figure B.57: The five gamma peaks of S3D4 in calibration data set C that are fit with the multi-peak fitting routine. Shown on the left is each of the five peaks with the best fit of the multi-peak fitting function shown in red. Shown on the right is the residual of the fit for each peak.

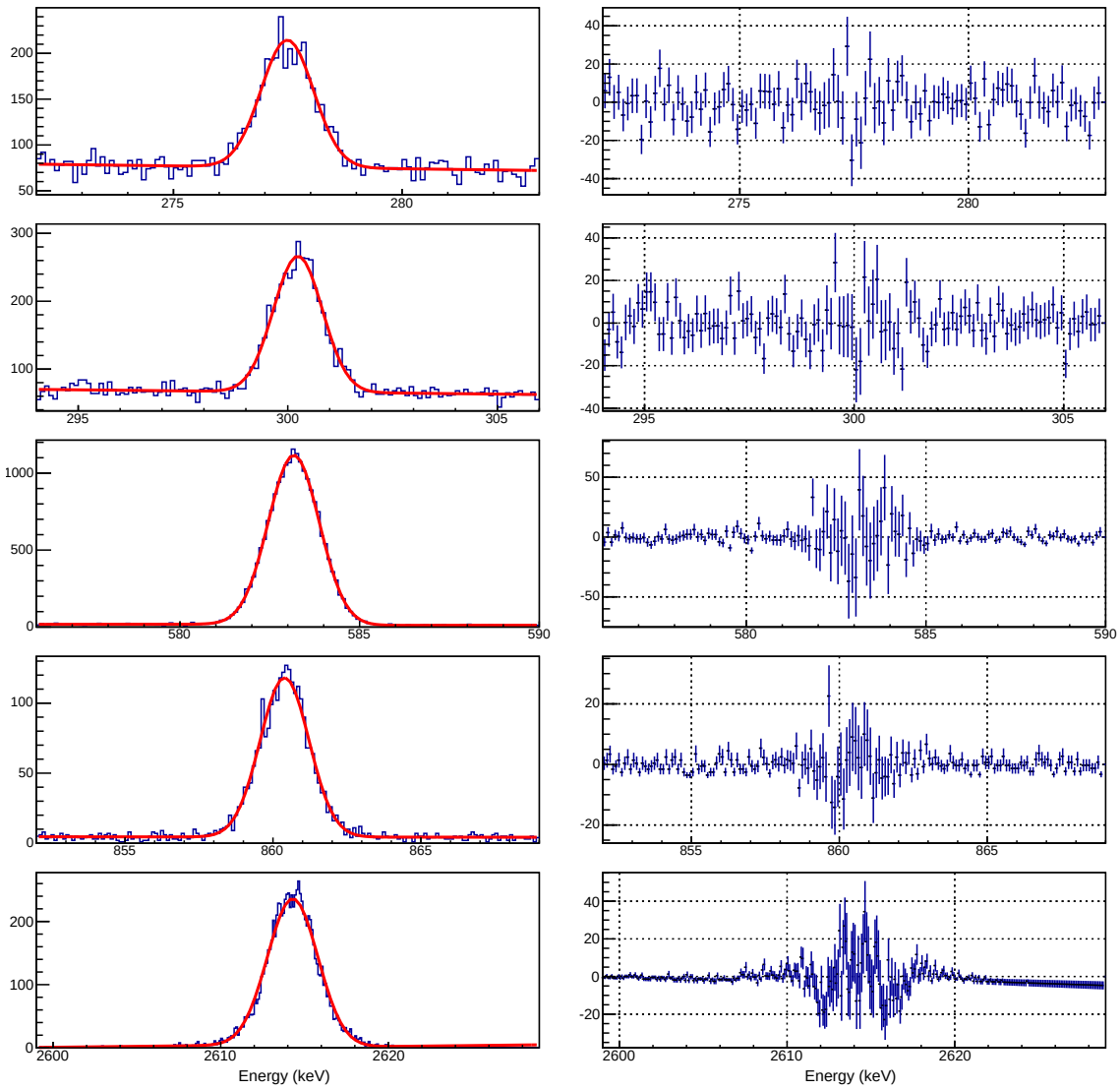

Figure B.58: The five gamma peaks of S3D4 in calibration data set D that are fit with the multi-peak fitting routine. Shown on the left is each of the five peaks with the best fit of the multi-peak fitting function shown in red. Shown on the right is the residual of the fit for each peak.

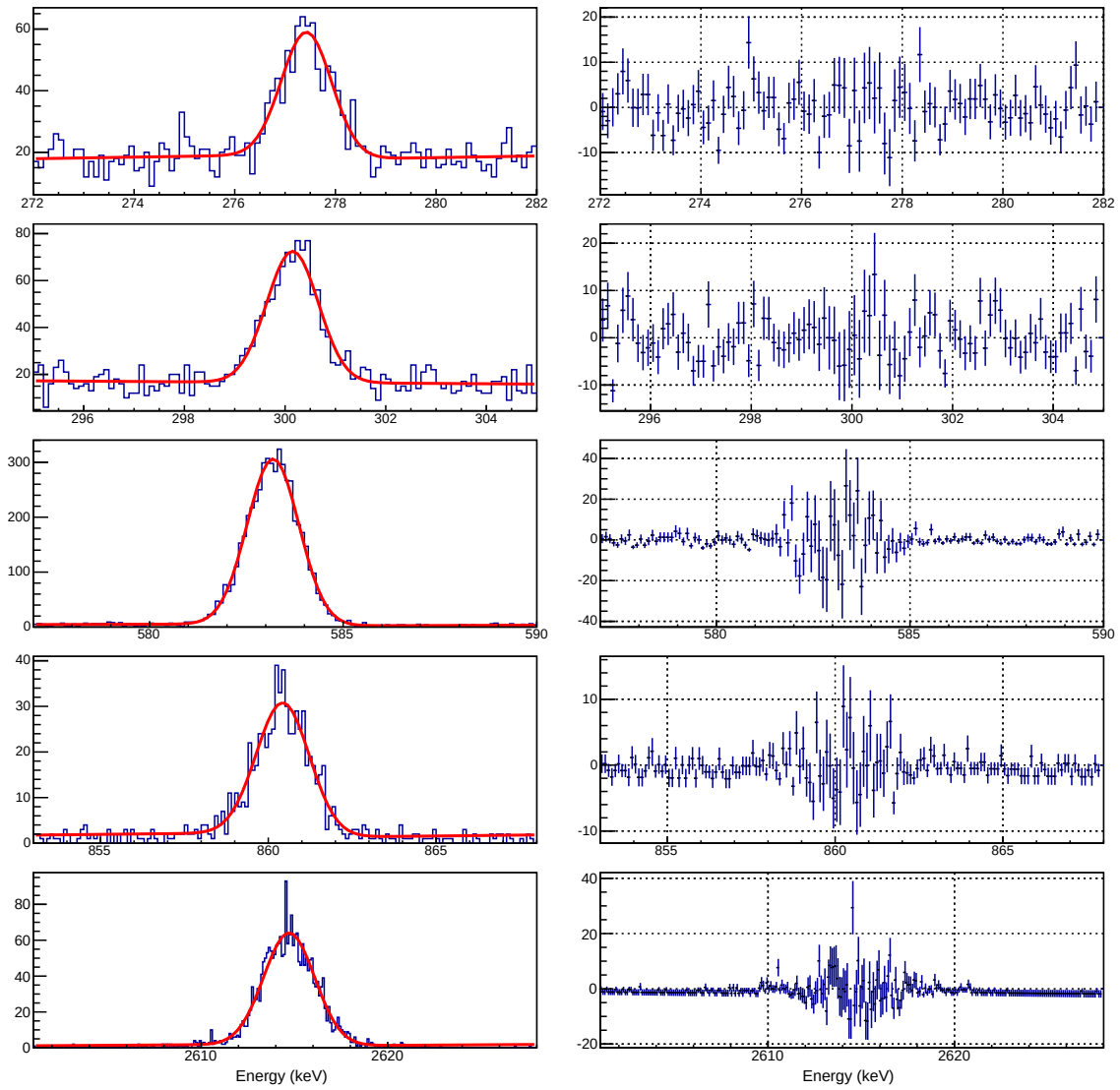

Figure B.59: The five gamma peaks of S3D4 in calibration data set E that are fit with the multi-peak fitting routine. Shown on the left is each of the five peaks with the best fit of the multi-peak fitting function shown in red. Shown on the right is the residual of the fit for each peak.

Table B.36: Common parameters of S3D5 for all calibration data.

	Calibration Data Set				
	A	B	C	D	E
σ_0 [keV]	-	0.30 (6)	0.36 (7)	0.59 (6)	0.3 (1)
$\sigma_1/10^{-2}$ [keV$^{1/2}$]	-	2.3 (2)	2.4 (2)	1.9 (4)	2.1 (5)
$\sigma_2/10^{-4}$	-	3.3 (5)	3.1 (6)	3.4 (7)	3 (1)
b_τ [keV]	-	$0^\dagger$	$0^\dagger$	$0^\dagger$	$0^\dagger$
m_τ	-	$0^\dagger$	$0^\dagger$	$0^\dagger$	$0^\dagger$
b_H	-	$0^\dagger$	$0^\dagger$	$0^\dagger$	$0^\dagger$
m_H [keV^{-1}]	-	$0^\dagger$	$0^\dagger$	$0^\dagger$	$0^\dagger$
Runtime [hrs]	0.	4.848	4.383	3.361	0.871
Fixed Parameters	-	$m_H = b_H = 0$			
	-	$m_\tau = b_\tau = 0$			

† The best fit results in the parameter b_H being consistent with zero. Therefore the final fit is performed with b_τ, m_τ, b_H and m_H fixed to be zero.

B.6 S3D5 of the PC (Detector B8473)

The runtime for S3D5 during data set A is zero, and therefore only four calibration data sets can be fit. In data sets C and D, all five gamma-peaks in S3D5 of the PC can be fit. In data sets B and E only four of the five gamma-peaks can be fit. Data set B is still used when fitting the common parameters over time. As discussed in Chapter 4, data set E is not used when fitting any of the common parameters over time.

B.6.1 Summary of Fit Results

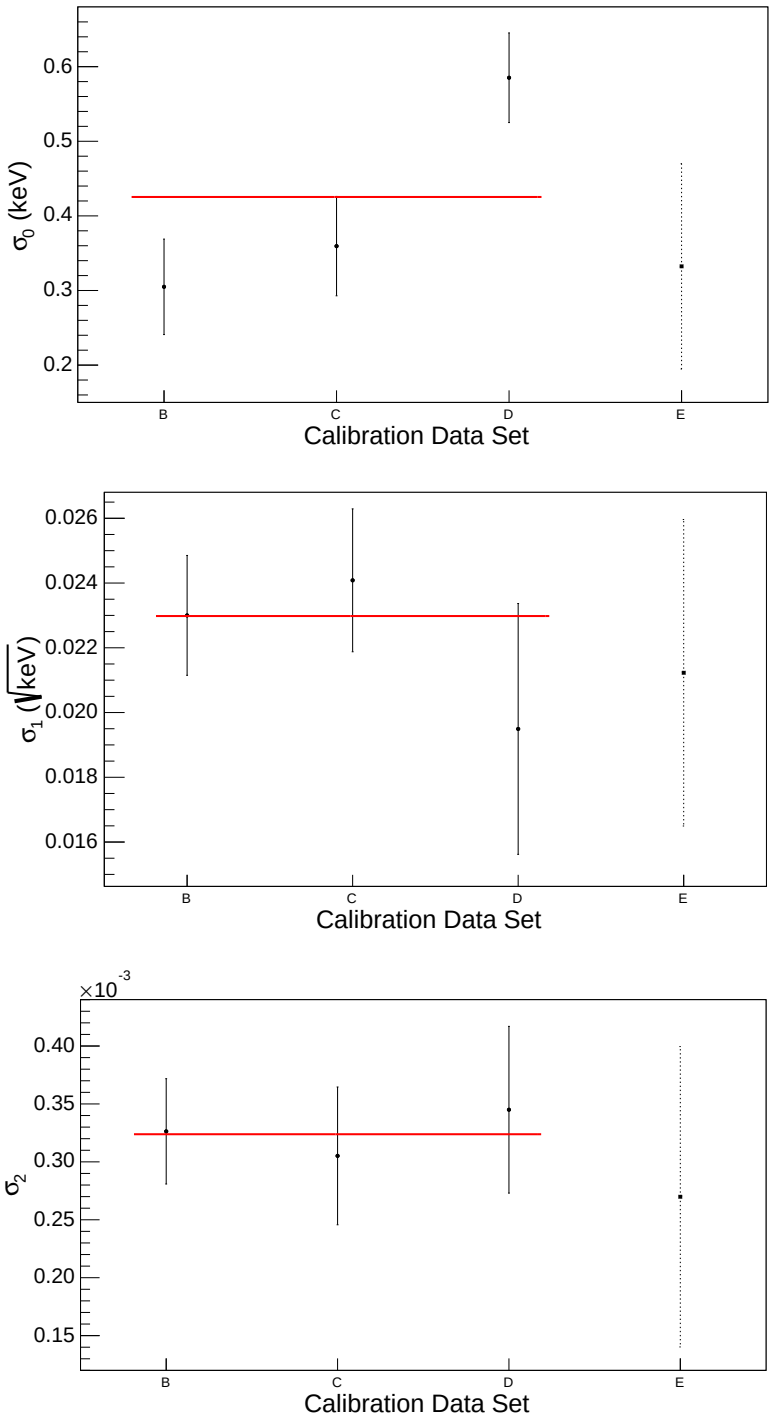

Figure B.60: Parameter σ_0 (top), σ_1 (middle) and σ_2 (bottom) for S3D5 over time. Data with solid error bars are fit with a constant over time. The best fits result in average values of: $\sigma_0 = 0.43\ (4)$ keV, $\sigma_1 = 2.3\ (1)\cdot 10^{-2}$ keV$^{1/2}$ and $\sigma_2 = 3.2\ (3)\cdot 10^{-4}$.

Table B.37: Peak #1 parameters of S3D5 for all calibration data.

	Calibration Data Set				
	A	B	C	D	E
μ [keV]	-	-	277.53 (3)	277.62 (6)	-
A/t $[cts/hr]$	-	-	45 (2)	44 (3)	-
H_{step}	-	-	0 (3)$\cdot 10^{-4}$	0.02 (2)	-
σ [keV]	-	-	0.55 (2)	0.68 (2)	-
τ [keV]	-	-	$0^{\dagger}$	$0^{\dagger}$	-
H_{tail}	-	-	$0^{\dagger}$	$0^{\dagger}$	-
M	-	-	277.53 (3)	277.62 (6)	-
Σ [keV]	-	-	0.55 (2)	0.68 (2)	-
FWHM [keV]	-	-	1.28 (5)	1.59 (6)	-
Runtime [hrs]	0.	4.848	4.383	3.361	0.871
Fixed	-	-	$m_H = b_H = 0$		-
Parameters	-	-	$m_\tau = b_\tau = 0$		-

† The best fit results in the parameter b_H being consistent with zero. Therefore the final fit is performed with b_τ, m_τ, b_H and m_H fixed to be zero.

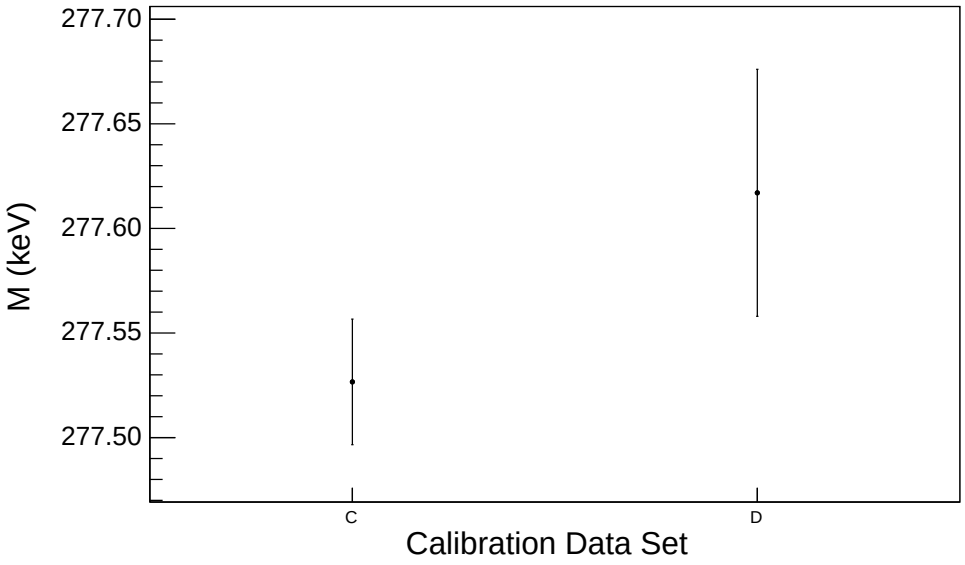

Figure B.61: The centroid (M) of peak #1 for S3D5 over time.

Table B.38: Peak #2 parameters of S3D5 for all calibration data.

Parameter	Calibration Data Set				
	A	B	C	D	E
μ [keV]	-	300.40 (2)	300.26 (3)	300.31 (4)	300.28 (4)
A/t $[cts/hr]$	-	62 (2)	59 (3)	63 (3)	65 (5)
H_{step}	-	0 (5)$\cdot 10^{-5}$	0.01 (1)	0.01 (1)	0 (2)$\cdot 10^{-4}$
σ [keV]	-	0.51 (2)	0.56 (2)	0.68 (2)	0.50 (4)
τ [keV]	-	0†	0†	0†	0†
H_{tail}	-	0†	0†	0†	0†
M	-	300.40 (2)	300.26 (3)	300.31 (4)	300.28 (4)
Σ [keV]	-	0.51 (2)	0.56 (2)	0.68 (2)	0.50 (4)
FWHM [keV]	-	1.20 (4)	1.31 (4)	1.61 (5)	1.18 (9)
Runtime [hrs]	0.	4.848	4.383	3.361	0.871
Fixed	-	$m_H = b_H = 0$			
Parameters	-	$m_\tau = b_\tau = 0$			

† The best fit results in the parameter b_H being consistent with zero. Therefore the final fit is performed with b_τ, m_τ, b_H and m_H fixed to be zero.

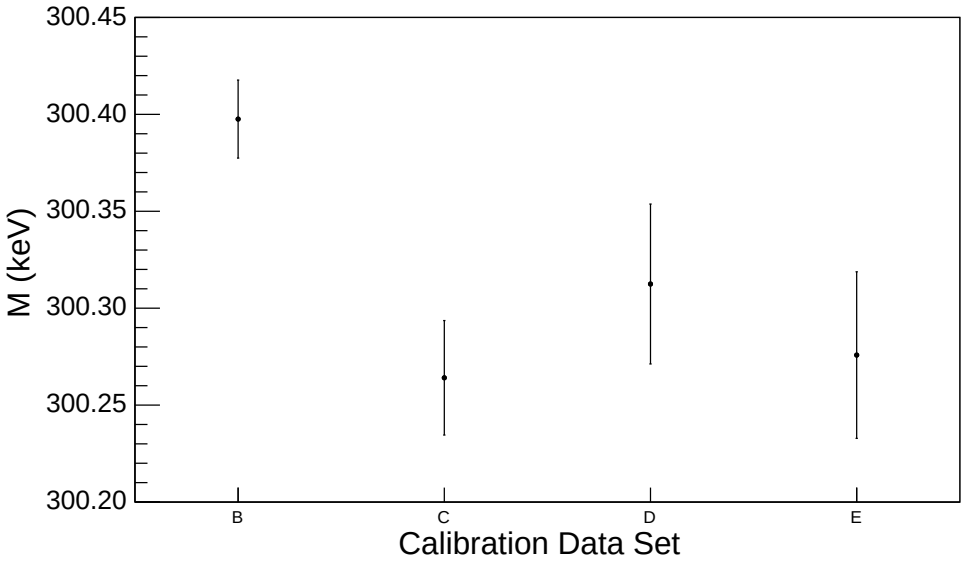

Figure B.62: The centroid (M) of peak #2 for S3D5 over time.

Table B.39: Peak #3 parameters of S3D5 for all calibration data.

Parameter	Calibration Data Set				
	A	B	C	D	E
μ [keV]	-	583.233 (7)	583.016 (8)	583.03 (1)	583.06 (2)
A/t $[cts/hr]$	-	430 (4)	421 (5)	414 (5)	405 (10)
H_{step}	-	4.8 (3)$\cdot 10^{-3}$	4 (1)$\cdot 10^{-3}$	5 (1)$\cdot 10^{-3}$	3 (3)$\cdot 10^{-3}$
σ [keV]	-	0.662 (5)	0.706 (6)	0.777 (7)	0.63 (1)
τ [keV]	-	$0^{\dagger}$	$0^{\dagger}$	$0^{\dagger}$	$0^{\dagger}$
H_{tail}	-	$0^{\dagger}$	$0^{\dagger}$	$0^{\dagger}$	$0^{\dagger}$
M	-	583.233 (7)	583.016 (8)	583.03 (1)	583.06 (2)
Σ [keV]	-	0.662 (5)	0.706 (6)	0.777 (7)	0.63 (1)
FWHM [keV]	-	1.56 (1)	1.66 (1)	1.83 (2)	1.49 (3)
Runtime [hrs]	0.	4.848	4.383	3.361	0.871
Fixed Parameters	-	$m_H = b_H = 0$			
	-	$m_\tau = b_\tau = 0$			

† The best fit results in the parameter b_H being consistent with zero. Therefore the final fit is performed with b_τ, m_τ, b_H and m_H fixed to be zero.

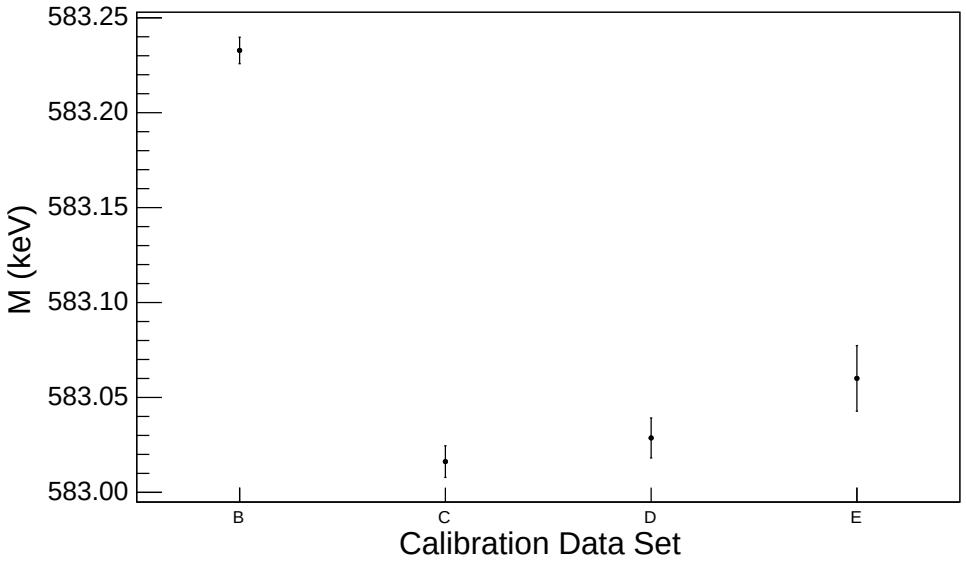

Figure B.63: The centroid (M) of peak #3 for S3D5 over time.

Table B.40: Peak #4 parameters of S3D5 for all calibration data.

Parameter	Calibration Data Set				
	A	B	C	D	E
μ [keV]	-	860.82 (3)	860.59 (3)	860.58 (4)	860.68 (6)
A/t $[cts/hr]$	-	54 (2)	50 (2)	49 (2)	48 (4)
H_{step}	-	0 (1)$\cdot 10^{-3}$	8 (4)$\cdot 10^{-3}$	2 (5)$\cdot 10^{-3}$	0 (6)$\cdot 10^{-4}$
σ [keV]	-	0.792 (10)	0.84 (1)	0.87 (2)	0.74 (3)
τ [keV]	-	0†	0†	0†	0†
H_{tail}	-	0†	0†	0†	0†
M	-	860.82 (3)	860.59 (3)	860.58 (4)	860.68 (6)
Σ [keV]	-	0.792 (10)	0.84 (1)	0.87 (2)	0.74 (3)
FWHM [keV]	-	1.87 (2)	1.97 (3)	2.05 (4)	1.75 (6)
Runtime [hrs]	0.	4.848	4.383	3.361	0.871
Fixed	-	$m_H = b_H = 0$			
Parameters	-	$m_\tau = b_\tau = 0$			

† The best fit results in the parameter b_H being consistent with zero. Therefore the final fit is performed with b_τ, m_τ, b_H and m_H fixed to be zero.

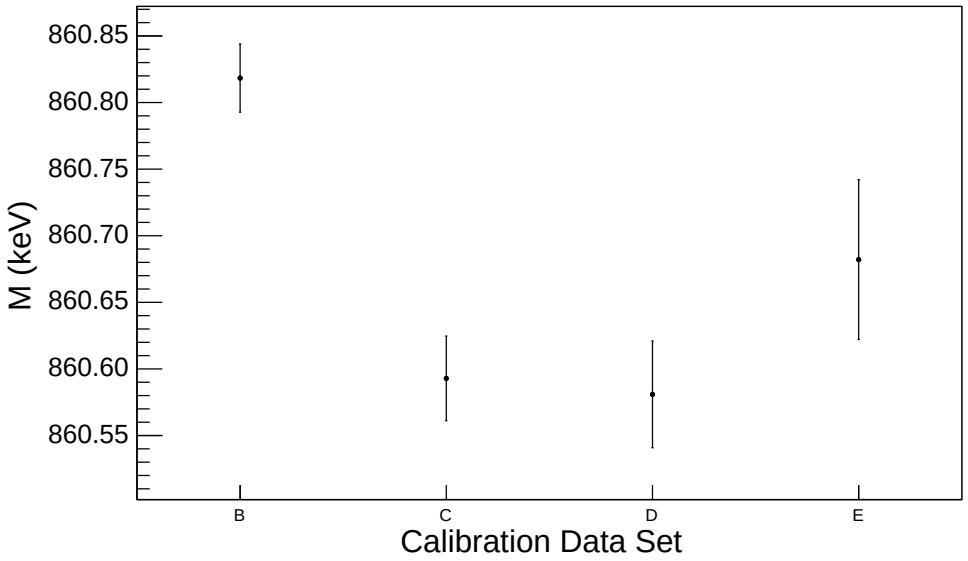

Figure B.64: The centroid (M) of peak #4 for S3D5 over time.

Table B.41: Peak #5 parameters of S3D5 for all calibration data.

Parameter	Calibration Data Set				
	A	B	C	D	E
μ [keV]	-	2614.29 (2)	2613.88 (3)	2613.92 (3)	2614.22 (6)
A/t $[cts/hr]$	-	192 (3)	187 (3)	180 (4)	173 (7)
H_{step}	-	9.1 (3)$\cdot 10^{-3}$	8.8 (9)$\cdot 10^{-3}$	8 (1)$\cdot 10^{-3}$	1.0 (4)$\cdot 10^{-2}$
σ [keV]	-	1.48 (2)	1.51 (2)	1.47 (3)	1.34 (5)
τ [keV]	-	$0^{\dagger}$	$0^{\dagger}$	$0^{\dagger}$	$0^{\dagger}$
H_{tail}	-	$0^{\dagger}$	$0^{\dagger}$	$0^{\dagger}$	$0^{\dagger}$
M	-	2614.29 (2)	2613.88 (3)	2613.92 (3)	2614.22 (6)
Σ [keV]	-	1.48 (2)	1.51 (2)	1.47 (3)	1.34 (5)
FWHM [keV]	-	3.50 (5)	3.56 (5)	3.45 (6)	3.1 (1)
Runtime [hrs]	0.	4.848	4.383	3.361	0.871
Fixed	-	$m_H = b_H = 0$			
Parameters	-	$m_\tau = b_\tau = 0$			

† The best fit results in the parameter b_H being consistent with zero. Therefore the final fit is performed with b_τ, m_τ, b_H and m_H fixed to be zero.

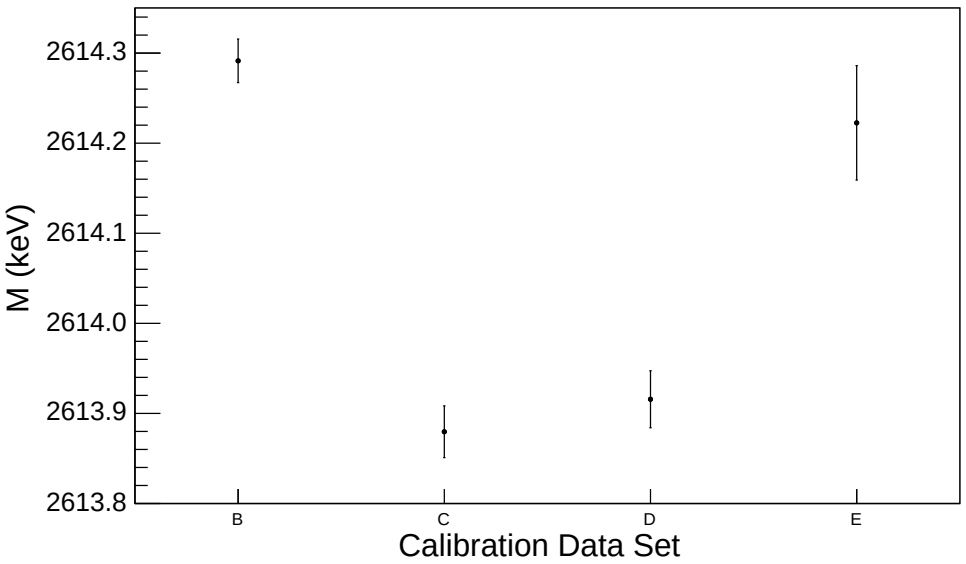

Figure B.65: The centroid (M) of peak #5 for S3D5 over time.

Table B.42: The peak rates during the four calibration data sets for S3D5. As a reminder, there are five peaks for two of the calibration data sets and four peaks for the other two calibration data sets. The peak rate is the area parameter divided by the runtime divided by the bin width (0.1 keV). Also shown is the ratio of each peak's rate to the 583-keV peak rate (i.e. Pk #3).

		Calibration Data Set				
		A	B	C	D	E
Pk Rate $\left[\frac{cts}{hr}\right]$	Pk #1	-	-	450 (20)	440 (30)	-
	Pk #2	-	620 (20)	590 (30)	630 (30)	650 (50)
	Pk #3	-	4300 (40)	4210 (50)	4140 (50)	4050 (100)
	Pk #4	-	540 (20)	500 (20)	490 (20)	480 (40)
	Pk #5	-	1920 (30)	1870 (30)	1800 (40)	1730 (70)
$\frac{\text{Pk } \#n \text{ Rate}}{\text{Pk } \#3 \text{ Rate}}$	$n = 1$	-	-	0.106 (6)	0.106 (7)	-
	$n = 2$	-	0.143 (5)	0.140 (6)	0.152 (8)	0.16 (1)
	$n = 3$	-	1.	1.	1.	1.
	$n = 4$	-	0.125 (4)	0.120 (4)	0.119 (5)	0.118 (9)
	$n = 5$	-	0.446 (8)	0.444 (9)	0.436 (1)	0.43 (2)

B.6.2 Individual Peak Fits

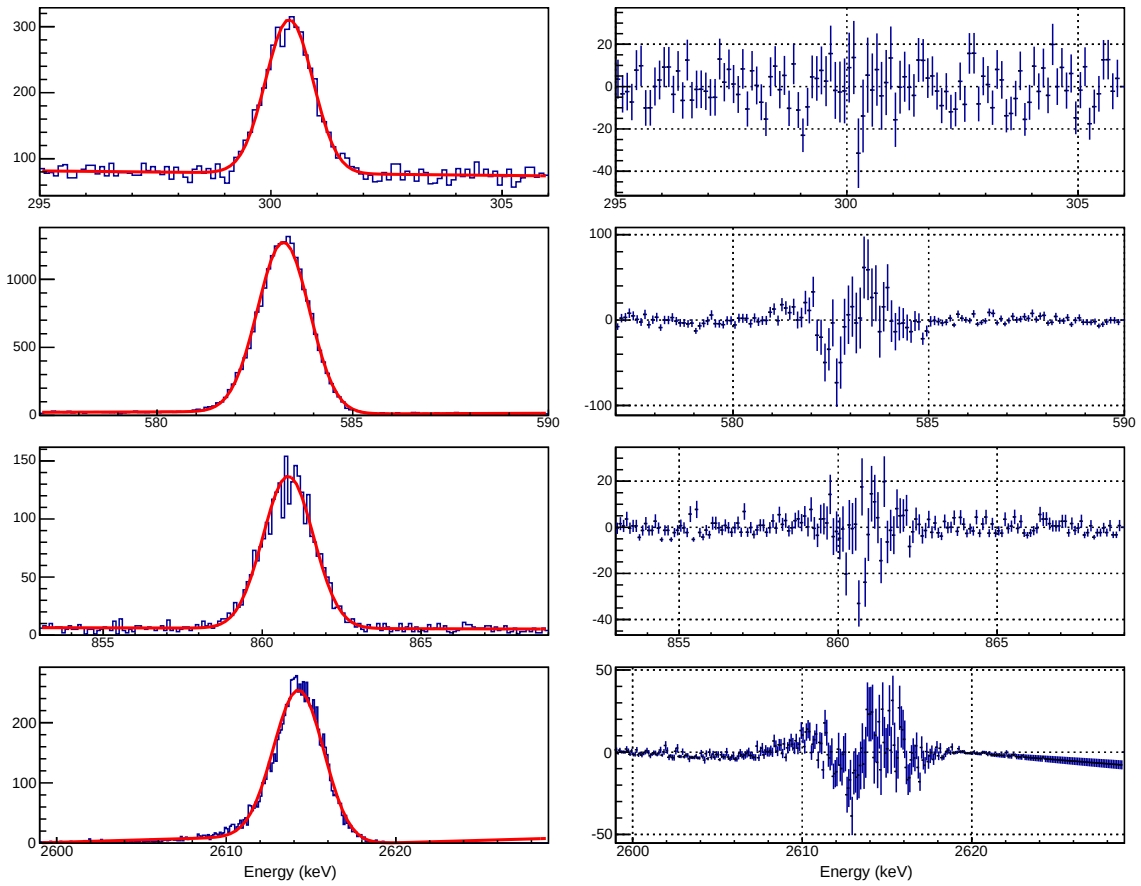

Figure B.66: The four gamma peaks of S3D5 in calibration data set B that are fit with the multi-peak fitting routine. Shown on the left is each of the four peaks with the best fit of the multi-peak fitting function shown in red. Shown on the right is the residual of the fit for each peak.

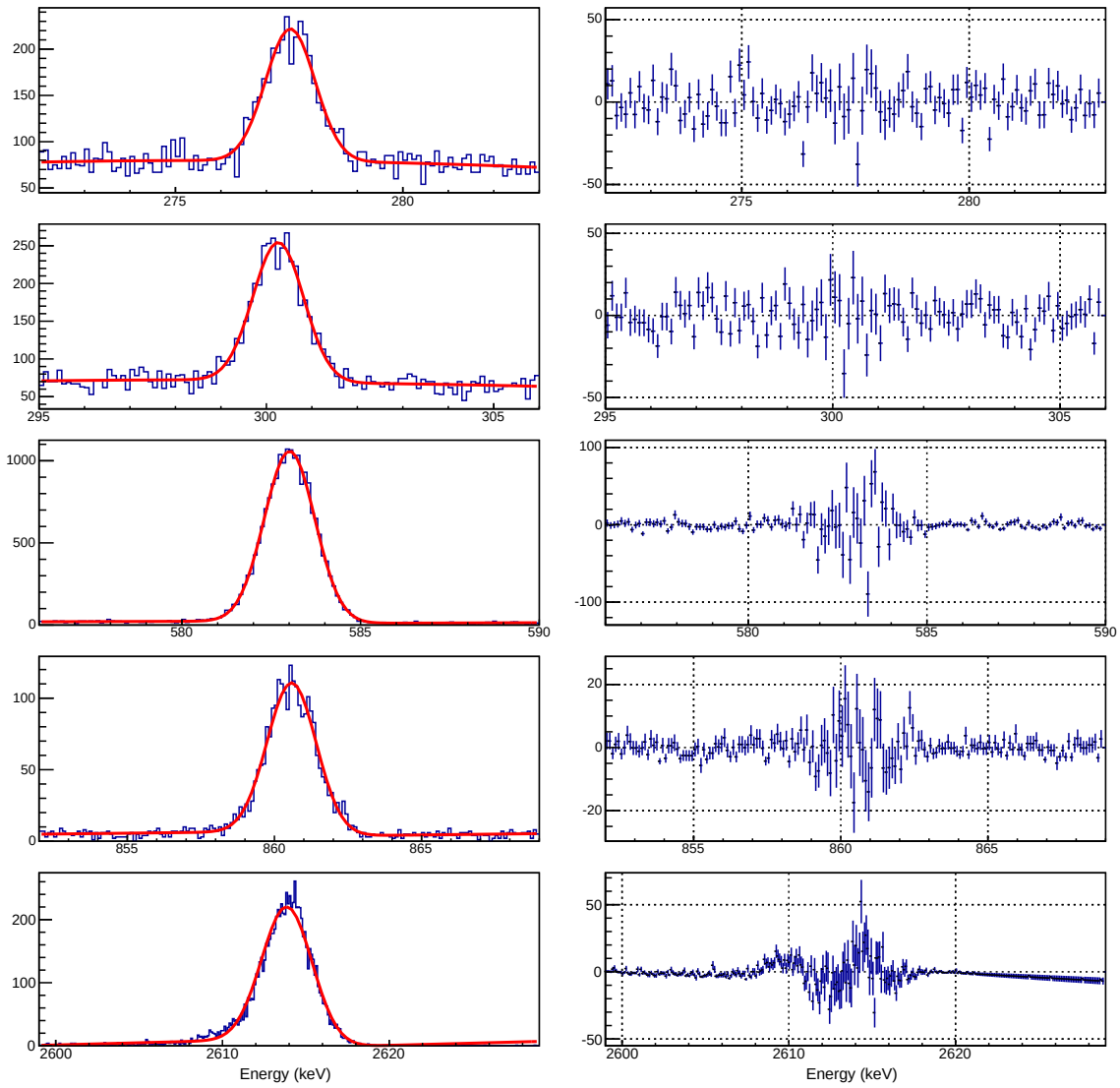

Figure B.67: The five gamma peaks of S3D5 in calibration data set C that are fit with the multi-peak fitting routine. Shown on the left is each of the five peaks with the best fit of the multi-peak fitting function shown in red. Shown on the right is the residual of the fit for each peak.

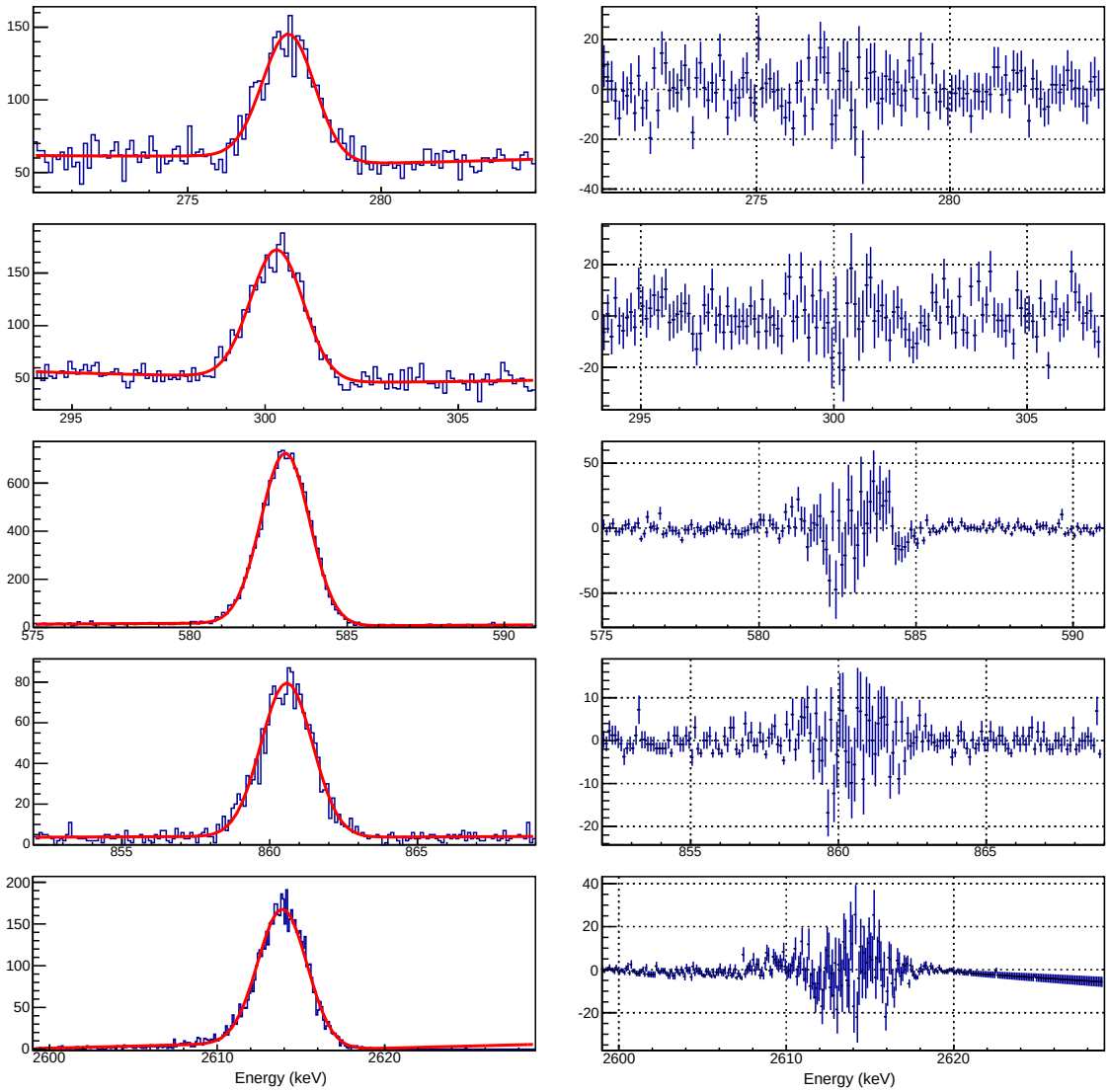

Figure B.68: The five gamma peaks of S3D5 in calibration data set D that are fit with the multi-peak fitting routine. Shown on the left is each of the five peaks with the best fit of the multi-peak fitting function shown in red. Shown on the right is the residual of the fit for each peak.

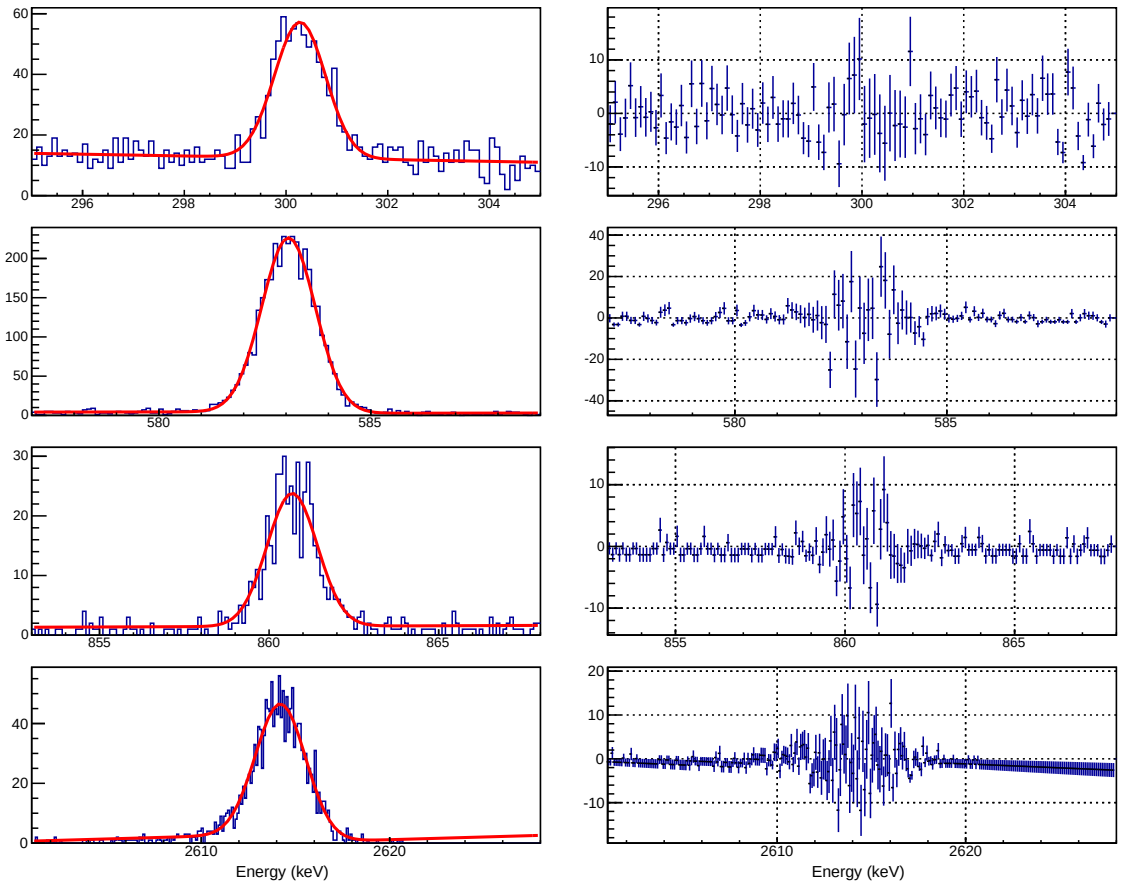

Figure B.69: The four gamma peaks of S3D5 in calibration data set E that are fit with the multi-peak fitting routine. Shown on the left is each of the four peaks with the best fit of the multi-peak fitting function shown in red. Shown on the right is the residual of the fit for each peak.

APPENDIX C: MaGe MASSES AND MATERIALS OF PROTOTYPE CRYOSTAT COMPONENTS

C.1 Overview

Table C.1: The major components of the Prototype module's cryostat and surrounding environment in the MaGe geometry. For each component the number of times the part is present throughout the PC geometry is listed, as well as its material composition in MaGe. The total mass is the mass of the component – as calculated by MaGe – multiplied by the number of times it is present in the PC geometry.

Component Name	#	Material	Total Mass [kg]
Cavern	1	Rock	$7.02{\cdot}10^{10}$
Walls and Floor	1	Concrete	$3.47{\cdot}10^{4}$
Muon Veto			
Muon Veto Side Panels	12	Plastic Scintillator	543
Muon Veto Floor Panels	12	Plastic Scintillator	269
Passive Shielding			
Outer Copper Shield	1	OFHC Cu	$1.39{\cdot}10^{3}$
Lead Shield	1	Ancient Lead	$4.88{\cdot}10^{4}$
Inner Cavity Volume	1	Nitrogen Gas	0.292
Radon Purge Box	1	SS	430
Cryostat and Clamping Hardware			
Cryostat Hoop	1	EFCu	12.8
Cryostat Top Lid	1	EFCu	7.01
Cryostat Bottom Lid	1	EFCu	21.2
Cross Arm Tube	1	EFCu	6.46
Cryostat Clamping Rails	16	EFCu	5.61
Cryostat Clamping Bolts	24	SS	0.259
Cryostat Clamping Nuts	24	SiBronze	$6.77{\cdot}10^{-2}$
Thermosyphon			
Thermosyphon Mount Plate	1	EFCu	0.463
Thermosyphon Tube	1	EFCu	3.31
Thermosyphon Hoop Adapter	1	EFCu	$7.90{\cdot}10^{-2}$
Thermosyphon Cold Plate Adapter	1	EFCu	1.05
Thermosyphon Bolts	6	EFCu	0.152
Liquid Nitrogen	1	Nitrogen Liquid	0.562
Thermal Shield			
Thermal Shield Can	1	EFCu	3.23
Thermal Shield Annulus	1	EFCu	0.579
Thermal Shield Supports	3	PEEK	$3.92{\cdot}10^{-4}$
Thermal Shield Wedges	3	EFCu	$3.71{\cdot}10^{-2}$
Thermal Shield Screws	14	SS	$2.21{\cdot}10^{-2}$
ColdPlate	1	EFCu	6.87

Table C.2: The major components of the string arrays in the PC MaGe geometry. For each component the number of times the part is present in a single string is listed, as well as its material composition in MaGe. The total mass is the mass of the component – as calculated by MaGe – multiplied by the number of times it is present in a single string.

Component Name	#	Material	Total Mass [g]
String Adapter Plate	1	EFCu	115
Adapter Plate Bolts	3	EFCu	14.7
Adapter Plate Nuts	3	EFCu	2.44
String Tie Rods	3	EFCu	72.3 String 1 20.7 String 2 72.3 String 3
Tie Rod Split Nuts	3	EFCu	2.26
Tie Rod Bottom Nuts	3	EFCu	4.88
Copper Spacers	3 String 1 3 String 2 0 String 3	EFCu	16.7 String 1 28.5 String 2 0 String 3
Cable Wire Segments	25	EFCu	1.26
Cable Insulation Segments	10	Parylene	0.426

Table C.3: The major components of the detector mounts in the PC MaGe geometry. For each component the number of times the part is present in a single detector mount is listed, as well as its material composition in MaGe. The total mass is the mass of the component – as calculated by MaGe – multiplied by the number of times it is present in a single detector mount.

Component Name	#	Material	Total Mass [g]
HV Ring	1	EFCu	47.7
HV Nuts	3	Teflon	2.17
Hollow Hex Rods	3	EFCu	27.9
Crystal Insulators	3	Teflon	$\begin{cases} 4.82 & \text{S1D3, S1D4} \\ 2.74 & \text{All others} \end{cases}$
Cable Guides	2	Teflon	0.688
Crystal Mounting Plate	1	EFCu	58.5
Contact Pin	1	EFCu	$8.35 \cdot 10^{-2}$
Center Bushing	1	Teflon	0.147
Spring LMFE Mount	1	EFCu	4.16
Spring Mount Nuts	3	EFCu	0.645
LMFE Cover Plate	1	EFCu	3.71
LMFE Substrate	1	Silica	0.105
LMFE Traces	1	Gold	$2.26 \cdot 10^{-4}$
Cable Wire Segments	8	EFCu	$5.95 \cdot 10^{-3}$
Cable Insulation Segments	2	Parylene	$1.50 \cdot 10^{-2}$

Table C.4: The major components of the temperature sensor assemblies in the PC MaGe geometry. For each component the number of times the part is present throughout the PC geometry is listed, as well as its material composition in MaGe. The total mass is the mass of the component – as calculated by MaGe – multiplied by the number of times it is present in the PC geometry.

Component Name	#	Material	Total Mass [g]
Temperature Sensor Clamps	5	Teflon	2.57
Temperature Sensor Screws	5	SS	1.49
Temperature Sensor Solder	5	Modified Lead	0.100

C.2 Detector Masses

Table C.5: The detector masses as calculated by MaGe, compared with the actual detector masses.

Detector	Manufacturer	MaGe Mass [g]	Measured Mass [g]
S1D1	CANBERRA	638.92	631
S1D2	CANBERRA	663.879	633
S1D3	ORTEC®	944.854	904
S1D4	ORTEC®	1060.14	1013.5
S2D1	CANBERRA	638.653	644
S3D1	CANBERRA	639.048	622
S3D2	CANBERRA	639.134	646
S3D3	CANBERRA	638.901	630
S3D4	CANBERRA	638.597	631
S3D5	CANBERRA	638.863	627

C.3 String 1 Copper Components: OFHC versus EFCu

Table C.6: OFHC Cu components in String 1 of the PC.

Part Name	Mass [g]
String Adapter Plate	115
Adapter Plate Nut _02	0.814
Tie Rod Bottom Nut _01	1.63
Tie Rod Bottom Nut _02	1.63
Tie Rod Bottom Nut _03	1.63
Copper Spacer _01	5.56
Copper Spacer _02	5.56
Copper Spacer _03	5.56
Detector 1 HV Ring	47.7
Detector 2 HV Ring	47.7
Detector 1 Hollow Hex Rod _01	9.31
Detector 1 Hollow Hex Rod _02	9.31
Detector 1 Hollow Hex Rod _03	9.31
Detector 1 Crystal Mounting Plate	58.5
Detector 2 Crystal Mounting Plate	58.5
Detector 3 Crystal Mounting Plate	58.5
Detector 4 Crystal Mounting Plate	58.5
Detector 1 Contact Pin	$8.35 \cdot 10^{-2}$
Detector 2 Contact Pin	$8.35 \cdot 10^{-2}$
Detector 4 Contact Pin	$8.35 \cdot 10^{-2}$
Detector 1 Spring Mount Nut _01	0.215
Detector 1 Spring Mount Nut _02	0.215
Detector 1 Spring Mount Nut _03	0.215
Detector 2 Spring Mount Nut _01	0.215
Detector 2 Spring Mount Nut _02	0.215
Detector 2 Spring Mount Nut _03	0.215
Detector 3 Spring Mount Nut _01	0.215
Detector 3 Spring Mount Nut _02	0.215
Detector 3 Spring Mount Nut _03	0.215
Detector 4 Spring Mount Nut _01	0.215
Detector 4 Spring Mount Nut _02	0.215
Detector 4 Spring Mount Nut _03	0.215
Detector 1 LMFE Cover Plate	3.71
Detector 2 LMFE Cover Plate	3.71
Detector 3 LMFE Cover Plate	3.71

Detector 4 LMFE Cover Plate	3.71
Total Mass	**516**

Table C.7: UGEFCu components in String 1 of the PC.

Part Name	Mass [g]
Adapter Plate Bolt _01	4.89
Adapter Plate Bolt _02	4.89
Adapter Plate Bolt _03	4.89
Adapter Plate Nut _01	0.814
Adapter Plate Nut _03	0.814
String Tie Rod _01	24.1
String Tie Rod _02	24.1
String Tie Rod _03	24.1
Detector 3 HV Ring	47.7
Detector 4 HV Ring	47.7
Detector 2 Hollow Hex Rod _01	9.31
Detector 2 Hollow Hex Rod _02	9.31
Detector 2 Hollow Hex Rod _03	9.31
Detector 3 Hollow Hex Rod _01	9.31
Detector 3 Hollow Hex Rod _02	9.31
Detector 3 Hollow Hex Rod _03	9.31
Detector 4 Hollow Hex Rod _01	9.31
Detector 4 Hollow Hex Rod _02	9.31
Detector 4 Hollow Hex Rod _03	9.31
Detector 3 Contact Pin	$8.35 \cdot 10^{-2}$
Detector 1 Spring LMFE Mount	4.16
Detector 2 Spring LMFE Mount	4.16
Detector 3 Spring LMFE Mount	4.16
Detector 4 Spring LMFE Mount	4.16
Total Mass	**285**

C.4 String 2 Copper Components: OFHC versus EFCu

Table C.8: OFHC Cu components in String 2 of the PC.

Part Name	Mass [g]
String Adapter Plate	115
Adapter Plate Bolt _01	4.89
Adapter Plate Bolt _02	4.89
Adapter Plate Bolt _03	4.89
Adapter Plate Nut _01	0.814
Adapter Plate Nut _02	0.814
Adapter Plate Nut _03	0.814
String Tie Rod _01	6.91
String Tie Rod _02	6.91
String Tie Rod _03	6.91
Tie Rod Split Nuts _01	0.752
Tie Rod Split Nuts _02	0.752
Tie Rod Split Nuts _03	0.752
Tie Rod Bottom Nut _01	1.63
Tie Rod Bottom Nut _02	1.63
Tie Rod Bottom Nut _03	1.63
Detector 1 HV Ring	47.7
Detector 1 Hollow Hex Rod _01	9.31
Detector 1 Hollow Hex Rod _02	9.31
Detector 1 Hollow Hex Rod _03	9.31
Detector 1 Crystal Mounting Plate	58.5
Detector 1 Contact Pin	$8.35 \cdot 10^{-2}$
Detector 1 Spring Mount Nut _01	0.215
Detector 1 Spring Mount Nut _02	0.215
Detector 1 Spring Mount Nut _03	0.215
Detector 1 LMFE Cover Plate	3.71
Total Mass	**299**

Table C.9: UGEFCu components in String 2 of the PC.

Part Name	Mass [g]
Copper Spacer _01	9.49
Copper Spacer _02	9.49
Copper Spacer _03	9.49
Detector 1 Spring LMFE Mount	4.16
Total Mass	**33**

C.5 String 3 Copper Components: OFHC versus EFCu

Table C.10: OFHC Cu components in String 3 of the PC.

Part Name	Mass [g]
String Adapter Plate	115
Tie Rod Bottom Nut _01	1.63
Tie Rod Bottom Nut _02	1.63
Tie Rod Bottom Nut _03	1.63
Detector 1 HV Ring	47.7
Detector 2 HV Ring	47.7
Detector 3 HV Ring	47.7
Detector 4 HV Ring	47.7
Detector 5 HV Ring	47.7
Detector 1 Hollow Hex Rod _01	9.31
Detector 1 Hollow Hex Rod _02	9.31
Detector 1 Hollow Hex Rod _03	9.31
Detector 2 Hollow Hex Rod _01	9.31
Detector 2 Hollow Hex Rod _02	9.31
Detector 2 Hollow Hex Rod _03	9.31
Detector 3 Hollow Hex Rod _01	9.31
Detector 3 Hollow Hex Rod _02	9.31
Detector 3 Hollow Hex Rod _03	9.31
Detector 4 Hollow Hex Rod _01	9.31
Detector 4 Hollow Hex Rod _02	9.31
Detector 4 Hollow Hex Rod _03	9.31

Detector 5 Hollow Hex Rod _01	9.31
Detector 5 Hollow Hex Rod _02	9.31
Detector 5 Hollow Hex Rod _03	9.31
Detector 2 Crystal Mounting Plate	58.5
Detector 3 Crystal Mounting Plate	58.5
Detector 4 Crystal Mounting Plate	58.5
Detector 5 Crystal Mounting Plate	58.5
Detector 1 Contact Pin	$8.35 \cdot 10^{-2}$
Detector 2 Contact Pin	$8.35 \cdot 10^{-2}$
Detector 3 Contact Pin	$8.35 \cdot 10^{-2}$
Detector 4 Contact Pin	$8.35 \cdot 10^{-2}$
Detector 5 Contact Pin	$8.35 \cdot 10^{-2}$
Detector 1 Spring Mount Nut _01	0.215
Detector 1 Spring Mount Nut _02	0.215
Detector 1 Spring Mount Nut _03	0.215
Detector 2 Spring Mount Nut _01	0.215
Detector 2 Spring Mount Nut _02	0.215
Detector 2 Spring Mount Nut _03	0.215
Detector 3 Spring Mount Nut _01	0.215
Detector 3 Spring Mount Nut _02	0.215
Detector 3 Spring Mount Nut _03	0.215
Detector 4 Spring Mount Nut _01	0.215
Detector 4 Spring Mount Nut _02	0.215
Detector 4 Spring Mount Nut _03	0.215
Detector 5 Spring Mount Nut _01	0.215
Detector 5 Spring Mount Nut _02	0.215
Detector 5 Spring Mount Nut _03	0.215
Detector 1 LMFE Cover Plate	3.71
Detector 3 LMFE Cover Plate	3.71
Detector 4 LMFE Cover Plate	3.71
Detector 5 LMFE Cover Plate	3.71
Total Mass	**753**

Table C.11: UGEFCu components in String 3 of the PC.

Part Name	Mass [g]
Adapter Plate Bolt _01	4.89
Adapter Plate Bolt _02	4.89
Adapter Plate Bolt _03	4.89
Adapter Plate Nut _01	0.815
Adapter Plate Nut _02	0.815
Adapter Plate Nut _03	0.815
String Tie Rod _01	24.1
String Tie Rod _02	24.1
String Tie Rod _03	24.1
Detector 1 Crystal Mounting Plate	58.5
Detector 1 Spring LMFE Mount	4.16
Detector 2 Spring LMFE Mount	4.16
Detector 3 Spring LMFE Mount	4.16
Detector 4 Spring LMFE Mount	4.16
Detector 5 Spring LMFE Mount	4.16
Detector 2 LMFE Cover Plate	3.71
Total Mass	**172**

APPENDIX D: MONTE CARLO FIT RESULTS

D.1 MC-Generated Energy Spectra

For each MC-fit group (listed in Table 6.2) a MC-generated energy spectrum can be made for each detector. What follows are the energy spectra for S3D2. The spectra are normalized so that the sum of their bin contents (in the fit range of 100–1674 keV) is equal to one.

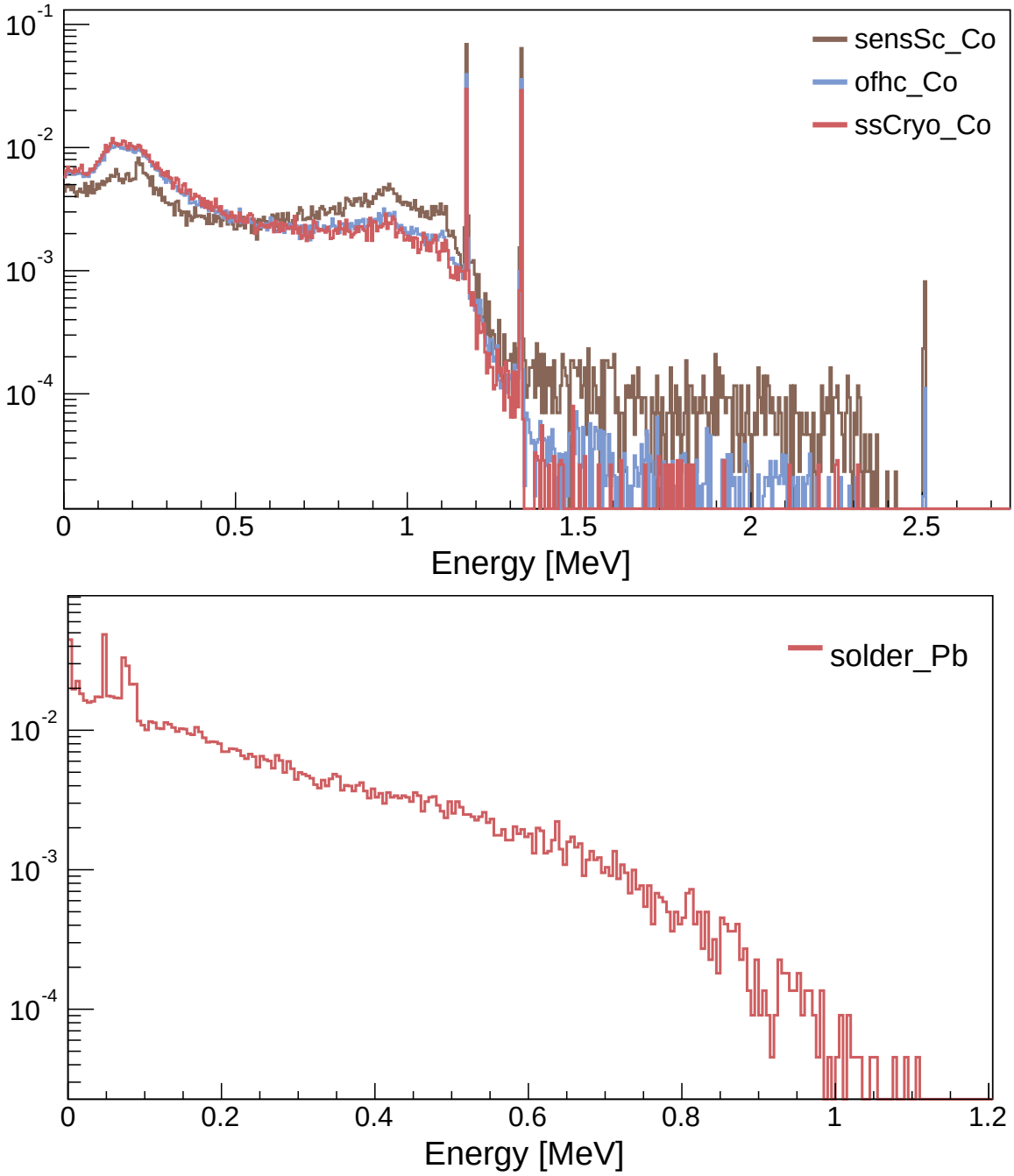

Figure D.1: The normalized MC-generated energy spectra for the MC-fit groups as seen by S3D2. Table 6.2 further details the parts and nuclides associated with each MC-fit group.

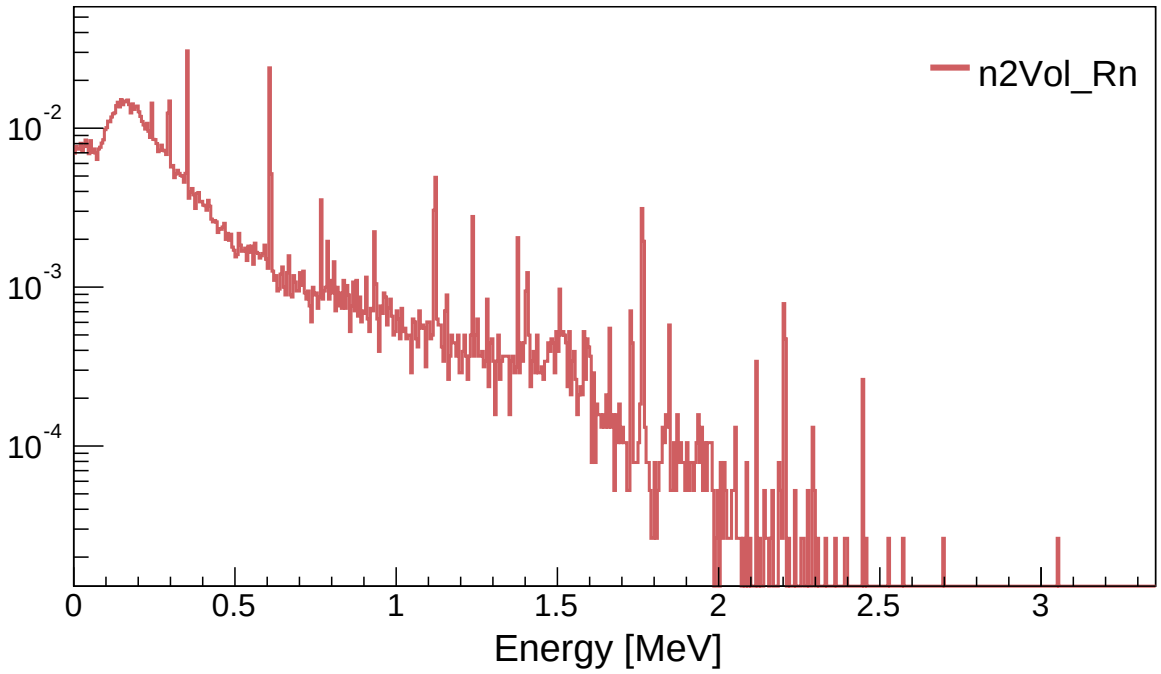

Figure D.2: The normalized MC-generated energy spectra for the MC-fit groups as seen by S3D2. Table 6.2 further details the parts and nuclides associated with each MC-fit group.

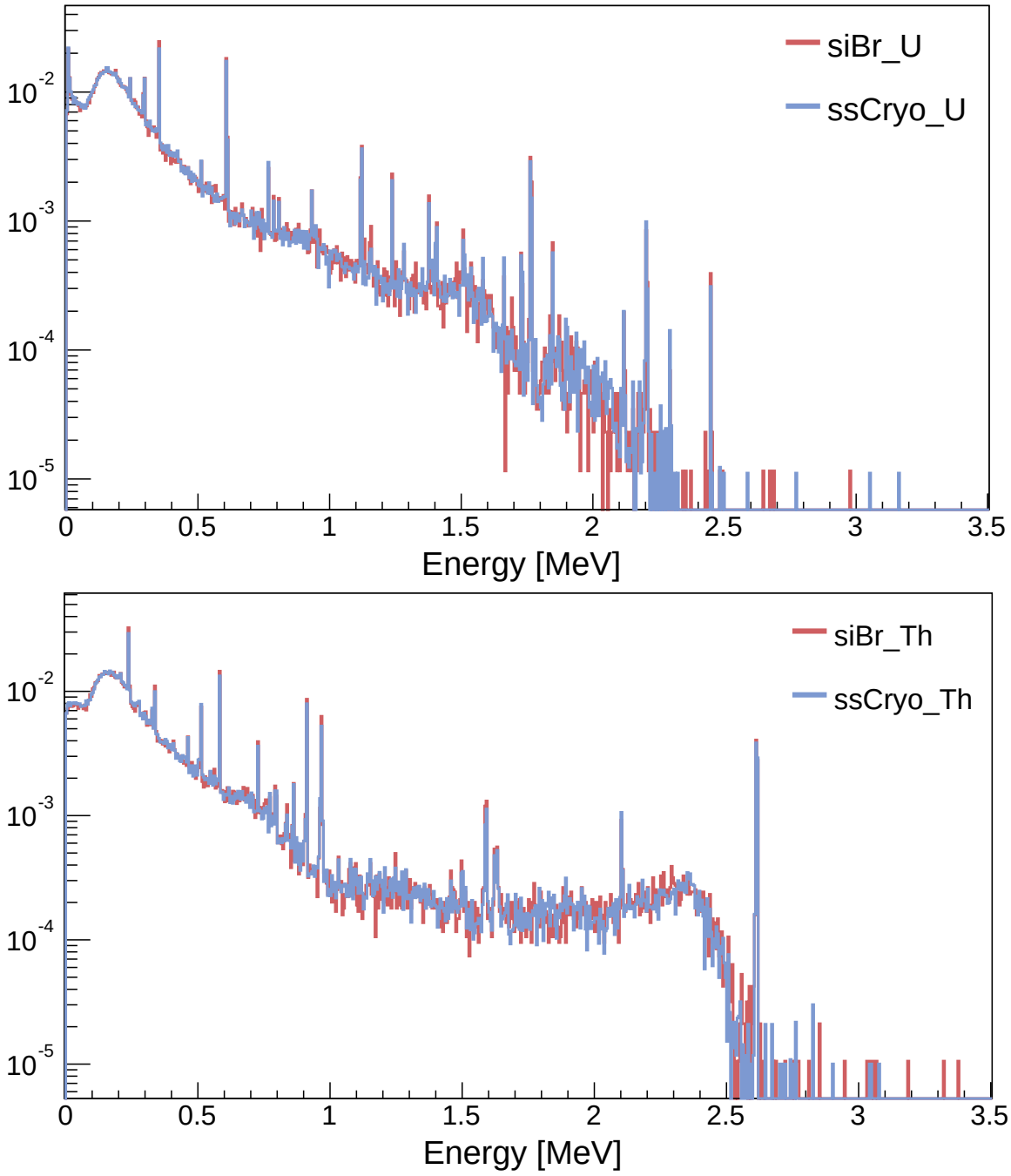

Figure D.3: The normalized MC-generated energy spectra for the MC-fit groups as seen by S3D2. Table 6.2 further details the parts and nuclides associated with each MC-fit group.

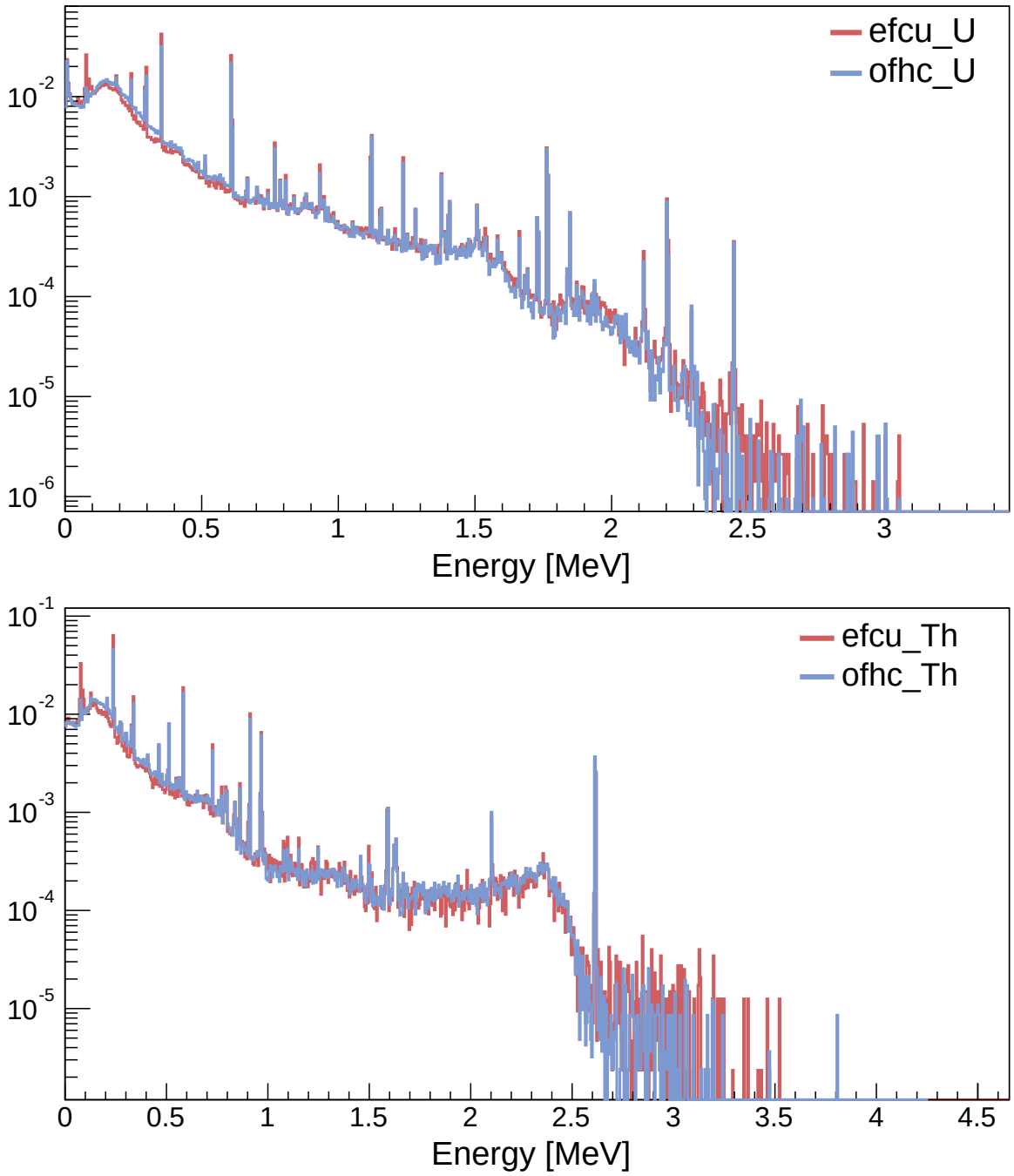

Figure D.4: The normalized MC-generated energy spectra for the MC-fit groups as seen by S3D2. Table 6.2 further details the parts and nuclides associated with each MC-fit group.

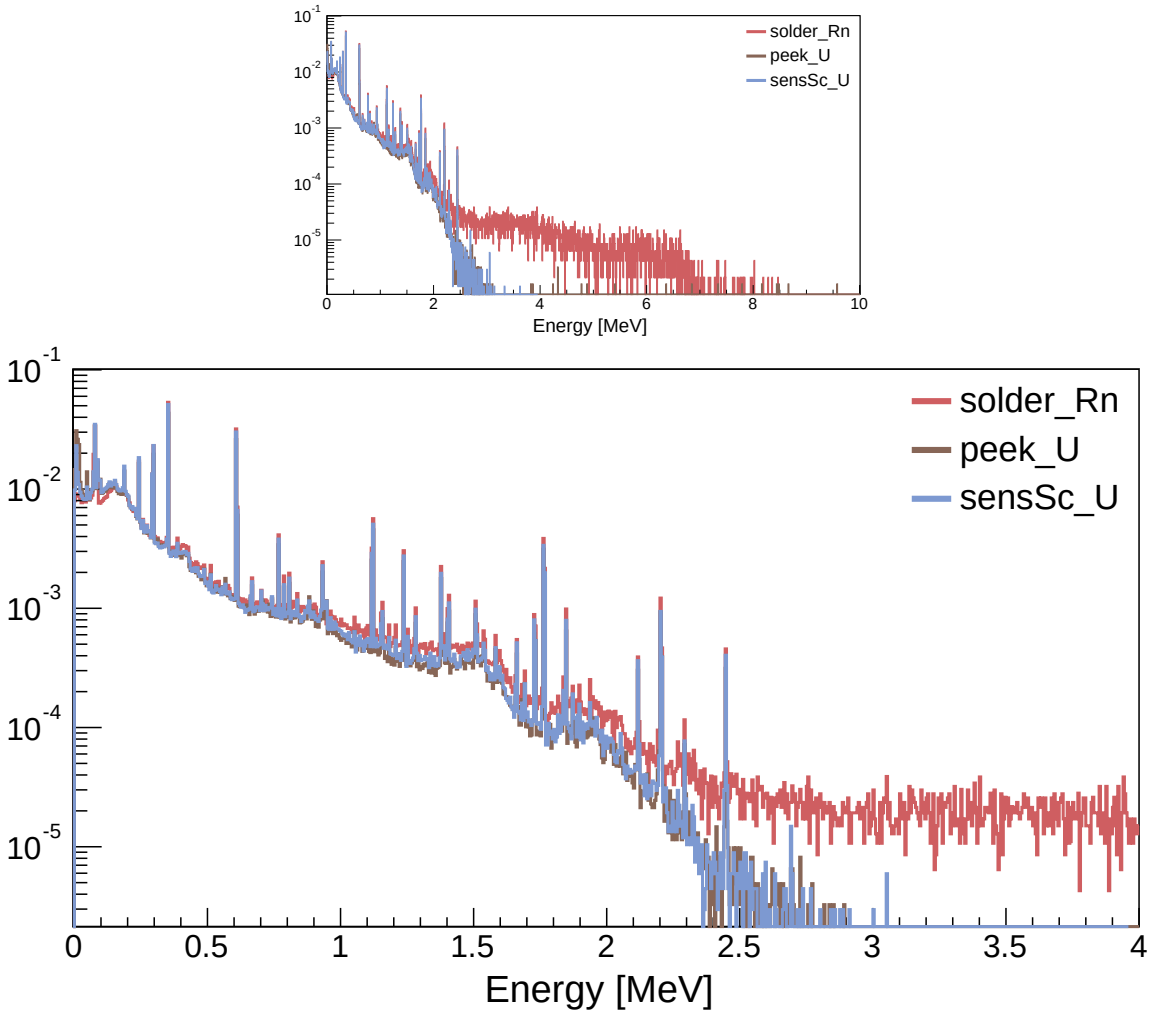

Figure D.5: The normalized MC-generated energy spectra for the MC-fit groups as seen by S3D2. Table 6.2 further details the parts and nuclides associated with each MC-fit group.

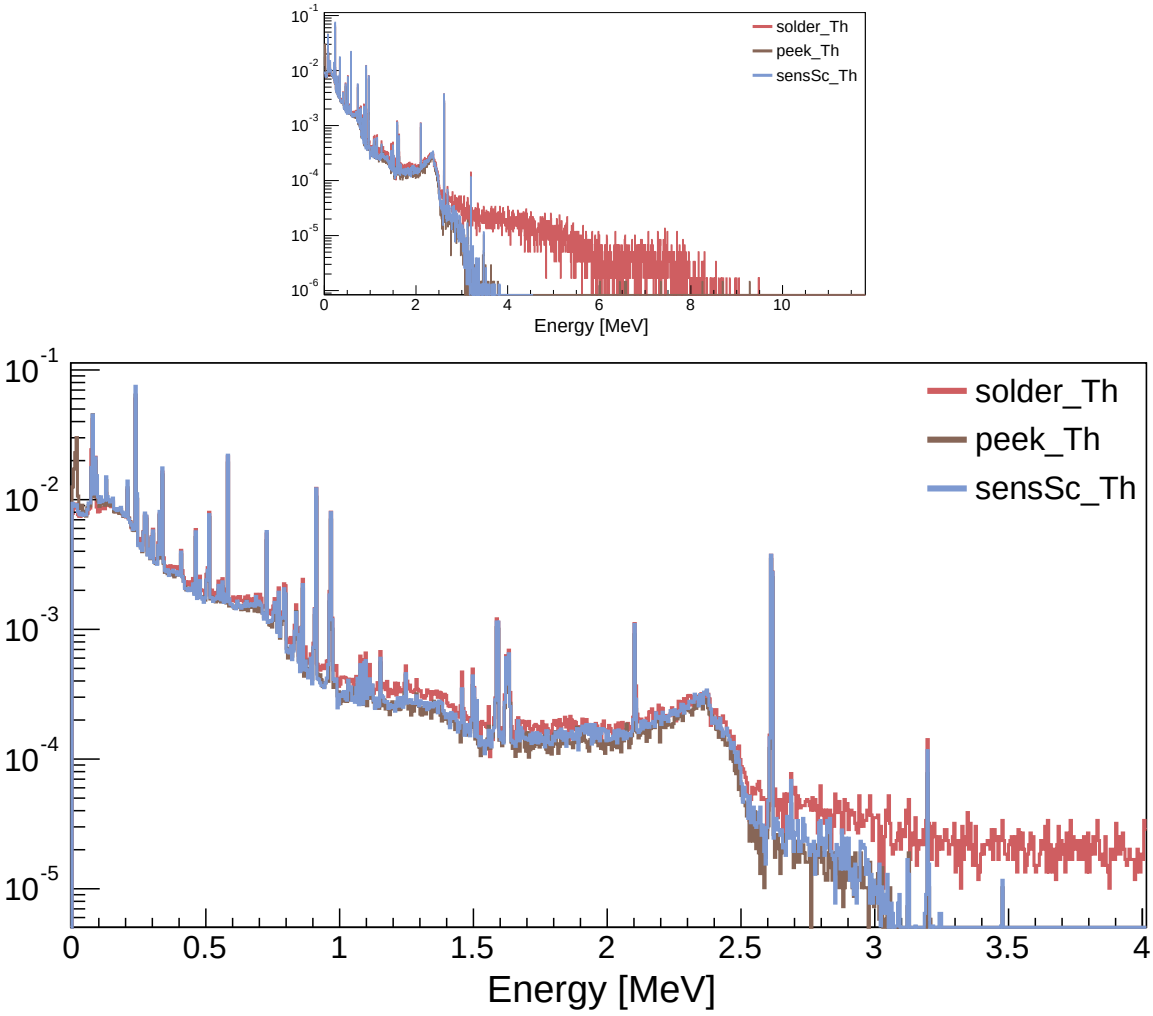

Figure D.6: The normalized MC-generated energy spectra for the MC-fit groups as seen by S3D2. Table 6.2 further details the parts and nuclides associated with each MC-fit group.

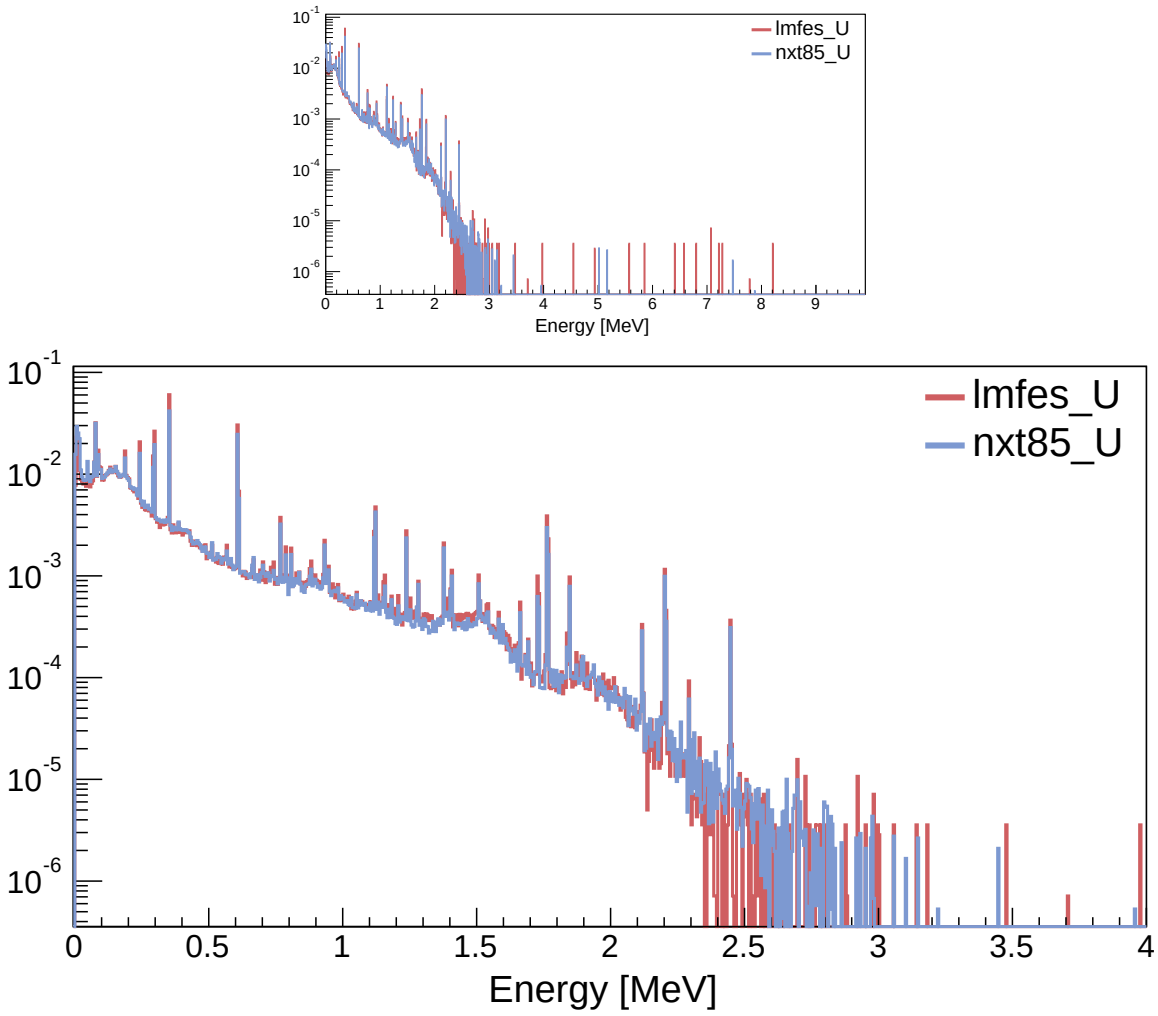

Figure D.7: The normalized MC-generated energy spectra for the MC-fit groups as seen by S3D2. Table 6.2 further details the parts and nuclides associated with each MC-fit group.

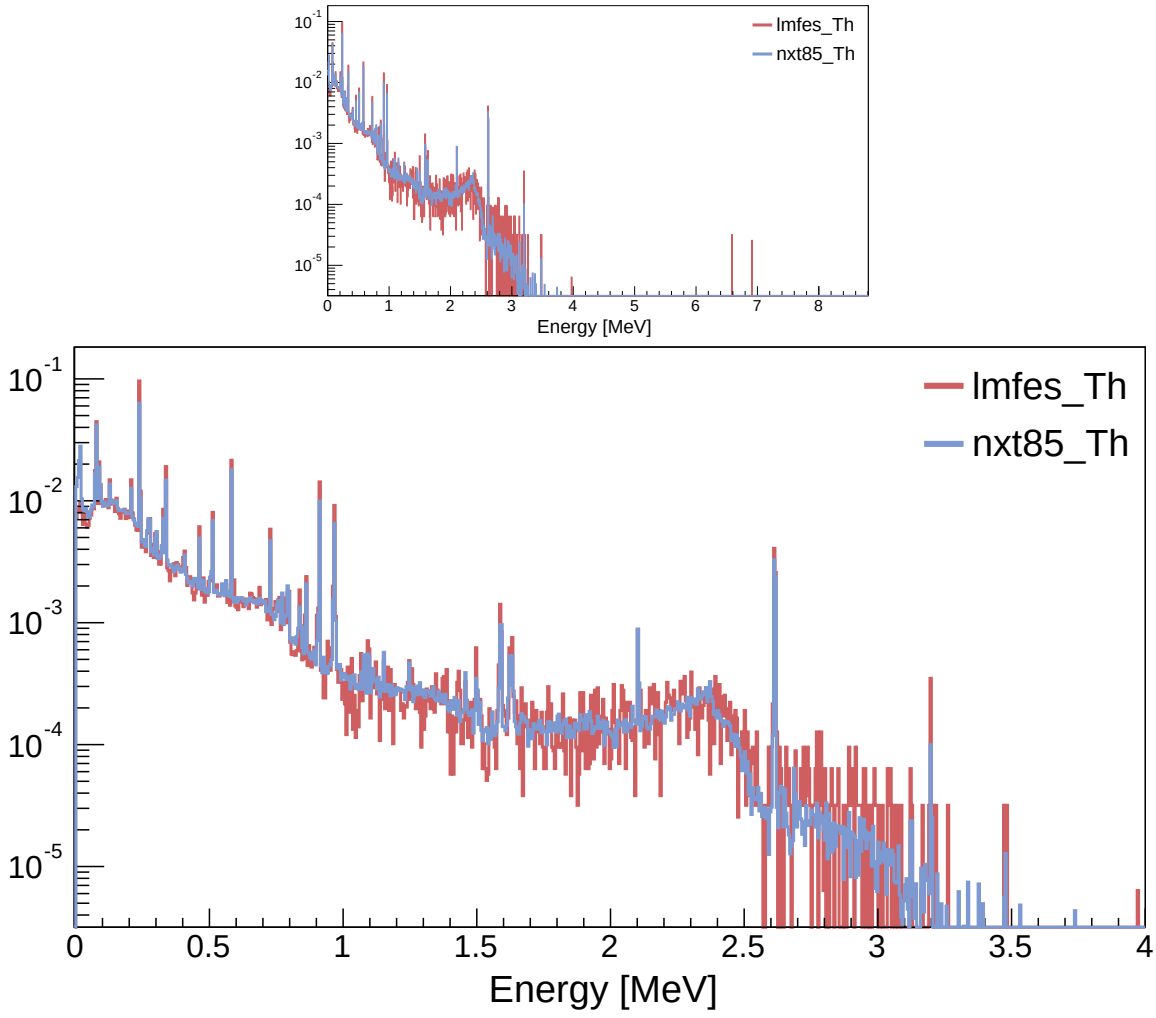

Figure D.8: The normalized MC-generated energy spectra for the MC-fit groups as seen by S3D2. Table 6.2 further details the parts and nuclides associated with each MC-fit group.

D.2 Low-Background Data with 83 Fit Parameters

D.2.1 S1D2 of the PC (Detector B8717)

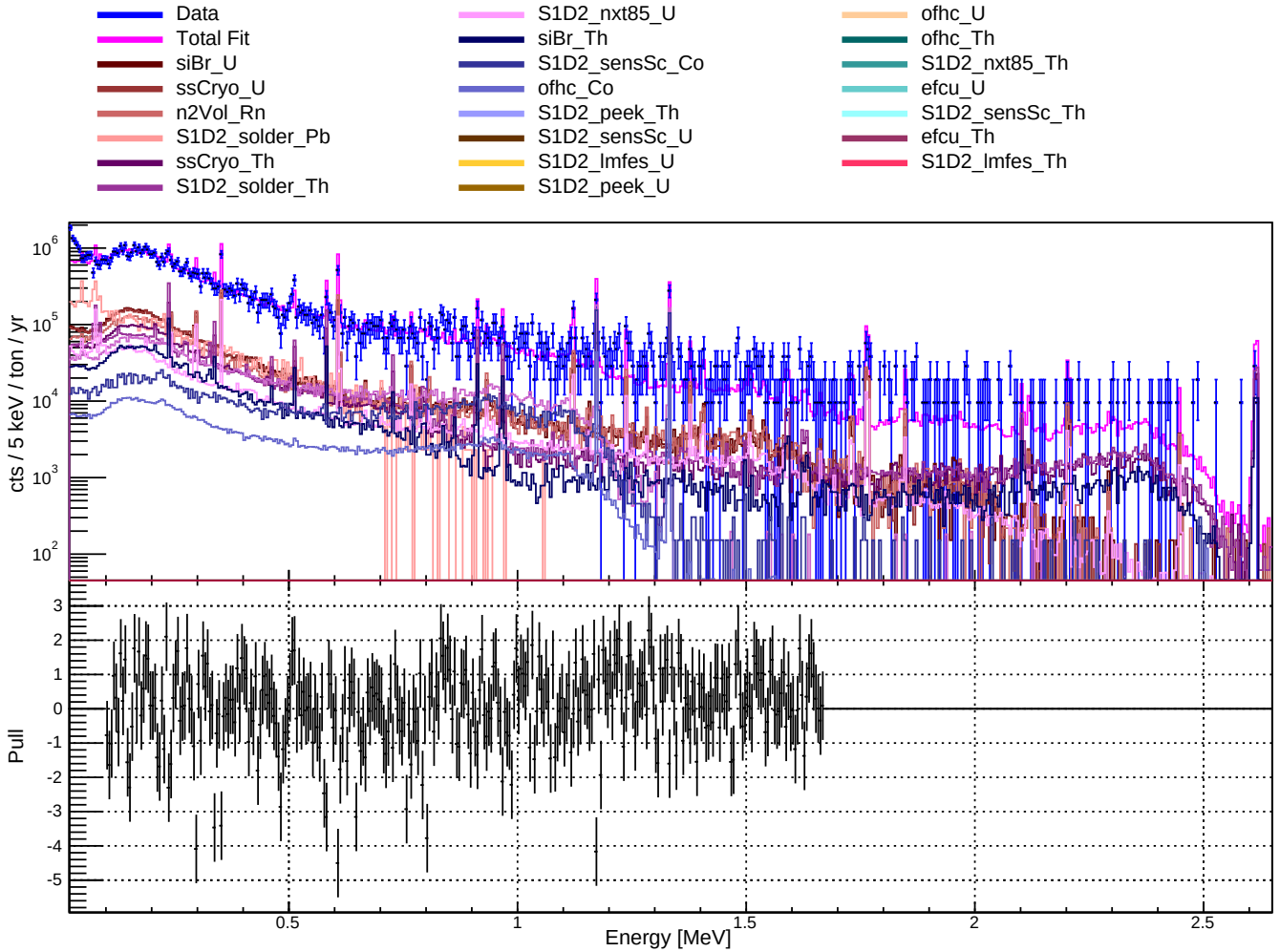

Figure D.9: (Top) The low-background energy spectrum of S1D2 (blue) and the fit to S1D2's data (pink). Also shown is each of the 23 MC-fit groups and the contribution they make to the total fit. In the accompanying legend, the MC-fit groups are listed in decreasing order (from top to bottom, left to right) by their contribution to the total fit. (Bottom) The pull resulting from the fit to the data.

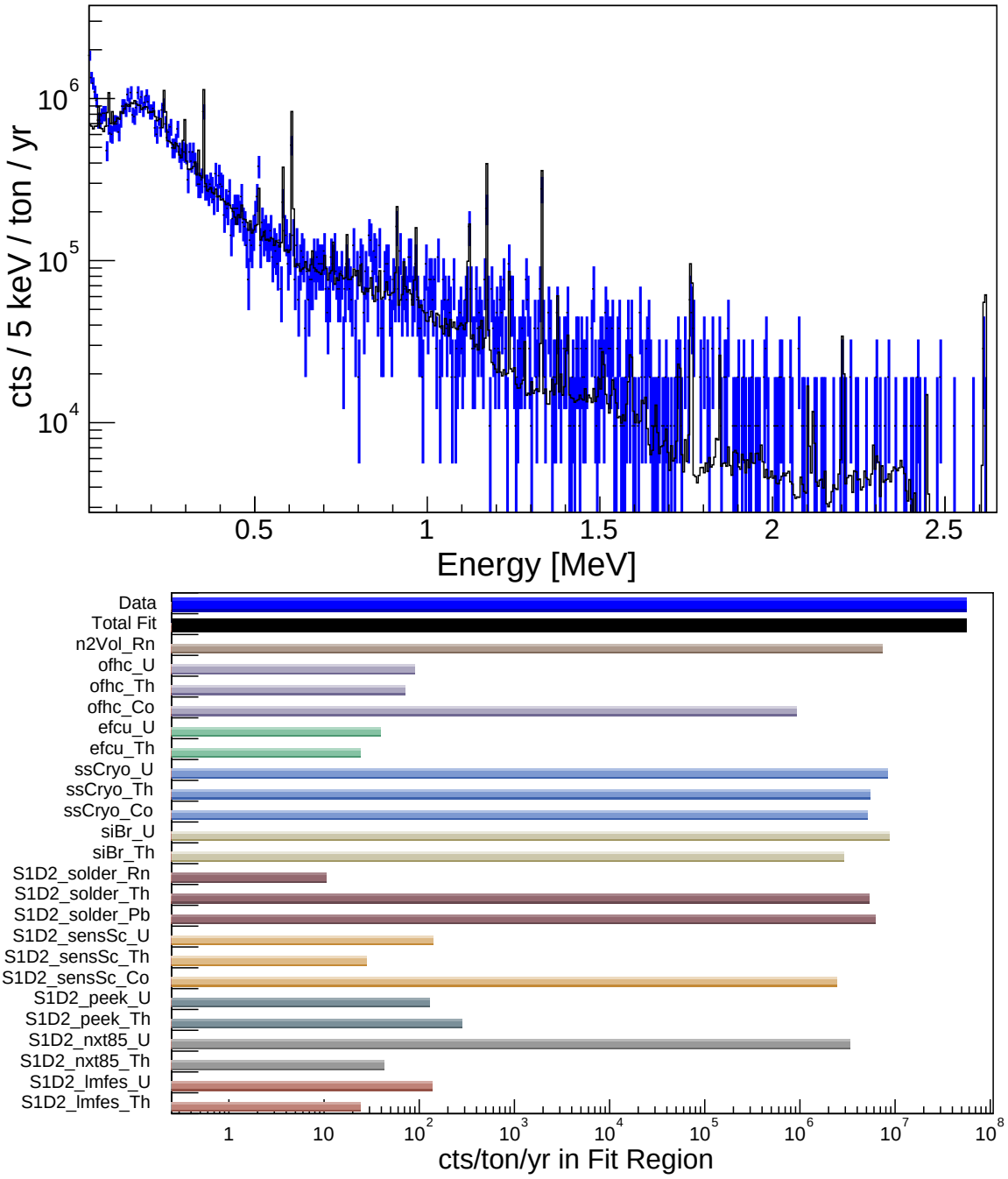

Figure D.10: (Top) The low-background energy spectrum of S1D2 (blue) and the fit to S1D2's data (black). (Bottom) The count rate in the fit region (100–1674 keV) for each MC-fit group, as seen by S1D2. To calculate the count rate, each MC-generated energy spectrum is scaled by the activity which resulted in the best fit to the low-background data.

D.2.2 S1D3 of the PC (Detector Ponama II)

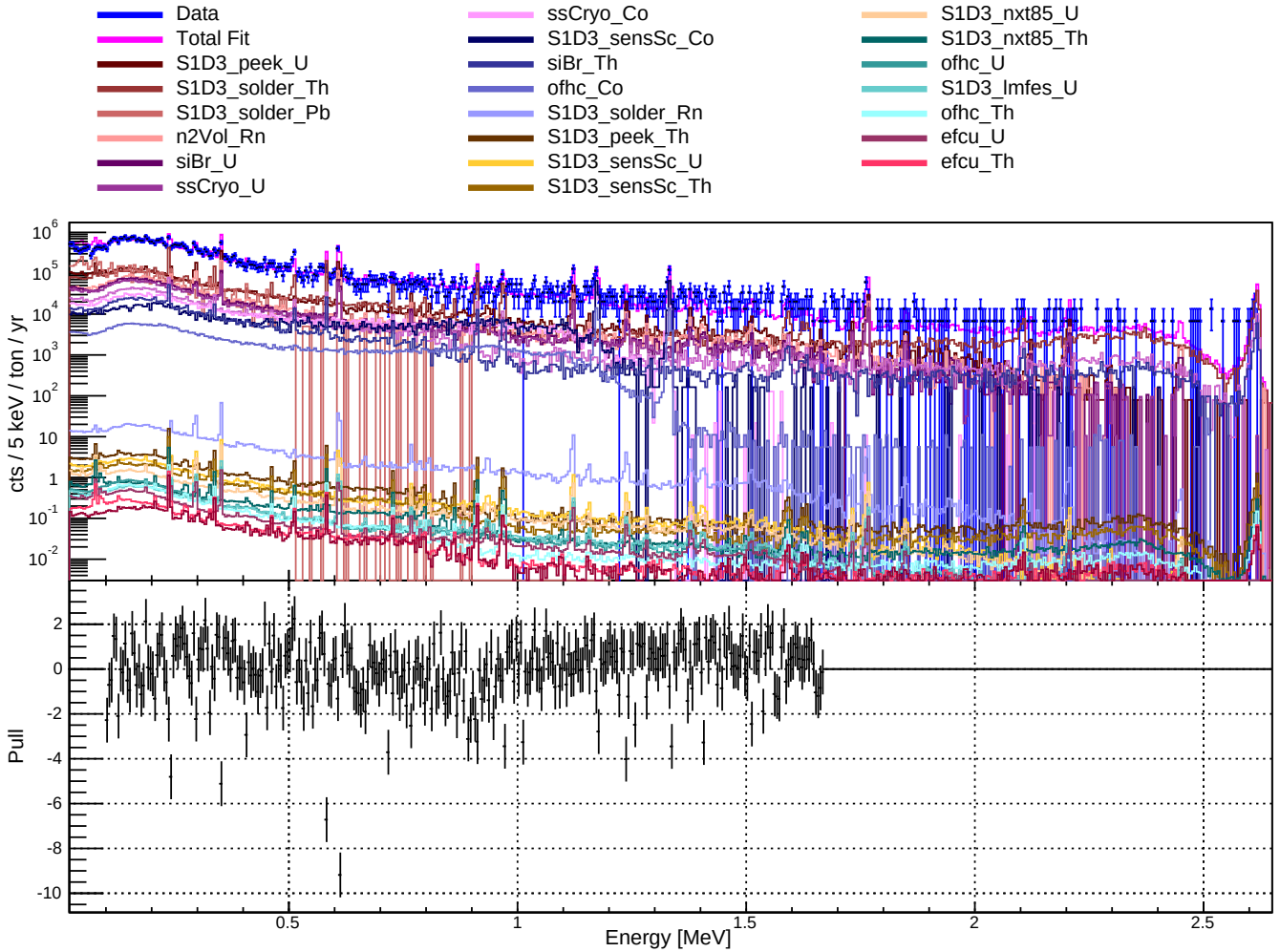

Figure D.11: (Top) The low-background energy spectrum of S1D3 (blue) and the fit to S1D3's data (pink). Also shown is each of the 23 MC-fit groups and the contribution they make to the total fit. In the accompanying legend, the MC-fit groups are listed in decreasing order (from top to bottom, left to right) by their contribution to the total fit. (Bottom) The pull resulting from the fit to the data.

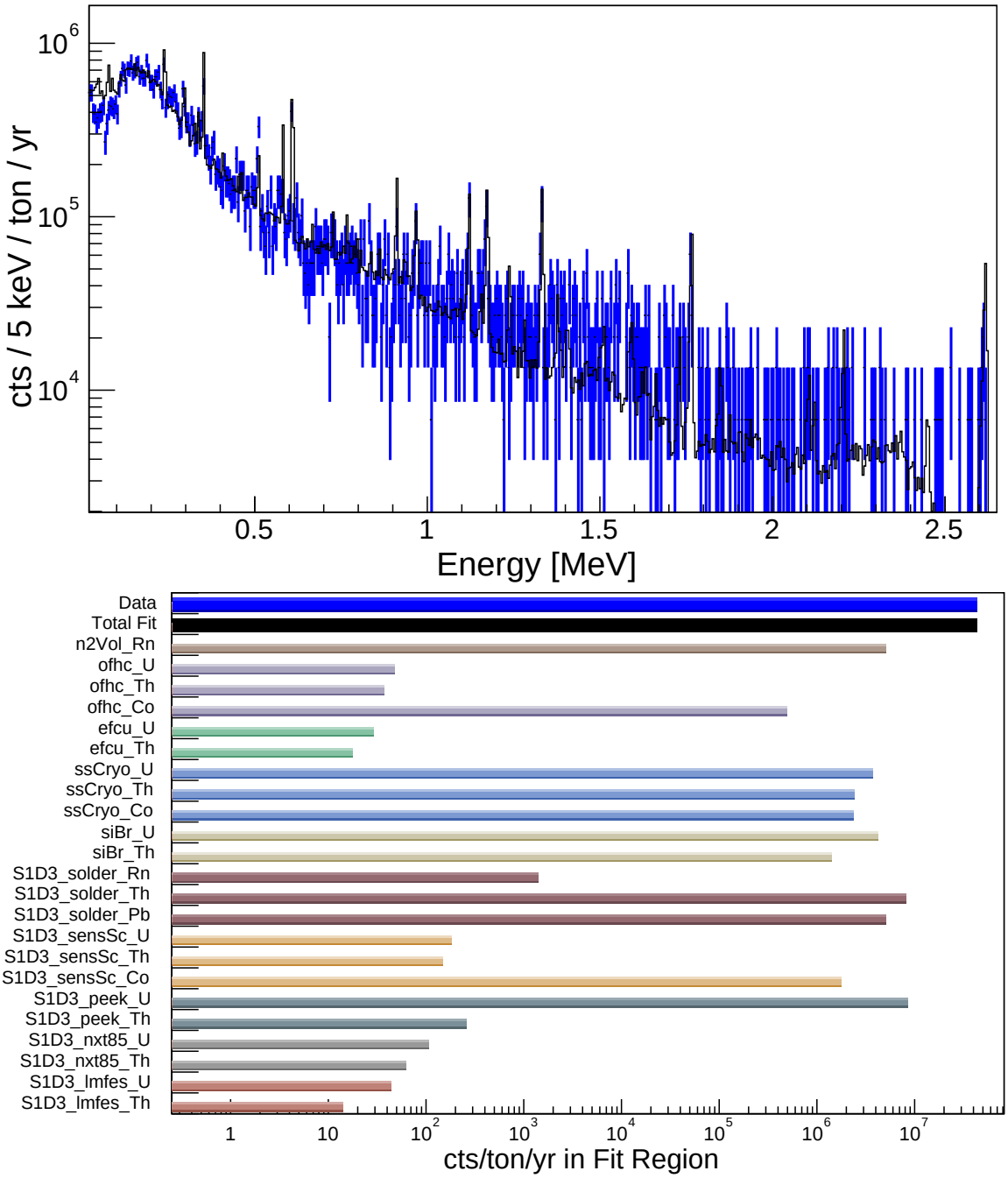

Figure D.12: (Top) The low-background energy spectrum of S1D3 (blue) and the fit to S1D3's data (black). (Bottom) The count rate in the fit region (100–1674 keV) for each MC-fit group, as seen by S1D3. To calculate the count rate, each MC-generated energy spectrum is scaled by the activity which resulted in the best fit to the low-background data.

D.2.3 S3D1 of the PC (Detector B8607)

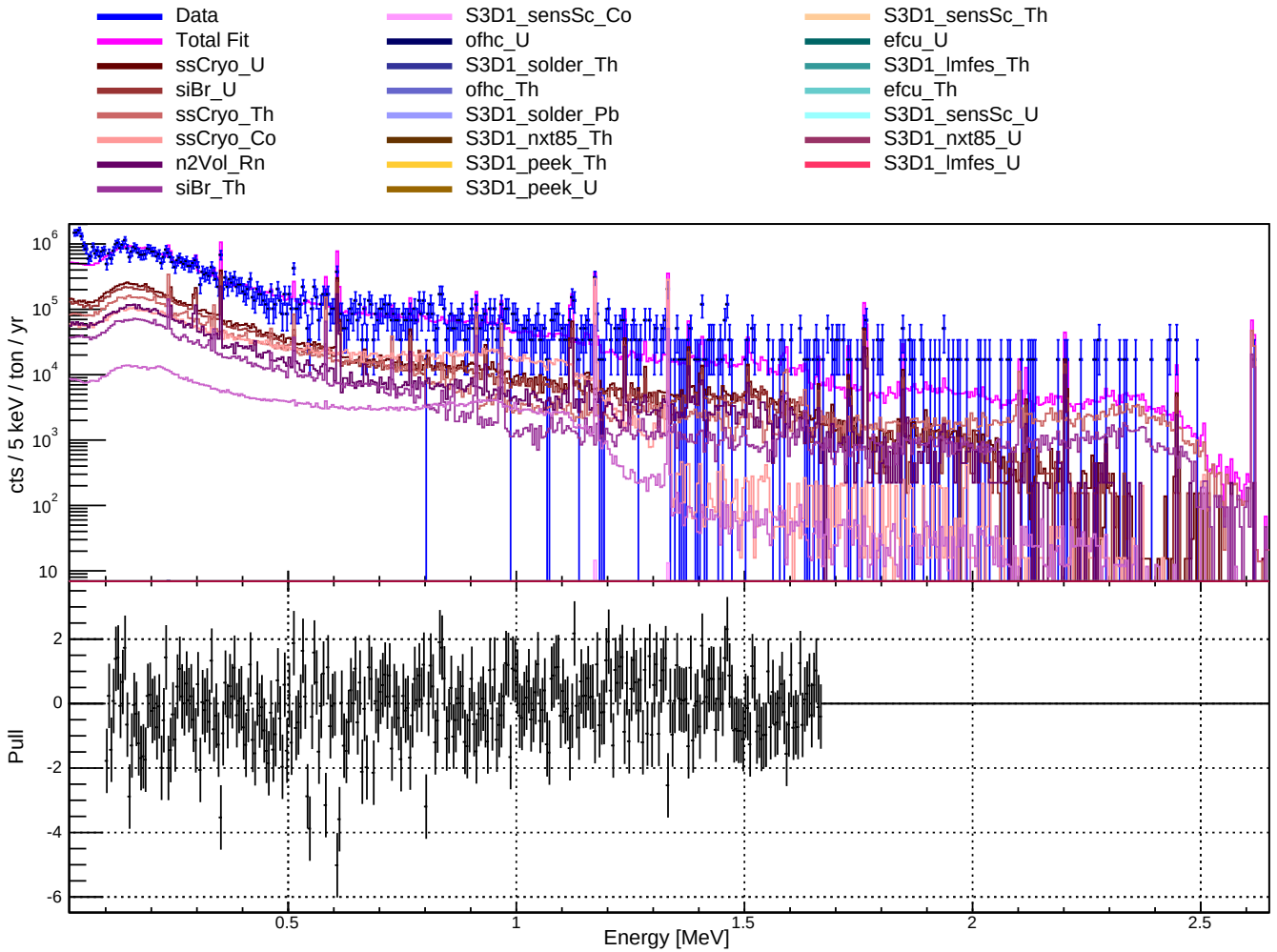

Figure D.13: (Top) The low-background energy spectrum of S3D1 (blue) and the fit to S3D1's data (pink). Also shown is each of the 23 MC-fit groups and the contribution they make to the total fit. In the accompanying legend, the MC-fit groups are listed in decreasing order (from top to bottom, left to right) by their contribution to the total fit. (Bottom) The pull resulting from the fit to the data.

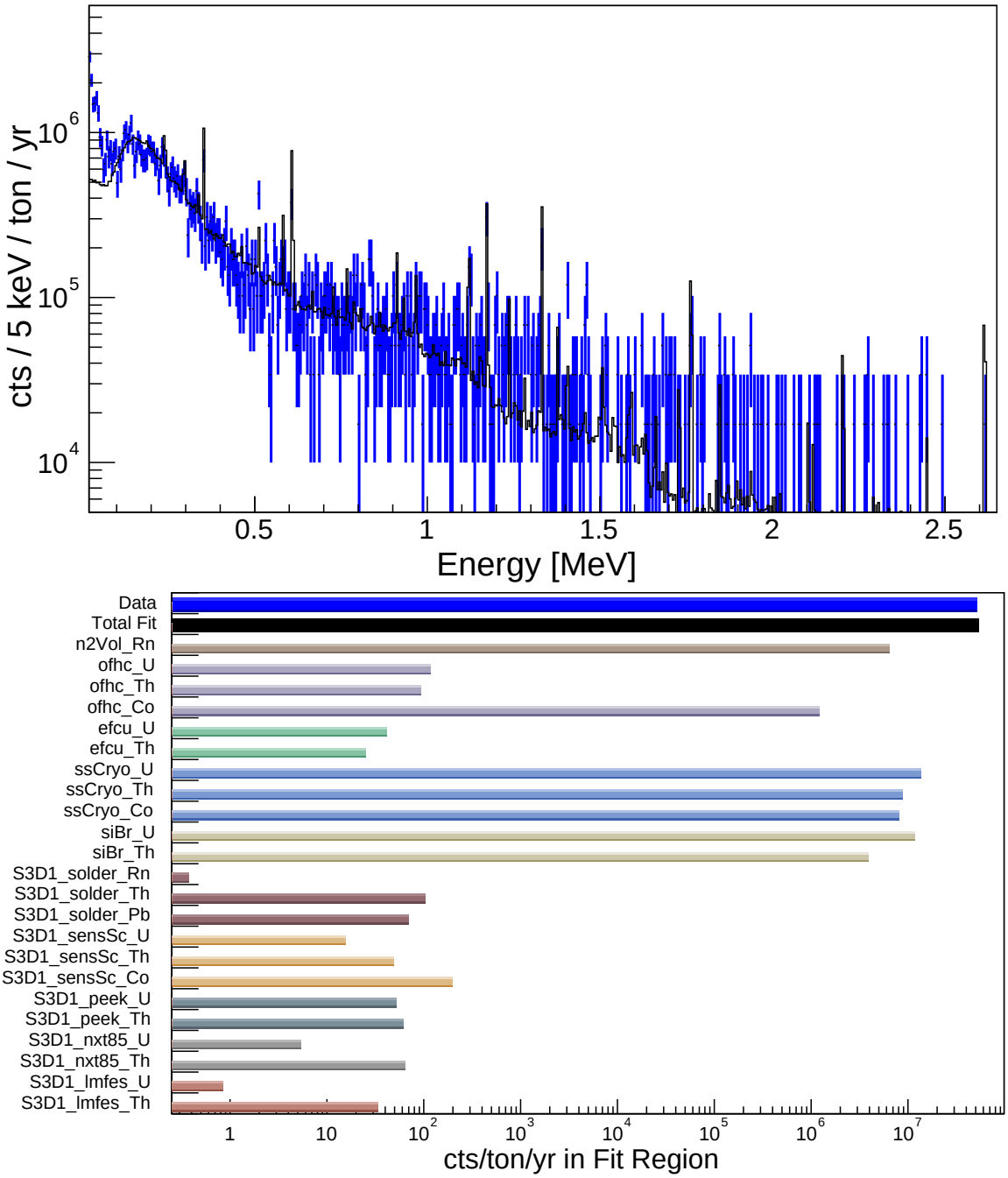

Figure D.14: (Top) The low-background energy spectrum of S3D1 (blue) and the fit to S3D1's data (black). (Bottom) The count rate in the fit region (100–1674 keV) for each MC-fit group, as seen by S3D1. To calculate the count rate, each MC-generated energy spectrum is scaled by the activity which resulted in the best fit to the low-background data.

D.2.4 S3D2 of the PC (Detector B8456)

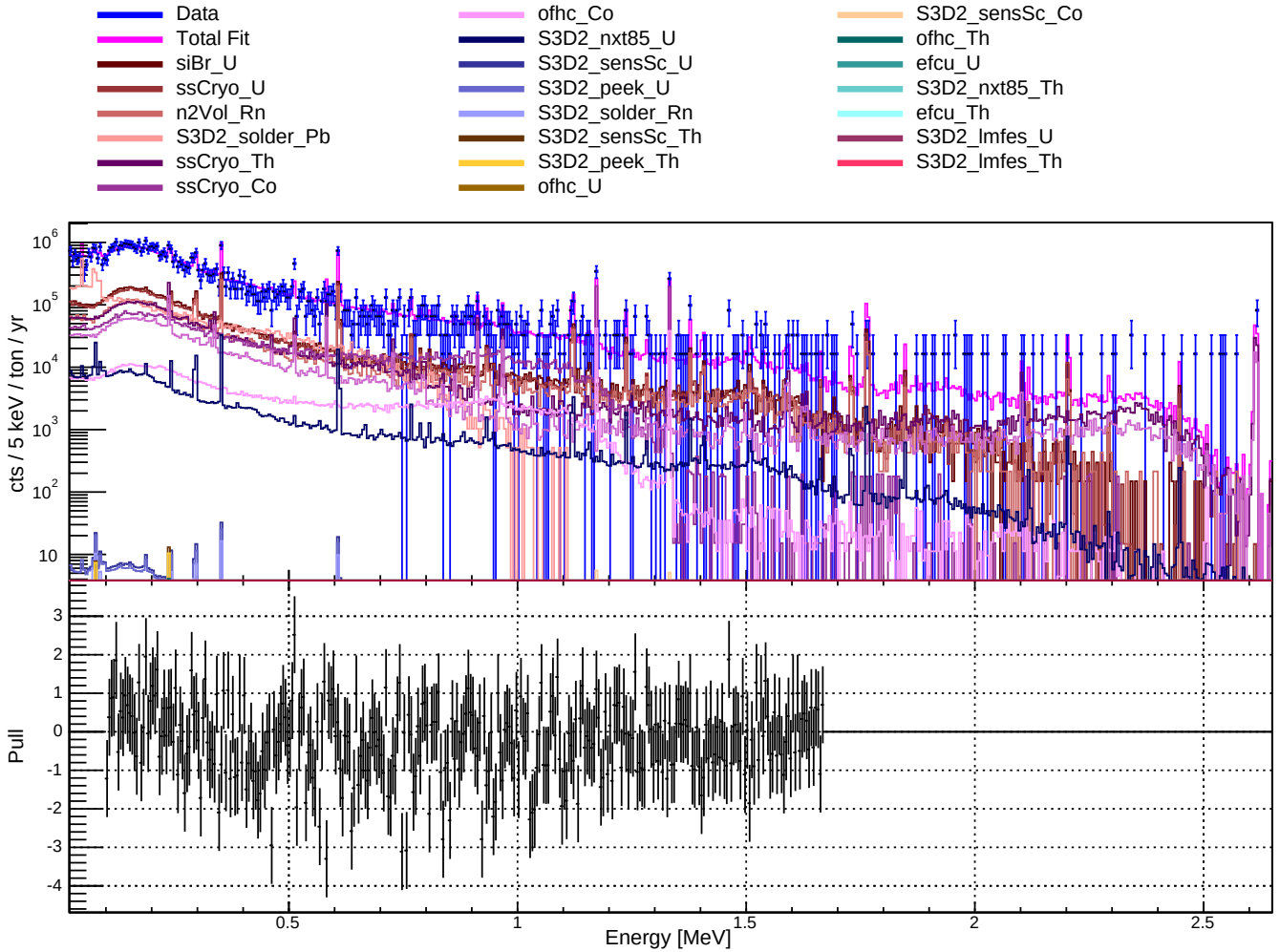

Figure D.15: (Top) The low-background energy spectrum of S3D2 (blue) and the fit to S3D2's data (pink). Also shown is each of the 23 MC-fit groups and the contribution they make to the total fit. In the accompanying legend, the MC-fit groups are listed in decreasing order (from top to bottom, left to right) by their contribution to the total fit. (Bottom) The pull resulting from the fit to the data.

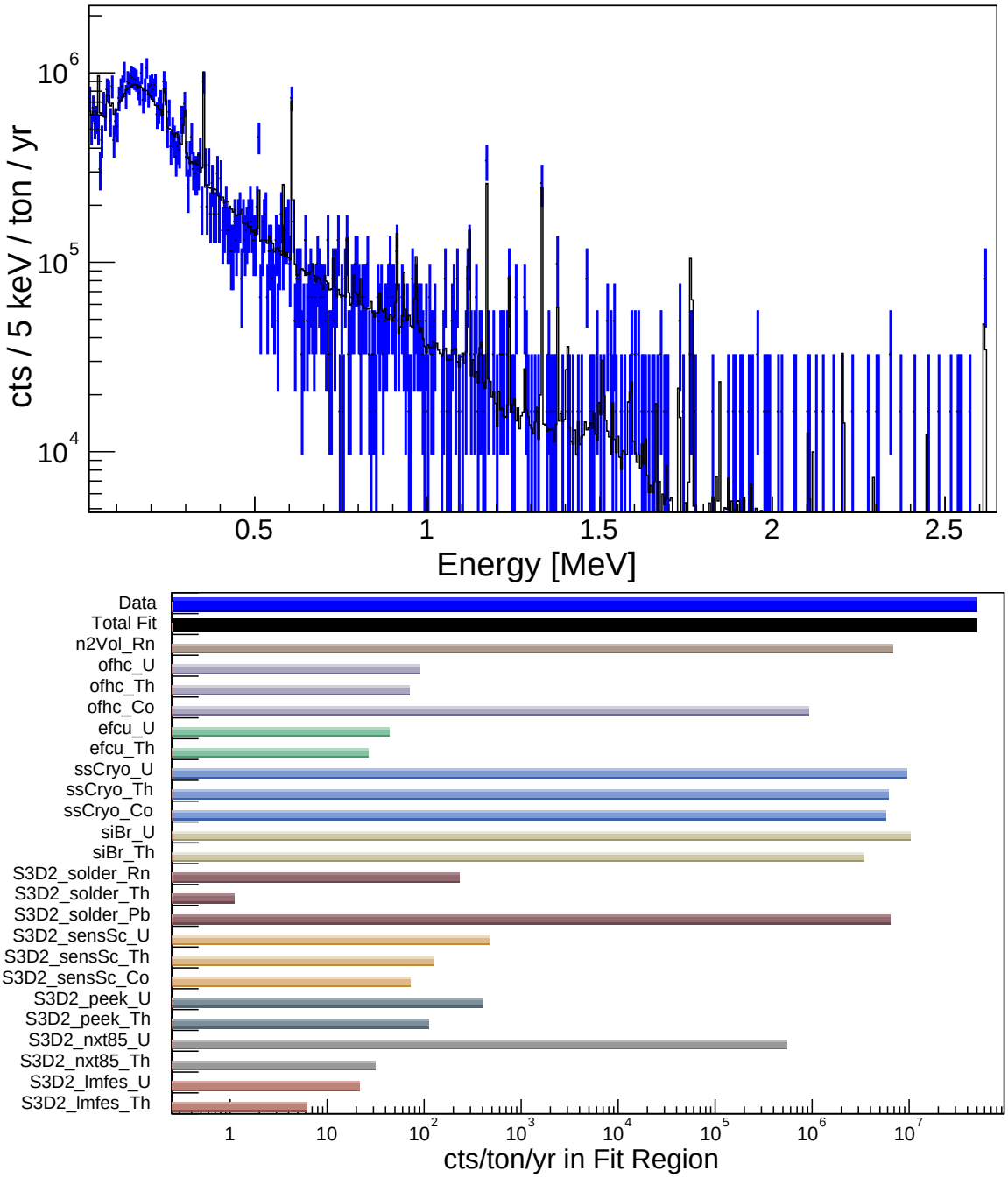

Figure D.16: (Top) The low-background energy spectrum of S3D2 (blue) and the fit to S3D2's data (black). (Bottom) The count rate in the fit region (100–1674 keV) for each MC-fit group, as seen by S3D2. To calculate the count rate, each MC-generated energy spectrum is scaled by the activity which resulted in the best fit to the low-background data.

D.2.5 S3D4 of the PC (Detector B8466)

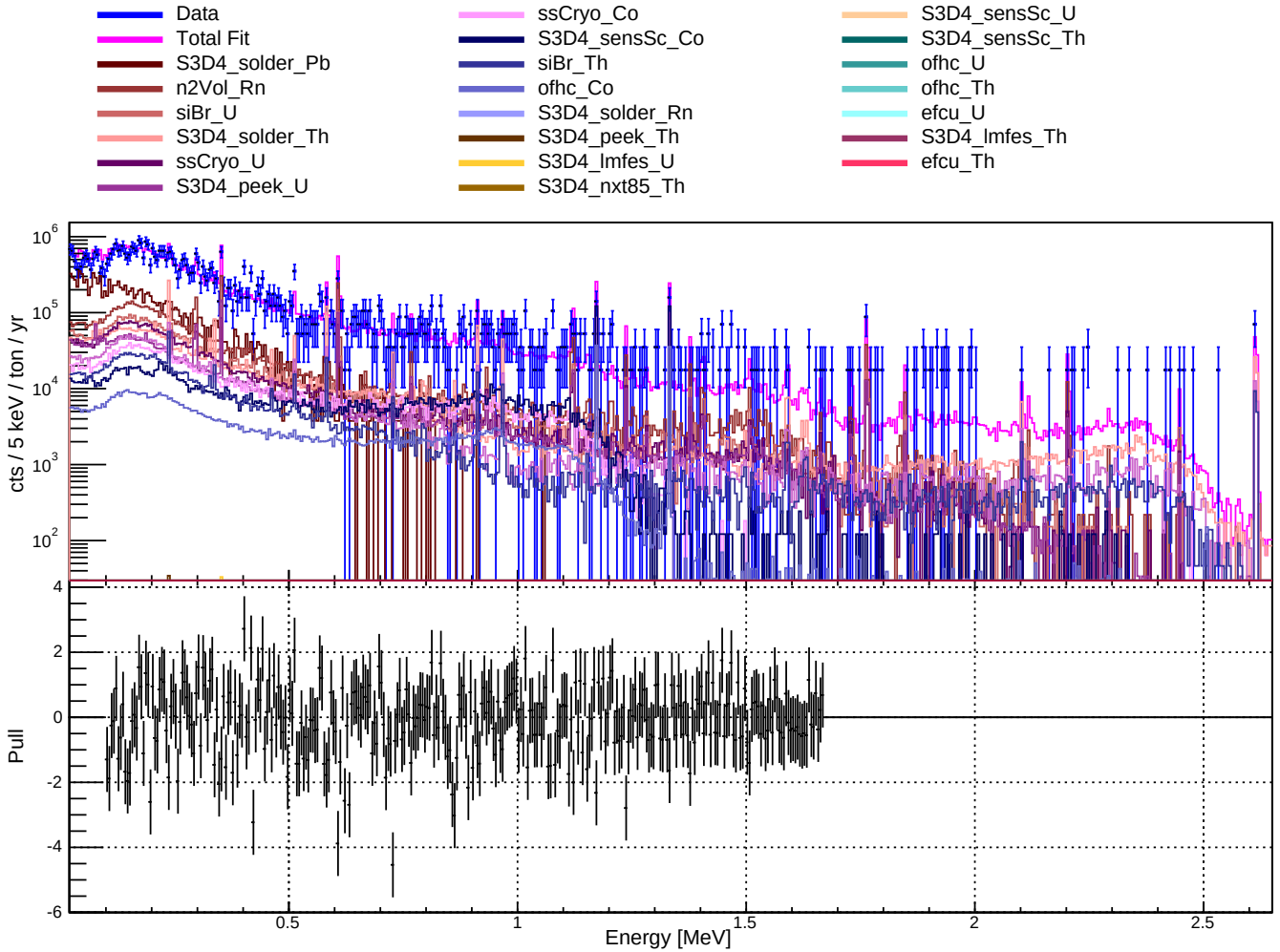

Figure D.17: (Top) The low-background energy spectrum of S3D4 (blue) and the fit to S3D4's data (pink). Also shown is each of the 23 MC-fit groups and the contribution they make to the total fit. In the accompanying legend, the MC-fit groups are listed in decreasing order (from top to bottom, left to right) by their contribution to the total fit. (Bottom) The pull resulting from the fit to the data.

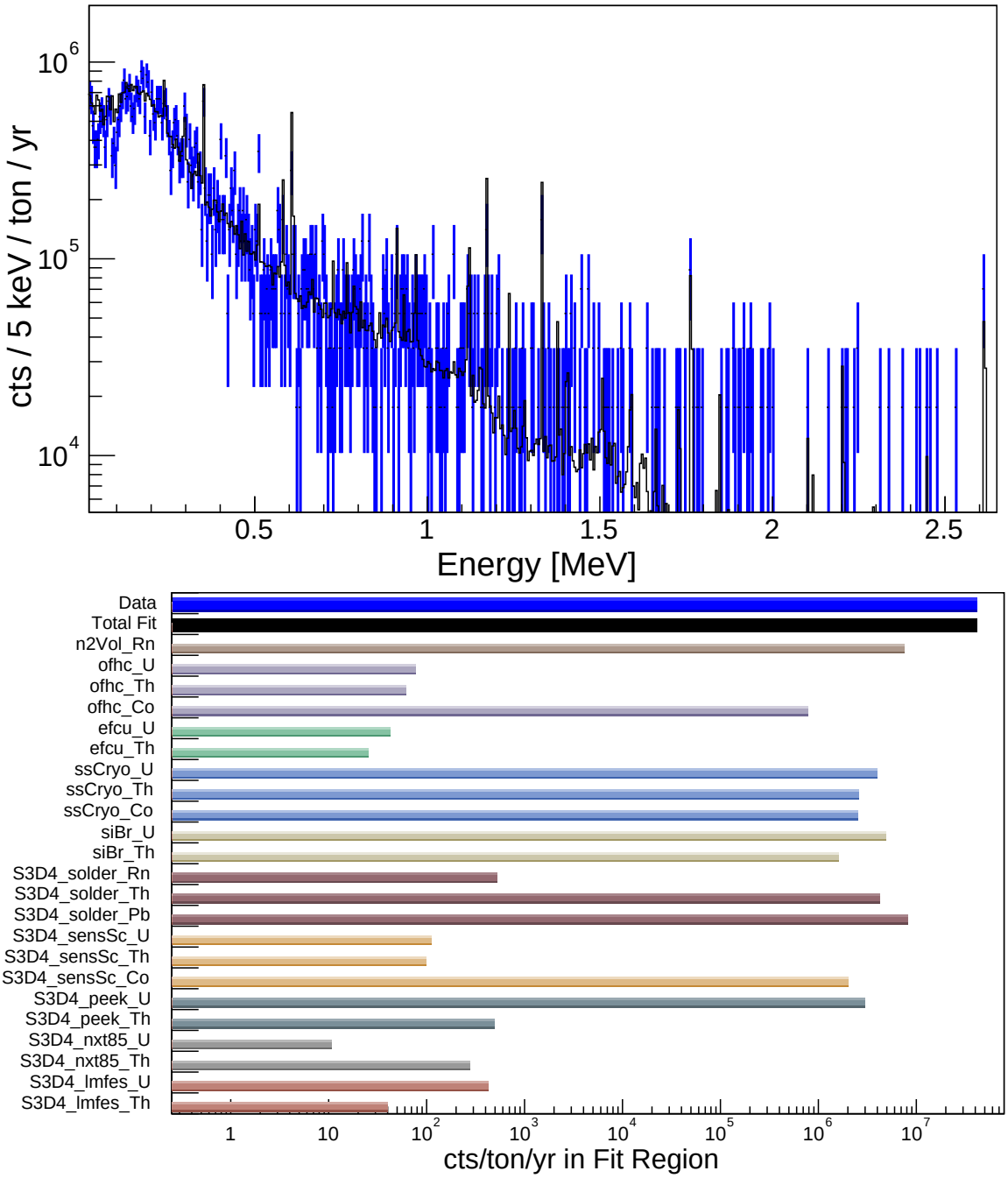

Figure D.18: (Top) The low-background energy spectrum of S3D4 (blue) and the fit to S3D4's data (black). (Bottom) The count rate in the fit region (100–1674 keV) for each MC-fit group, as seen by S3D4. To calculate the count rate, each MC-generated energy spectrum is scaled by the activity which resulted in the best fit to the low-background data.

D.2.6 S3D5 of the PC (Detector B8473)

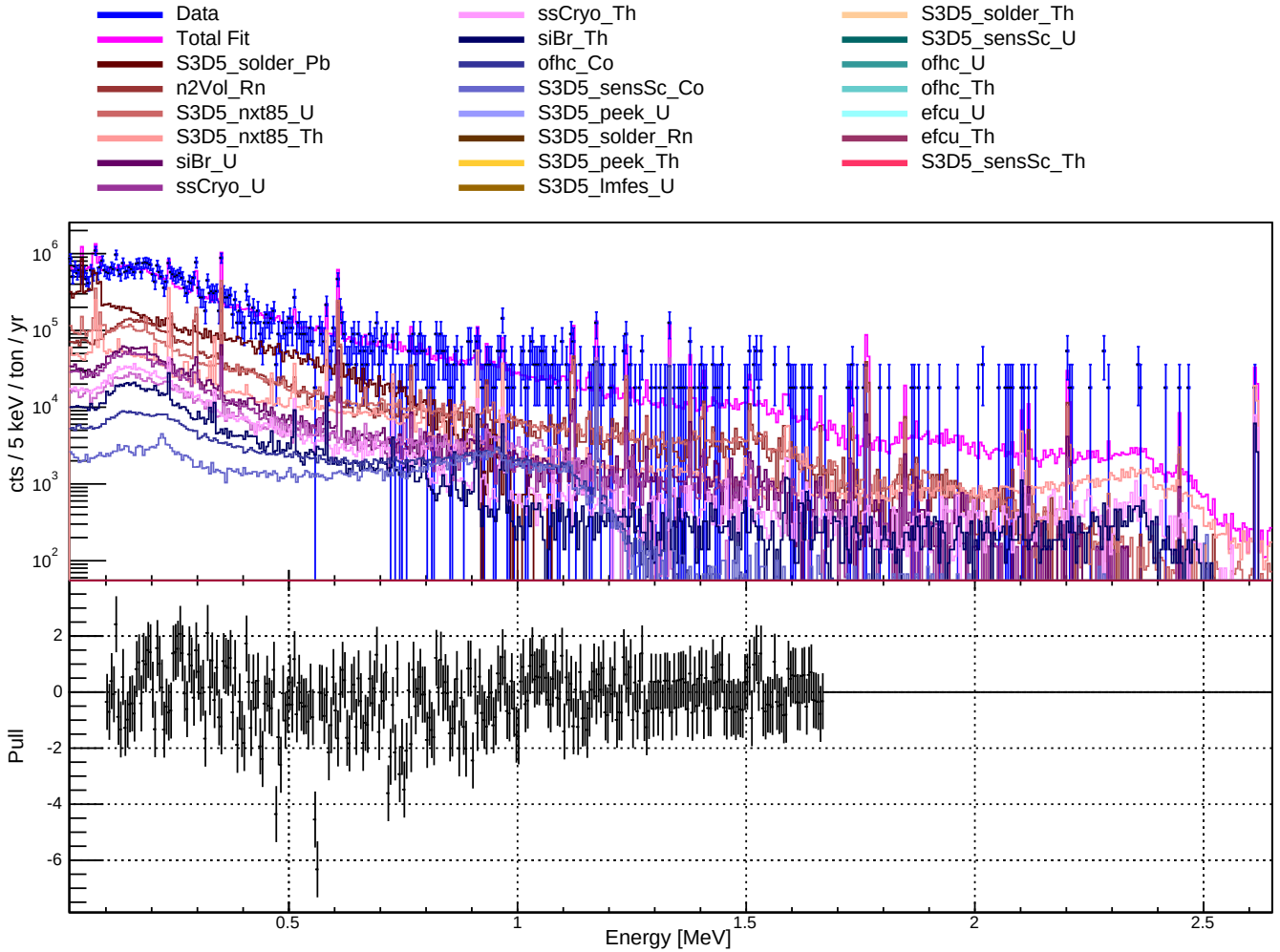

Figure D.19: (Top) The low-background energy spectrum of S3D5 (blue) and the fit to S3D5's data (pink). Also shown is each of the 23 MC-fit groups and the contribution they make to the total fit. In the accompanying legend, the MC-fit groups are listed in decreasing order (from top to bottom, left to right) by their contribution to the total fit. (Bottom) The pull resulting from the fit to the data.

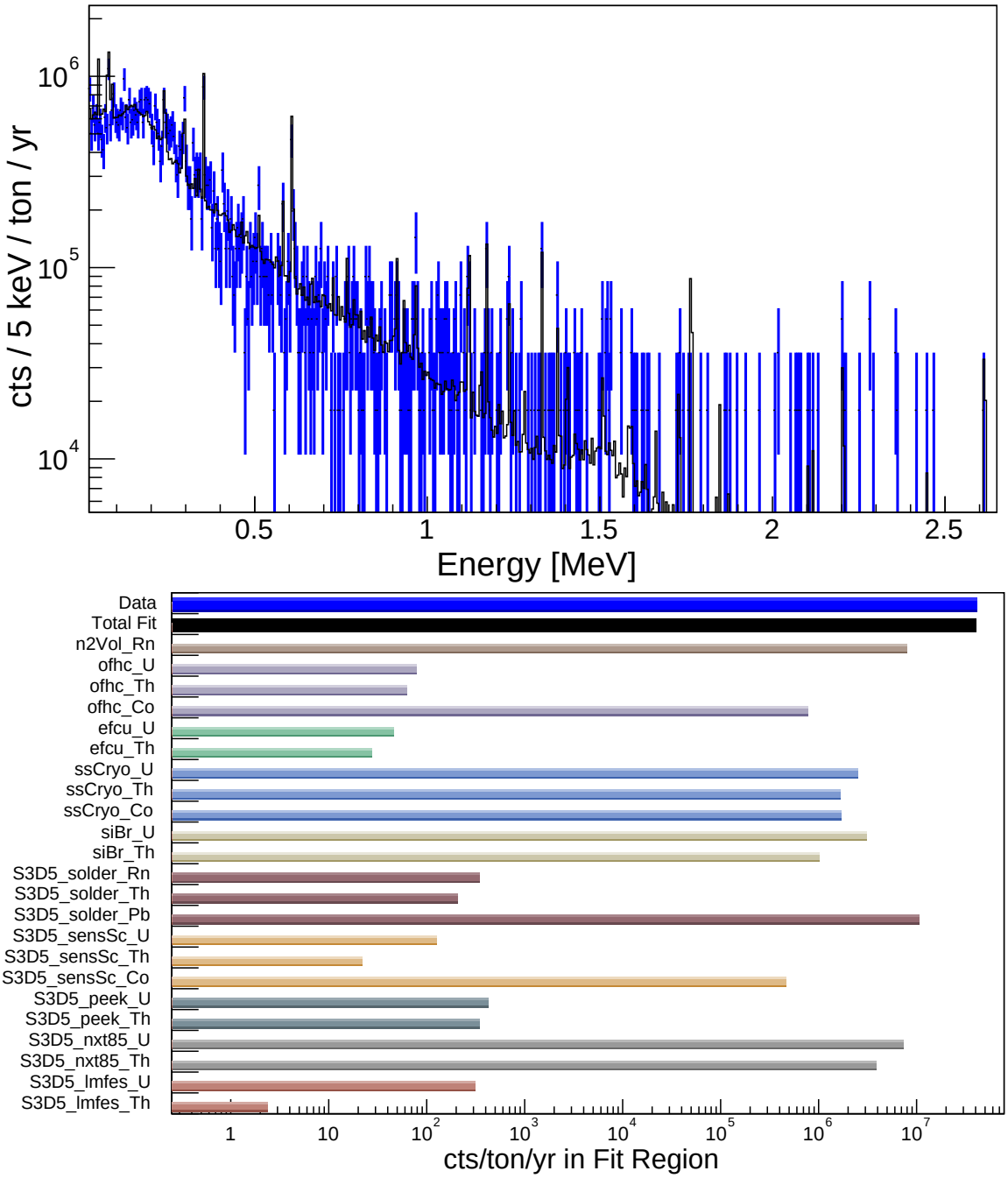

Figure D.20: (Top) The low-background energy spectrum of S3D5 (blue) and the fit to S3D5's data (black). (Bottom) The count rate in the fit region (100–1674 keV) for each MC-fit group, as seen by S3D5. To calculate the count rate, each MC-generated energy spectrum is scaled by the activity which resulted in the best fit to the low-background data.

D.2.7 Histogram of Pulls

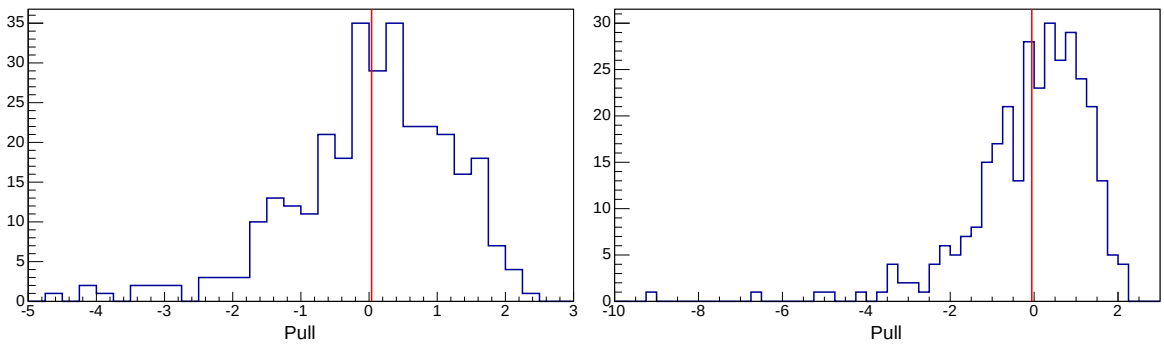

Figure D.21: A histogram of the pull values resulting from the fit to the low-background data for S1D2 and S1D3.

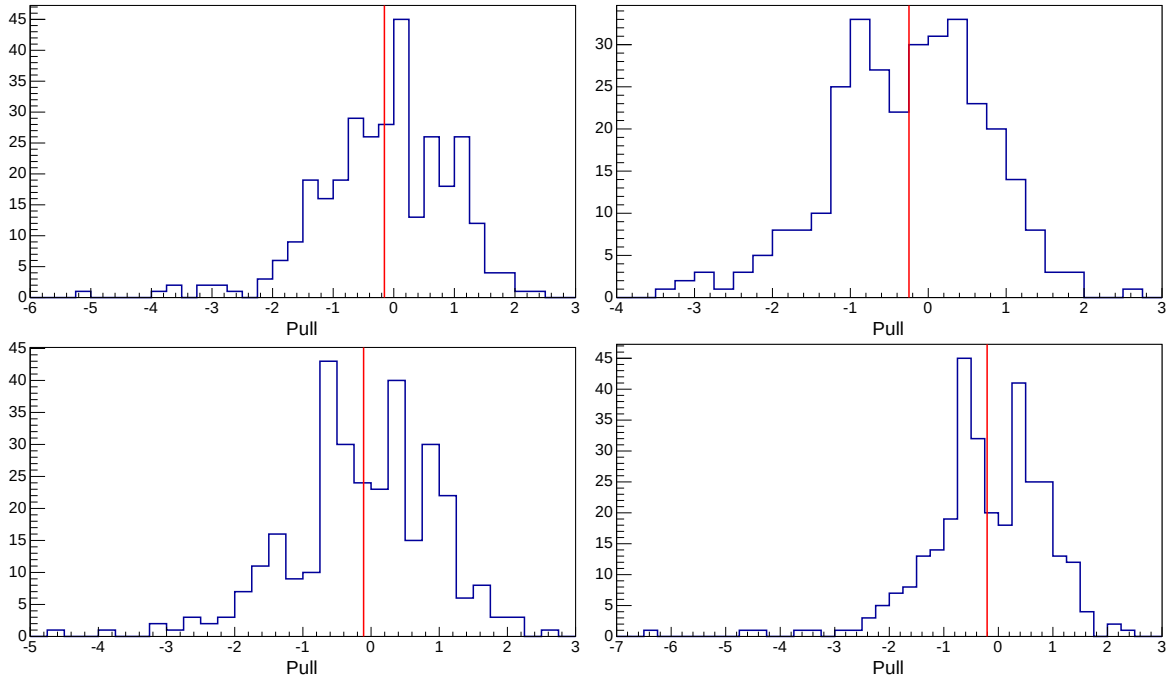

Figure D.22: A histogram of the pull values resulting from the fit to the low-background data for S3D1, S3D2, S3D4 and S3D5.

D.3 High-Radon Data with 1 Fit Parameter

D.3.1 S1D2 of the PC (Detector B8717)

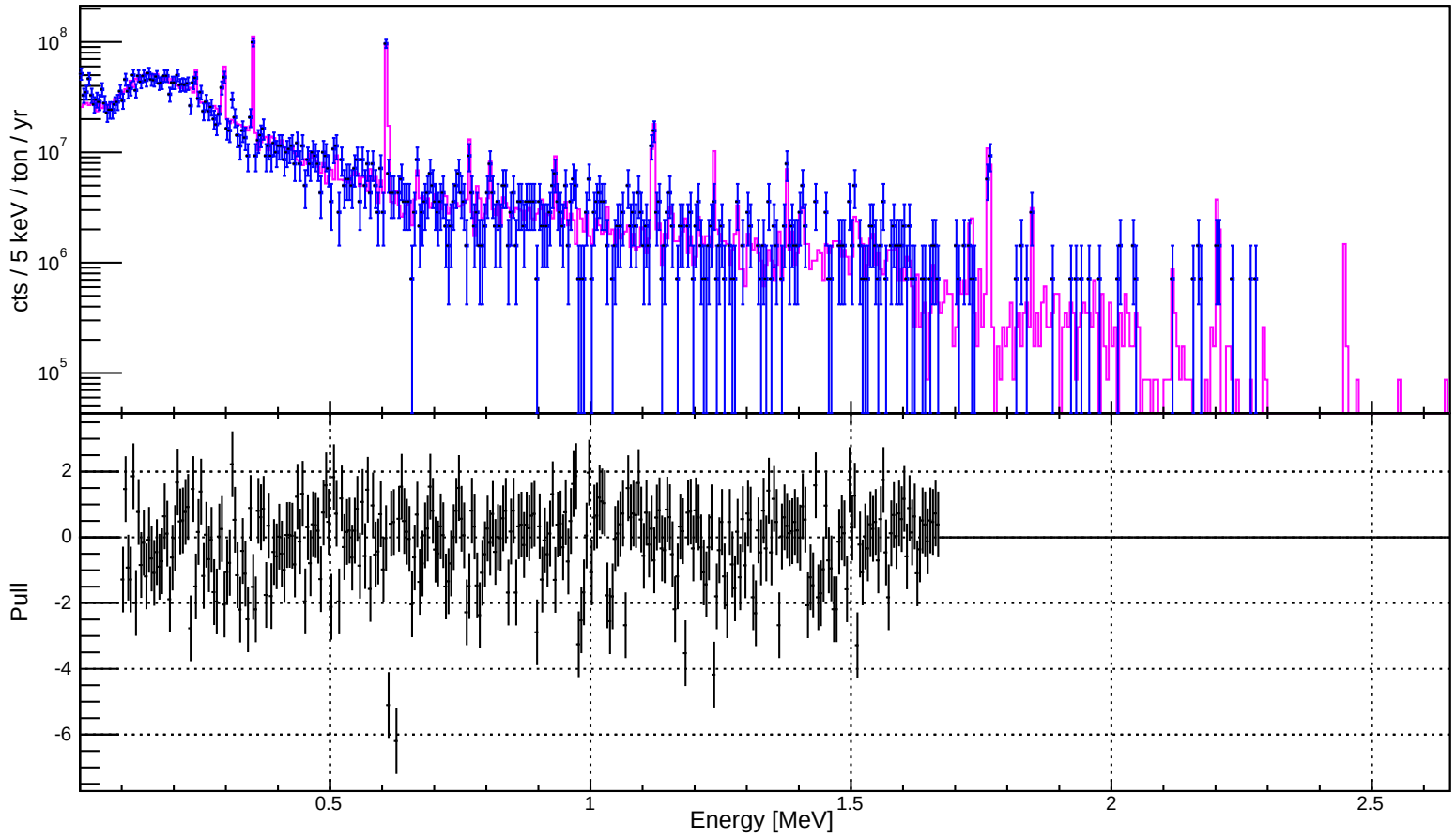

Figure D.23: The high-Rn energy spectrum of S1D2 (blue) and the 1-parameter fit to S1D2's data (pink). The one parameter is that corresponding to the "n2Vol_Rn" MC-fit group. (Bottom) The pull resulting from the fit to the data.

D.3.2 S1D3 of the PC (Detector Ponama II)

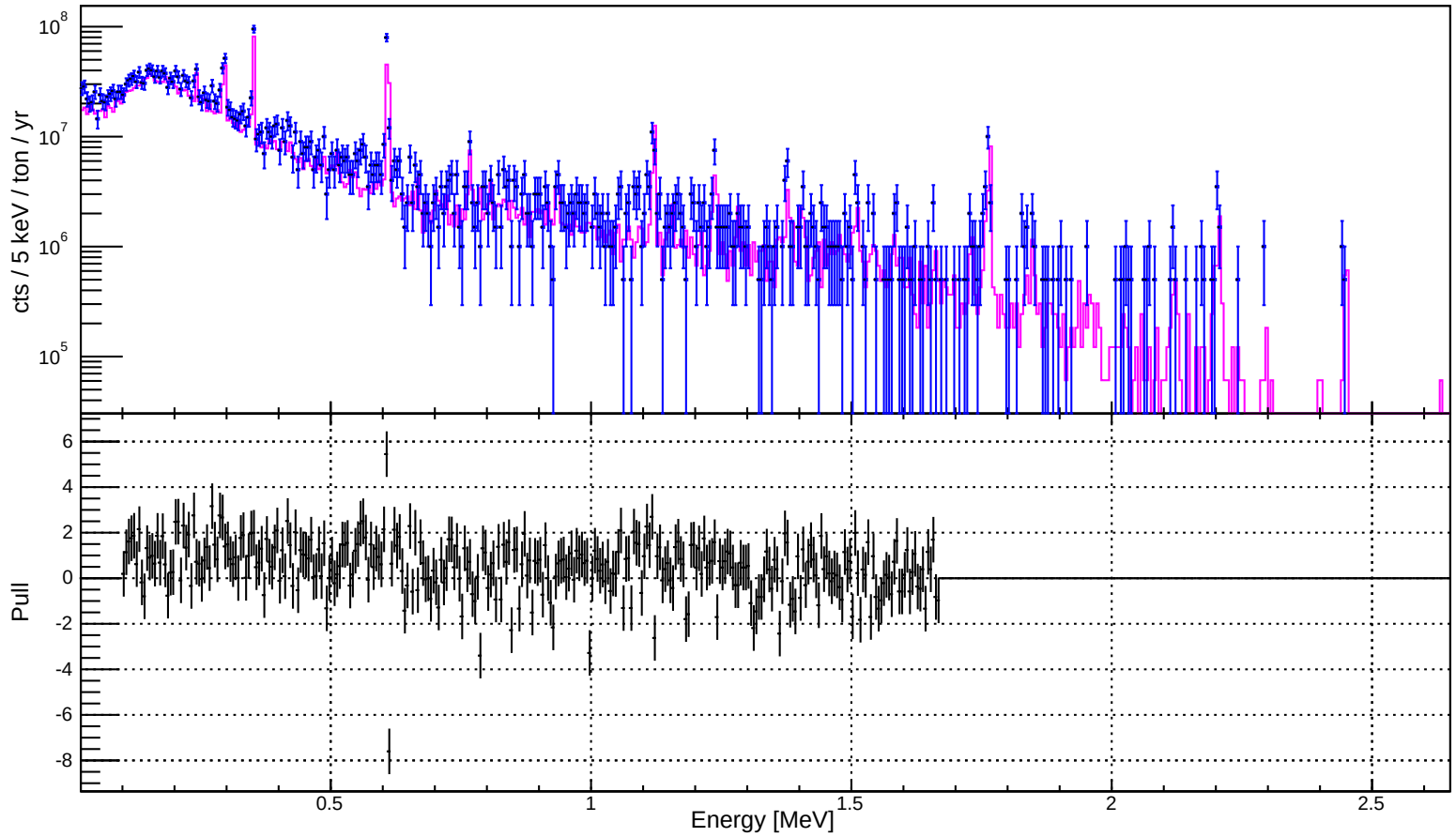

Figure D.24: The high-Rn energy spectrum of S1D3 (blue) and the 1-parameter fit to S1D3's data (pink). The one parameter is that corresponding to the "n2Vol_Rn" MC-fit group. (Bottom) The pull resulting from the fit to the data.

D.3.3 S3D1 of the PC (Detector B8607)

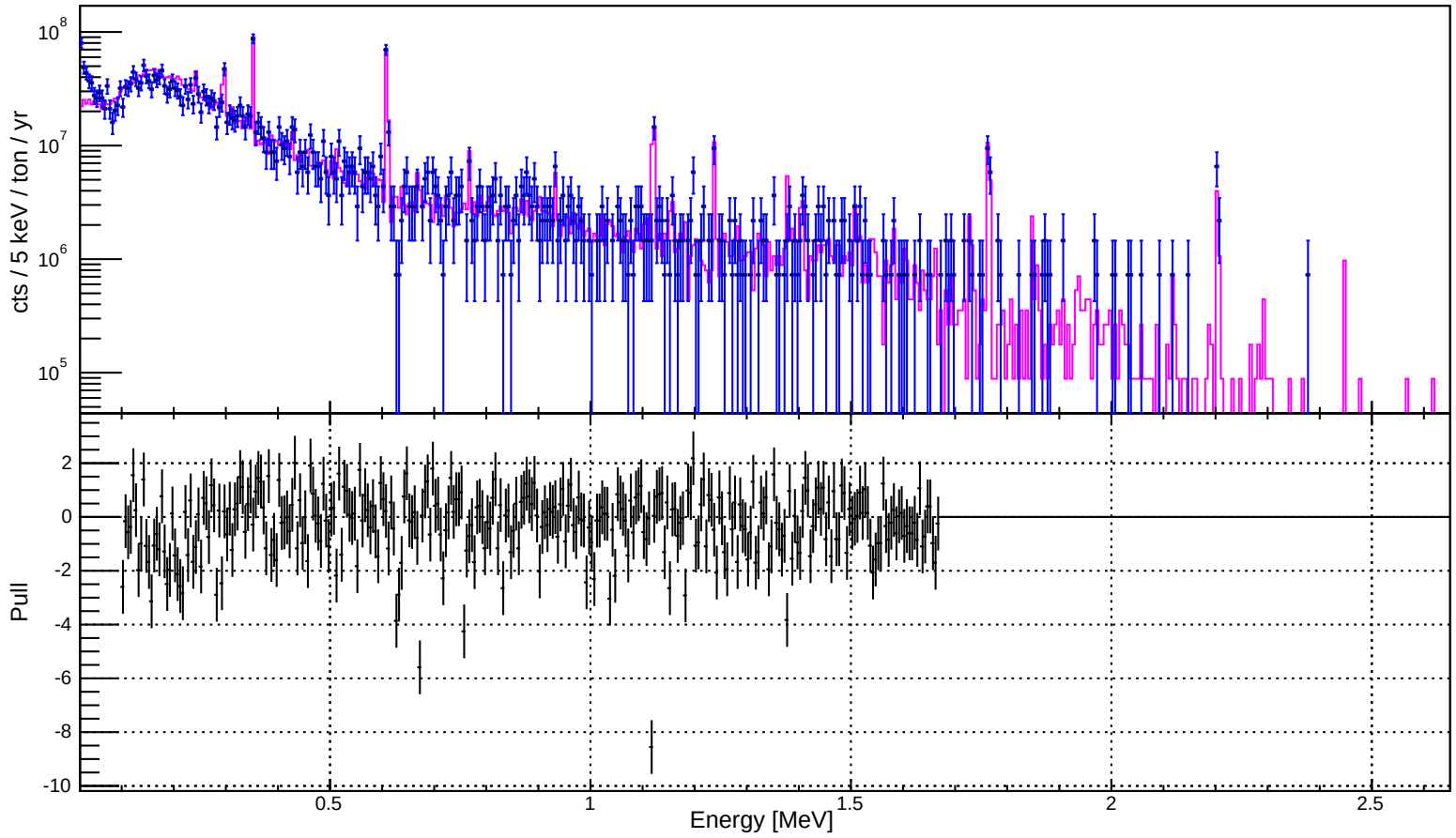

Figure D.25: The high-Rn energy spectrum of S3D1 (blue) and the 1-parameter fit to S3D1's data (pink). The one parameter is that corresponding to the "n2Vol_Rn" MC-fit group. (Bottom) The pull resulting from the fit to the data.

D.3.4 S3D2 of the PC (Detector B8456)

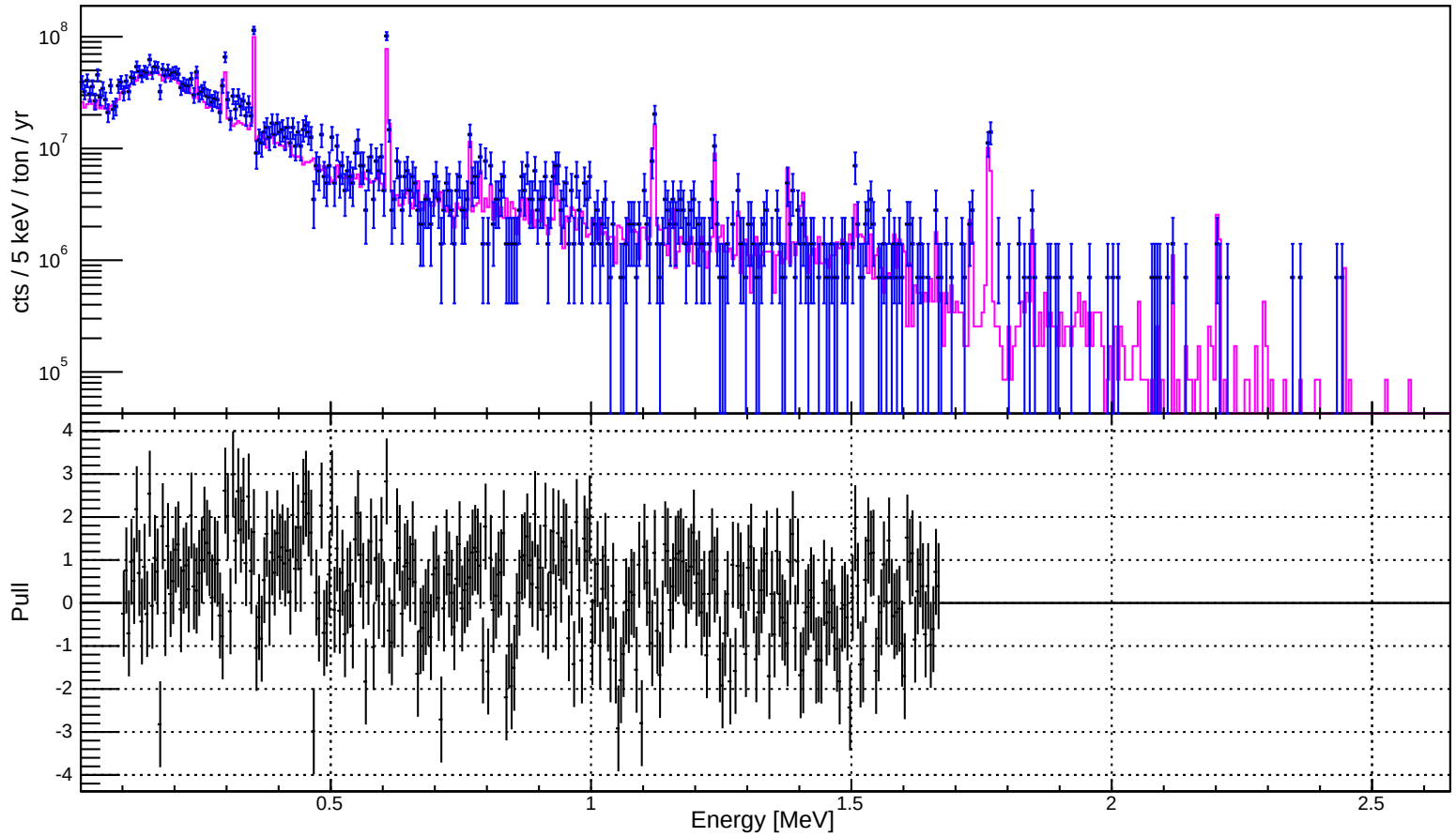

Figure D.26: The high-Rn energy spectrum of S3D2 (blue) and the 1-parameter fit to S3D2's data (pink). The one parameter is that corresponding to the "n2Vol_Rn" MC-fit group. (Bottom) The pull resulting from the fit to the data.

D.3.5 S3D4 of the PC (Detector B8466)

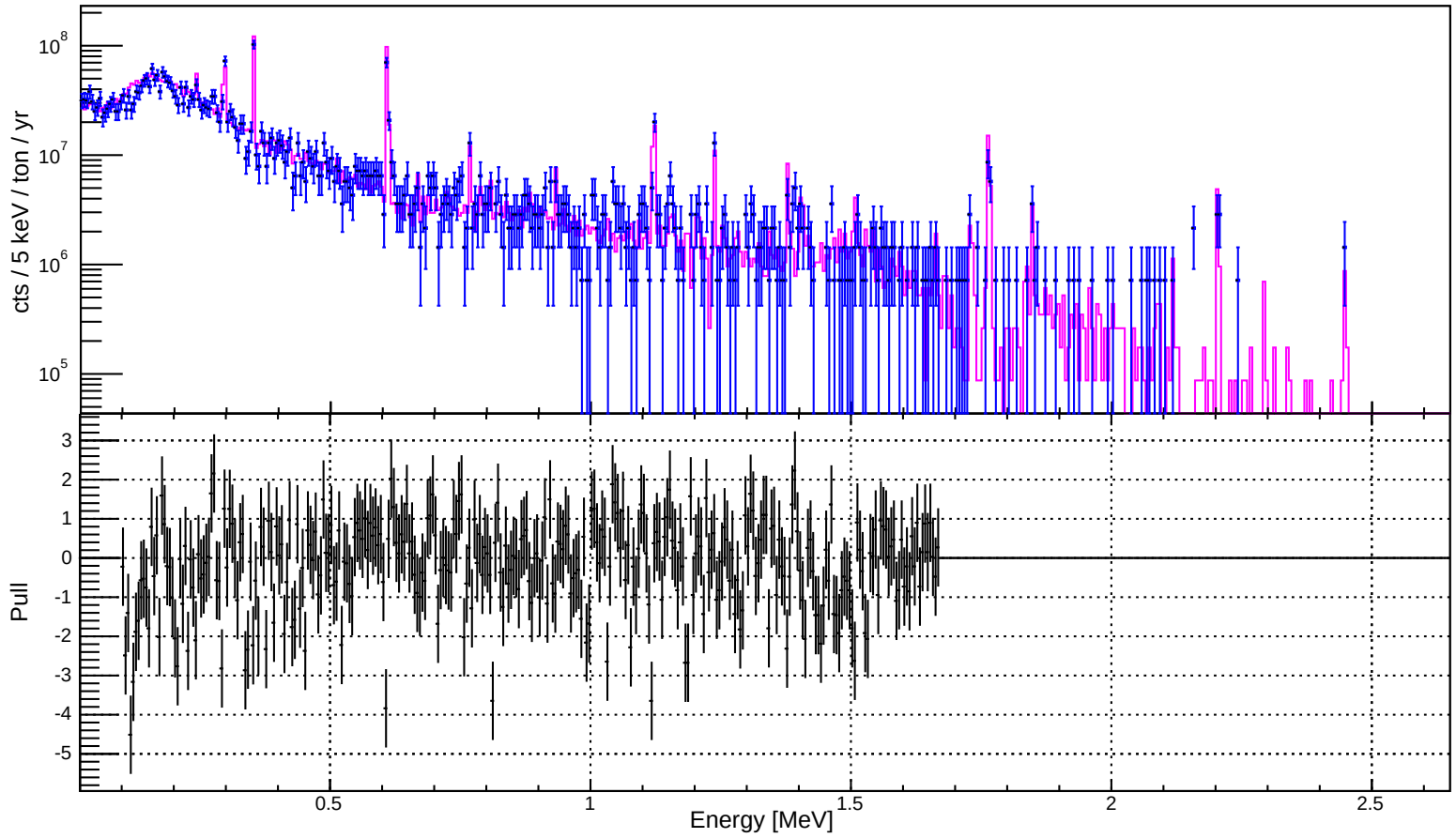

Figure D.27: The high-Rn energy spectrum of S3D4 (blue) and the 1-parameter fit to S3D4's data (pink). The one parameter is that corresponding to the "n2Vol_Rn" MC-fit group. (Bottom) The pull resulting from the fit to the data.

D.3.6 S3D5 of the PC (Detector B8473)

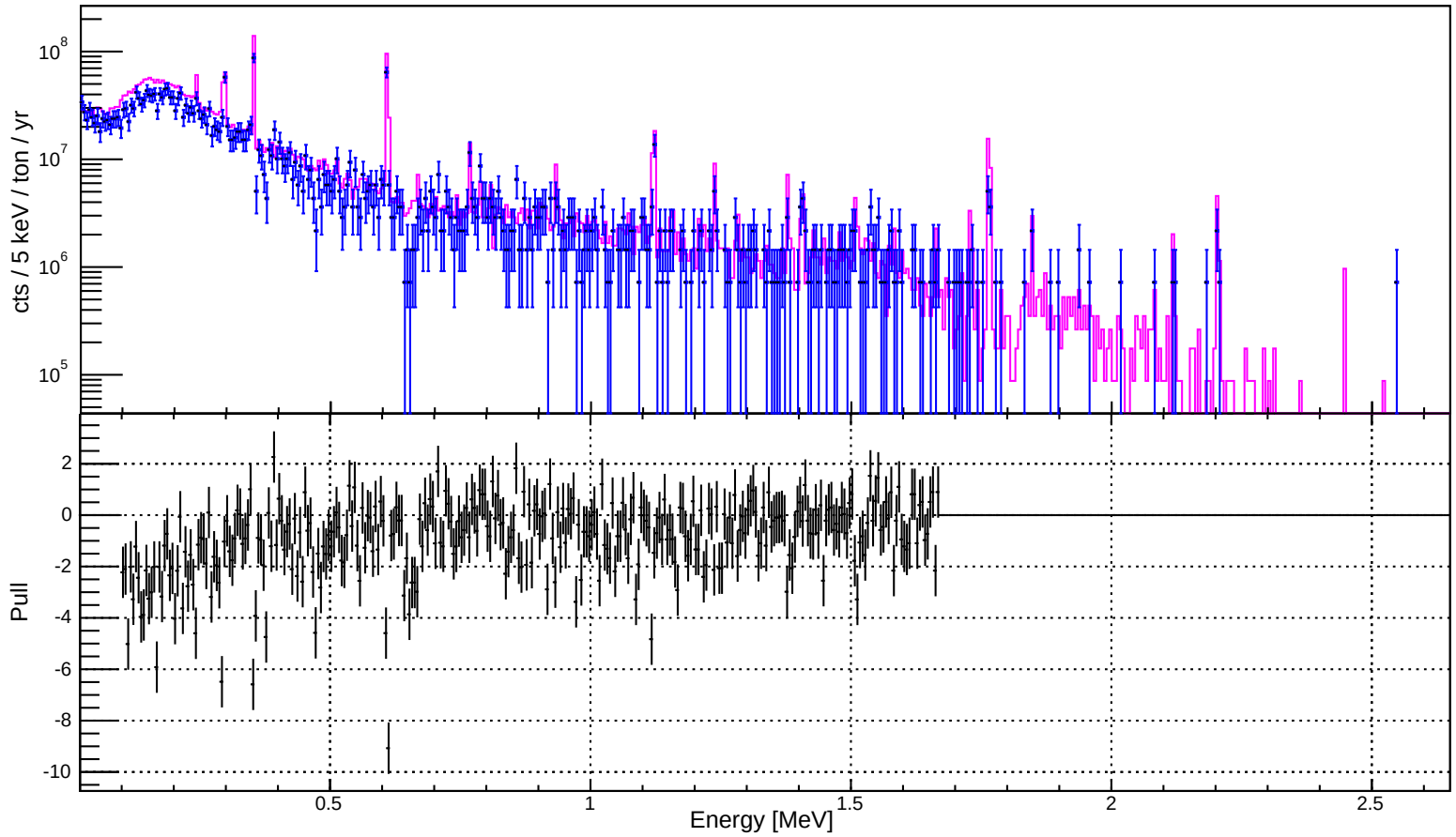

Figure D.28: (Top) The high-Rn energy spectrum of S3D5 (blue) and the 1-parameter fit to S3D5's data (pink). The one parameter is that corresponding to the "n2Vol_Rn" MC-fit group. (Bottom) The pull resulting from the fit to the data.

D.3.7 Histogram of Pulls

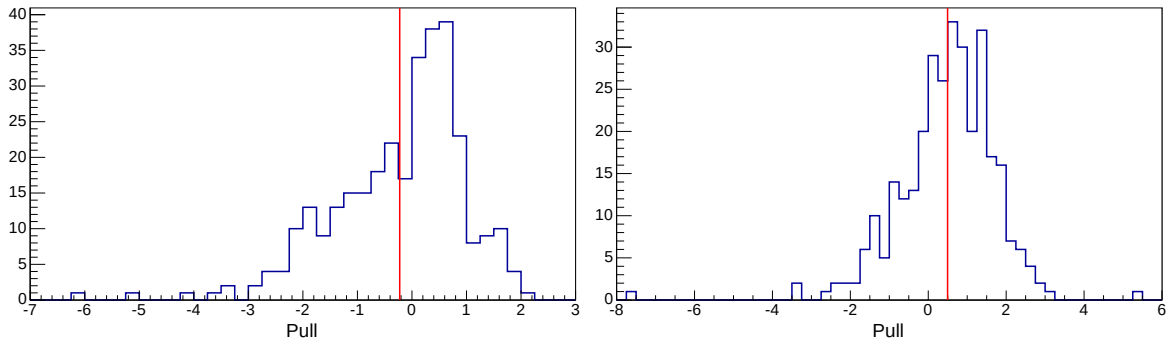

Figure D.29: A histogram of the pull values resulting from the 1-parameter fit to the high-Rn data for S1D2 and S1D3.

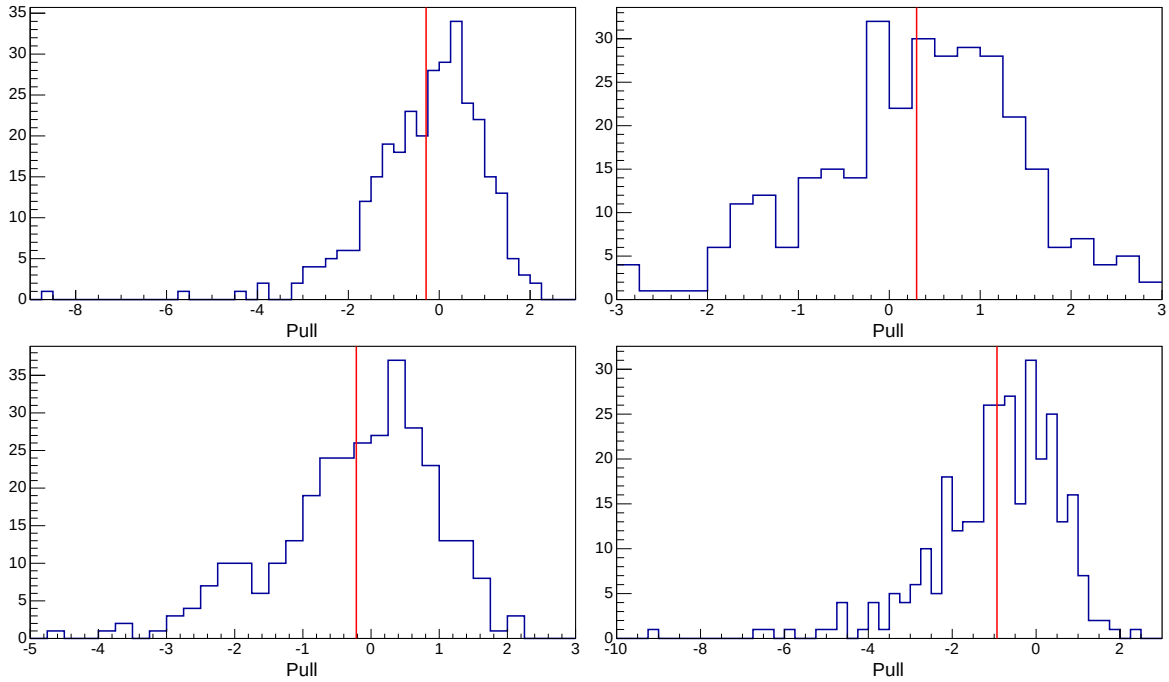

Figure D.30: A histogram of the pull values resulting from the 1-parameter fit to the high-Rn data for S3D1, S3D2, S3D4 and S3D5.

D.4 High-Radon Data with 83 Fit Parameters

D.4.1 S1D2 of the PC (Detector B8717)

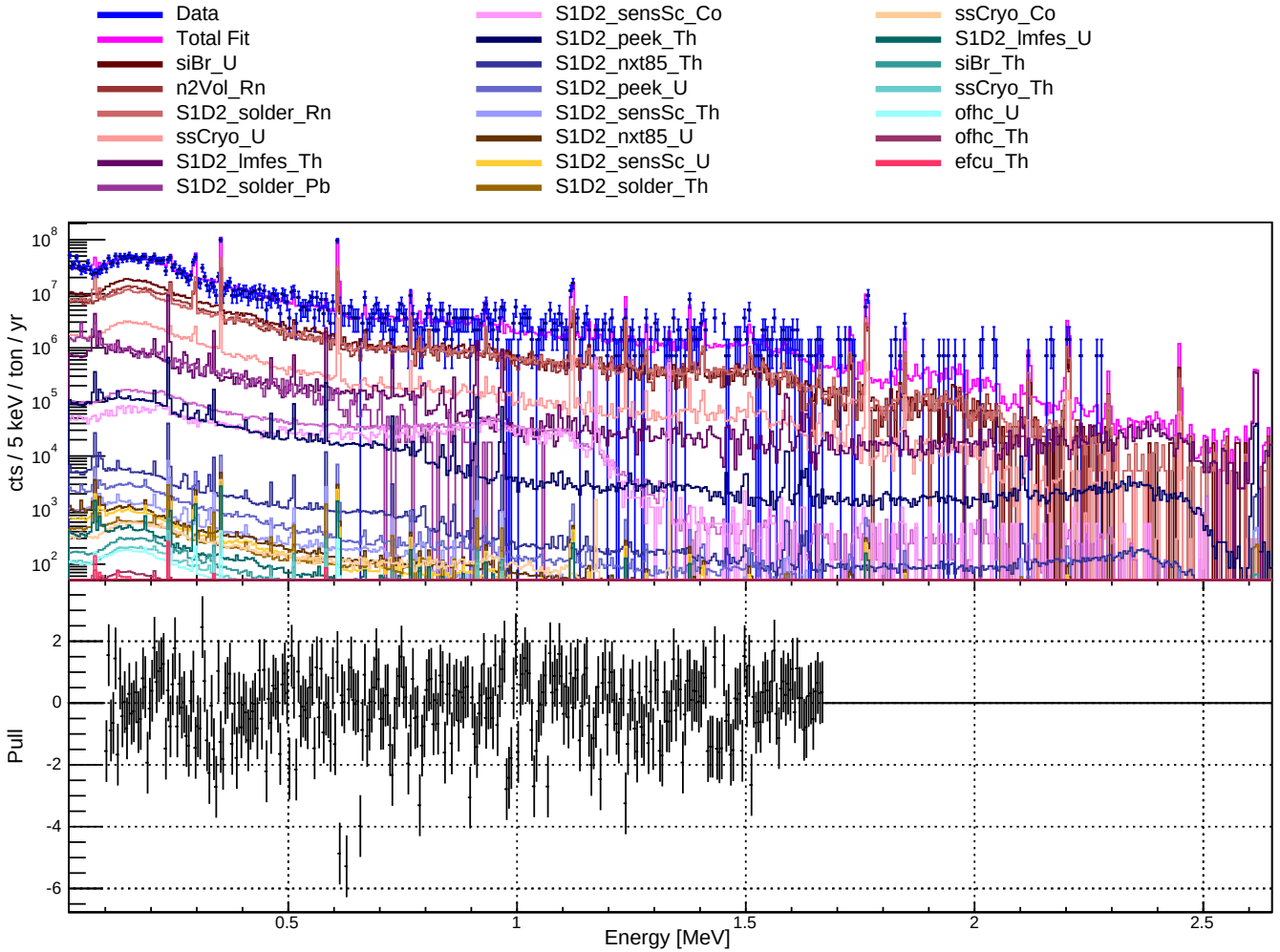

Figure D.31: (Top) The high-Rn energy spectrum of S1D2 (blue) and the 83-parameter fit to S1D2's data (pink). Also shown is each of the 23 MC-fit groups and the contribution they make to the total fit. In the accompanying legend, the MC-fit groups are listed in decreasing order (from top to bottom, left to right) by their contribution to the total fit. (Bottom) The pull resulting from the fit to the data.

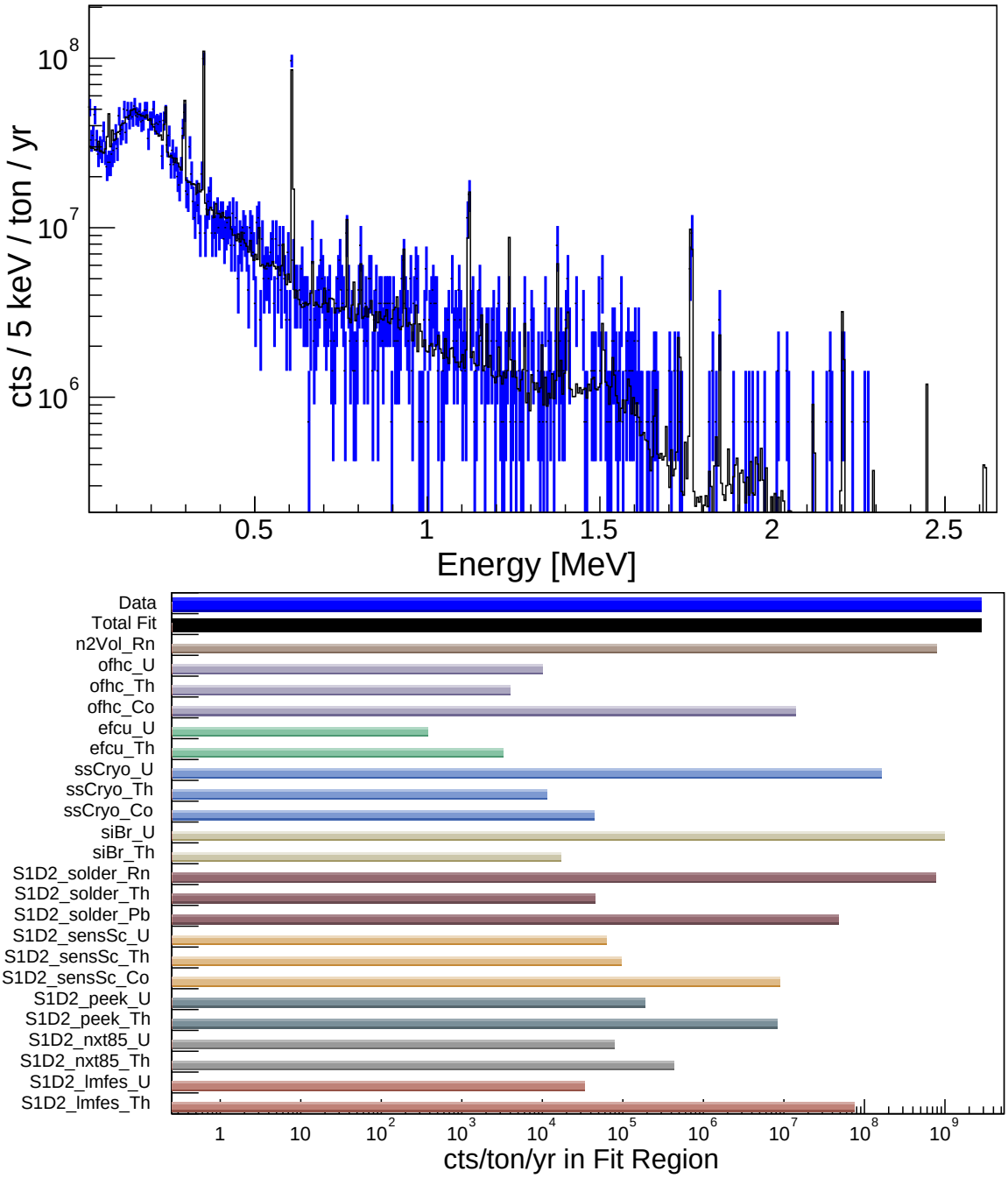

Figure D.32: (Top) The high-Rn energy spectrum of S1D2 (blue) and the 83-parameter fit to S1D2's data (black). (Bottom) The count rate in the fit region (100–1674 keV) for each MC-fit group, as seen by S1D2. To calculate the count rate, each MC-generated energy spectrum is scaled by the activity which resulted in the best 83-parameter fit to the high-Rn data.

D.4.2 S1D3 of the PC (Detector Ponama II)

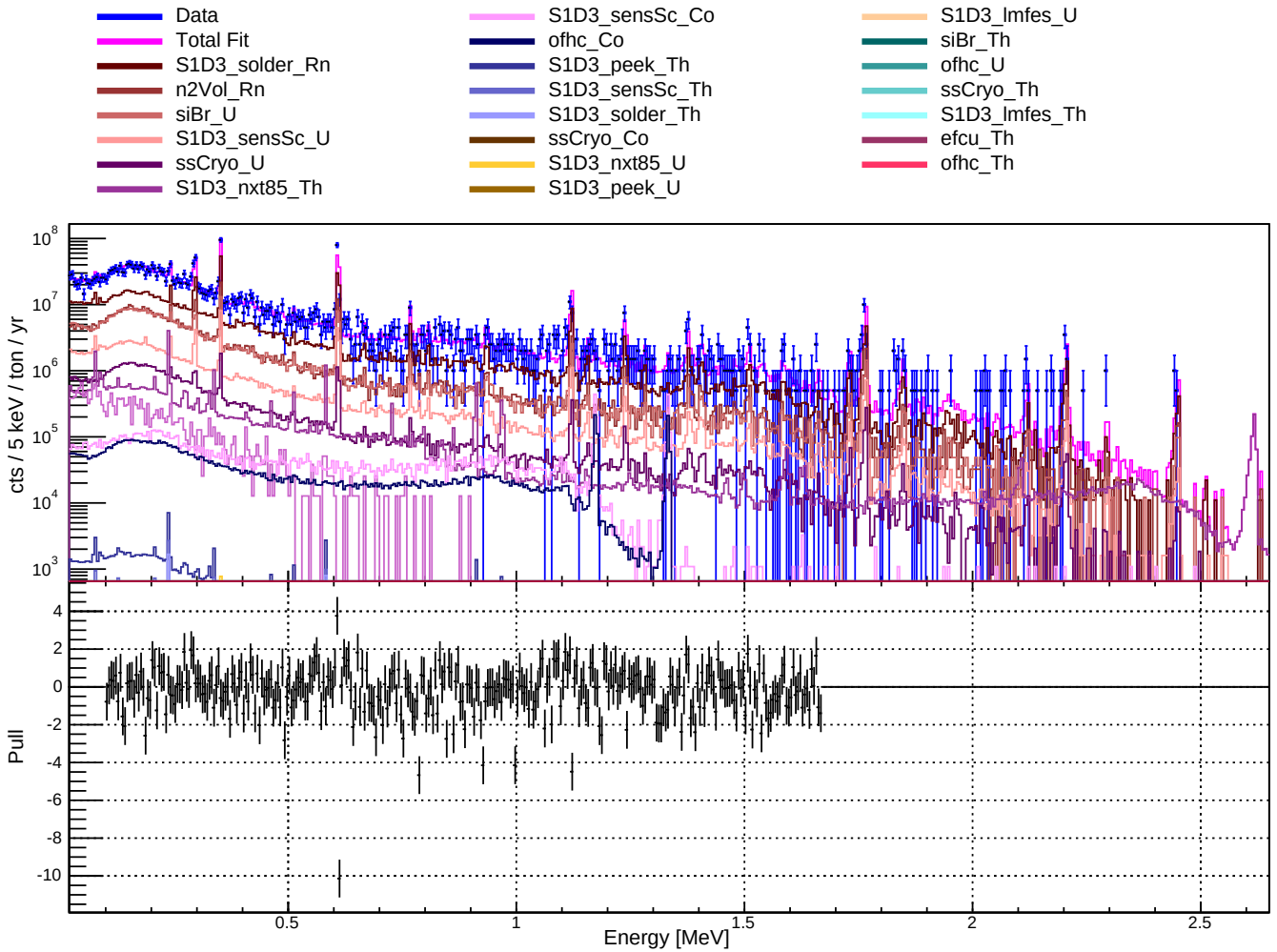

Figure D.33: (Top) The high-Rn energy spectrum of S1D3 (blue) and the 83-parameter fit to S1D3's data (pink). Also shown is each of the 23 MC-fit groups and the contribution they make to the total fit. In the accompanying legend, the MC-fit groups are listed in decreasing order (from top to bottom, left to right) by their contribution to the total fit. (Bottom) The pull resulting from the fit to the data.

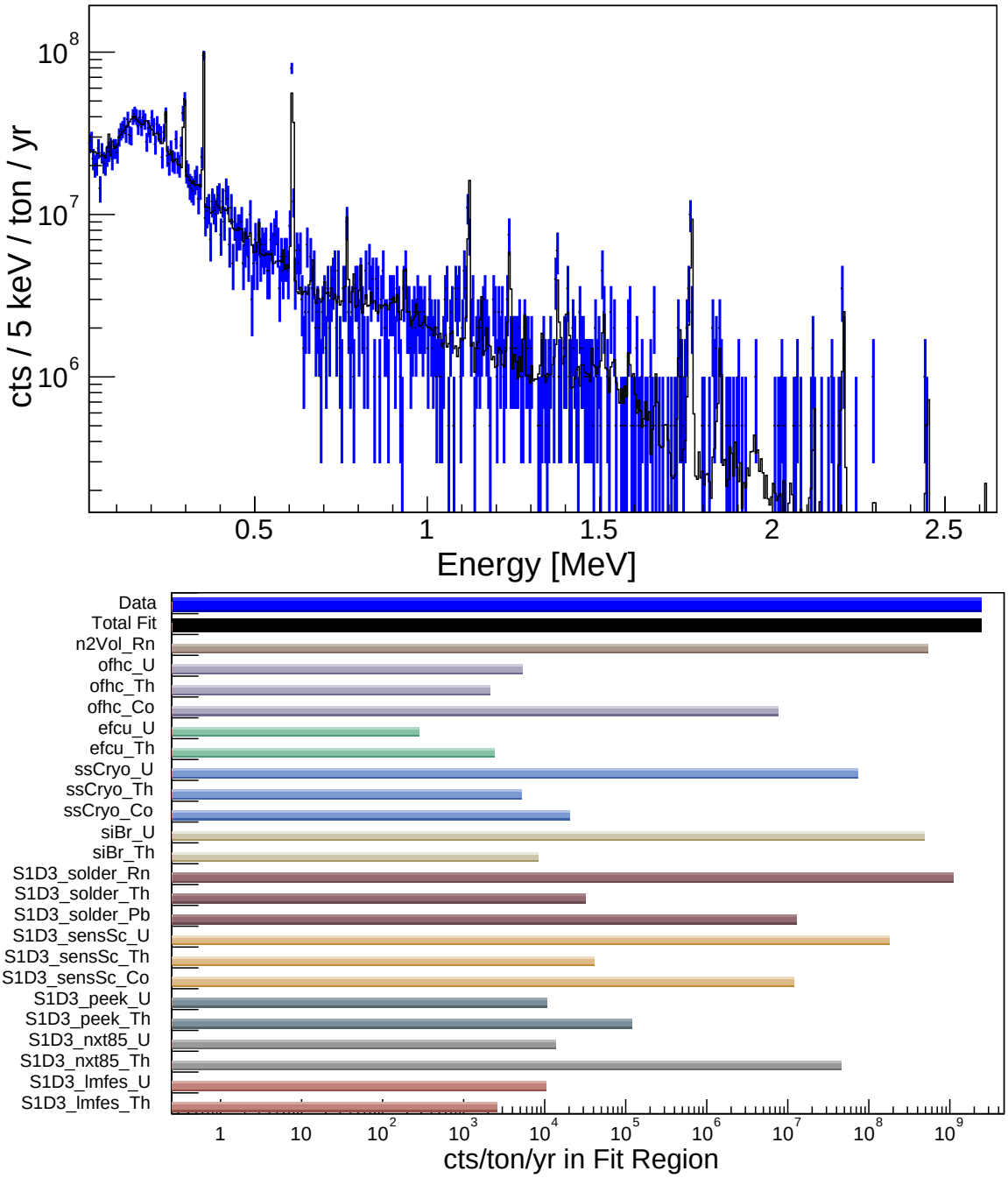

Figure D.34: (Top) The high-Rn energy spectrum of S1D3 (blue) and the 83-parameter fit to S1D3's data (black). (Bottom) The count rate in the fit region (100–1674 keV) for each MC-fit group, as seen by S1D3. To calculate the count rate, each MC-generated energy spectrum is scaled by the activity which resulted in the best 83-parameter fit to the high-Rn data.

D.4.3 S3D1 of the PC (Detector B8607)

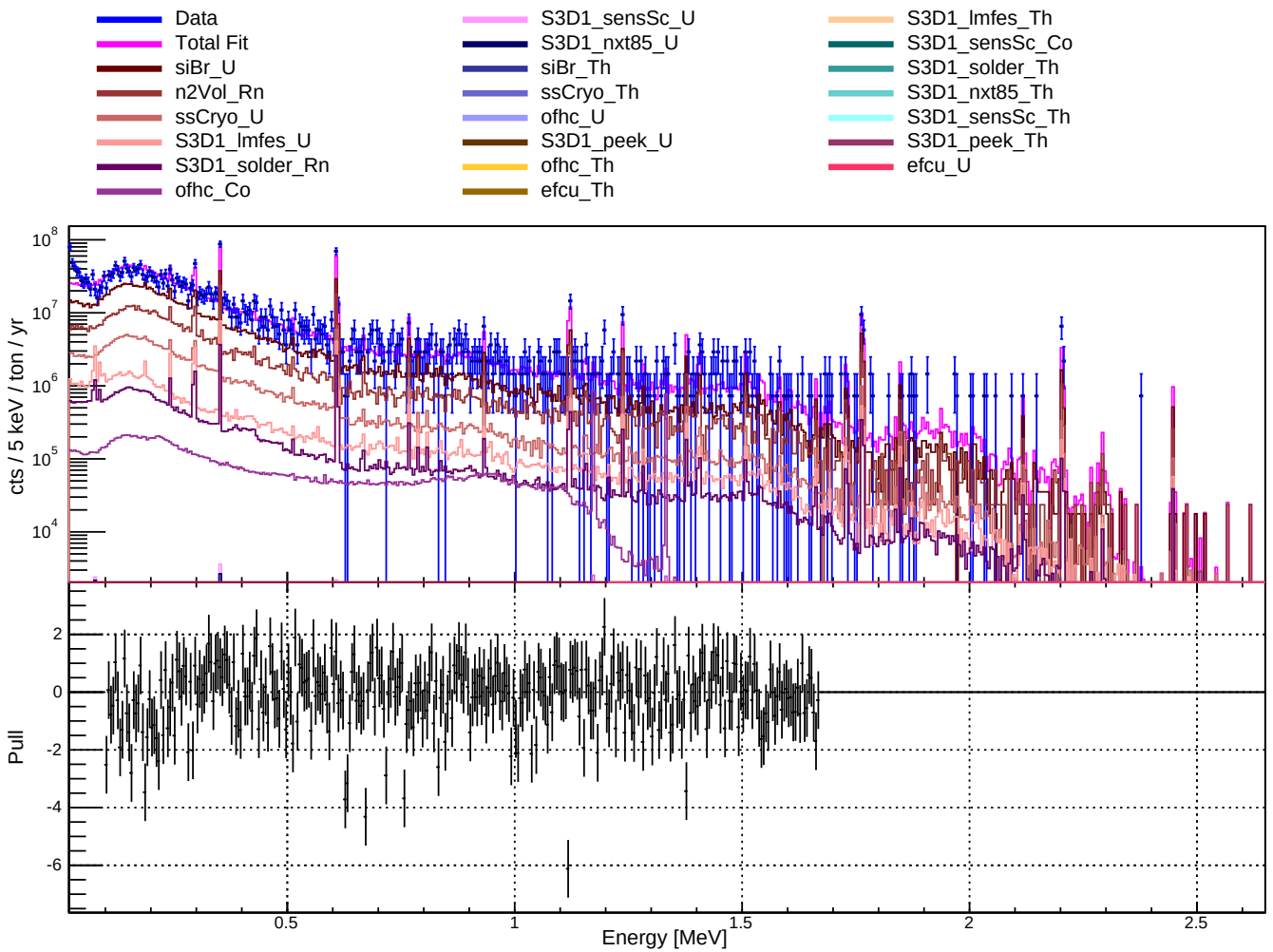

Figure D.35: (Top) The high-Rn energy spectrum of S3D1 (blue) and the 83-parameter fit to S3D1's data (pink). Also shown is each of the 23 MC-fit groups and the contribution they make to the total fit. In the accompanying legend, the MC-fit groups are listed in decreasing order (from top to bottom, left to right) by their contribution to the total fit. (Bottom) The pull resulting from the fit to the data.

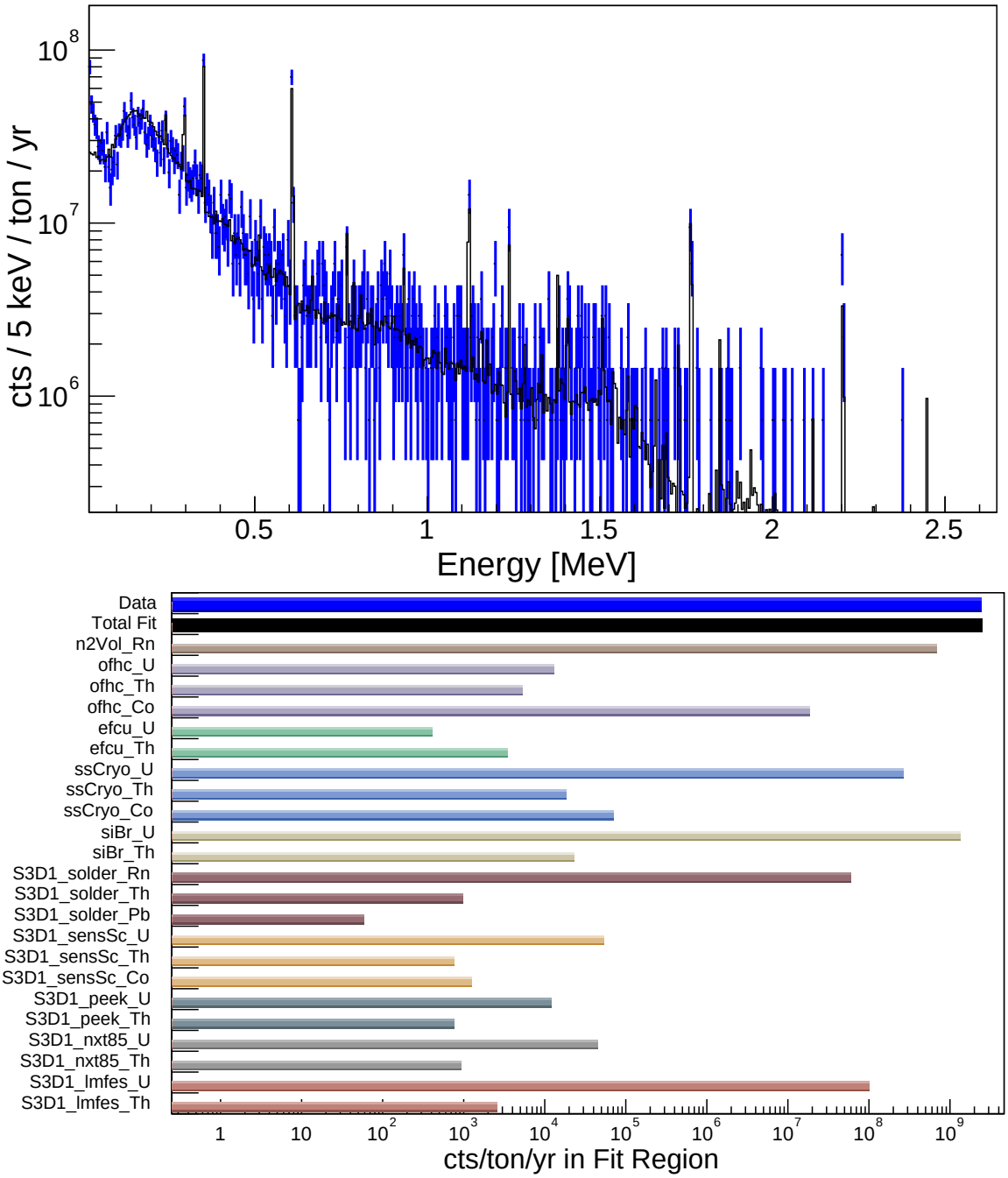

Figure D.36: (Top) The high-Rn energy spectrum of S3D1 (blue) and the 83-parameter fit to S3D1's data (black). (Bottom) The count rate in the fit region (100–1674 keV) for each MC-fit group, as seen by S3D1. To calculate the count rate, each MC-generated energy spectrum is scaled by the activity which resulted in the best 83-parameter fit to the high-Rn data.

D.4.4 S3D2 of the PC (Detector B8456)

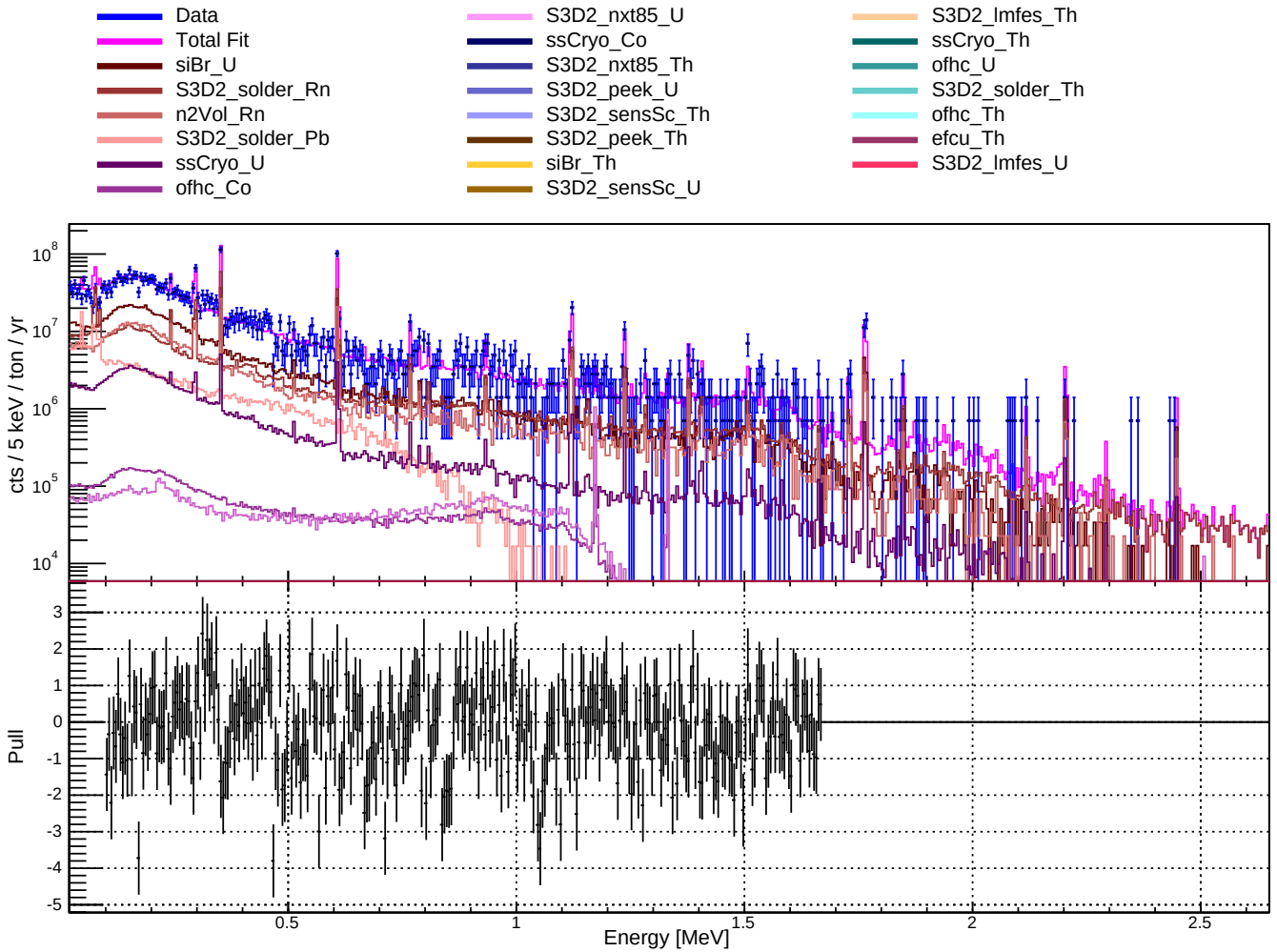

Figure D.37: (Top) The high-Rn energy spectrum of S3D2 (blue) and the 83-parameter fit to S3D2's data (pink). Also shown is each of the 23 MC-fit groups and the contribution they make to the total fit. In the accompanying legend, the MC-fit groups are listed in decreasing order (from top to bottom, left to right) by their contribution to the total fit. (Bottom) The pull resulting from the fit to the data.

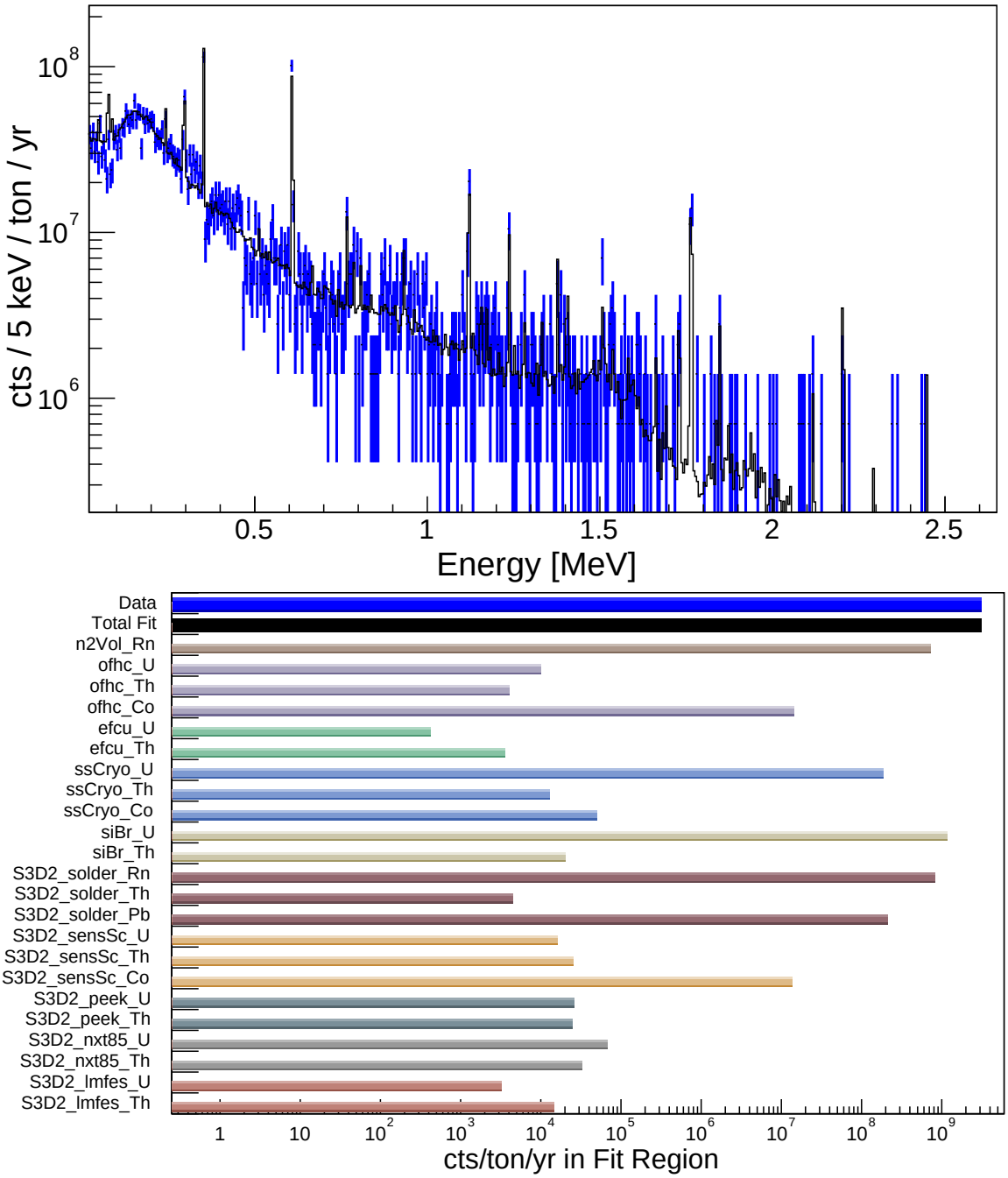

Figure D.38: (Top) The high-Rn energy spectrum of S3D2 (blue) and the 83-parameter fit to S3D2's data (black). (Bottom) The count rate in the fit region (100–1674 keV) for each MC-fit group, as seen by S3D2. To calculate the count rate, each MC-generated energy spectrum is scaled by the activity which resulted in the best 83-parameter fit to the high-Rn data.

D.4.5 S3D4 of the PC (Detector B8466)

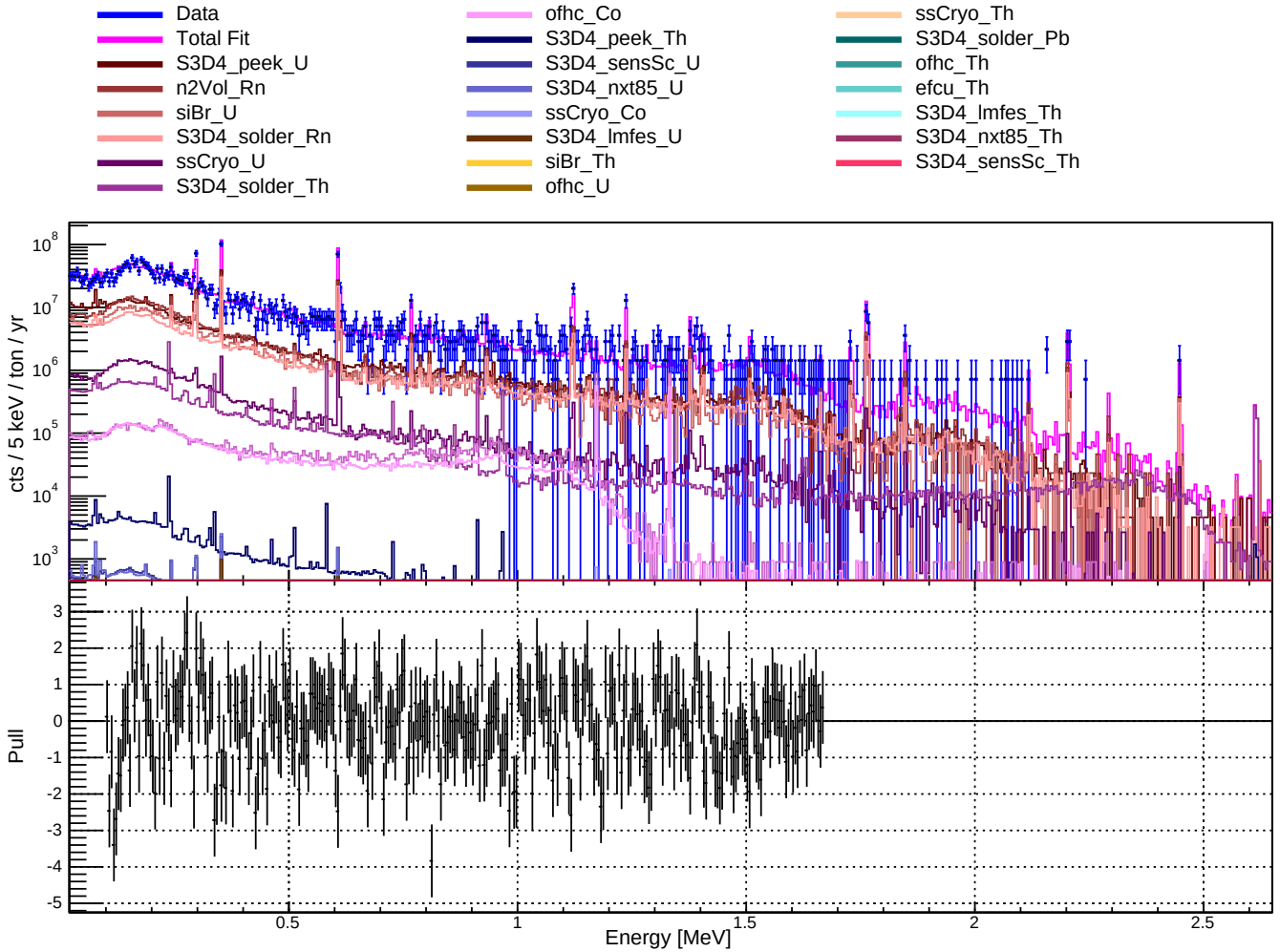

Figure D.39: (Top) The high-Rn energy spectrum of S3D4 (blue) and the 83-parameter fit to S3D4's data (pink). Also shown is each of the 23 MC-fit groups and the contribution they make to the total fit. In the accompanying legend, the MC-fit groups are listed in decreasing order (from top to bottom, left to right) by their contribution to the total fit. (Bottom) The pull resulting from the fit to the data.

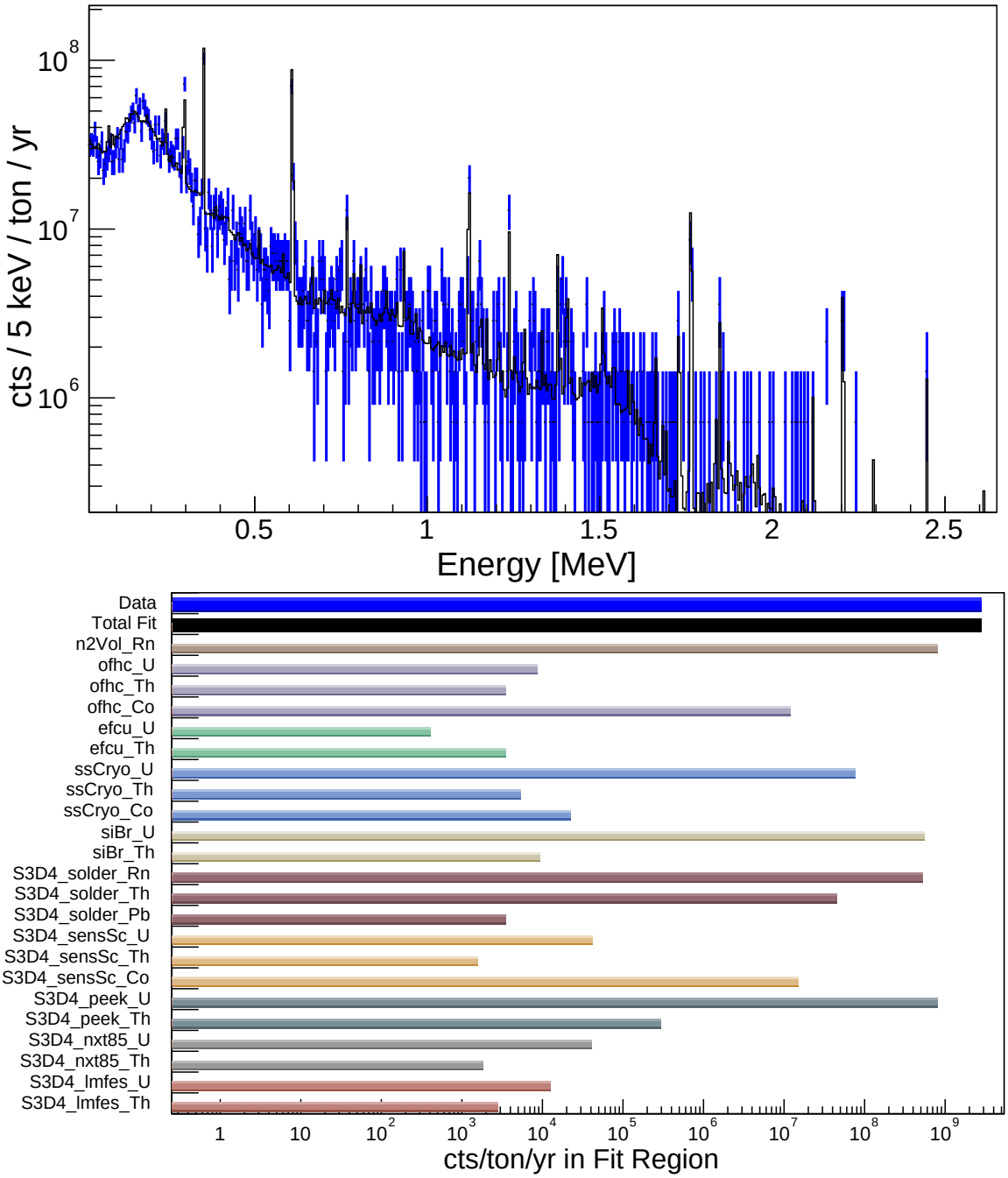

Figure D.40: (Top) The high-Rn energy spectrum of S3D4 (blue) and the 83-parameter fit to S3D4's data (black). (Bottom) The count rate in the fit region (100–1674 keV) for each MC-fit group, as seen by S3D4. To calculate the count rate, each MC-generated energy spectrum is scaled by the activity which resulted in the best 83-parameter fit to the high-Rn data.

D.4.6 S3D5 of the PC (Detector B8473)

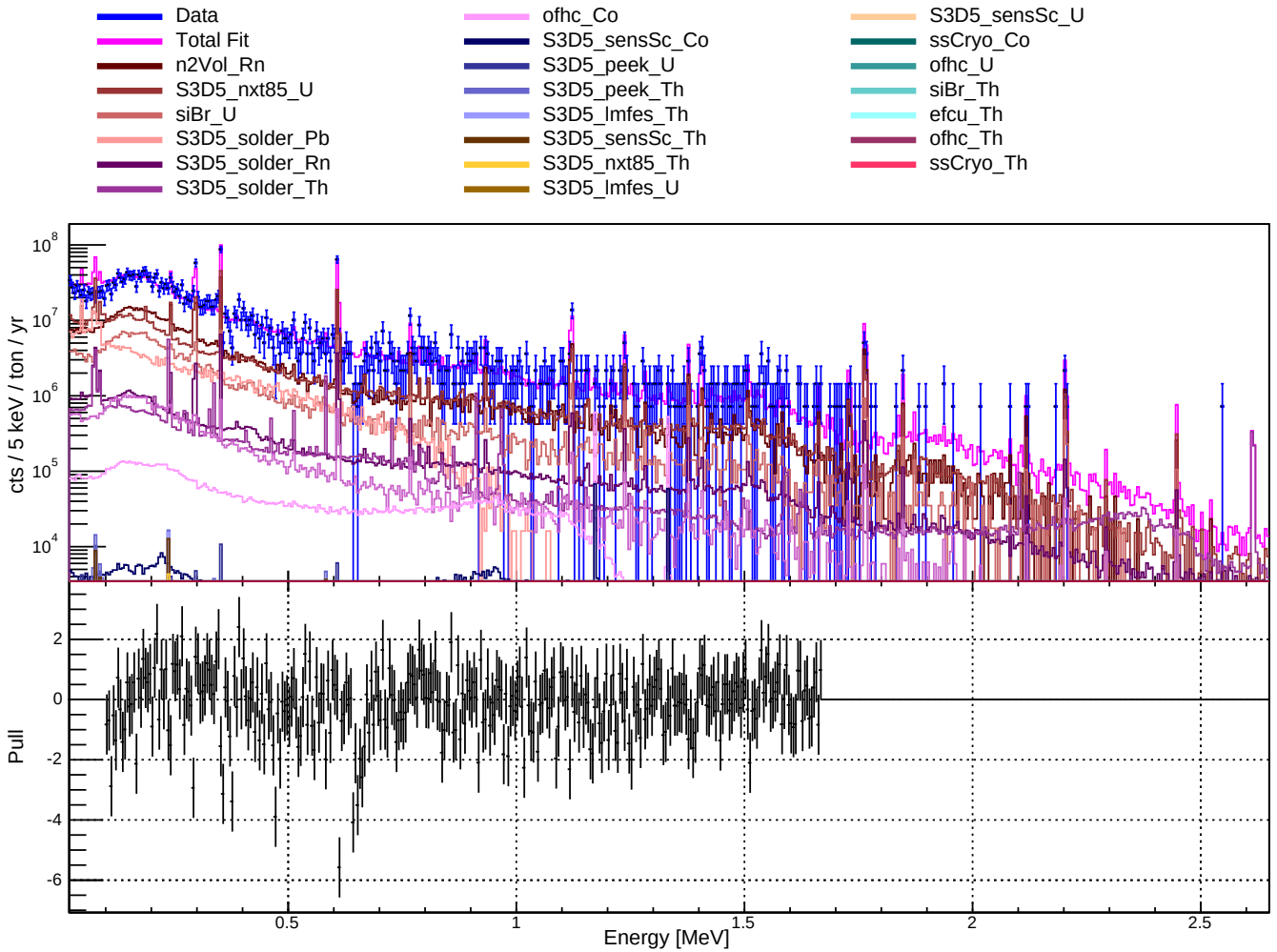

Figure D.41: (Top) The high-Rn energy spectrum of S3D5 (blue) and the 83-parameter fit to S3D5's data (pink). Also shown is each of the 23 MC-fit groups and the contribution they make to the total fit. In the accompanying legend, the MC-fit groups are listed in decreasing order (from top to bottom, left to right) by their contribution to the total fit. (Bottom) The pull resulting from the fit to the data.

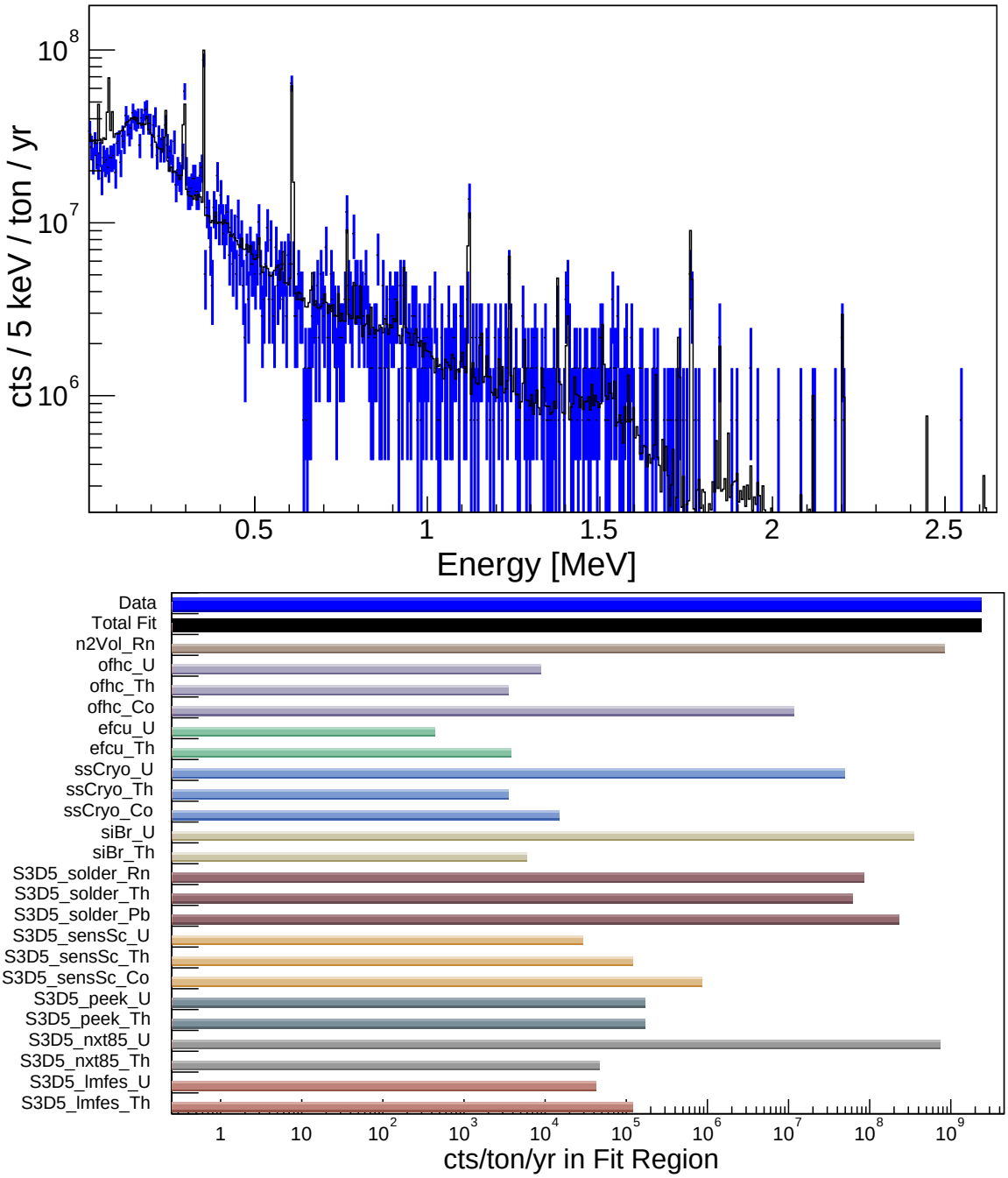

Figure D.42: (Top) The high-Rn energy spectrum of S3D5 (blue) and the 83-parameter fit to S3D5's data (black). (Bottom) The count rate in the fit region (100–1674 keV) for each MC-fit group, as seen by S3D5. To calculate the count rate, each MC-generated energy spectrum is scaled by the activity which resulted in the best 83-parameter fit to the high-Rn data.

D.4.7 Histogram of Pulls

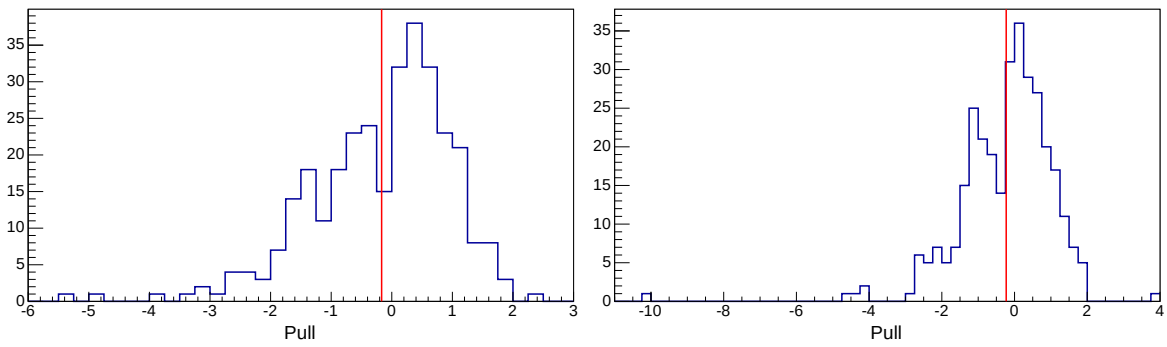

Figure D.43: A histogram of the pull values resulting from the 83-parameter fit to the high-Rn data for S1D2 and S1D3.

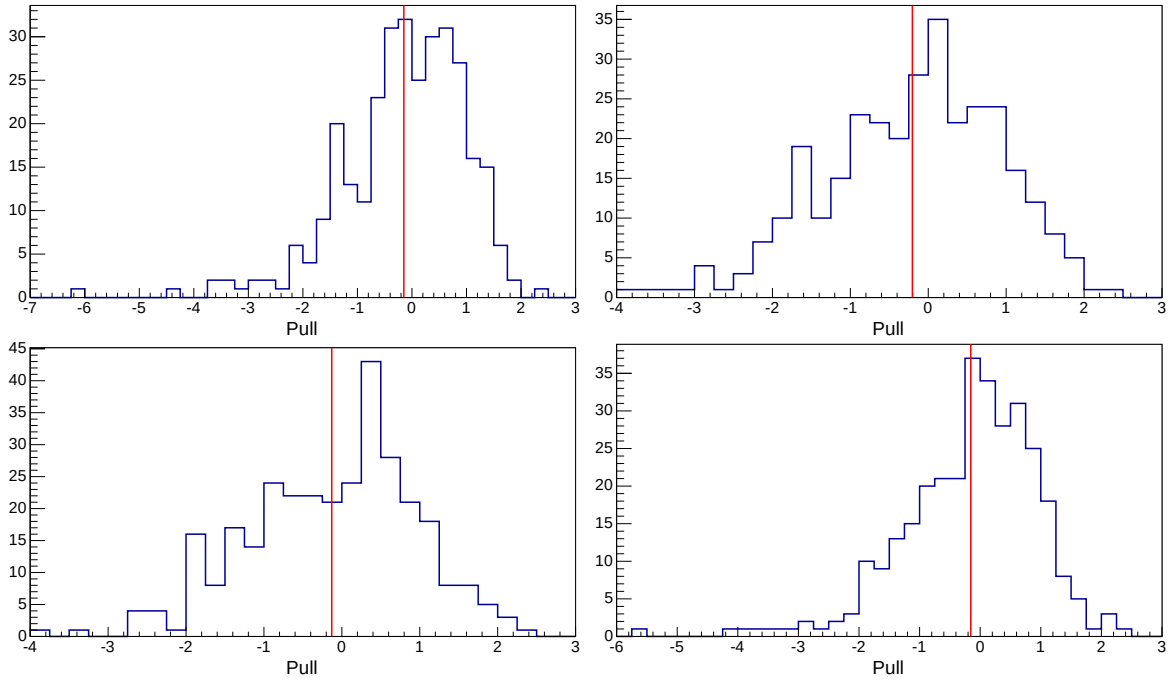

Figure D.44: A histogram of the pull values resulting from the 83-parameter fit to the high-Rn data for S3D1, S3D2, S3D4 and S3D5.

BIBLIOGRAPHY

[Aal04] C. Aalseth et al., "Neutrinoless double beta decay and direct searches for neutrino mass", APS Multidivisional Neutrino Study (2004).

[Abg14] N. Abgrall et al., "The MAJORANA DEMONSTRATOR Neutrinoless Double-Beta Decay Experiment", Advances in High Energy Physics **2014**, 365432 (2014).

[Abg15] N. Abgrall et al., "The MAJORANA Parts Tracking Database", Nucl. Instrum. Methods Phys. A **779**, 52 (2015).

[Abgon] N. Abgrall et al., "The MAJORANA DEMONSTRATOR Radioassay Program", Nucl. Instrum. Methods Phys. A (2015, in preparation).

[Alb14] J. B. Albert et al., "Improved measurement of the $2\nu\beta\beta$ half-life of ^{136}Xe with the EXO-200 detector", Phys. Rev. C **89**, 015502 (2014).

[All03] J. Allison et al., "Geant4 - a simulation toolkit", Nucl. Instrum. Methods Phys. A **506**, 250 (2003).

[All06] J. Allison et al., "Geant4 developments and applications", IEEE Transactions on Nuclear Science **53**, 270 (2006).

[Arn08] C. Arnaboldi et al., "Results from a search for the $0\nu\beta\beta$-decay of ^{130}Te", Phys. Rev. C **78** (2008).

[Arn11] R. Arnold et al., "Measurement of the $\beta\beta$ Decay Half-Life of ^{130}Te with the NEMO-3 Detector", Phys. Rev. Lett. **107**, 062504 (2011).

[Aug12] M. Auger et al., "Search for neutrinoless double-beta decay in ^{136}Xe with EXO-200", Phys. Rev. Lett. **109** (2012).

[Ber12] J. Beringer et al., "Review of Particle Physics", Phys. Rev. D **86**, 010001 (2012).

[Bev69] P. Bevington and D. K. Robinson, *Data Reduction and Error Analysis for the Physical Sciences*, McGraw-Hill, 1969.

[Bos11] M. Boswell et al., "MaGe - a Geant4-Based Monte Carlo Application Framework for Low-Background Germanium Experiments", IEEE Transactions on Nuclear Science **58**, 1212 (2011).

[Bru96] R. Brun and F. Rademakers, "{ROOT} — An object oriented data analysis framework", in *AIHENP Workshop, Lausanne*, 1996.

[Bru97] R. Brun and F. Rademakers, "{ROOT} — An object oriented data analysis framework", Nucl. Instrum. Methods Phys. A **389**, 81 (1997).

[Bun85] K. Bunzl and W. Kracke, "Natural Radioactive Contaminants in Solder", Nucl. Instrum. Methods Phys. A **238**, 191 (1985).

[CC56] F. R. C.L. Cowan et al., "Detection of the Free Neutrino: a Confirmation", Science **124**, 103 (1956).

[Col13] T. G. Collaboration et al., "Measurement of the half-life of the two-neutrino double beta decay of 76 Ge with the GERDA experiment", Journal of Physics G: Nuclear and Particle Physics **40**, 035110 (2013).

[Cow98] G. Cowan, *Statistical Data Analysis*, Oxford University Press, 1998.

[Det15] J. Detwiler, "Private Communications", 2015.

[Ell02] S. Elliott and P. Vogel, "Double Beta Decay", Annu. Rev. Nucl. Part. Sci. **52**, 115 (2002).

[Fes85] H. Fesefeldt, 1985.

[Fin13] P. Finnerty, *A Direct Dark Matter Search with the* MAJORANA *Low-Background Broad Energy Germanium Detector*, Ph.D. thesis, University of North Carolina at Chapel Hill, 2013.

[Gan13] A. Gando et al., "Limit on Neutrinoless $\beta\beta$ Decay of ^{136}Xe from the First Phase of KamLAND-Zen and Comparison with the Positive Claim in ^{76}Ge", Phys. Rev. Lett. **110**, 062502 (2013).

[Gil07] G. R. Gilmore, *Practical Gamma-ray Spectrometry*, John Wiley & Sons, Ltd, second edition, 2007.

[Hel80] R. Helmer and M. Lee, "Analytical Functions for Fitting Peaks from Ge Semiconductor Detectors", Nucl. Instrum. Methods **178**, 499 (1980).

[Hop08] E. Hoppe et al., "A method for removing surface contamination on ultra-pure copper spectrometer components", J. Radioanal. Nucl. Chem. **276**, 645 (2008).

[How04] M. Howe et al., "Sudbury Neutrino Observatory Neutral Current Detector Acquisition Software Overview", IEEE Transactions on Nuclear Science **51**, 878 (2004).

[INL] "Idaho National Laboratory Online Spectrum Catalog for Germanium", `http://www4vip.inl.gov/gammaray/catalogs/ge/catalog_ge.shtml`.

[Jam04a] F. James, "MINUIT: The Interpretation of Errors", (2004).

[Jam04b] F. James and M. Winkler, "MINUIT User's Guide", (2004).

[KK01] H. Klapdor-Kleingrothaus et al., "Latest Results from the Heidelberg-Moscow double beta decay experiment", Eur. Phys. J. **A12** (2001).

[KK04] H. Klapdor-Kleingrothaus et al., "Search for neutrinoless double beta decay with enriched ^{76}Ge in Gran Sasso 1990-2003", Phys. Lett. B **586**, 198 (2004).

[KK06] H. Klapdor-Kleingrothaus and I. Krivosheina, "The Evidence for the Observation of $0\nu\beta\beta$ Decay: The Identification of $0\nu\beta\beta$ Events From the Full Spectra", Mod. Phys. Lett. A **21**, 1547 (2006).

[Lau09] M. Laubenstein and G. Heusser, "Cosmogenic Radionuclides in Metals as Indicator for Sea Level Exposure History", Applied Radiation and Isotopes **67**, 750 (2009).

[LC08] J. W. L. Camilleri, E. Lisi, "Neutrino Masses and Mixings: Status and Prospects", Annu. Rev. Nucl. Part. Sci. **58**, 343 (2008).

[Lon90] L. Longoria, A. Naboulsi, P. Gray, and T. MacMahon, "Analytical peak fitting for gamma-ray spectrum analysis with Ge detectors", Nucl. Instrum. Methods Phys. A **299**, 308 (1990).

[Mac14] C. Macolino et al., "Results on Neutrinoless Double-Beta Decay of ^{76}Ge from GERDA Phase I", Mod. Phys. Lett. A **29**, 1430001 (2014).

[Mas15] R. Massarczyk, "Private Communications", 2015.

[Mei06] D.-M. Mei and A. Hime, "Muon-induced background study for underground laboratories", Phys. Rev. D **73** (2006).

[NER] "NERSC", `http://www.nersc.gov`.

[NND] "National Nuclear Data Center, Chart of Nuclides", `http://www.nndc.bnl.gov/chart/`.

[NO13] R. A. N.R. Overman, E.W. Hoppe, "Surface cleaning techniques: ultra-trace ICP-MS sample preparation and assay of HDPE", J. Radioanal. Nucl. Chem. **296**, 1303 (2013).

[Oli14] K. Olive et al., Chin. Phys. C **38** (2014).

[Par91] J. Parker et al., *Passive Nondestructive Assay of Nuclear Materials*, Los Alamos National Laboratory, 1991.

[Poo01] A. Poon, X. Chen, and C. Okada, "Statistical Limitation of the In-situ Monitoring Technique", 2001.

[Rad] "DURRIDGE RAD7", `http://www.durridge.com/products_rad7.shtml`.

[Rad00] D. Radford, *Radware: Notes on the use of the program gf3*, Oak Ridge National Laboratory, 2000.

[Rad13] D. Radford, "Private Communications", 2013.

[Sch82] J. Schechter and J. Valle, "Neutrinoless double-β decay in SU(2)×U(1) theories", Phys. Rev. D **25**, 2951 (1982).

[Sch12] A. Schubert, *Searching for neutrinoless double-beta decay of germanium-76 in the presence of backgrounds*, Ph.D. thesis, University of Washington, 2012.

[SiB] "Properties of Silicon Bronze", `http://www.onlinemetals.com/productguides/bronzeguide.cfm`.

[Str12] J. Strain et al., "Parts Cleaning for the MAJORANA DEMONSTRATOR", TUNL LI Progress Report (2011-2012).

[Zim12] S. Zimmermann, J. Anderson, D. Doering, J. Joseph, C. Lionberger, T. Stezelberger, and H. Yaver, "Implementation and Performance of the Electronics and Computing System of the Gamma Ray Energy Tracking In-Beam Nuclear Array (GRETINA)", Nuclear Science, IEEE Transactions on **59**, 2494 (2012).